UNIVERSITY OF CALIFORNIA
RIVERSIDE

Molecular Beam Epitaxy and High-Pressure Studies of van der Waals Magnets

A Dissertation submitted in partial satisfaction
of the requirements for the degree of

Doctor of Philosophy

in

Materials Science and Engineering

by

Dante J. O'Hara

September 2019

Dissertation Committee:

Professor Harry Tom, Chairperson
Professor Roland Kawakami
Professor Jing Shi

Copyright by
Dante J. O'Hara
2019

The Dissertation of Dante J. O'Hara is approved:

Committee Chairperson

University of California, Riverside

Acknowledgments

Struggle is an understatement of graduate school. While I am writing this I am also struggling with words to describe my experience in graduate school. There were many late nights, many ups and downs, many arguments, and many learning curves. This will all develop me into the scientist I hope to become and I will be forever indebted to those who have been a part of this journey.

I have to first thank my undergraduate mentors for pushing me to go to graduate school. These include: Dr. Ernest Levister, Jr., Elmer Thomas, Dr. Leopold Green, Jr., Steven Henderson, and Dr. Desire Whitmore. Second, I have to thank my PhD advisor, Professor Roland Kawakami, for giving me the opportunity to go to graduate school and mentoring me to become a good materials scientist. I would not be here without you, and I am very thankful for that regardless of any disagreements we may have had throughout our time together. Third, I would like thank Dr. Adrian Swartz for being my undergraduate research mentor and exposing me to materials research when I did not know anything.

I would also like to thank my labmates during the years after the group left for OSU, specifically Dr. Patrick Odenthal for teaching me MBE and Dr. Walid Amamou for helping me get on my first publication and also being a good roommate for 3 years. During the OSU years, I would also like to thank a couple of folks: Dr. Adam Ahmed, Dr. Igor Pinchuk and Dr. Jinsong Xu for being such good colleagues on the MBE front and great friends outside of the lab; Drs. Elizabeth and Tim McCormick for being awesome roommates/great friends to grab a drink with and vent to about primarily lab or relationship problems; Professors Jyoti Katoch and Simran Singh for being great friends and mentors;

Tiancong Zhu for helping so much on projects especially on 2D magnetism (I would have not had my first two papers without you).

I will also like to thank several MBE collaborators at OSU. Choong Hee Lee, Sriram Krishnamoorthy, Zhanbo Xia, Yuewei Zhang, Brelon May, Mark Brenner, Prof. Siddharth Rajan, Prof. Roberto Myers, and many more that became great friends and mentors during my time in Ohio. I am very thankful for all of your support and the late nights together in the MBE lab.

Last, I would like to thank several scientists at LLNL for allowing me to intern at the lab and also sponsor me as a GEM fellow and Lawrence Graduate Scholar. These include: Dr. Ibo Matthews, Dr. Scott McCall, Dr. Alex Baker, Dr. Ryan Stillwell, and Dr. Jason Jeffries. Thank you all for your help and guidance and I will forever appreciate your time for mentoring me on this journey.

A portion of the text in Chapter 3 appears in "Molecular beam epitaxy of 2D-layered gallium selenide on GaN substrates" J. Appl. Phys. 121 (9), 094302 (2017) by C. H. Lee, S. Krishnamoorthy, D. J. O'Hara, M. R. Brenner, J. M. Johnson, J. S. Jamison, R. C. Myers, R. K. Kawakami, J. Hwang, S. Rajan. The dissertation author was one of the primary researchers on this project and third author. Another portion of the text in Chapter 3 appears in "Large-area $SnSe_2$/GaN heterojunction diodes grown by molecular beam epitaxy" Appl. Phys. Lett. 111 (20), 202101 (2017) by C. H. Lee, S. Krishnamoorthy, P. K. Paul, D. J. O'Hara, M. R. Brenner, R. K. Kawakami, A. R. Arehart, S. Rajan. The dissertation author was one of the primary researchers that developed the material and also fourth author on the publication.

A portion of the text in Chapter 4 appears in "Room temperature intrinsic ferromagnetism in epitaxial manganese selenide films in the monolayer limit" Nano Lett. 18 (5), 3125-3131 (2018) by D. J. O'Hara, T. Zhu, A. H. Trout, A. S. Ahmed, Y. K. Luo, C. H. Lee, M. R. Brenner, S. Rajan, J. A. Gupta, D. W. McComb, R. K. Kawakami. The dissertation author was the primary researcher and author.

A portion of the text in Chapter 5 appears in "Importance of paramagnetic background subtraction for determining the magnetic moment in epitaxially grown ultrathin van der waals magnets" IEEE Mag. Lett. 9, 1-5 (2018) by D. J. O'Hara, T. Zhu, R. K. Kawakami. The dissertation author was the primary researcher and author.

Part of the funding for this work was generously provided through the Lawrence Graduate Scholar Program. This work was performed under the auspices of the US Department of Energy by Lawrence Livermore National Laboratory (LLNL) under Contract No. DE-AC52-07NA27344. A portion of the work in Chapter 8 was performed at HPCAT (Sector 16), Advanced Photon Source (APS), Argonne National Laboratory. HPCAT operations are supported by DOE-NNSA's Office of Experimental Sciences. The Advanced Photon Source is a U.S. Department of Energy (DOE) Office of Science User Facility operated for the DOE Office of Science by Argonne National Laboratory under Contract No. DE-AC02-06CH11357. A portion of the work in Appendix A was performed at beamline 6.3.1 at the Advanced Light Source (ALS), Lawrence Berkeley National Laboratory. The Advanced Light Source is supported by the Director, Office of Science, Office of Basic Energy Sciences, of the U.S. Department of Energy under Contract No. DE-AC02-05CH11321. LLNL-TH-788497.

To my mother for all of her much needed support.

ABSTRACT OF THE DISSERTATION

Molecular Beam Epitaxy and High-Pressure Studies of van der Waals Magnets

by

Dante J. O'Hara

Doctor of Philosophy, Graduate Program in Materials Science and Engineering
University of California, Riverside, September 2019
Professor Harry Tom, Chairperson

Van der Waals (vdW) magnets provide an exciting opportunity for exploring two-dimensional (2D) magnetism for next generation scientific and technological advances. While previously realized in 3D ultrathin films where the magnetism is stabilized via substrate-assisted magnetic anisotropy, recent reports have shown intrinsic ferromagnetism at low temperatures (< 60 K) in isolated μm-sized flakes mechanically exfoliated from a bulk single-crystal down to a single-atomic layer. This opens up the possibility to truly study magnetism in free-standing 2D layers without direct effects from the underlying substrate and being intrinsically susceptible to surface effects such as atomic adsorbates, electrostatic gating, and proximity-induced phenomena. This dissertation examines the molecular beam epitaxy (MBE) growth and characterization of new 2D magnets, monolayers of $MnSe_2$ and VSe_2, that show ferromagnetic ordering above room temperature. Growth on different substrates and varying the substrate temperature during growth affects the growth mode and morphology of the deposited 2D magnet and also affects the measured magnetization. Direct atomic and magnetic imaging via scanning transmission electron microscopy (STEM)

and scanning tunneling microscopy (STM) show stable 2D magnetic layers.

Due to the lack of dangling bonds at the surface of these 2D magnets, applying external epitaxial strain is a challenge. Later in this dissertation, the magnetic, electronic, and structural properties of vdW-layered, Fe-deficient $Fe_{3-x}GeTe_2$ are systematically investigated by the application of high pressure. Fe_3GeTe_2 is of particular interest due to its high Curie temperature, T_c, strong perpendicular magnetic anisotropy, and tunable magnetic properties depending on the concentration of Fe and its thickness. Electrical and magneto-transport measurements show a suppression in T_c with an increasing pressure up to 20 GPa. The decrease in T_c is due to the lattice shrinkage from pressurization which leads to a weakening of the exchange interaction. These observations showcase the tunability in vdW magnets via pressure which can complement other external stimuli such as chemical doping, making them candidates for future spintronic, electronic and photonic devices.

Contents

List of Figures **xiii**

List of Tables **xvi**

1 Toward Magnetism in the Ultrathin Limit **1**
1.1 Introduction to Magnetism and Magnetic Materials 1
1.2 Magnetic Anisotropy 6
1.2.1 Magnetocrystalline Anisotropy 6
1.2.2 Shape Anisotropy 7
1.2.3 Surface Anisotropy 8
1.3 Magnetism in Low Dimensions 9
1.4 Magnetism in van der Waals Materials 12

2 Experimental Techniques **20**
2.1 Molecular Beam Epitaxy (MBE) 20
2.1.1 Introduction to MBE 20
2.1.2 Vacuum Science Fundamentals 21
2.1.3 Growth Chamber Basics 23
2.1.4 Reflection High-Energy Electron Diffraction (RHEED) 25
2.1.5 Growth Modes 30
2.1.6 Types of Epitaxial Growth 32
2.2 Structural Characterization 34
2.2.1 X-Ray Diffraction (XRD) 34
2.2.2 X-Ray Reflectometry (XRR) 36
2.2.3 Atomic Force Microscopy (AFM) 38
2.2.4 Scanning Tunneling Microscopy (STM) 39
2.2.5 Scanning Transmission Electron Microscopy (STEM) 41
2.3 Magnetometry 42
2.3.1 Superconducting Quantum Interference Device (SQUID) 42
2.3.2 Vibrating Sample Magnetometer (VSM) 43
2.3.3 Ordinary Magnetoresistance (MR) 45
2.3.4 Anomalous Hall Effect (AHE) 46

2.4 High Pressure Measurement Tools . . . 47
2.4.1 Piston Pressure Cells . . . 47
2.4.2 Diamond Anvil Cells (DACs) . . . 48
2.4.3 Designer DACs . . . 50
2.4.4 Pressure Calibration . . . 53
2.5 Synchrotron Experiments . . . 55
2.5.1 X-ray Magnetic Circular Dichrorism (XMCD) . . . 55
2.5.2 Powder XRD . . . 56

3 Molecular Beam Epitaxy of Non-Magnetic 2D Semiconductors and Their Heterostructures 59
3.1 Motivation . . . 59
3.2 Molecular Beam Epitaxy of 2D-Layered GaSe on GaN Substrates . . . 60
3.3 Large-Area $SnSe_2$/GaN Heterojunction Diodes Grown by Molecular Beam Epitaxy . . . 75
3.4 Conclusion . . . 80

4 Room Temperature Intrinsic Ferromagnetism in Epitaxial Manganese Selenide Films in the Monolayer Limit 81
4.1 Abstract . . . 81
4.2 Introduction . . . 82
4.3 Results and Discussion . . . 84
4.4 Conclusions . . . 96

5 Importance of Paramagnetic Background Subtraction for Determining the Magnetic Moment in Epitaxially Grown Ultrathin van der Waals Magnets 97
5.1 Abstract . . . 97
5.2 Introduction . . . 98
5.3 Experimental Methods . . . 101
5.4 Results and Discussion . . . 105
5.5 Conclusions . . . 109

6 Integration of $MnSe_2$ on Topological Insulator, Bi_2Se_3 111
6.1 Motivation . . . 111
6.2 Results and Discussion . . . 112
6.3 Conclusions . . . 120

7 Epitaxial growth of van der Waals VSe_2 layers on HOPG and GaAs Surfaces 121
7.1 Motivation . . . 121
7.2 Introduction . . . 122
7.3 Experimental Methods . . . 125
7.4 MBE Growth of VSe_2 on GaAs(111) substrates . . . 126
7.5 Growth of VSe_2 on HOPG surfaces . . . 131

7.6 Conclusions 139

8 Suppression of Magnetic Ordering in Fe-Deficient $Fe_3 - xGeTe_2$ from Application of Pressure 141
8.1 Abstract 141
8.2 Introduction 142
8.3 Methods 144
8.4 Results and Discussion 145
8.5 Conclusions 158

9 Conclusions 159

Bibliography 160

A Thermal processing of Co/Sm multilayered films via isochronal magnetic field annealing 188
A.1 Abstract 188
A.2 Introduction 189
A.3 Materials and Methods 190
A.4 Experimental Results and Discussion 192
A.5 Summary and Conclusions 197

B MBE Growth Recipes 198
B.1 γ-GaSe on GaAs(111)B 198
B.2 $SnSe_2$ on GaAs(111)B 199
B.3 Monolayer $MnSe_2$ and α-MnSe(111) 200
B.4 VSe_2 growth on GaAs(111)B 201

List of Figures

1.1 Ordering of magnetic moments . . . 3
1.2 Ferromagnetic hysteresis loop . . . 4
1.3 Antiferromagnetic modes in fcc lattice . . . 5
1.4 Magnetocrystalline anisotropy in bcc Fe . . . 7
1.5 Surface anisotropy . . . 8
1.6 M(H) loops of Mn-doped $SnSe_2$ . . . 13
1.7 Proximity effect of graphene on YIG . . . 14
1.8 Observation of antiferromagnetic ordering in $FePS_3$ . . . 16
1.9 Crystal structure and magnetic properties of layered CrI_3 . . . 17
1.10 Ferromagnetic ordering in exfoliated $Cr_2Ge_2Te_6$ . . . 18

2.1 MBE growth chamber . . . 24
2.2 Schematic of RHEED construction from electron gun to sample to RHEED screen . . . 26
2.3 Different types of RHEED patterns shown on a screen . . . 27
2.4 Wood notation on fcc(100) . . . 29
2.5 Schematic of RHEED instensity oscillations . . . 31
2.6 Different types of epitaxial growth . . . 33
2.7 XRD Bragg diffraction . . . 35
2.8 X-ray reflectometry profile . . . 37
2.9 Basic operation principle of AFM . . . 39
2.10 STM imaging of Si(111) 7×7 surface . . . 40
2.11 Basic operation principle of a VSM . . . 44
2.12 Exploded view of SQUID pressure cell . . . 48
2.13 SQUID piston pressure cell . . . 49
2.14 Schematic of a *designer* DAC . . . 51
2.15 Optical micrograph of *designer* diamond with metal microprobes . . . 52
2.16 Laboratory photo of *designer* DAC . . . 53
2.17 Debye-Sherrer geometry used for powder XRD experiments . . . 56
2.18 Calibration image scan for powder XRD . . . 57

3.1 Structural characterization of GaSe grown on sapphire(0001) substrates by MBE . . . 62
3.2 AFM images as a function of growth temperature and BEP flux ratio . . . 64
3.3 RHEED, XRD and AFM images of GaSe grown on GaN at same conditions as sapphire . . . 66
3.4 Structural characterization of GaSe grown on GaN at different conditions . 67
3.5 Two-step MBE growth of GaSe on GaN(0001) . . . 68
3.6 AFM and Raman mapping of GaSe after two-step growth on GaN(0001) . . 70
3.7 Cross-section STEM image of GaSe film growth after first-step of growth procedure . . . 72
3.8 Cross-sectional STEM images of GaSe after two-step growth procedure . . . 73
3.9 Structural characterization of $SnSe_2$ growth on GaN(0001) . . . 76
3.10 AFM and Raman spectroscopy of $SnSe_2$ on GaN(0001) . . . 78

4.1 MBE growth and structural properties of monolayer $MnSe_x$ . . . 85
4.2 Out-of-plane room temperature SQUID magnetometry measurements on 1 ML $MnSe_x$ . . . 87
4.3 Structural and magnetic characterization of thick $MnSe_x$ films . . . 89
4.4 RHEED line profile and high resolution imaging of the α-MnSe/GaSe interface 92
4.5 Crystal structure diagrams of α-MnSe(111) and monolayer 1T-$MnSe_2$ . . . 95

5.1 Lattice structure and properties of monolayer 1T-$MnSe_2$ . . . 100
5.2 Room temperature, out-of-plane magnetic hysteresis loop of 1 ML $MnSe_2$. 102
5.3 0 ML $MnSe_2$ magnetization control measurements with standard linear background subtraction and Brillouin function fitting . . . 103
5.4 1 ML $MnSe_2$ magnetic hysteresis loop using new background subtraction method considering diamagnetic and paramagnetic components using a Brillouin function background subtraction method . . . 106

6.1 RHEED images and STM measurements on Bi_2Se_3 grown on sapphire(0001) substrates . . . 113
6.2 STM measurements showing $MnSe_x$ grown on Bi_2Se_3 . . . 114
6.3 STM topography and spectroscopy measurements showing $MnSe_x$ grown on Bi_2Se_3 . . . 116
6.4 SP-STM on 1T-$MnSe_2$ showing ferromagnetism . . . 117
6.5 SP-STM of bilayer α-MnSe(111) . . . 118
6.6 Structural characterization of 40 nm α-MnSe(111) on Bi_2Se_3 . . . 119

7.1 RHEED images of VSe_2 on GaAs(111) . . . 124
7.2 Structural characterization of thick VSe_2 films grown by MBE on GaAs . . 126
7.3 XPS of 1 ML VSe_2 on GaAs . . . 128
7.4 STM of VSe_2 on GaAs(111) . . . 130
7.5 RHEED and AFM images of HOPG substrate and VSe_2 grown on HOPG at 250°C showing streaky patterns and flat dendrite sub-monolayer coverage . 132

7.6 RHEED and AFM images showcasing change in grain growth of VSe_2 overlayers on HOPG . . . 133
7.7 Zoomed in AFM images showcasing change in grain growth of VSe_2 overlayers on HOPG . . . 135
7.8 Post-annealed VSe_2 films on HOPG substrates . . . 137
7.9 Magnetic properties of ML VSe_2 on HOPG . . . 138

8.1 Structural and magnetic properties of $Fe_{2.75}GeTe_2$ at ambient and low hydrostatic pressures . . . 146
8.2 High pressure XRD measurements on $Fe_{2.75}GeTe_2$ . . . 149
8.3 High pressure electrical transport measurements on $Fe_{2.75}GeTe_2$ . . . 151
8.4 High pressure magnetotransport measurements on $Fe_{2.75}GeTe_2$ . . . 152
8.5 Suppression of magnetic ordering temperature in $Fe_{2.75}GeTe_2$ . . . 155
8.6 Relative bond distance of magnetic atoms as a function of pressure . . . 156

A.1 Thermal processing of $(Sm/Co)_n$ multilayered films. . . . 191
A.2 Magnetic field annealing on $(Sm(21.9\ Å)/Co(100\ Å))_{167}$ multilayered films. 194
A.3 Element-specific XMCD on a $(Sm(21.9\ Å)/Co(100\ Å))_{167}$ multilayered film after an 800 K anneal under a 10 kOe field. . . . 196

List of Tables

2.1 Different pumping levels for vacuum systems. 23

5.1 Detailed description of Brillouin fitting parameters to determine magnetic moment in 1 ML $MnSe_2$ and 0 ML $MnSe_2$ control samples. 108

8.1 Determination of magnetic ordering temperature at select pressures. 154

Chapter 1

Toward Magnetism in the Ultrathin Limit

1.1 Introduction to Magnetism and Magnetic Materials

Magnetism and magnetic materials have become heavily involved in our everyday lives. This begins with the discovery of the "South pointer" in ancient China or what we've come to know as the navigational compass, which aligns its suspended needle with the Earth's magnetic field. Since then, research in magnetism has led to many early discoveries including a current-carrying wire coil producing a magnetic field (e.g. electromagnetism), and magneto-optics such as the Faraday effect [1, 2]. Developing a basic understanding of the physics led to advances in quantum mechanics such as the discovery of an electron's spin which is the origin of the electron's intrinsic magnetic moment (μ_B). High-frequency magnetic resonance, spin-based electronics and material advances such as rare-earth magnets

providing a large energy product for future permanent magnets were later discovered. These technological advances are in modern-day speakers, electric motors, television screens, and generators for wind turbines.

Spin-based electronics or "spintronics" which exploits both the charge and spin degrees of freedom of an electron, has been an exploding field since the discovery of the giant magnetoresistance (GMR) effect in 1988 by Albert Fert and Peter Grünberg [3, 4] and a related phenomena known as tunneling magnetoresistance (TMR) [5, 6, 7, 8]. This discovery has led to major advances in the computer industry leading to high density storage media, non-volatile memory, low-energy magnetic devices, and also advances toward cloud computing and quantum information [9, 10, 11, 12]. This area of study is heavily dependent on the advancement and development of high quality thin film materials as is the consumer electronics industry (e.g. Moore's Law). This has led to breakthroughs and discoveries of new quantum materials such as topological insulators, high temperature superconductors, 2D semiconductors and magnets, magnetic insulators, etc.

It is important to distinguish certain concepts in magnetism before moving forward. Different types of magnets including ferromagnets, antiferromagnets, paramagnets, diamagnets, and ferrimagnets all exhibit different properties (depicted in Figure 1.1. Both paramagnets and diamagnets are non-magnetic materials. For paramagnets, the magnetic dipoles in the material are all randomly oriented and do not polarize unless a very high external magnetic field is applied to the sample and does not retain its magnetization when the external field is turned off. In diamagnets, the slope of the magnetization curve is negative as the magnetic field is swept from negative to positive (or vice versa). This response

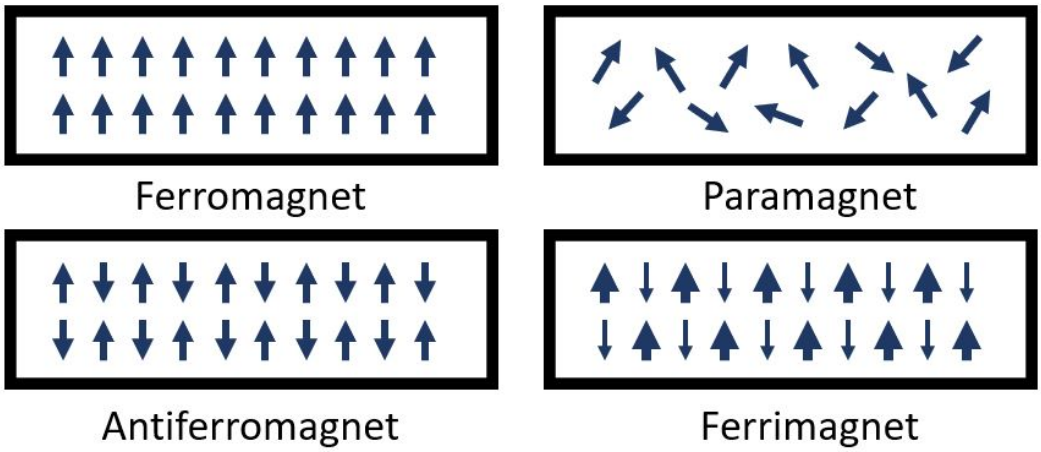


Figure 1.1: Ordering of the magnetic moments in magnetic materials.

is due to the atomic orbitals being completely filled or empty and the diamagnetic material repelling the magnetic flux from the external magnetic field [1, 2, 13].

Ferromagnets, in particular, show an irreversible nonlinear response of magnetization to an applied magnetic field. This is shown via a hysteresis loop explained by the ferromagnet's intrinsic property of spontaneous magnetization due to the alignment of atomic magnetic moments (Figure 1.2). The magnetization is dependent on temperature where at a specific temperature, named the Curie temperature (T_c), the magnetization falls to zero and undergoes a phase transition. The phase transition is due to thermal fluctuations causing disorder in the atomic moments at higher temperature while it is ordered below the T_c. The ferromagnetic hysteresis loop shows interesting features related to energy loss. Hard magnetic materials (e.g. CoPt [14]) typically have broad, square loops while soft magnetic materials (e.g. Py [15]) have narrow loops. This feature is related to the coercive

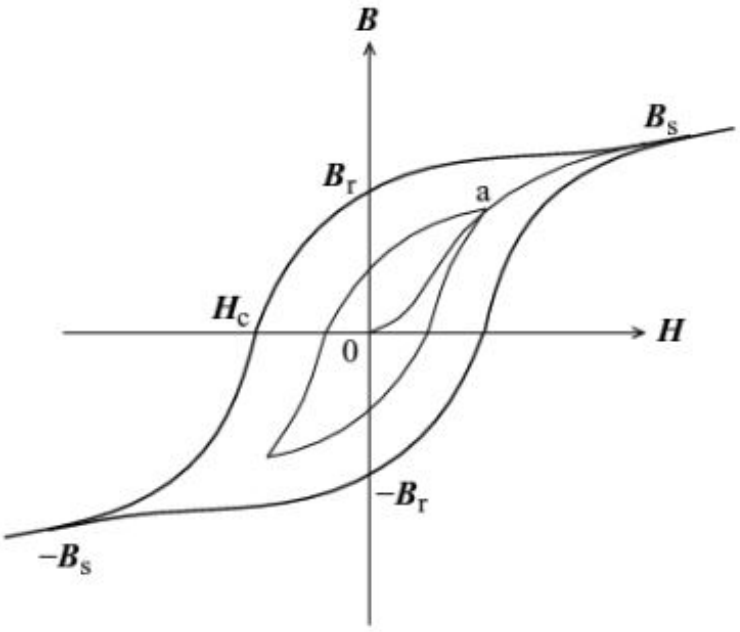


Figure 1.2: An example of a ferromagnetic hysteresis loop with different components labeled (discussed in text). Adapted from [2].

field (H_c), which is the force required to flip the magnetization in the opposite direction. The field this switches at typically depends on the domain structure and anisotropy energy [1]. The saturation magnetization (when all magnetic moments align with field, M_s), saturation field (the field at which all moments align, H_s), and remanent magnetization (amount of aligned magnetization left over after field is shut off, M_r) are features of the ferromagnetic hysteresis loop and are all dependent on the magnetic anisotropy energy [1, 2]. We will discuss magnetic anisotropy more in the next section.

Antiferromagnetism and ferrimagnetism are similar in that the interaction between the magnetic moments tend to align adjacent moments antiparallel to each other. The difference between the two is that in an antiferromagnetic material, the overall net

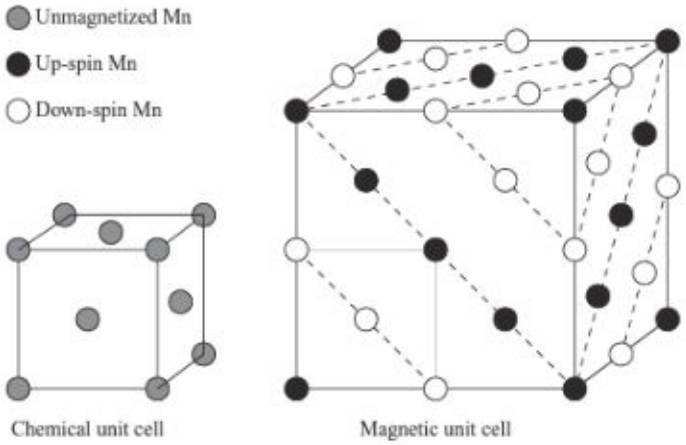


Figure 1.3: Type II (or Type A) antiferromagnetic mode for the MnO fcc(111) lattice. Adapted from [1].

magnetization is zero, while the net magnetization in a ferrimagnet is not zero. Most oxides that possess a nonzero net magnetization are typically ferrimagnets, like Fe_3O_4 and YFe_5O_{12} (YIG) [16, 17]. In terms of susceptibility, antiferromagnets order at a temperature below the Néel temperature, T_N. The way they are typically characterized is through susceptibility measurements (M vs. T) or high field (M vs. H) scans since it takes a large external magentic field to polarize the antiparallel spin alignment. Interestingly, there are different magnetic modes for antiferromagnets in cubic lattices, particularly the fcc. Shown in Figure 1.3, a structure with alternating ferromagnetic planes along the [001] is a Type I antiferromagnet, while a structure with alternating ferromagnetic (111) planes is a Type II (or Type A) antiferromagnet [1]. Type III is made up of alternating antiferromagnetic planes [1]. This understanding will come in handy later in this dissertation.

1.2 Magnetic Anisotropy

Magnetic anisotropy is the directional dependence of a material's magnetic properties. An easy axis is an energetically favorable direction of a magnetic material. The family of easy directions are usually equivalent and the actual direction of magnetization can be along either of them. The hard axis is typically characterized by the higher magnetic field needed to saturate the sample magnetization while the easy axis reversal is usually characterized by lower saturation fields and square hysteresis loops. In hard magnets, the easy axis anisotropy energy is typically strong as opposed to soft magnets. The anisotropy energy (E_a) is typically represented by the equation below:

$$E_a = K_1 sin^2\theta \tag{1.1}$$

1.2.1 Magnetocrystalline Anisotropy

Magnetocrystalline anisotropy is an intrinsic property of crystalline magnetic materials. The direction of the magnetic moments is pointed along the energetically favorable easy axes of the crystal which is largely dependent on the crystal symmetry. Its microscopic origin is related to the crystal-field interaction and spin-orbit coupling. This crystal-field interaction tends to stabilize a particular orbital, and by spin-orbit interaction the magnetic moment is aligned in a particular crystallographic direction [1]. For example in Fe, the cube edges <100> are easy directions and the cube diagonals <111> are hard directions. Crystals that are hexagonal such as Co, have easy directions along the c axes, [0001]. This does not apply to polycrystalline or amorphous samples without a preferred orientation of the grains.

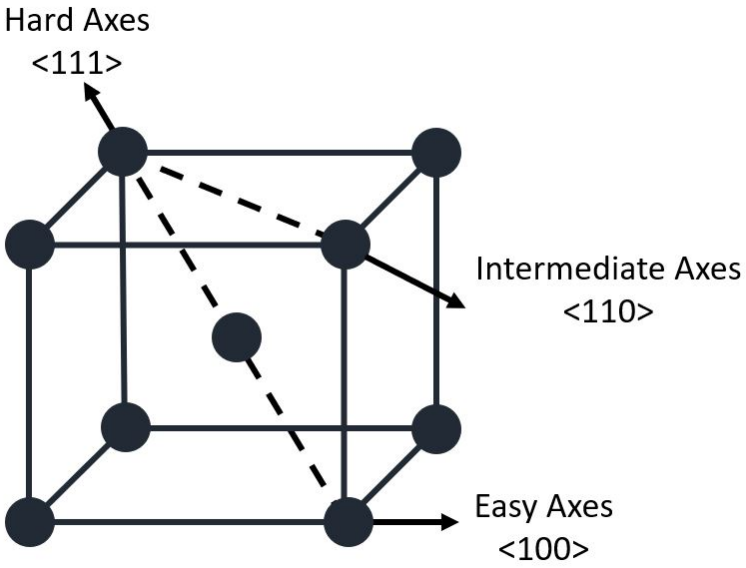


Figure 1.4: Magnetocrystalline anisotropy in bcc Fe.

1.2.2 Shape Anisotropy

Shape anisotropy has a magnetostatic origin which is closely related to demagnetizing fields. The demagnetizing field, H_d, is created by the magnetization, M, of the sample and is directly proportional to the size of the sample, N_d. The demagnetizing fields are usually written as

$$H_d = N_d M \tag{1.2}$$

In the case of a perfectly spherical sample, the magnetization will point along all axes. If it is not perfectly spherical, then it will prefer to lie along a long axis. For the case of this dissertation, we will mainly focus on thin films. In the case of a thin film (which may be crystalline or non-crystalline), the shape anisotropy overcomes the bulk magnetocrystalline anisotropy. The magnetic moments will prefer to point along the crystalline easy

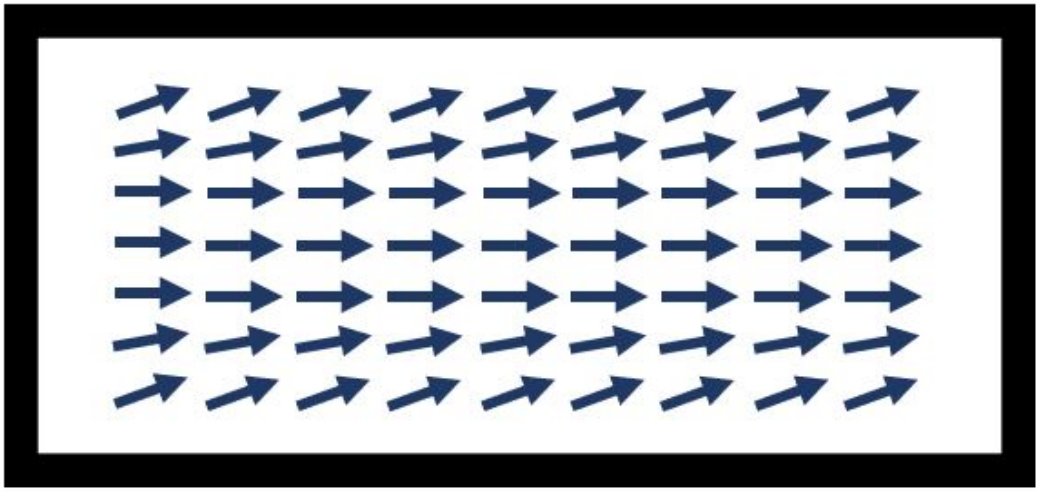


Figure 1.5: Surface magnetic moments beginning to tilt outward at spin-reorientation transition thickness.

axes but since the demagnetizing fields will be too large along the z direction, the moments will prefer to point along the in-plane family of easy directions. A high field is typically necessary to overcome the demagnetizing field.

1.2.3 Surface Anisotropy

The third and last type of magnetic anisotropy that I will be discussing in this dissertation is the surface anisotropy which typically happens in metallic ultrathin magnetic films at their interfaces. When a thin film reaches a thickness where the interface breaks symmetry, the moments will deflect out of plane (depicted in Figure 1.5). This is also represented by a competition between shape anisotropy and the surface component of magnetocrystalline anisotropy [1]. An example of this is growing wedged magnetic films on top of metallic substrates such as Ag and Au where at higher thicknesses the magnetic

moments prefer to lie in the sample plane (dominated by its shape) but when the thickness decreases they tend to tilt out of the plane (dominated by surface) [18, 19, 20, 21, 22, 23]. This region where the magnetic moments change orientation of its preferred axes is called the spin-reorientation transition (SRT) [18, 19, 24, 25, 26, 27, 28, 29]. The samples need to be of high quality to realize this reorientation of the spins, which requires a growth technique such as molecular beam epitaxy (MBE) and an ultra-clean substrate.

1.3 Magnetism in Low Dimensions

In order to scale down samples for next generation magneto-electronics and spintronic devices we have to keep in mind that there are more constraints and significant challenges in moving toward lower dimensions (<3) [30, 31]. Magnetic excitations, also known as spin waves, play a significant role in the stability of the magnetic ordering while the dimension of the system is reduced.

Electron spins have different interactions with an applied magnetic field and are dependent on temperature. Spins precess under an applied field, H, where the precession of spins couple around an ordered moment and also propagate through the lattice which can destroy the long range magnetic ordering at T_c [1, 13, 32]. Think of spin waves (or magnons) as oscillations in the relative orientations of spins on a lattice, whereas lattice waves (or phonons) are oscillations of the relative positions of atoms on a lattice. At $T = 0$, the spin wave modes are stable while $T > 0$ the thermal population is occupied. The dispersion relationship for magnons is shown below,

$$\hbar\omega_k \approx 4JS(1 - coska) \tag{1.3}$$

where $\hbar$ is Planck's constant, ω_k is the frequency for the spin wave, J is the nearest-neighbor exchange interaction, S is the total spin angular momentum, k is the wave vector and a is the interatomic spacing [1, 13, 32]. Magnons behave like Boson modes meaning they follow Bose-Einstein statistics shown here,

$$n(E) = \frac{1}{e^{\frac{\hbar\omega_k}{k_B T}} - 1} \tag{1.4}$$

where $n(E)$ is the number of magnons at a given energy (or mode), and k_B is the Boltzmann constant [1, 13, 32]. The general spin wave dispersion for ferromagnets is $\sim \mathrm{k}^2$ [32]. Using Equations 1.3 and 1.4, Mermin and Wagner found that the total number of thermally excited magnons integrated over all modes (at low energies) diverges in 1-D and 2-D, leading to magnetism (ferromagnetic or antiferromagnetic) being unstable at a finite temperature above $T = 0$. This is commonly known as the Mermin-Wagner theorem [33].

While this theorem provides an important benchmark, it does not take into account interaction with a substrate, a finite film thickness, surface texture, and additional interactions which may induce symmetry breaking. Uniaxial magnetocrystalline anisotropy is a requirement for stabilizing ferromagnetism in two-dimensions (2D), which creates an extra term in the spin wave dispersion relationship, or a non-zero spin wave excitation gap in the lowest energy mode of the acoustic magnon branch. This is known as the 2D Ising Model [34, 35, 36, 37, 38]. This can be thought of as an "all surface" system that has an intrinsic surface anisotropy which creates a finite T_c as opposed to a 3D system where the T_c is directly related to the exchange interaction.

Of the model discussed, it is important to note that this is for a highly localized system such as rare-earth f-electron magnets. In the Stoner criterion, a delocalized

or itinerant ferromagnet can be understood in terms of the spin density of states (spin-DOS) [13, 39]. In the spin-DOS there is a spin imbalance when the number of up spins ($N_{\uparrow}$) exceeds the number of down spins ($N_{\downarrow}$). In this picture, spontaneous magnetization arises from a spin imbalance from the net spin-DOS ($N_{\uparrow}$ - $N_{\downarrow}$). According to the Stoner criterion, metals having a large value of spin-DOS at the Fermi level or having a large value of the exchange interaction tend to be ferromagnetic [1, 13].

Prior studies on fabricating "two-dimensional" (2D) magnetic materials primarily focused on reducing the thickness of 3D metallic ferromagnets (e.g. Fe, Ni, CoFeB, etc.) to several atomic layers through thin film deposition techniques on ultraclean substrate surfaces [20, 40, 41, 42, 43, 44, 45, 46, 47, 48, 49, 50, 51, 52, 53, 54, 55]. In these structures, the magnetic ordering is stabilized through lattice-strain-induced magnetic anisotropy, which also determines their spin-reorientation transition thickness from shape to surface anisotropy. 2D magnetism is not limited to these systems. Atomic layers of non-magnetic 3D materials have also shown artificial ferromagnetic ordering at their surfaces with an example being elemental vanadium epitaxially grown on Ag(100) substrates [56]. Similar theoretical predictions have been made for monolayer $4d$ elements (Tc, Ru, Rh, Pd) and $5d$ elements (Os, Ir) on Ag(100) surfaces but so far no success has been reported on these materials [57, 58].

Magnetic ultrathin films fabricated down to the 2D limit are unavoidably affected by the underlying substrate, which makes it challenging to study 2D magnetism in free-standing monolayers. An isolated or suspended layer could exhibit a largely weakened or possibly no substrate effect and is therefore a good platform for studying magnetism in 2D

which will be discussed in the next section.

1.4 Magnetism in van der Waals Materials

Since the isolation of monolayer graphene (e.g. a single isolated atomic sheet of graphite) via scotch tape micromechanical exfoliation in 2004 [59], there have been intense efforts to search for new 2D van der Waals materials. Of these discovered include superconducting metals (e.g. $NbSe_2$) [60, 61], direct band gap semiconductors (e.g. transition metal dichalcogenides (TMDCs) such as MoS_2) [62], insulators (e.g. h-BN) [63], topological insulators (e.g. Bi_2Se_3) [61, 64], and other elemental 2D materials such as phosphorene, silicene, germanene, antimonene, and stanene [65]. Due to the unique physical and chemical properties compared to their bulk counterparts, ultrathin 2D van der Waals materials, especially down to thicknesses of one or several atomic layers, have become a focus of the scientific community [66].

Magnetic properties of van der Waals 2D materials have been historically underinvestigated. 2D magnets have the potential to be extremely important for future magnetoelectronic and spintronic devices as they continue to scale to smaller thicknesses for low-energy applications [67, 68, 69, 70]. Furthermore, the magnetic properties can couple with rich electrical and optical properties via layer stacking techniques, leading to fascinating magnetoelectric and magneto-optic physics.

Many previous studies have tried various ways to induce ferromagnetic ordering into non-magnetic 2D van der Waals materials. This includes various types of defect engineering [72, 73, 74, 75, 76, 77, 78, 79], induced magnetism via strain [80], compositional

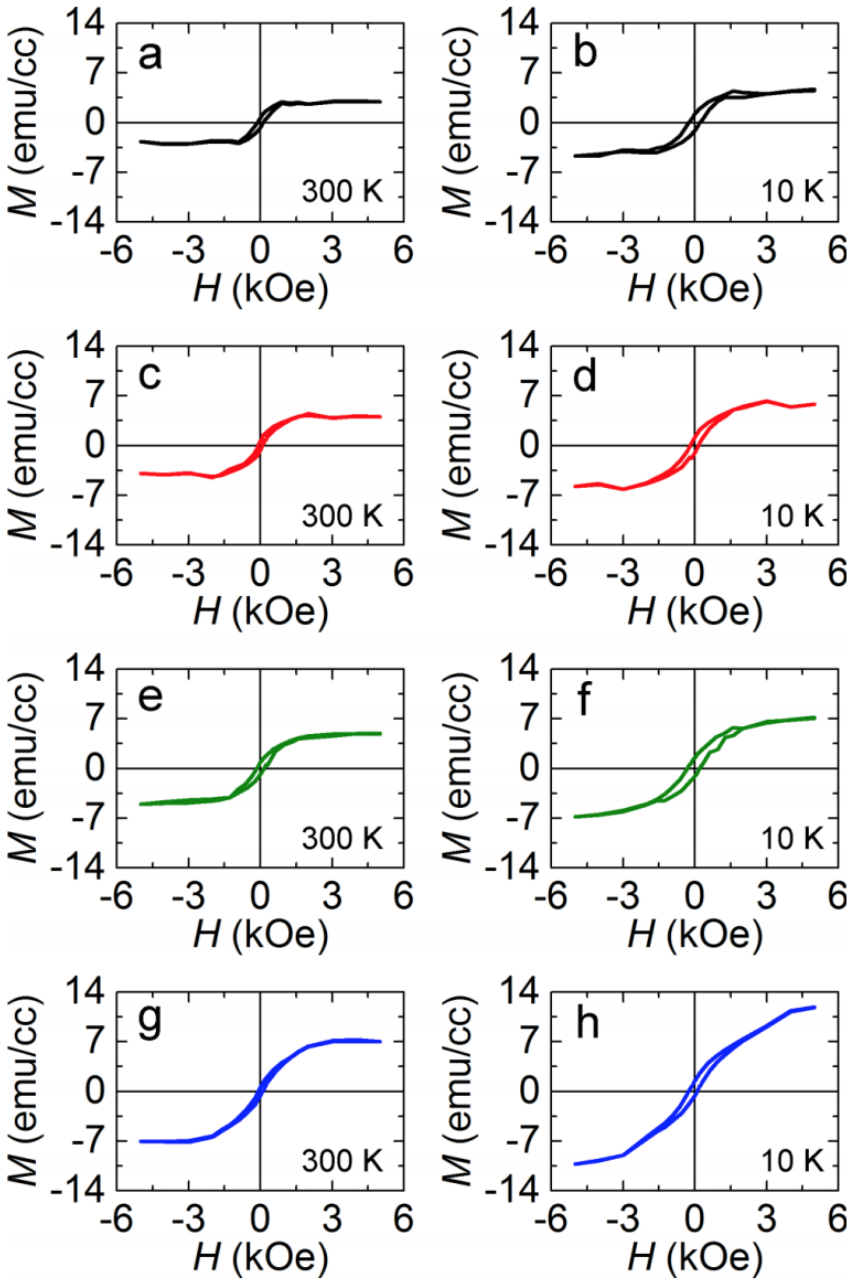


Figure 1.6: Out-of-plane hysteresis loops of $Sn_{1x}Mn_xSe_2$ films grown at Mn effusion cell temperatures of 670°C ((a) and (b)), 690°C ((c) and (d)), 740°C ((e) and (f)), and 760°C ((g) and (h)) measured at 300 K and 10 K. Adapted from [71].

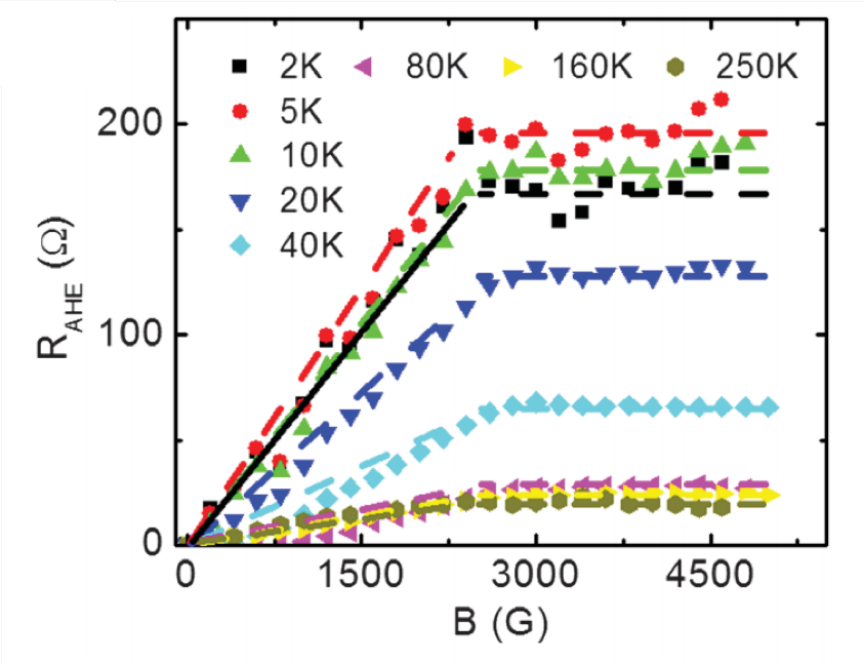


Figure 1.7: AHE resistance at different temperatures of graphene on YIG. Adapted from [16].

alloying [71], or the proximity effect [16, 17, 81] to induce a magnetic moment at the interface of the non-magnetic 2D material.

A few examples are worth discussing here, including "decorating" an isolated layer of graphene with atomic hydrogen adatoms. In McCreary, *et al.*, researchers used an *in situ* atomic hydrogen source to deposit cracked hydrogen molecules onto the surface of a graphene spin-valve [72]. It is important to note that graphene has a long spin-diffusion length, which makes it a prime candidate to study spin diffusion across a long channel. The researchers noticed that while they measured a non-local graphene spin-valve and deposited atomic hydrogen onto the surface, they observed a new "kink" in the non-local resistance scan. With theoretical assistance, they learned that this "kink" was signature of a localized magnetic moment in graphene. While not a full sheet of magnetic moments, this was still

an advancement in a new field of study.

A few years later, scientists began studying the effects of depositing magnetic impurities into non-magnetic 2D semiconductors during MBE growth [71, 82, 83]. There has been many theoretical predictions about magnetic doping of Mn, Cr, and V into TMDCs such as MoS_2 [84], which is a motivating factor for attempting these studies. One would expect similarities to 3D semiconductors such as $Ga_{1-x}Mn_xAs$ due to the existence of Ruderman-Kittel-Kasuya-Yosida (RKKY) interactions, where the exchange between localized d electrons (from the magnetic impurity) is mediated by s conduction electrons (from the non-magnetic semiconductor) giving rise to a ferromagnetic signal [85]. In Dong, *et al.*, researchers grew thin films of Mn-doped $SnSe_2$ on GaAs(111)B substrates [71]. They showed that with up to $\sim$70% of Mn impurities, the crystal structure of $SnSe_2$ is unchanged and they are able to observe a weak ferromagnetic moment up to room temperature of about $\sim$0.09 μ_B. Since the magnetic moment is extremely weak, it may be due to antiferromagnetic ordering with a few uncompensated spins throughout the doped structure, giving rise to a weak moment.

In parallel, there has also been many attempts to induce magnetism into a non-magnetic 2D van der Waals layer via the magnetic proximity effect [16, 17, 87, 88, 89]. In this case, 2D materials are deposited or stacked onto a underlying magnetic substrate, preferably a magnetic insulator in order to perform device measurements without current shunting to a conducting substrate. An example being the work of Wang, *et al.* [16] where they transferred a single layer of graphene onto YIG, etched it into a Hall bar geometry and observed an anomalous Hall effect (AHE) signal up to room temperature which is indicative

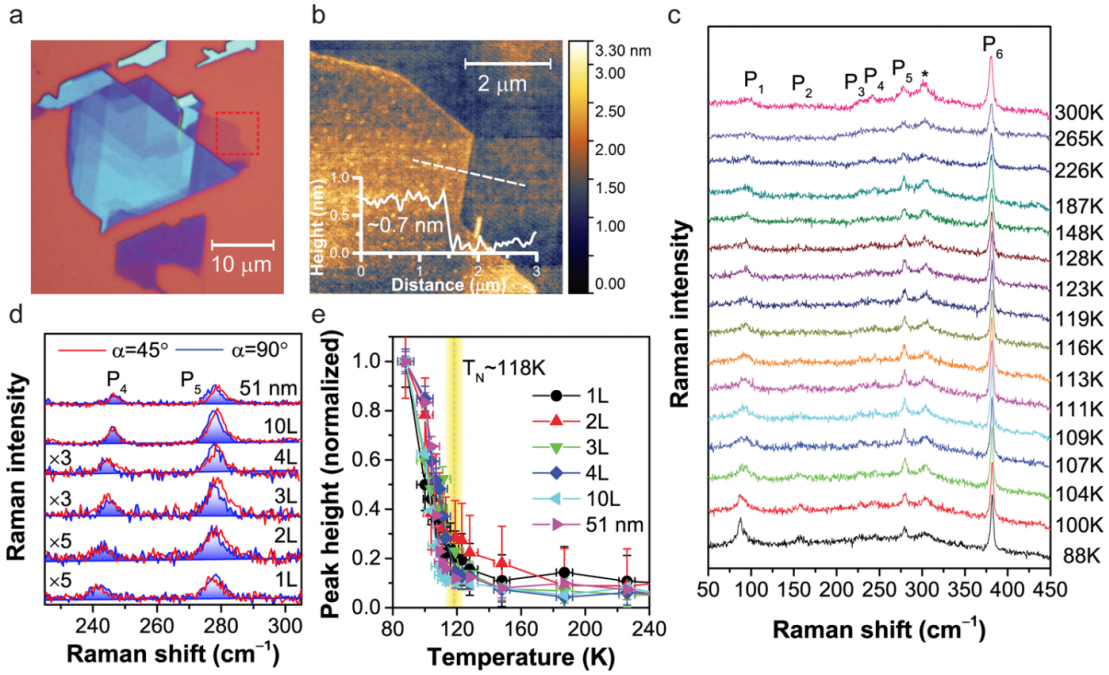


Figure 1.8: (a) Optical contrast and (b) atomic force microscope images of 1L $FePS_3$ on SiO_2/Si substrate. (c) Temperature dependence of Raman spectrum of 1L $FePS_3$ with polarization direction of $\alpha = \beta = 45°$. *indicates a signal from the Si substrate. (d) Thickness dependence of P_3 and P_4 with polarization direction of $\alpha = 45°$ (red curves) and $\alpha = 90°$ (blue curves) at 300 K. (e) Temperature dependence of P_{1a} peak height for different thicknesses. Adapted from [86].

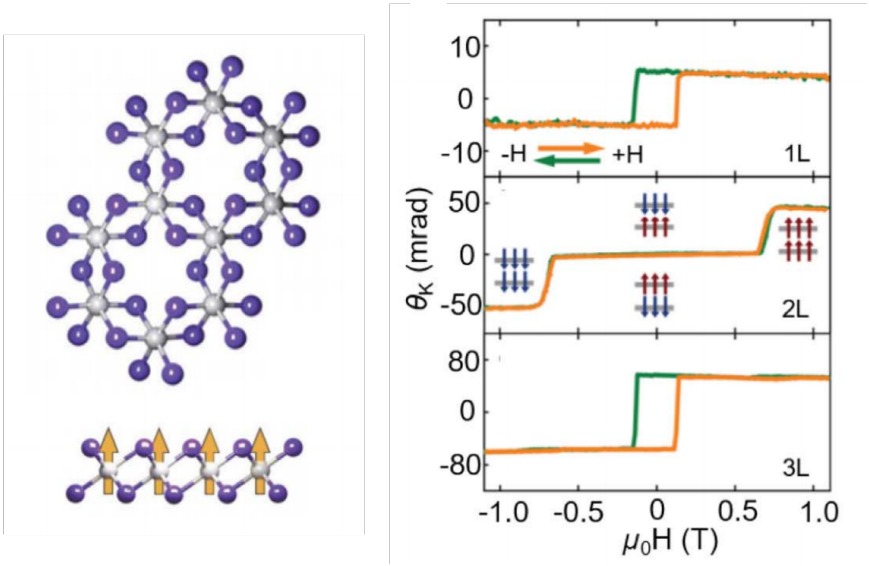


Figure 1.9: Crystal structure and MOKE of layered CrI_3. Adapted from [90].

of ferromagnetic ordering in the graphene layer (shown in Figure 1.7).

With all the above mentioned, intrinsic magnetism in 2D materials had not been observed until 2016 with antiferromagnetic ordering in single atomic layers of van der Waals $FePS_3$ [86, 91, 92]. In Lee, *et al.* [86], researchers used polarized Raman spectroscopy to show an antiferromagnetic phase transition below the T_N at 118 K. A year later, two important results were reported in *Nature* journals showing intrinsic ferromagnetism down to the monolayer limit in CrI_3 [90] (Figure 1.9) and a bilayer in $Cr_2Ge_2Te_6$ [93] (Figure 1.10). In both works, the magneto-optic Kerr effect (MOKE) was employed to measure the magnetic properties as a function of applied magnetic field and layer thickness. The T_c in both systems decreased from a bulk value of 61 K to 45 K in CrI_3 and 30 K in $Cr_2Ge_2Te_6$ which is similar to other 3D ferromagnets in the ultrathin limit. Interestingly, in CrI_3, the magnetic ordering has a thickness dependence that switches from ferromagnetic in the odd

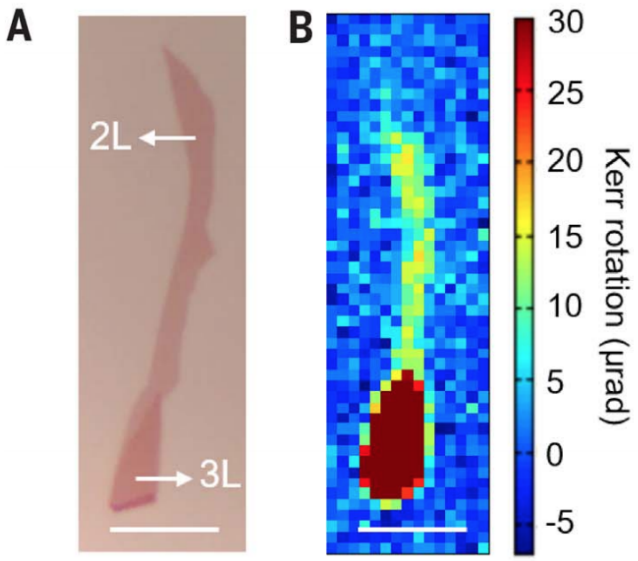


Figure 1.10: (a) Optical image of exfoliated $Cr_2Ge_2Te_6$ and (b) corresponding MOKE imaging. Scale bar is 10 μm. Adapted from [93].

layer to antiferromagnetic in the even layer while increasing in magnitude while the periods of the said layers increases [90, 94].

Since these results were reported, an extreme interest in looking for new 2D magnets, tuning their properties, and showing their potential in future technologies has garnered [95]. Electric field control of the magnetic properties through electrostatic gating [96] has been shown in structures such as CrI_3 [90] and $Cr_2Ge_2Te_6$ [93] while tunneling magnetoresistance measurements showing up one million percent in graphene/CrI_3/graphene heterojunctions [97, 98, 99, 100, 101]. Structures such as Fe_3GeTe_2 [102, 103, 104] show thickness dependent hysteresis with interesting magnetic domain structures and can also be tuned via Fe vacancies. While these are very exciting results, they are all realized at low temperatures and in exfoliated micron-sized flakes.

In order to move toward industrial applications, 2D magnets need to be wafer

scale and have magnetic ordering up to room temperature or above. A few works have been reported on exfoliated flakes showing gate-tunable ferromagnetism in Fe_3GeTe_2 [105], in which the ferromagnetic signal persists to room temperature. MBE is a powerful tool, in which it can synthesize ultraclean samples to large scalability, grow non-equilibrium phases of materials, and precisely control thicknesses. This has been a crucial growth technique in the metallic ultrathin films area of study for studying spin-reorientation transitions and is also a good tool for growing van der Waals materials. Recently two works have been published showing room temperature ferromagnetism in van der Waals 1T-VSe_2 [106] and 1T-$MnSe_2$ [107] layers grown by MBE. These works will be discussed throughout this dissertation.

Chapter 2

Experimental Techniques

In this Chapter, I will discuss the experimental methods that were used to obtain the results shared in this dissertation. These include thin film deposition methods such as molecular beam epitaxy, structural and magnetic characterization methods including X-ray diffraction and SQUID magnetometry and the subsequent physical understanding of these techniques.

2.1 Molecular Beam Epitaxy (MBE)

2.1.1 Introduction to MBE

Molecular beam epitaxy (MBE) is a common physical vapor deposition (PVD) technique for depositing crystalline films onto crystalline surfaces in a ultra-high vacuum (UHV) environment. It is particularly useful for synthesizing high purity and high crystalline quality thin films with a minimal amount of structural defects. MBE can be thought of as "atomic spray painting" where gaseous-phase molecules evaporate out of a thermal

effusion source onto a surface in a layer-by-layer fashion. Founded in the late 1960s by Bell Labs as a reaction to the development of the first transistor and early semiconductor technologies, MBE was used to grow and study high quality semiconductor films such as GaAs [108, 109, 110, 111]. A vast variety of materials have been synthesized via MBE since then, including complex oxides [112, 113], compositional alloys [114, 115, 116], superlattices [3], dilute magnetic semiconductors [78, 111], van der Waals-layered topological insulators, superconductors [117, 118] and metal chalcogenides [64]. As we will discuss further in later sections, MBE is a useful deposition technique for:

(1) Development of high purity materials with low defect density.

(2) Precise control over thickness of deposited material(s).

2.1.2 Vacuum Science Fundamentals

Typical thin film growth techniques require a vacuum environment in order to produce materials with a low amount of impurities (see Table 2.1). For example, direct current (DC) magnetron sputtering takes place in a growth chamber which typically operates in a rough (760 to 1×10^{-3} Torr) to high vacuum (1×10^{-3} to 1×10^{-9} Torr) environment, using a series of roughing and turbo pumps. In the case of MBE, a series of roughing, turbo, ion and cryogenic pumping is required to bring the pressure of the growth chamber from atmospheric (760 Torr) to UHV (1×10^{-9} to 1×10^{-12} Torr). This ultra-clean environment is required to grow a film of high purity, which comes from clean and outgassed source material and therefore increasing the mean free path of molecular beams. It is important to note that, you cannot just simply get to a UHV environment by just plugging pumps in, there are specific procedures to doing so and it requires patience and consistent moni-

toring of partial pressures and the overall pressure in the system. An example step-by-step procedure of bringing a chamber to UHV pressures is listed here:

(1) Pump down chamber with scroll pump to roughing vacuum (see Table 2.1).

(2) Once reaching rough vacuum regime, turn on turbo pump to bring chamber to high vacuum.

(3) Once reaching high vacuum regime, turn on ion pump to bring into UHV regime.

(4) At high vacuum or UHV, open to cryogenic pump (if necessary).

(5) Bake chamber at $\sim$150°C (including thermal evaporators) for 24-72 hours to desorb water from the chamber walls.

(6) Fire titanium sublimation pump out any further contaminants.

Also, if you have a large volume of high vapor pressure material throughout your chamber that has a low evaporation temperature (near the bake out temperature), the likelihood of cleaning your chamber properly via a bake out is low. The proper way to clean out these types of chambers is a series of pumping as well as cooling of a liquid nitrogen (LN_2) cryoshroud for several days and to grow a few low-quality samples to further outgas and pump out the chamber. The excessive growths and pumping will act as "getters" where the deposited "getter" materials will react with the other vapors in the chamber and will remove them from the evacuated space.

Type of Pumping	Pressure Range (Torr)
Roughing	760 to 1×10^{-3}
High Vacuum	1×10^{-3} to 1×10^{-9}
UHV	1×10^{-9} to 1×10^{-12}

Table 2.1: Different pumping levels for vacuum systems.

2.1.3 Growth Chamber Basics

MBE chambers are typically a massive piece of stainless steel in a spherical shape roughly between 1 and 5 feet (see Figure 2.1). They are usually designed in a fashion where the sample manipulation and temperature control are inserted from the top and 8 to 12 Knudsen thermal effusion cells are geometrically oriented toward the sample surface from the side or bottom of the vacuum chamber. The thermal effusion cells are masked with pneumatic shutters to prevent them from contaminating other growths and cells if not in use, the shutters are also very useful for controlling thicknesses very precisely. MBE chambers are usually equipped with an ion gauge to measure pressures ranging from high vacuum to UHV and a residual gas analyzer (RGA) to measure partial pressures of elemental gases in the chamber. The chamber may also be equipped with capabilities to measure thickness such as a quartz crystal monitor (QCM) that changes in frequency when a different atomic mass hits the surface of the QCM which can then be converted into a Å/min growth rate. Typical ways MBE growers' measure deposition rates are via a nude ion gauge (also commonly known as a beam flux monitor, BFM) attached to a continuous azimuthal rotator (CAR) or reflection high-energy electron diffraction (RHEED) oscillations (discussed later).

The MBE growth chamber is typically connected to other vacuum "zones" to keep samples under vacuum to keep them clean from oxidation or being deposited on from sitting

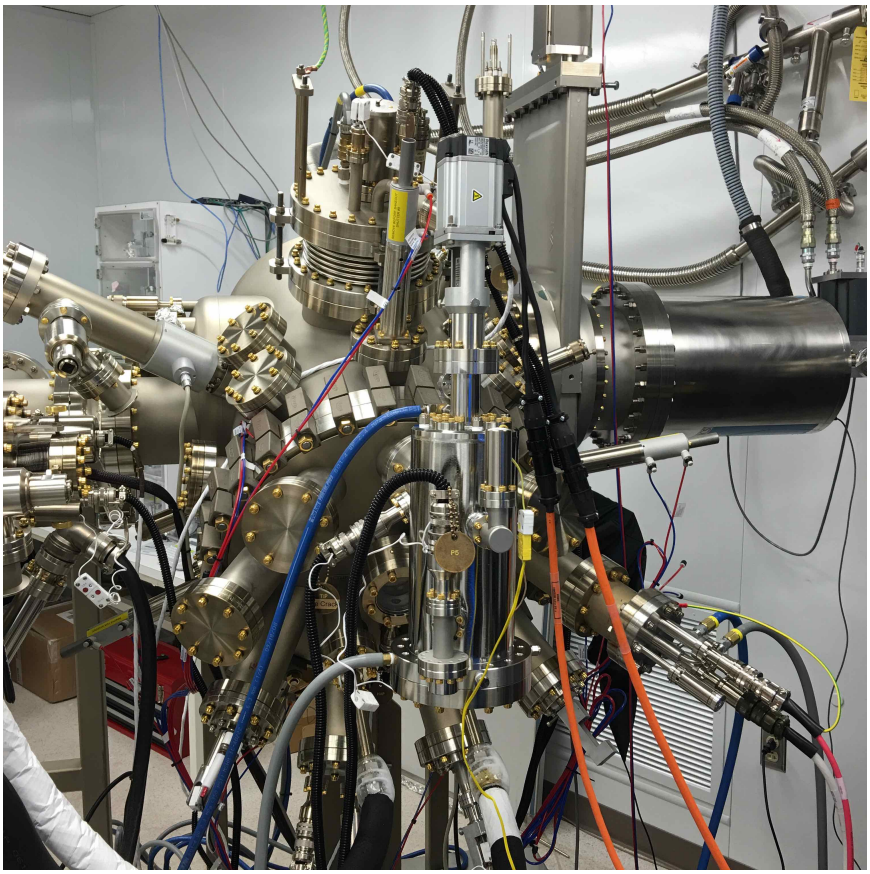


Figure 2.1: MBE growth chamber in semiconductor epitaxy and analysis laboratory (SEAL) at The Ohio State University.

in the chamber overnight and to transfer other samples to the growth chamber without breaking vacuum. These zones are typically called the "buffer chamber" and the "load lock." The load lock is typically a region of the vacuum apparatus that breaks vacuum a few times throughout the day to load/unload samples for growth/characterization.

Depending on sample loading designs (varies from chamber to chamber), a user can load one or multiple substrates for growth on a substrate carrier/holder. Samples are loaded and are pumped from atmospheric pressure to high vacuum in a matter of minutes to hours. The samples will then be transferred to the buffer chamber which is typically under

UHV and may have capabilities such as substrate annealing or sputtering in order to clean the sample surface. The sample can then be loaded into the MBE growth chamber and the surface can be monitored via electron diffraction techniques (discussed next section) prior to further sample preparation and subsequent growth.

2.1.4 Reflection High-Energy Electron Diffraction (RHEED)

MBE chambers are also typically equipped with a reflection high energy electron diffraction (RHEED) gun that is used to monitor the sample surface in real time or "during growth" [119]. *In situ* RHEED is extremely useful in determining the following: (1) growth rates (in monolayer (ML) per second, ML/sec.), (2) lattice parameters (e.g. structural phase transitions), (3) crystalline symmetry (e.g. 4 fold vs. 6 fold), (4) epitaxial registry (e.g. lattice mismatch), (5) surface roughness, (6) and growth modes (e.g. step flow versus island growth). The basic principle of RHEED is using high energy electrons to reflect off of a sample surface at grazing incidence (0.5-5°) and the diffracted electrons (5-50 keV) interfere constructively to form patterns on a fluorescent screen opposite from the RHEED gun in the chamber. The image that appears on the screen is collected via a CCD camera and can be interpreted on a computer screen.

A crystalline surface can be viewed as a 2D $x-y$ plane consisting of a periodic arrangement of atoms in real space. High energy electrons (k_0) from the RHEED gun will reflect off of the substrate surface and thus diffract from the 2D periodic plane. The steeper the incidence angle, the deeper the electrons will penetrate the substrate before before reflecting and leading to a more intensified RHEED pattern. Further, a Fourier transform

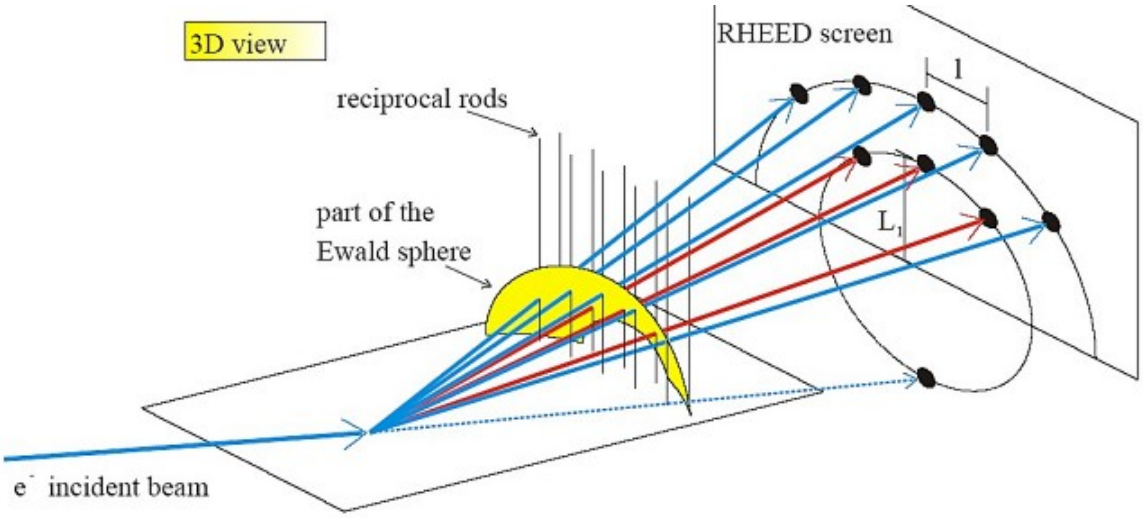


Figure 2.2: Schematic of RHEED showing high-energy electrons diffracting off of sample surface. Adapted from [120].

can convert this periodic plane into a reciprocal lattice and the arrangement of atoms will be viewed as infinite rods using the relationship

$$k_a = \frac{2\pi}{a} \tag{2.1}$$

where k_a is the reciprocal space lattice and a is the real space lattice. A Ewald construction is used to meet the diffraction conditions for when the periodic lattice rods intersect with the geometrically constructed sphere at k_x and k_y components in reciprocal space (depicted in Figure 2.2).

Patterns that are seen on the RHEED screen can change in size depending on the terrace size, roughness and growth mode. Figure 2.3 shows some of the fundamental RHEED patterns typically observed during MBE growth and also shows the corresponding common real space structures these patterns represent. Usually, sharp streaks represent an atomically flat surface and a sample with rotational symmetry represents higher atomic

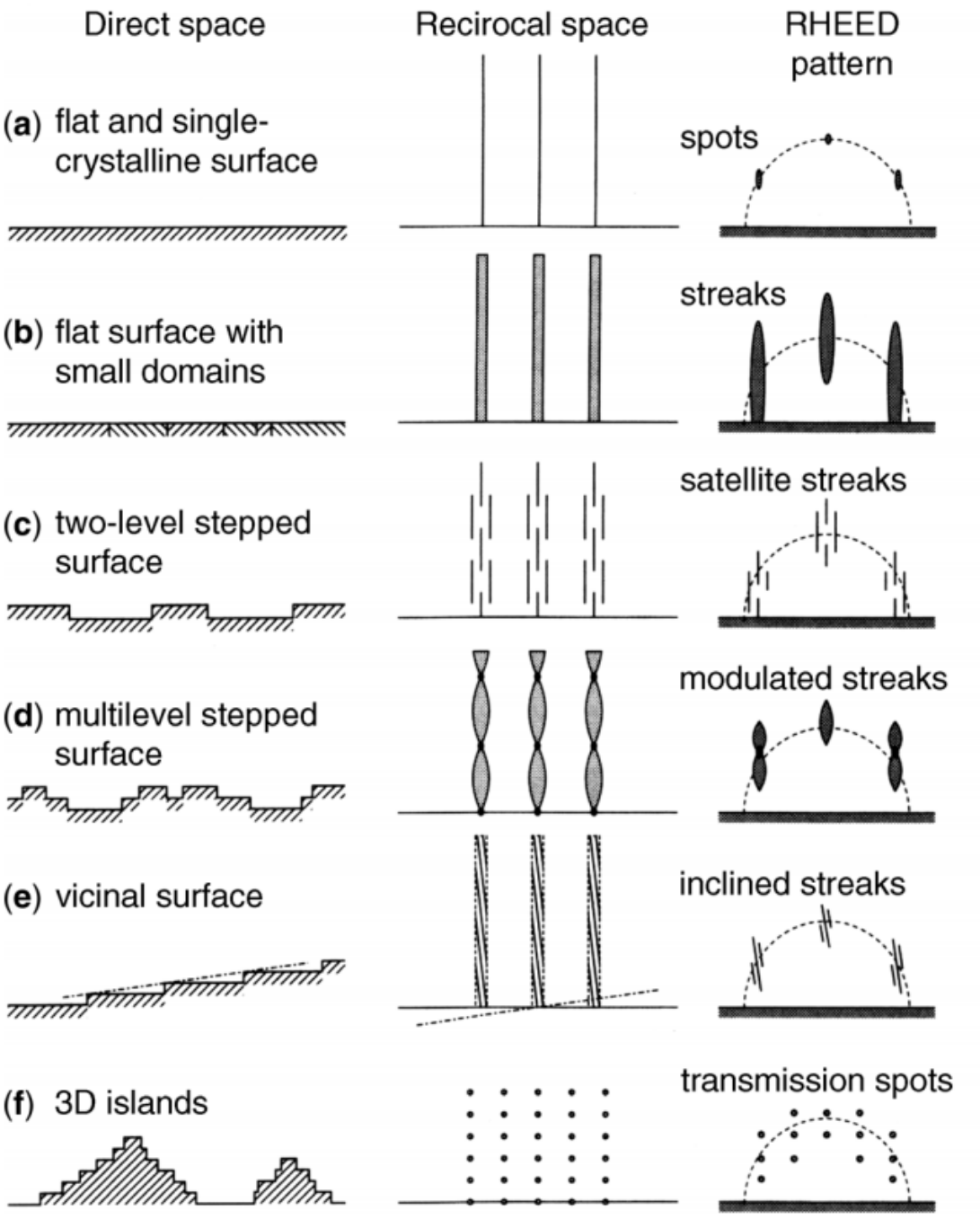


Figure 2.3: Different types of RHEED patterns shown on a screen. Typical patterns are shown in (a), (b) and (f). Adapted from ref [119].

ordering and high crystalline quality. There are also RHEED patterns that can give users further information about their crystal structures such as surface reconstructions which you may see after thermally annealing semiconductors such as GaAs(100) or Si(111) or depositing adsorbates on a crystalline surface such as Cu adatoms on Pt(100) substrates [121]. Surface superstructures or reconstructions are usually described with respect to the bulk crystal structure and are typically defined by Wood's notation which are described via

$$p(|b_1|/|a_1| \times |b_2|/|a_2|)R\theta - X \tag{2.2}$$

where p or c is to denote either primitive or centered surface lattice, b is the adsorbate or overlayer unit cell vectors, a is the bulk surface unit cell vector, $R\theta$ is the rotation angle and X is the chemical symbol of the adsorbed species [122]. An example of surface reconstructions defined by Wood notations is shown below in Figure 2.4. A (2×1) periodicity reconstruction in GaAs(100) means that the surface unit cell is twice as long in the a direction and the same length in the b direction with respect to the bulk unit cell. These reconstructions occur due to dangling bonds at the GaAs surface, which creates an interface that can be reconstructed into a lower-energy structure. RHEED is one technique that can measure the differences in these surface reconstructions while comparing to the bulk structure during the sample preparation and the growth process and a complementary technique that can measure the atoms in real space (which will be discussed later) is scanning tunneling microscopy (STM).

Another interesting feature that is determined from RHEED is the growth rate through intensity oscillations. The principle involves variation of constructive and destructive interference from electron scattering which can be monitored by integrating the primary

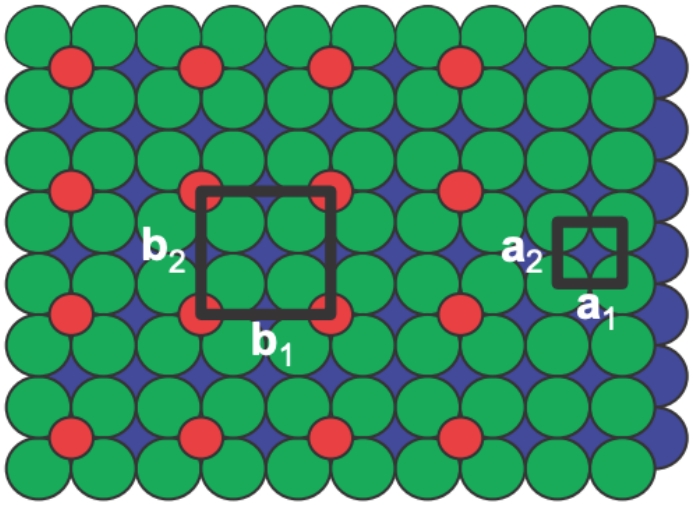


Figure 2.4: Example of using Wood Notation in fcc(100) where the structure here is p(2 × 2). Adapted from ref [122].

RHEED spot intensity. A smooth surface provides an intense, coherent primary spot (denoted 00), whilst a rough surface provides a weak, incoherent primary spot. This is depicted in Figure 2.5 where the degree of coverage corresponds to each fraction of a full layer of growth, hence low intensity is partial coverage deposited and high intensity for the smooth surface after full coverage. It is a simple case of counting the number of oscillations (1 oscillation = 1 ML) and averaging them over time (in seconds) to determine the growth rate in ML/sec. These oscillations will eventually dampen out in thicker layers which depends on how smooth the starting surface was and on the deposited material moving toward an equilibrium in surface roughness.

2.1.5 Growth Modes

Epitaxy typically takes place by depositing atomic layers on a smooth, lattice-matched surface. The growth may then proceed in an atomically flat, layer-by-layer fashion, which is referred to as the Frank-Van der Merve growth mode [122]. Two-dimensional nucleation sites form at the surface and the morphology is dependent on on the surface energy of the deposited layer versus the surface energy of the substrate. Eventually, in thicker deposits, the layers will coalesce from the nuclei on the surface. In the absence of terrace steps and defects like screw dislocations, growth of atomically flat surfaces in the layer-by-layer mode proceeds by clusters of adsorbed atoms with a sufficient size. They provide more preferential sites (2D nucleation sites) for the attachment of further atoms at their perimeter to go to higher thicknesses.

An intermediate case is referred to as Stranski-Krastanow growth mode, also termed layer-plus-island growth [122]. After exceeding some critical coverage, the growth changes to the Volmer-Weber case, creating islands or a three-dimensional growth mode [122]. Such change may be induced by the gradual accumulation of strain in the epitaxial layer. The overlayer then resumes growth in form of 3D islands, leaving a 2D wetting layer underneath. It should be noted that the critical thickness pointed out here lies usually below that required for the formation of misfit dislocations, due to lattice matching constraints. Stranski-Krastanow growth mode has been used in recent years for growth of defect-free quantum dots or nanowires [122].

These particular growth modes arise from a thermodynamic consideration of the interface energies. Which mode of nucleation, 2D or 3D, is thermodynamically preference

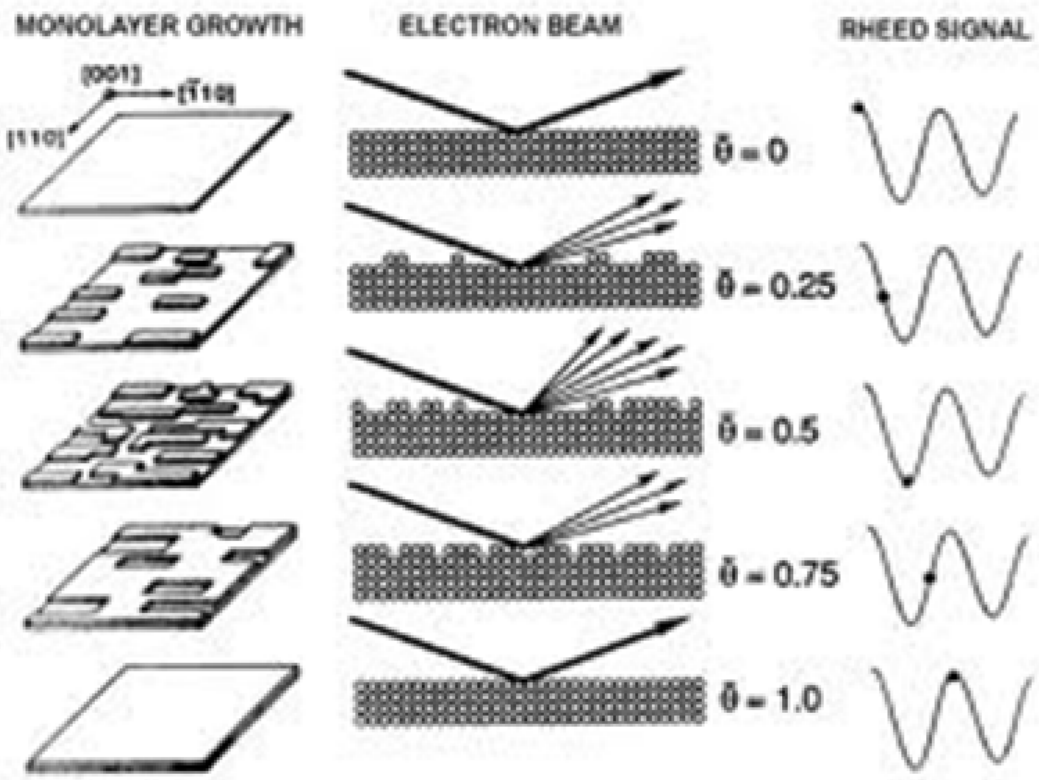


Figure 2.5: Schematic of RHEED intensity oscillations during epitaxial growth. Adapted from ref [119].

depends on the difference in interface energies and strain. For materials with low surface mobility of adatoms, columnar growth may be obtained. Similar to Volmer-Weber growth, islands nucleate, but they do not merge to continuous layers when growth proceeds.

2.1.6 Types of Epitaxial Growth

During epitaxial growth, lattice matching constraints play an enormous role in determining what material to grow on top of a crystalline substrate. The way to determine this is by calculating the percent difference from the in-plane lattice constant of the substrate to the as-deposited film, also known as the lattice mismatch. The lattice constant is directly related to the crystal structure of the material.

The three types of well-known epitaxial growths are homoepitaxy, heteroepitaxy, and van der Waals epitaxy (Figure 2.6). Homoepitaxy has to do with growing the same material as the substrate, A (e.g. $A_{overlayer}$ grown on $A_{substrate}$). The growth should be relatively straight forward since the crystal structures match, but will need to take into account the thermodynamics and adatom mobility in order to have a high-quality epitaxial growth. Heteroepitaxy involves growing a different material, B, on substrate A (e.g. $B_{overlayer}$ grown on $A_{substrate}$). Here, lattice matching constraints will play a role. As discussed similarly in the growth modes section, the deposited material will follow the substrate's lattice constant up to a critical thickness (dependent on the lattice mismatch) and then convert to its crystal structure. This region of growth up to a critical thickness usually consists of misfit dislocations which effects electronic device performance in semiconductors [64, 122].

The third and most important type of epitaxial growth for this dissertation is van

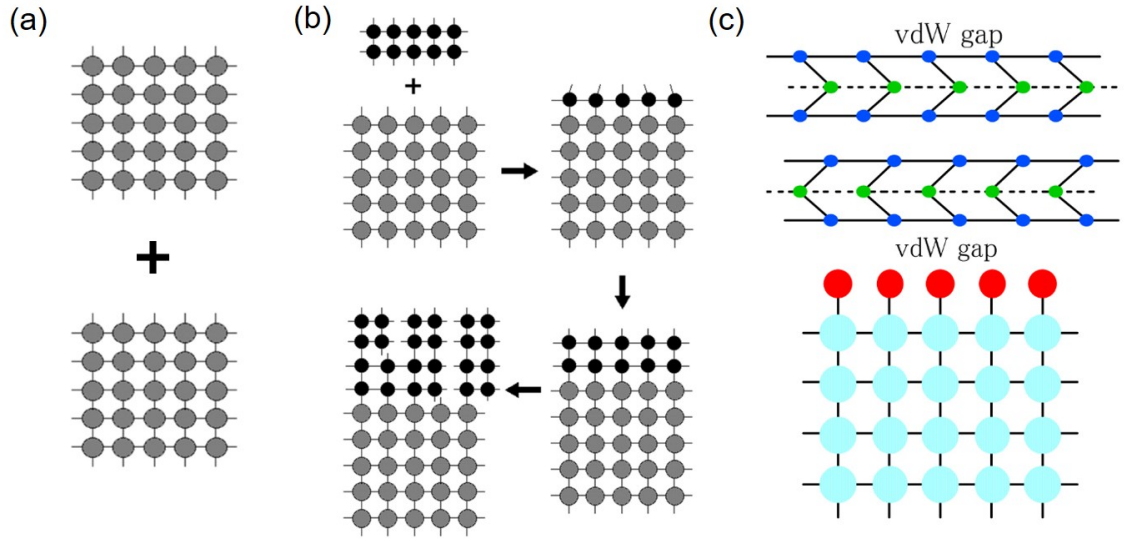


Figure 2.6: Different types of epitaxial growth. (a) Homoepitaxy. (b) Heteroepitaxy. (c) van der Waals epitaxy. Adapted from [123, 124].

der Waals epitaxy, which was discovered by Atsushi Koma in the early 1990s [124, 125, 126]. Usually dangling bonds appear on a clean surface of a 3D substrate and this makes it difficult to grow good heteroepitaxial films without a good lattice match in the constituent materials. On the other hand, materials such as graphite, or transition metal dicalcogenides (e.g. MoS_2), have a layered structure consisting of two-dimensional unit layers separated by a van der Waals gap. Each intralayer is formed via strong covalent bonds, while there is a weak van der Waals interaction between layers. These van der Waals materials can be easily exfoliated (via scotch tape) and the cleaved surface has a very wide and flat terrace without active dangling bonds. When adatoms are deposited on this inert surface, only the weak van der Waals interaction works between the substrate and the grown material. This results in a much smaller lattice mismatch distortion in the grown film even if it has a different lattice constant or crystal structure from the substrate. Consequently single

crystalline heteroepitaxial growth of layered materials can be achieved from the first layer on the van der Waals substrate. Initially, van der Waals epitaxy was the growth of a van der Waals material onto another van der Waals layered substrate. Later, it was extended to the growth of van der Waals materials onto 3D crystalline substrates, which have active dangling bonds on their clean surfaces. If these active dangling bonds are regularly terminated by suitable atoms, the surface will be inactive like a cleaved surface of a van der Waals material. A crystalline film of a van der Waals material can then be heteroepitaxially grown on such a passivated surface via weak interaction. This is depicted in Figure 2.6 An example of this is Se-terminated GaAs(111)B, H-terminated Si(111), or F-terminated CaF_2(111) [123, 124, 125, 126].

2.2 Structural Characterization

2.2.1 X-Ray Diffraction (XRD)

XRD techniques give information about the structure of solids which are the arrangement of the atoms that compose the solid. It permits a nondestructive structural analyses, although it is relatively low in sensitivity. There are three different types of XRD methods depending on the type of sample, which include: the powder method (for polycrystalline samples, discussed later), the single crystal method, and the amorphous method. XRD scans can give different types of qualitative and quantitative information including:

(1) Structural phases in the solid (e.g. peak indexing)

(2) Phase fractions that compose the solid (e.g. intensity of peaks)

(3) The quantity of materials that are crystallized

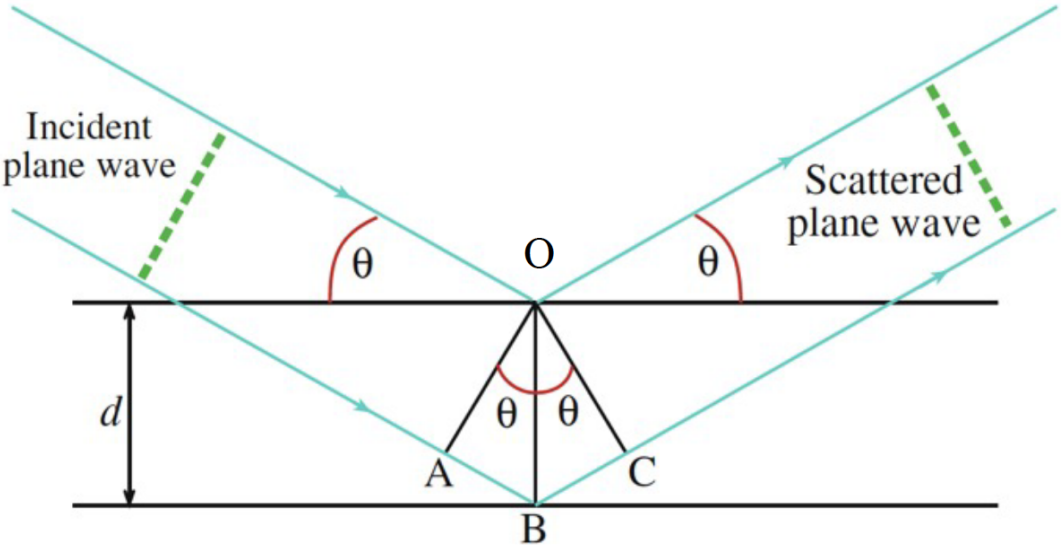


Figure 2.7: An example of XRD Bragg diffraction off of crystalline planes of a sample.

(4) Strain/stress in the solid (e.g. reciprocal space mapping)

(5) The size of crystallites that compose the solid

(6) Average orientation of crystallites that compose the solid

The basic principle of the XRD setup is shown in Figure 2.7. To measure your sample, incoming X-rays (produced from a Cu K-α radiation source) constructively interfere with the sample and diffract from crystal planes following Bragg's law

$$n\lambda = 2dsin\theta \tag{2.3}$$

where n is the integer number, λ is the wavelength of the X-ray source (typically Cu Kα, $\lambda =$ 1.54 Å), d is the spacing between planes (typically denotes the out-of-plane lattice parameter or c), and θ is the angle of diffraction. Some crystal Bragg reflections may have different intensities than others which may be due to the structure factor, polarization, Lorentz force,

multiplicity, temperature, or absorption. In order to determine the d-spacing, the following equations below can be used for six crystal structures

$$Cubic : \frac{1}{d^2} = \frac{h^2 + k^2 + l^2}{a^2} \tag{2.4}$$

$$Tetragonal : \frac{1}{d^2} = \frac{h^2 + k^2}{a^2} + \frac{l^2}{c^2} \tag{2.5}$$

$$Orthorhombic : \frac{1}{d^2} = \frac{h^2}{a^2} + \frac{k^2}{b^2} + \frac{l^2}{c^2} \tag{2.6}$$

$$Hexagonal : \frac{1}{d^2} = \frac{4}{3}(\frac{h^2 + hk + k^2}{a^2}) + \frac{l^2}{c^2} \tag{2.7}$$

$$Rhombohedral : \frac{1}{d^2} = \frac{(h^2 + k^2 + l^2)sin^2\alpha + 2(hk + kl + hl)(cos^2\alpha - cos\alpha)}{a^2(1 - 3cos^2\alpha + 2cos^3\alpha)} \tag{2.8}$$

$$Monoclinic : \frac{1}{d^2} = \frac{1}{sin^2\beta}(\frac{h^2}{a^2} + \frac{k^2 sin^2\beta}{b^2} + \frac{l^2}{c^2} + \frac{2hlcos\beta}{ac}) \tag{2.9}$$

where h, k, l are the Miller indices, a, b, c are the lattice parameters, d is the interplanar spacing, and α and β are the angles between the lattice parameters.

2.2.2 X-Ray Reflectometry (XRR)

Another X-ray technique, known as X-ray reflectometry, is a complementary measurement to atomic force microscopy (which will be discussed next) in terms of determining quantitative information on the thickness and roughness of samples deposited on wafers. XRR analysis can be performed on both crystalline and amorphous materials. The basic principle is when X-rays are exposed to a material's flat surface at a grazing incidence, total reflection will occur at or below a certain angle. This angle is exceedingly small and is referred to as the critical angle (θ_c). The angle varies depending upon the electronic density of the material. The higher the incident X-ray angle relative to the θ_c, the deeper

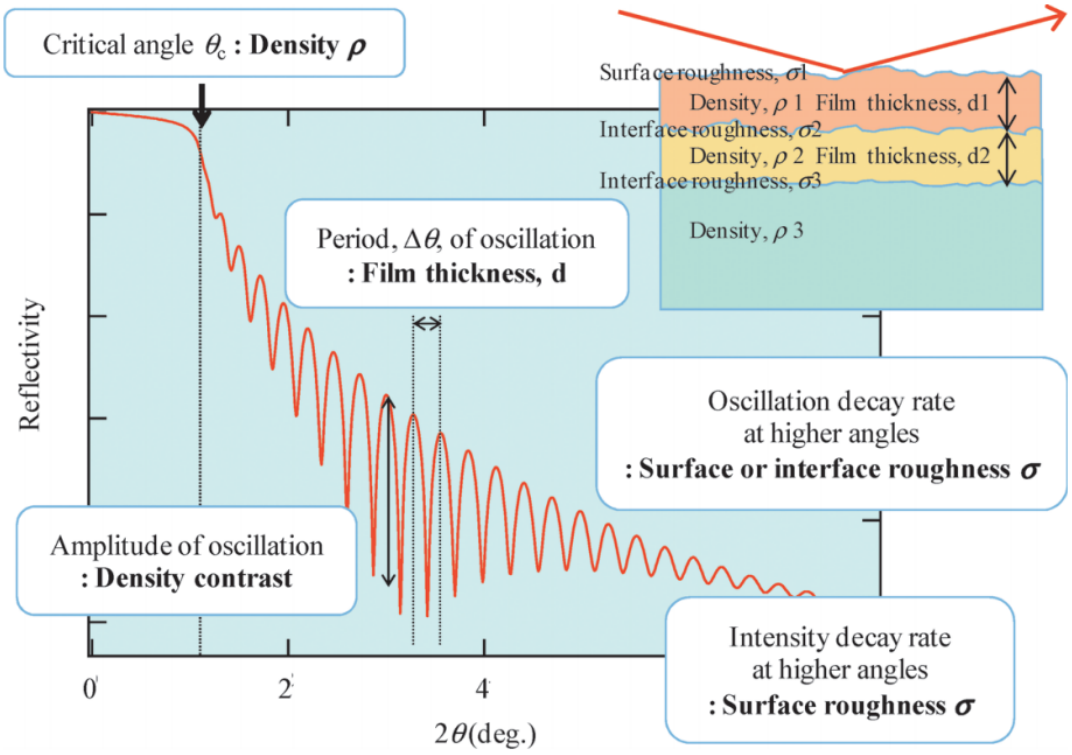


Figure 2.8: Relation between profile of the XRR and the structure parameters. Adapted from [127].

the X-rays transmit into the material. With a material whose surface is ideally flat, the reflectivity suddenly decreases at angles above the θ_c proportional to θ^4.

If the material surface is rough, it causes a more drastic decrease in reflectivity. If a substrate is evenly overlaid with another material having a different electronic density, then reflected X-rays from the interface between the substrate and the overlayer film as well as from the top surface of the film will either constructively or destructively interfere with each other. This will result in an interference-induced oscillation pattern or Kiessig fringes (shown in Figure 2.8). Two oscillation frequencies may show for a bilayer heterostructure sample. The periodicity of the oscillation depends on the film thickness, and the thicker the film, the shorter period of the oscillations. Therefore, XRR is a powerful tool that can determine the electron density profile, the vertical properties (layer thicknesses) as well as the lateral properties (roughness and correlation properties of interfaces or lateral layer structure) and characterization of multilayers.

2.2.3 Atomic Force Microscopy (AFM)

Atomic force microscopy is a powerful tool for determining surface morphology and roughness of a material. The basic principle of AFM is shown in Figure 2.9. A sharp tip (typically of SiN) is mounted onto the end of a cantilever which is oscillated at a chosen frequency while a laser is focused on the back of the cantilever. The reflected laser light is collected by a four-quadrant photodiode using a lock-in amplifier to isolate the noise from the signal. As the tip is brought into contact with the sample surface, van der Waals forces will interact with the tip and push it back. This tip deflection is picked up by the photodiode

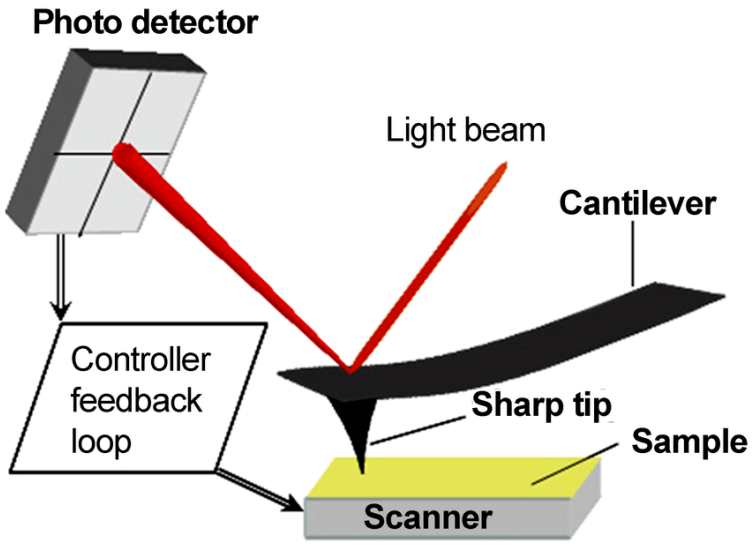


Figure 2.9: Basic principle of AFM. Adapted from [128].

as a voltage and converted into a topography output. Data is collected by scanning the tip in a lateral area across the sample and producing a 2D map of the surface. The tip can be operated in contact or tapping modes and also has options use other types of tips to perform conductive and magnetic force microscopy. The lateral resolution is ∼30 nm and vertical resolution can be up to 0.01 nm.

2.2.4 Scanning Tunneling Microscopy (STM)

A scanning tunneling microscope (STM) is an instrument for imaging surfaces at the atomic level. The resolution of the STM is of 0.1 nm lateral resolution and 0.01 nm depth resolution. Within this resolution, individual atoms within materials may be routinely imaged and manipulated.

STM is based on the concept of quantum tunneling [129]. When a conducting tip is

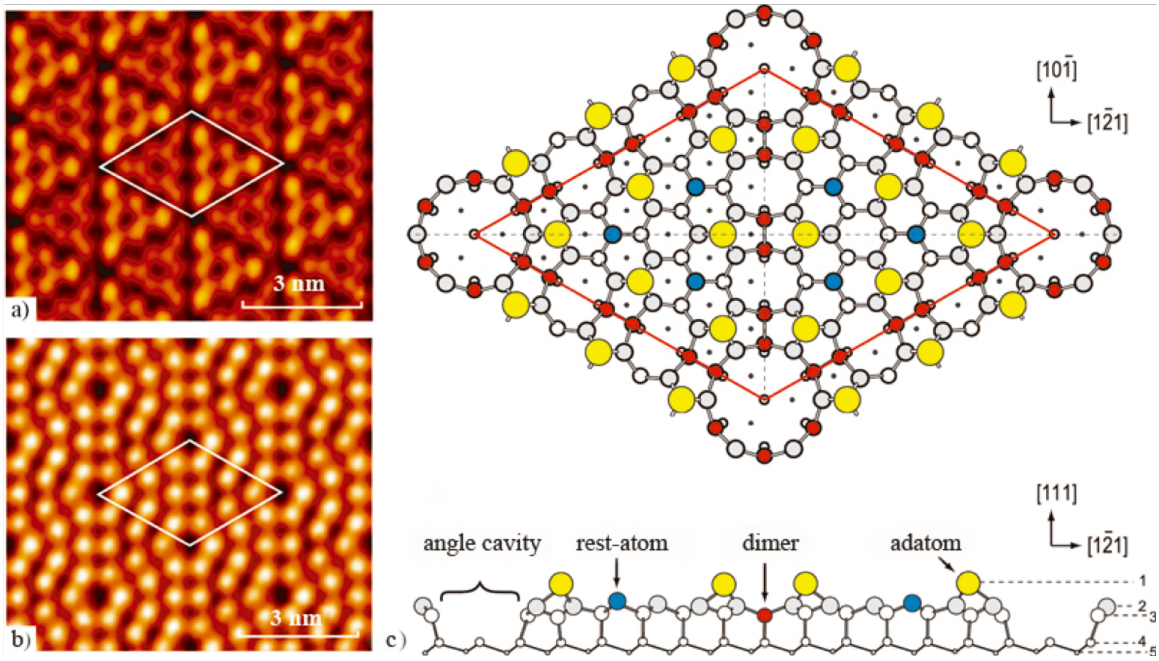


Figure 2.10: STM imaging of Si(111) 7 × 7 surface. (a-b) filled and unfilled electronic states of the surface and (c) Schematic representation of surface. Yellow, red, and blue circles represent Si atoms, Si dimers, second layer Si rest-atoms. Adapted from [129].

brought very near to the surface to be examined, a voltage bias applied the tip and surface can allow electrons to tunnel through the vacuum barrier between them. The resulting tunneling current is a function of tip position, applied voltage, and the local density of states of the sample. Information such as topography is acquired by monitoring the current as the tip's position scans across the surface, and is usually displayed in image form (see Figure 2.10). STM can be a challenging and time consuming measurement technique, as it requires extremely clean and stable surfaces, well-prepared and sharp tips, excellent vibration control, and sophisticated electronic communication.

To measure specific magnetic textures (e.g. magnetic domain structures, skyrmions, or other complex magnetic phases) down to the atomic scale, a magnetic tip is used [130, 131, 132]. This process is called spin-polarized STM (SP-STM). The principle operation

is having an extremely sharp tip coated with a thin layer of magnetic material (typically Cr) which is moved over a sample. For a magnetized tip, electrons with spins matching the tip's magnetization will have a higher chance of tunneling. This phenomenon is the effect of tunneling magnetoresistance (TMR) and the tip/surface interaction essentially acts as a spin valve.

2.2.5 Scanning Transmission Electron Microscopy (STEM)

Scanning transmission electron microscope (STEM) is a type of TEM. TEM is an extremely powerful tool for materials science in order to monitor structural defects such as misfit dislocations and impurities, image interfaces to look for strain and phase transitions, and to observe atomic imaging due to the high resolution. This is a microscopy technique during which a beam of high energy electrons is transmitted through a very thin specimen to form an image on a detector. The specimen is usually a very tiny cross-section extracted from a larger material less than 100 nm thick. Due to the short de Broglie wavelength of high energy electrons the resolution limit of such microscopes can reach 0.5 Å for the best high-resolution aberration-corrected TEMs. High-resolution TEM has become an extremely useful tool in studying atomic interfaces of MBE-grown films after growth and will be mentioned throughout this dissertation.

For preparation, samples post-growth are first capped with a thick metallic layer (typically Pt or Au). The sample is then thinned (via a focused ion beam, FIB) to make a slice of 30-50 μm. The slice is then removed via a probe from the larger sample and is then further thinned down by the FIB and ion milling to $\sim$10 nm. This geometry is necessary for electrons to travel through the specimen easily. Finally, the specimen will be transferred

to a TEM chamber for the actual experiment.

TEMs have a wide range of operating modes such as imaging (STEM, and Lorentz TEM), diffraction, and spectroscopic measurements. For this dissertation we will focus on STEM or imaging modes. Imaging methods use information from the electron waves leaving the sample to form an image. The time-averaged intensity, I, of the image, can be approximated as

$$I(x) = \frac{k}{t_1 - t_0} \int_{t_0}^{t_1} \Psi \Psi^* dt \tag{2.10}$$

where k is the electron momentum vector and Ψ is the electron wavefunction. The observed image depends not only on the amplitude of the electrons, but also on the phase which may take effect for extremely thin specimens. The specimen is illuminated with a parallel electron beam, formed via beam shaping from a combination of condenser lenses and apertures. After electron and sample interaction, two types of electrons exist: unscattered and scattered. To achieve an image, a combination of the objective aperture and signal from the diffracted beam is used to create bright field and dark field images, then the selected signal is magnified and projected on a screen via projector lenses.

2.3 Magnetometry

2.3.1 Superconducting Quantum Interference Device (SQUID)

A SQUID is a very sensitive magnetometer that operates on the principle of a Josephson junction that measures down to a single quantum flux (ϕ_0) of

$$\phi_0 = \frac{2\pi\hbar}{2e} = 2.0678 \times 10^{-15} Tm^2 \tag{2.11}$$

where $\hbar$ is Planck's constant and e is the charge of an electron [133]. The SQUID consists of two superconductors separated by thin insulating layers to form two parallel Josephson junctions and is used in a magnetometer to detect small magnetic fields, B, as low as 5 $\times$ 10^{-18} T. An external magnetic field is applied to a sample and a pick-up coil measures the response of the sample to the magnetic field. This is done through the principle of Faraday's law and converts the voltage signal into a total magnetic moment in electromagnetic unit (emu). SQUID is a very useful technique for measuring very small or ultrathin magnetic samples which may also be its limitation when trying to exclude impurities from a measurement [134]. Typical operation includes:

(1) Loading a specimen in a non-magnetic straw in either in-plane or out-of-plane orientation with respect to the external magnetic field of SQUID.

(2) Attach the sample-straw holder to a DC or reciprocating sample option (RSO) rod and load into sample space of SQUID magnetometer.

(3) Vent/purge sample space three times to clean out any dust or debris.

(4) Open sample space to SQUID via gate valve and slide down to position slowly (speed will depend on the temperature of the system).

(5) Once sample is below its magnetic or superconducting ordering temperature, run centering scan to find sample and to position it with respect to the coils.

(6) Run sample sequence (e.g. M(T) or M(H)).

2.3.2 Vibrating Sample Magnetometer (VSM)

VSM, which refers to vibrating sample magnetometry, is an instrument that measures the magnetic properties of materials. It is similar to SQUID in terms of the quanti-

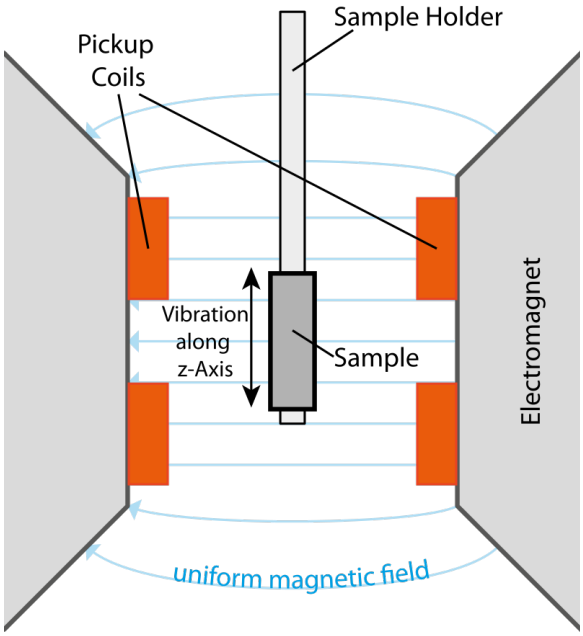


Figure 2.11: Basic principle of VSM. Adapted from link: https://en.wikipedia.org/wiki/Vibrating-sample-magnetometer.

tative information that you gather about a material's magnetic moment but it is much less sensitive to small magnetic fields and the physical principle of operation is quite different.

It consists of an electromagnet capable of applying a desired external magnetic field along a desired axis and a cavity composed of a solenoid coil. The sample is placed inside this cavity under a uniform magnetic field while being under vibration at a known frequency. This oscillatory motion of a magnetic moment will produce a change in the magnetic flux inside the cavity and will be picked up by the nearby coils. The induced voltage is proportional to the material's magnetic moment. This magnetic moment, μ is related to the flux through

$$\phi_B = \mu \frac{B}{I} \tag{2.12}$$

with B being the magnetic field generated by the effective current I circulating in the detection coil. The measurement is performed by sweeping the applied magnetic field, H, and determining the magnitude of the magnetic moment at each applied field, producing a μ (or m) vs. H plot. This can be converted to magnetization M vs. H through dividing m by the volume, V of the film of interest. This is depicted in Figure 2.11.

VSM is a bulk magnetization measurement (like SQUID) which picks up the signal generated by the sample holder and the substrate on which the film is grown. While all these components are non-magnetic, they will each contribute a diamagnetic linear background, which must be subtracted during analysis. VSM's may come with other advantageous options such as an oven option where samples may be heated to temperatures up to 1000 K while measuring the magnetic properties. Also, if measuring in air, magnetic samples that have non-magnetic electrical probes can be measured while under an applied electric field.

2.3.3 Ordinary Magnetoresistance (MR)

Ordinary MR is the change of electrical resistance in a material due to an externally-applied magnetic field. This is due to reduction of the mean free path in the current direction when the electrons complete a significant fraction of a cyclotron orbit before they are scattered. MR effects associated with cyclotron motion can be significant when $\omega_c\tau \geq 1$, where τ is the time between scattering events. The effect is initially quadratic in B. The longer the relaxation time, the greater the influence of magnetic field on the resistivity [135]. This MR depends on the interband scattering; and in fact it is strictly zero in the single-band free-electron model [135]. The MR is small ($\approx$1% in 1 T) in metals where scattering is strong, but it may be much larger in semimetals and semiconductors, where the electron

mobility is high. MR is typically denoted by a percentage to compare with other materials or effects on the sample, this is denoted by

$$\frac{\Delta R}{R}(\%) = \frac{R_{xx}(H) - R_{xx}(0)}{R_{xx}(0)} \times 100\% \tag{2.13}$$

This is typically denoted as R_{xx} for the electrical resistance or ρ_{xx} for the resistivity. MR is generally positive in metals but may change due to its band structure or other exotic physical properties [135]. MR depends on the magnitude of the applied magnetic field and the orientation of the applied current with respect to the field. For this dissertation, we will focus on transverse MR, where the applied magnetic field, H, is perpendicular (or transverse) to the applied current direction.

2.3.4 Anomalous Hall Effect (AHE)

The ordinary Hall effect comes into the picture due to the Lorentz force. When an electrical current (of electrons) is passed through a conductor and a perpendicular magnetic field is applied, the electrons are deflected and accumulate at the edge of sample until the electric field they create is sufficient enough to balance the Lorentz force. This is typically used to determine a material's carrier density and mobility.

The AHE is observed in a sample with broken time-reversal symmetry or in other words, a ferromagnetic impurity that deflects the electrons and creating a net spin population at the edge of the sample. The Hall resistance, R_{xy}, is significantly different for ferromagnetic conductors opposed to non-magnetic conductors. As mentioned earlier, R_{xy} increases linear with applied field, H_z, in non-magnetic materials while it is non-linear and saturates at a higher field in ferromagnets. This saturation is proportional to the magneti-

zation, M_z, in the ferromagnet. This is given by

$$R_{xy} = R_0 H_z + R_s M_z \tag{2.14}$$

where R_0 is the electrical resistance related to charge carriers or the ordinary Hall effect and the second term, R_s, is related to the material parameters (which may give rise to the magnetic ordering). The microscopic origin of the AHE is may be due to extrinsic mechanisms such as skew scattering or side jump and in some structures is dominated by the intrinsic Berry curvature [136]. This measurement is most useful for measuring hysteresis loops in ferromagnetic conductors with an out-of-plane magnetic anisotropy.

2.4 High Pressure Measurement Tools

2.4.1 Piston Pressure Cells

For hydrostatic pressures up to ∼1 GPa, piston pressure cells are typically used. The DC Quantum Design SQUID magnetometers are equipped with an attachment for these pressure cells (shown in Figure 2.12). For loading, samples are placed inside a small cylindrical plastic tube along with a Sn manometer (for determining the pressure) and a transmitting medium. This is then placed in the middle of the pressure cell held in by extrusion disks and ceramic pistons. Pressure (P) is determined by the T_c of the superconducting Sn manometer, this is shown by the equation below [137]:

$$T_c(P) = T_c(0) - (0.4823 \pm 0.002)P + (0.0207 \pm 0.0005)P^2 \tag{2.15}$$

Samples are then externally pressurized via a piston hydraulic press. After each pressurization, samples are attached to the DC SQUID rod via threading and loaded into the

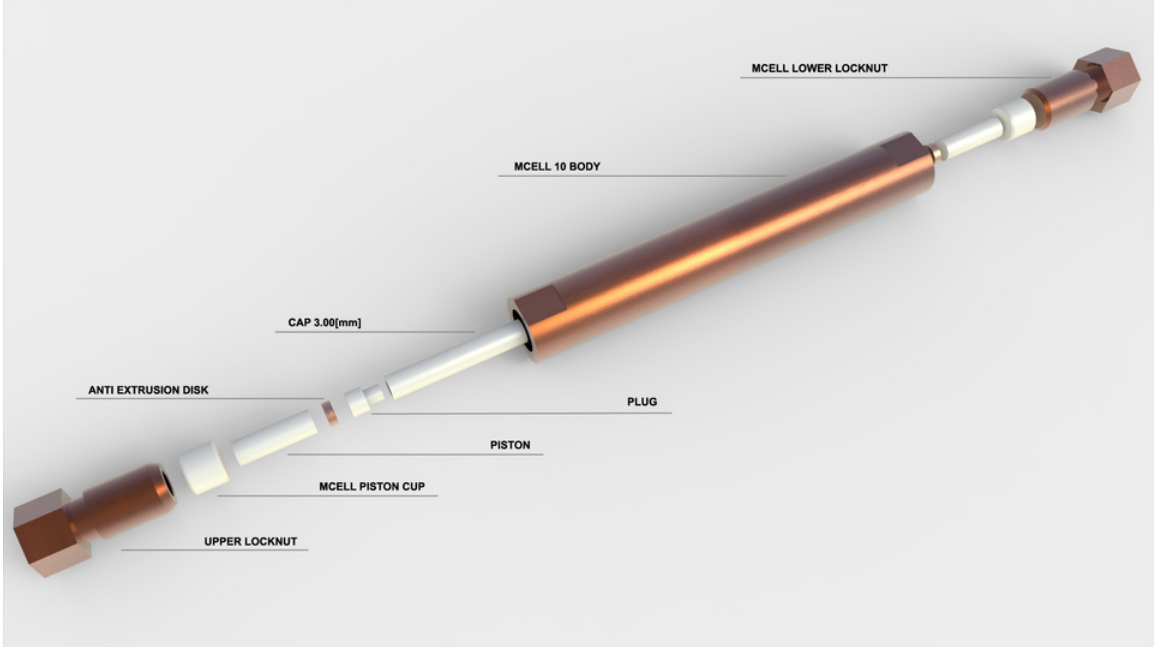


Figure 2.12: Exploded view of SQUID pressure cell components. Taken from link: https://grabcad.com/library/mcell-10-high-pressure-cell-1.

measurement system. The loaded cell is shown in 2.13. The pressure cell is then cooled down slowly below the transition temperature of the Sn manometer and positioned accordingly. The pressure cell must be thermalized at 300 K before inserting or removing from the measurement chamber.

2.4.2 Diamond Anvil Cells (DACs)

Diamond anvil cells (DACs) are instruments that can place samples under high pressures. This is particularly useful for looking at physical phenomena that only occurs under extreme conditions such as high temperature and pressures like the Earth's core. A DAC consists of two opposing diamonds with a sample compressed between the polished culets (tips) on each diamond. These diamonds are typically attached via a glue such as



Figure 2.13: Loaded SQUID pressure cell.

stycast to a tungsten carbide backing plate which are held in by set screws on an exterior housing for protection. A metal gasket (typically rhenium) is placed between the two diamond culets and the desired sample is placed inside the center hole of the gasket along with a pressure marker (if necessary) and a pressure-transmitting medium. For this dissertation, I will be discussing about DACs with culet sizes of 500 μm that can pressurize samples up to $\sim$40 GPa. The exterior housing of the DAC is held together with four screws to bring the diamonds into contact with eachother and to increase/decrease pressure. The housing is also designed to allow a gas-driven membrane to be attached. This provides more consistent pressure increments and the DAC does not need to be removed from the experimental apparatus to pressurize.

2.4.3 Designer DACs

Lawrence Livermore National Laboratory (LLNL) owns a pair of designer diamond anvils that contain eight electrical probes. These are meant to perform electrical transport measurements down to temperatures as low as 1.8 K and up to external magnetic fields as high as 16 T. The cell is made of Cu-Be to minimize the effects of stray fields and the gaskets are made of non-magnetic steel, MP35N. A standard 300 μm diamond is paired with a 250 μm *designer* diamond with eight tungsten electrical probes lithographically deposited onto the culet surface and encapsulated with chemical vapor deposition (CVD) synthetic diamond [138, 139, 140]. A schematic and laboratory photo is shown in Figures 2.14 and 2.16. The tungsten probes are only exposed in the center of the culet of the diamond in which they are connected to larger tungsten pads deposited on the pavilion of the diamond. The larger tungsten pads are used to connect to gold wires, which are soldered to external copper wires for connecting to a measurement system.

The gasket for the sample is initially indented to a 40 μm thickness and a hole is drilled through the center using a wire-electrical discharge machine (EDM). A bulk crystal (crystalline or non-crystalline) is polished or cleaved to $\sim$10 μm in thickness with a cross sectional area of $\sim$50 $\times$ 50 μm^2. It is carefully placed onto the tungsten probes which are centered in the gasket hole. It is imperative that the sample remain on the probes when closing the pressure cell. This means that traditional pressure media (e.g. Ne, silicone gel, organic solvents, etc.) cannot be utilized and instead steatite is used. Steatite is more susceptible to pressure gradients than other pressure media, but is solid under ambient conditions and only minimally influences the sample position when assembled. By applying

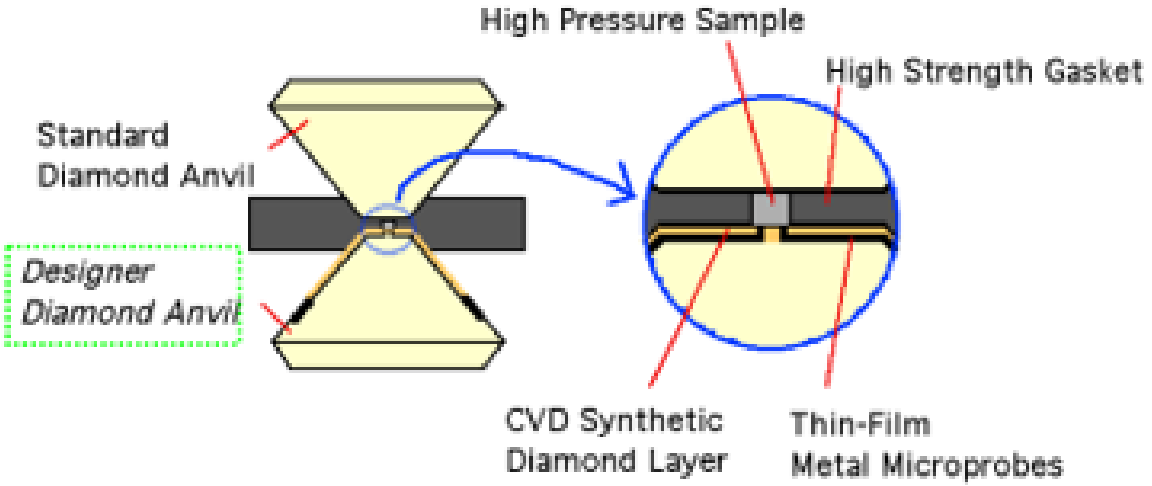


Figure 2.14: Schematic of *designer* DAC. Tungsten microprobes are deposited onto a standard diamond and encapsulated in CVD synthetic diamond. The culet of the diamond is then polished to provide a smooth surface. By placing a sample on the tungsten probes and pressurizing the cell, electrical connections can be achieved. Adapted from [138].

a modest pressure (approximately 0.5 GPa for a new sample loading), electrical connections between the sample and the tungsten probes can be achieved. Pressure in the designer-DAC is controlled with an external piston which is driven up or down with a small dial that has a 100:1 force ratio.

The cell is designed for a physical property measurement system (PPMS) by Quantum Design. The geometry is such that the magnetic field of the PPMS will be normal to the sample plane while the current (and voltage) will be parallel to the sample surface. To measure different crystalline axes or attempt to perform angular-dependent measurement, the samples must be polished along different axes. Depending on the cleavage plane, it may result in crystals failing at lower pressures, less signal-to-noise ratio, and a challenging cell assembly. For these reasons, it is generally best to start these measurements with oriented crystals, and to only attempt alternate orientations if necessary. Van der Waals crystals are

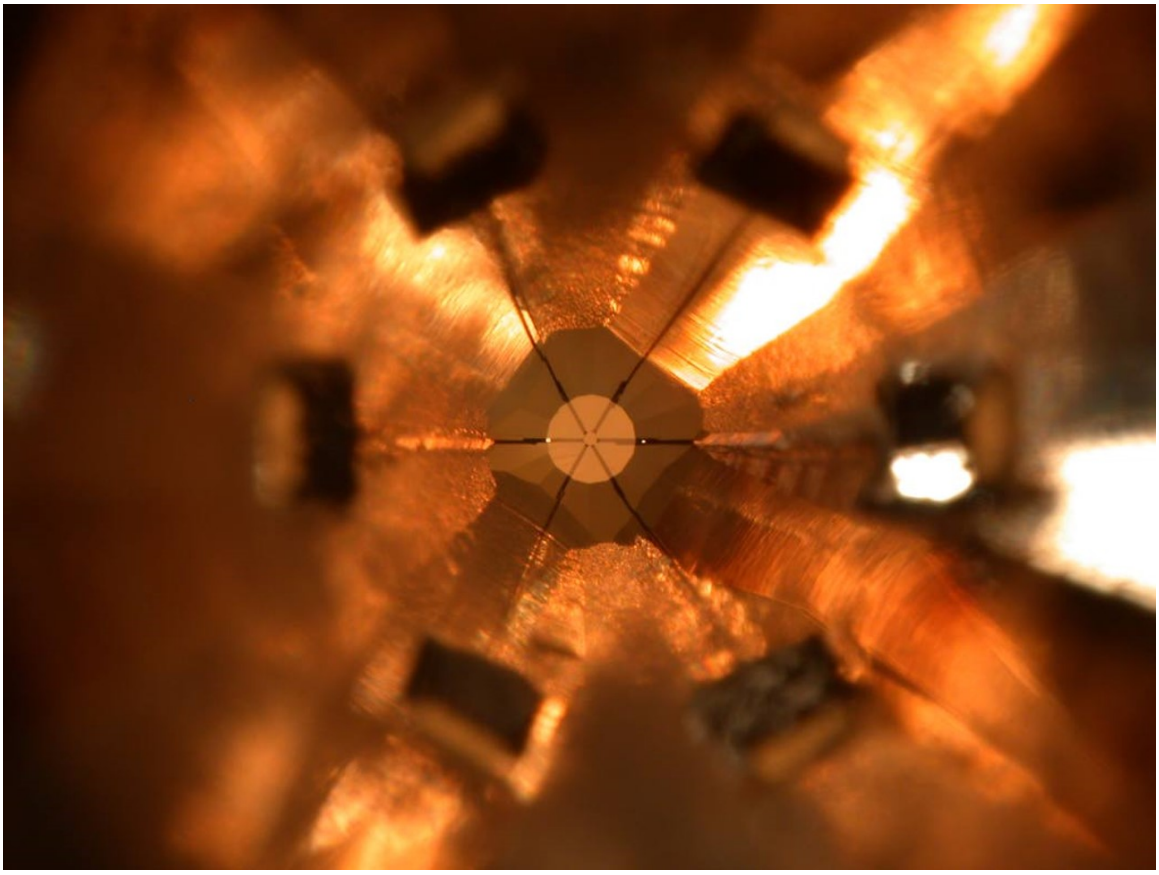


Figure 2.15: Optical photograph of *designer* diamond with metal probes. The deposited metal leads are connected to pads on the edge of the diamond which are then connected to external wires for measurements. Adapted from [141].

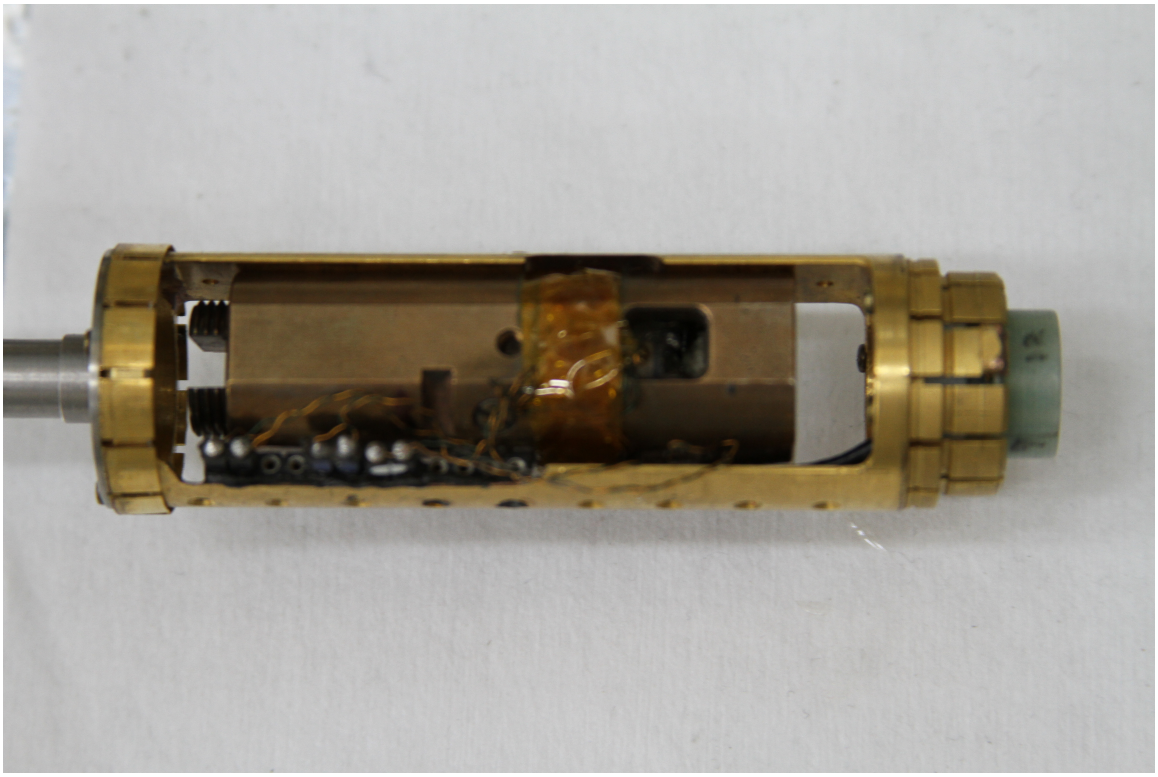


Figure 2.16: Laboratory photo of *designer* DAC attached to PPMS rod for measurements.

preferred for assembly due to the weak bonding between layers (meaning easy cleavage), but during pressurization challenges may arise such as folding and tearing which may lead to electrical contact problems and/or large changes in data.

2.4.4 Pressure Calibration

When assembling and pressurizing a DAC, the quickest method of checking pressure is by measuring the ruby fluorescence. A low-power laser is focused onto one of the rubies, and the fluorescence is measured with a spectrometer. The pressure can be calcu-

lated by the following equation

$$P(Mbar) = \frac{a}{b}\Big[\Big(\frac{\lambda_0 + \Delta\lambda}{\lambda_0}\Big)^b - 1\Big] \tag{2.16}$$

where $a = 19.04$, $b = 5$, λ_0 is the wavelength measured at 1 bar and $\Delta\lambda$ is the lineshift observed under pressure [142]. This is the preferred method for measuring pressure when performing spectroscopic measurements or when using the *designer* DAC. When performing XRD measurements, the best method to determine the pressure is by measuring the contraction of the unit cell of a material with a well known equation of state (EOS). Typically copper or gold are used for this purpose, where a small amount of powder is mixed with the sample and the diffraction pattern is measured alongside that of the sample. The diffraction pattern is analyzed to calculate the unit cell volume, and, combined with the bulk modulus and its derivative, is sufficient to calculate the pressure. For this work, only gold was used, which has a bulk modulus of $B = 148$-180 GPa and a pressure derivative of $B' = 6.43$ [143]. These values were then used to calculate the pressure via the Rose-Vinet EOS [144]. The EOS's are shown below starting with the third-order Birch-Murnaghan [145]

$$P(V) = \frac{3}{2}B_0\Big[\Big(\frac{V_0}{V}\Big)^{7/3} - \Big(\frac{V_0}{V}\Big)^{5/3}\Big]\Big\{1 + \frac{3}{4}(B_0' - 4)\Big[\Big(\frac{V_0}{V}\Big)^{2/3} - 1\Big]\Big\} \tag{2.17}$$

and Rose-Vinet

$$P(V) = 3B_0\Big(\frac{1-\eta}{\eta^2}\Big)e^{1.5(B_0'-1)(1-\eta)} \tag{2.18}$$

where $\eta = \sqrt[3]{\frac{V}{V_0}}$, B_0 is the bulk modulus, B' is the pressure derivative, and V_0 is the volume at ambient pressure.

2.5 Synchrotron Experiments

2.5.1 X-ray Magnetic Circular Dichrorism (XMCD)

XMCD was performed at both the Advanced Light Source (ALS) of Lawrence Berkeley National Laboratory (LBNL) on beamline 6.3.1 and at 4-ID-C of the Advanced Photon Source (APS) of Argonne National Laboratory (ANL). The XMCD is defined as the difference between the x-ray absorption spectra (XAS) for antiparallel and parallel configuration of the light helicity and magnetic field direction [146, 147]. The $2p$ core level is split in a $j = 3/2$ state (L_3 edge) and $j = 1/2$ state (L_2 edge), where spin and orbit are coupled parallel and antiparallel, respectively. In the first step, the emission with the light helicity vector parallel (antiparallel) to the $2p$ orbital moment results in excited electrons of preferred spin up (down) direction. Finally, these excited electrons have to find a place in the $3d$ valence band, and if there are less spin-up than spin-down *holes* available, the XMCD spectrum displays a net negative L_3 and positive L_2 peaks. XMCD is advantageous due to the following:

(1) Element-specificity.

(2) Orbital sensitivity.

(3) Selection rules.

(4) Magnetic sensitivity.

(5) High energy resolution.

(6) Well-defined core-level states.

(7) Sum rules.

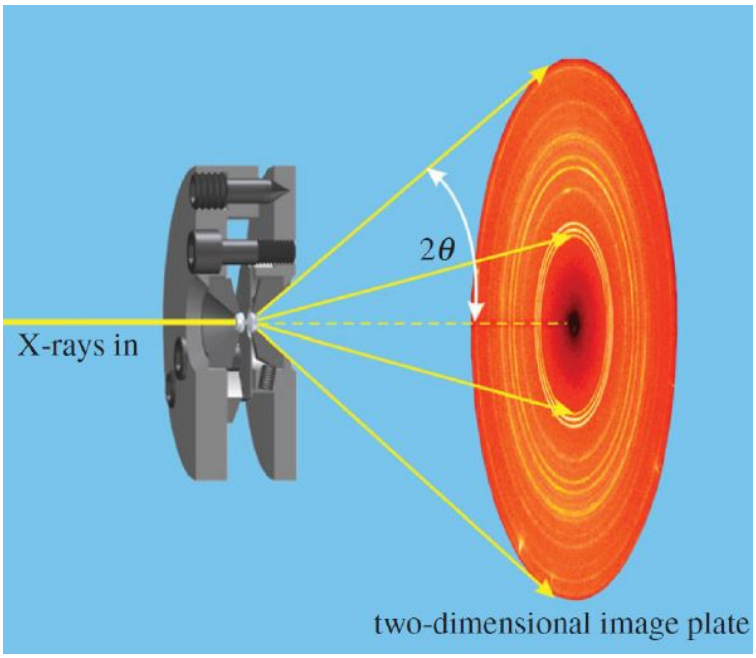


Figure 2.17: Debye-Sherrer geometry used for powder XRD experiments. Adapted from [150].

2.5.2 Powder XRD

XRD under high pressure was perfomed at sector 16-BMD of the APS at ANL. These beamlines are dedicated to high-pressure experiments and use the Debye-Sherrer geometry shown in Figure 2.17. The powder XRD patterns are acquired on a 2D image plate, where an example pattern is shown in Figure 2.18 and are integrated with *Dioptas* [148] to obtain 1D I(θ) plots [149].

The typical beam energy is 30 keV, chosen to avoid any excessive attenuation through the DAC components, and to maximize the incident flux. The sample is powdered and loaded into a DAC, along with pressure marker (e.g. Au, Cu or NaCl) and a ruby (the pressure marker is chosen depending on overlapping of peaks). The DAC is then pressurized using Ne as a pressure medium and loaded into the beamline hutch. The X-ray beam is

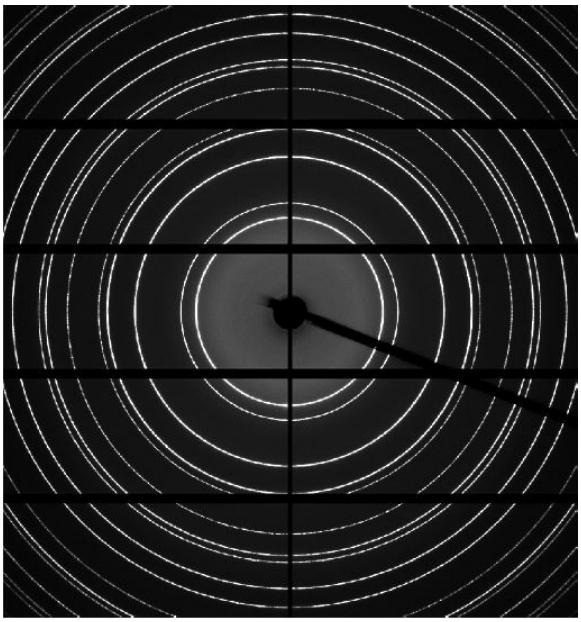


Figure 2.18: CeO_2 image scan for calibration. Black lines are the image plate and diode.

initially aligned to the powder by performing transmission and rocking curve scans. The exact position is then slowly refined by maximizing sample and pressure marker peaks and by minimizing or avoiding gasket diffraction peaks.

As discussed in an earlier section, peak positions are defined via Bragg's Law. For high-pressure powder XRD, peak positions and intensities are particularly important for refinement. The analysis in this work is performed using a combination of GSAS-II and *UnitCell* to refine lattice parameters [151, 152]. The steps below are used to refine the given data and determine lattice parameters:

(1) Refine diffraction pattern of CeO_2 calibration sample (Figure 2.18) to determine instrument parameters (corresponds to peak broadening due to the instrumentation)

(2) Refine diffraction pattern of pressure-dependent sample using *fixed* instru-

mentation parameters and only allow the lattice parameters, peak intensity, indexing, and peak broadening vary with pressure.

Due to peak broadening that occurs under pressurization, peaks begin to merge and will become challenging to index properly resulting in inadequate fittings and refinements at varied pressures. In this case, the merging peaks are removed for the pressures that they overlap and if this causes continued inconsistencies in the lattice parameters, they are removed for all XRD spectra.

Chapter 3

Molecular Beam Epitaxy of Non-Magnetic 2D Semiconductors and Their Heterostructures

3.1 Motivation

In this chapter, I will discuss the development of non-magnetic 2D semiconductors on 3D substrates, primarily on GaN(0001). The materials discussed will be GaSe and $SnSe_2$, which will be a baseline for later work discussed in this dissertation.

3.2 Molecular Beam Epitaxy of 2D-Layered GaSe on GaN Substrates

Two-dimensional (2D) metal chalcogenides are of great scientific interest for electronic as well as optical devices due to their unique structural, electrical, and mechanical properties, such as wide range of bandgaps, [62, 153] valley-polarized carriers, [154, 155] strong spinorbit coupling, [156] and superconductivity [157]. Recently, artificial stacking of these layered materials is being heavily explored to create heterostructures for novel applications. Most of these studies have been carried out by transferring layered flakes or films from minerals [158, 159] or synthesized materials obtained using chemical vapor transport (CVT) [160, 161] or chemical vapor deposition (CVD) methods [162, 163]. In contrast to such stacking methods, epitaxial techniques such as metal organic chemical vapor deposition and molecular beam epitaxy (MBE) provide a more practical approach to achieving large area epitaxial materials with precise control of layer thickness and doping. In addition, the absence of out-of-plane dangling bonds in layered materials can enable van der Waals epitaxy (vdWE) on highly lattice-mismatched substrate without lattice matching constraints [124, 125]. For instance, growth of gallium selenide (GaSe) on mica substrates with a significant lattice mismatch of 35% has been reported [124].

Van der Waals epitaxy was first introduced by Koma and co-workers and has been proven to be a powerful route to realize heteroepitaxy of 2D materials [125]. More recently, renewed interest in 2D materials has led to the exploration of MBE growth of several materials, including GaSe, [164, 165, 166] $MoSe_2$, [167, 168, 169, 170, 171] WSe_2, [172] and $HfSe_2$ [173]. In this Chapter, I report our work on growth of GaSe, which has a

layered crystal structure consisting of repeating units of covalently bonded Se-Ga-Ga-Se held together by weak van der Waals force.

Layered GaSe, however, occurs in several polytypes displaying different stacking sequences, leading to ϵ-, β-, γ-, and δ- phases of the material [174]. Most common polytypes, epsilon (consists of two layers per unit cell and has the space group, $D1^{3h}$) and b (consists of two layers and has the space group, $D4^{6h}$), have a 2H stacking sequence [175]. Bulk ϵ-GaSe is a 2 eV direct bandgap semiconductor and has been explored for applications in nonlinear optics, photovoltaics, and photodetectors [176, 177].

Single crystal MBE growth of GaSe on GaAs(111)B substrates has been reported by Ueno *et al.* [178] It has also been shown that GaSe and Ga_2Se_3 can be grown on GaAs(001) substrates depending on the surface reconstruction [179]. Vinh *et al.* demonstrated the growth of single crystal GaSe film on Si(111) substrate with 7 $\times$ 7 surface reconstruction [180]. In addition, recent studies report that the growth of GaSe on sapphire substrates produces crystalline films with random in-plane orientation of the domains [164].

However, there have not been reports on GaSe growth on wide bandgap semiconductors such as gallium nitride (GaN). Epitaxially grown high quality 2D materials on GaN can enable vertical 2D/3D heterostructures [181, 182] that can enable vertical tunneling devices, [181] heterojunction bipolar transistors (HBT), and hot electron transistors. We demonstrate the growth of highly crystalline centimeter-scale few layer GaSe films on bulk 3D materials such as sapphire and GaN. First, we have investigated the growth of continuous GaSe film on sapphire substrates at various growth conditions and utilized the optimized condition to grow GaSe on a GaN substrate. We report a two-step growth method to grow

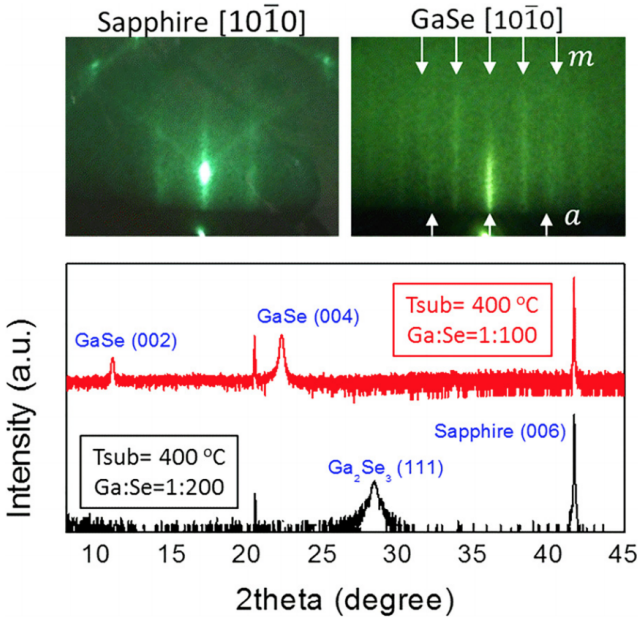


Figure 3.1: RHEED patterns observed along [10$\bar{1}$0] azimuth for (a) sapphire substrate and (b) GaSe film. (c) XRD spectra of GaSe grown at 400°C with Ga:Se of 1:200 (black) and 1:100 (red). Se flux was maintained at 1×10^{-6} Torr.

crystalline GaSe on GaN substrates by employing a high temperature nucleation step for growth of single crystal domains followed by the second step at lower growth temperature to achieve coalescence of the film.

MBE growths were performed in a Veeco Gen930 system with a standard thermal effusion cell for gallium. While previous reports on GaSe growth use the standard Knudson-type effusion cell to evaporate selenium, in this work, we use a valved cracker source to supply Se. Se was evaporated using a valved cracker source with the cracker zone at 950°C in order to obtain Se_2 species of Se [183]. Growth was monitored *in situ* using reflection high-energy electron diffraction (RHEED). Prior to the growth, *c*-plane sapphire and Fe-doped insulating GaN(0001)/sapphire substrates were solvent cleaned, annealed at 400°C under ultra-high vacuum conditions (1×10^{-9} Torr), and loaded into the growth chamber

(base pressure 7 $\times$ 10^{-10} Torr). Sapphire substrates were then annealed at 850°C in the growth chamber for 30 min. before ramping down the substrate temperature for GaSe growth (400-500°C). The Gallium sub-oxides on GaN substrates were removed *in situ* prior to the growth by using the following Ga polish technique. GaN substrates were exposed to a Ga flux of 1 $\times$ 10^{-8} Torr until the RHEED showed an amorphous pattern at 400°C. The substrate was then heated to 700°C for 30 min., followed by a ramp down to the growth temperature. Streaky RHEED patterns with Kikuchi line patterns were obtained prior to initiation of GaSe growths on sapphire and GaN substrates. The substrate temperature was measured using the thermocouple attached with the continuous azimuthal rotation (CAR) heater. The beam-equivalent pressure (BEP) of Se was fixed at 1 $\times$ 10^{-6} and 1 $\times$ 10^{-5} Torr during growth and was measured using a nude ion gauge with a tungsten filament. Samples were grown at different substrate temperatures (350-600°C) and Ga:Se flux ratios. The growth was initiated by opening the Se shutter for 2 min. followed by opening of the Ga source at the growth temperature.

The crystalline quality of the GaSe films were evaluated through X-ray diffraction (XRD) (Bruker, D8 Discover) and Raman spectra (Renishaw) with a 1 mW laser at 514 nm. The surface morphology of the samples was examined by atomic force microscopy (AFM) (Veeco Instrument, DI 3000). The microstructure of GaSe was examined by cross sectional scanning transmission electron microscopy (STEM). Due to the oxidation of GaSe in ambient conditions, [184] AFM scans were performed immediately after the growth. XRD was measured after covering the GaSe surface with SPR955 photoresist. For the STEM measurements, the photoresist was removed using solvents and the surface was capped

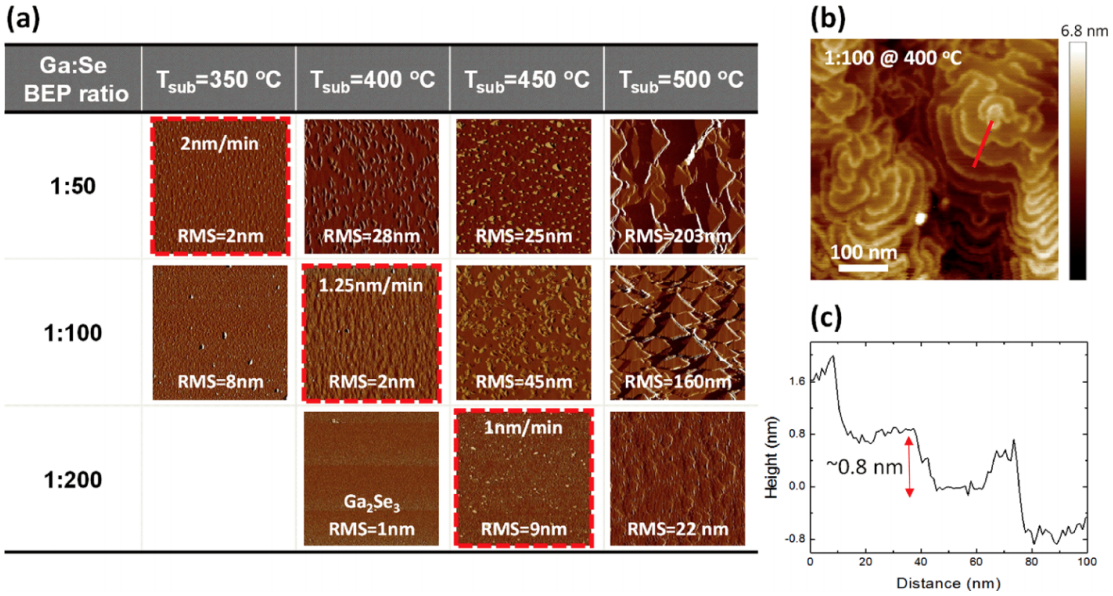


Figure 3.2: (a) AFM images of GaSe as a function of growth temperature and Ga:Se BEP flux ratio. RMS surface roughness is marked in the image. Red boxes indicate growth conditions to obtain relatively smooth surface morphology. (b) Surface morphology of GaSe film grown at the optimized condition (400°C, Ga:Se 1:100) showing atomic steps. (c) Step height of GaSe film taken from the red line in (b).

with Au metal immediately to prevent oxidation. Graphical illustrations of GaSe crystal structure was generated using *VESTA* software [185].

Growth of GaSe was explored on *c*-plane sapphire substrates by varying the substrate temperature and the Ga:Se flux ratio. *C*-plane sapphire was chosen due to the hexagonal symmetry of the basal plane, which is similar to that of GaSe, and the high chemical and thermal stability of sapphire. The substrate temperature was varied from 350°C to 500°C, while changing the Ga:Se ratio from 1:50 to 1:200, and holding the Se flux at 1×10^{-6} Torr. Growth was performed for one hour. The Se shutter was opened for two minutes and the streaky RHEED pattern of sapphire substrates (Fig. 3.1(a)) remained before the opening of the Ga shutter indicating that the sticking of Se adatoms is very poor

in the absence of Ga flux. Upon opening the Ga shutter, the RHEED pattern corresponding to m- (1 0 $\bar{1}$ 0) and a- (1 1 $\bar{2}$ 0) planes of GaSe was observed, and the RHEED pattern did not change along the different azimuths (i.e., in-plane rotation of the substrate). The coexistence of the RHEED patterns corresponding to the m- and a-planes of GaSe was also reported earlier [164]. This indicates that GaSe nucleated with random in-plane orientation. However, no polycrystalline rings were observed in the RHEED. The inverse of the ratio of spacing between m-plane and a-plane streaks in the RHEED image (Figure 3.1(b)) was measured to be 1.72, which is very close to the theoretical value of 3. XRD spectra of the samples grown in the range of conditions mentioned above, with the exception of the extremely Se-rich condition (T_{sub} = 400°C, Ga:Se 1:200) showed diffraction peaks corresponding to the (002) family of planes in layered-GaSe. However, with extremely Se-rich condition, the Ga_2Se_3 phase was observed in XRD and a spotty RHEED pattern was observed. The growth window for GaSe in order to maintain a streaky RHEED pattern was found to be very narrow at a given substrate temperature. The RHEED pattern remained streaky and the intensity remained constant only at a certain Ga flux at a given substrate temperature. Higher Ga flux resulted in complete RHEED dimming and lower Ga flux resulted in a spotty RHEED pattern.

Surface morphology of GaSe films as a function of growth conditions is shown in Figure 3.2(a). At 350°C, a Ga:Se ratio of 1:50 resulted in a relatively smooth surface morphology, while a reduced Ga flux (Ga:Se = 1:100) was required at a growth temperature of 400°C. With an increase in substrate temperature from 350°C to 450°C, relatively smooth surface morphology could be maintained only with a reduction of Ga flux. This

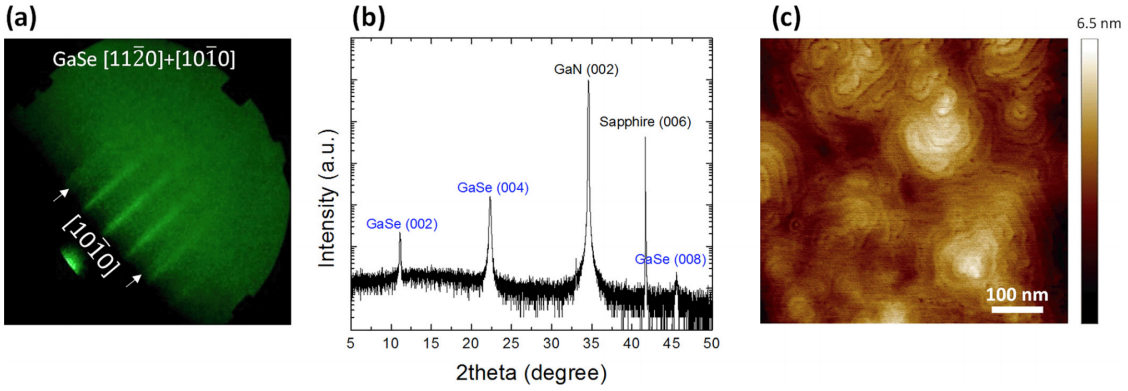


Figure 3.3: (a) RHEED pattern of GaSe showing coexistence of a- and m-planes. (b) XRD pattern, and (c) surface morphology of GaSe film grown on GaN substrate.

can be explained as follows. With an increase in substrate temperature, the sticking coefficient of Se is expected to reduce exponentially and hence the Ga flux that is required to maintain stoichiometry at the surface is lower at higher substrate temperatures. This is also expected to result in a reduction in the growth rate of GaSe with an increase in the substrate temperature, assuming unity sticking coefficient for Ga adatoms at the growth temperature used. This observation is in agreement with the RHEED patterns observed during the growth. At the optimized conditions, where the adsorbed Ga and Se adatoms are close to stoichiometry, the RHEED pattern remained streaky throughout the growth. However, when the Ga flux is higher than the stoichiometry (Ga:Se = 1:50, T_{sub} = 400°C, 450°C) the RHEED showed an amorphous pattern indicating the presence of excess Ga on the surface during the growth. With Se-rich conditions, a spotty (i.e., rough) RHEED pattern was observed. At higher substrate temperatures (>500°C), the Se sticking coefficient is very low and no growth was observed. At the optimized conditions with streaky RHEED pattern and bright RHEED intensity, atomic steps were clearly observed (Fig. 3.2(b)). The step height measured from AFM (0.8 nm) matches closely with the thickness of monolayer

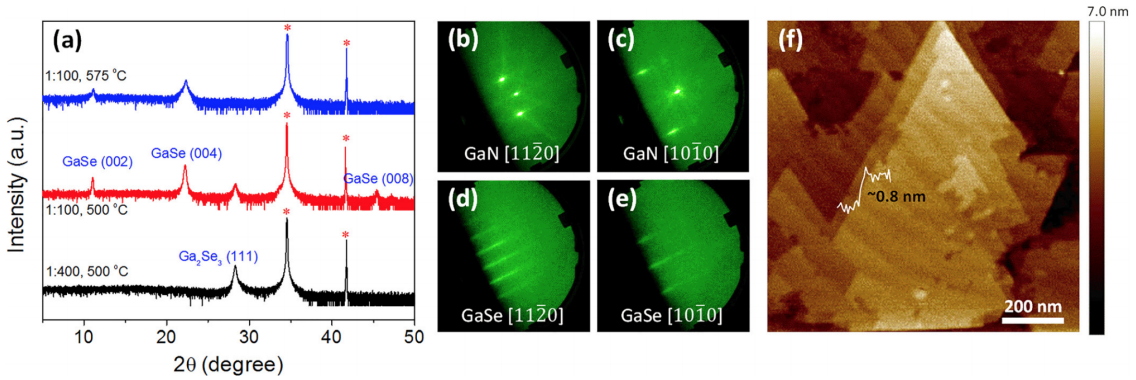


Figure 3.4: (a) The XRD spectra for GaSe film grown at different conditions with Se flux at 1×10^{-5} Torr. The asterisks indicate the substrate peaks of GaN (002) and sapphire (006) at 34.5° and 42°, respectively. ((b)(e)) RHEED patterns of GaN and GaSe along the [11$\bar{2}$0] and [10$\bar{1}$0] azimuth showing basal plane alignment. (f) AFM image of the GaSe film showing aligned triangular domains.

GaSe. The growth rate was found to be 1.25 nm/min with a total film thickness of 75 nm. In addition, we suspect the particles on GaSe surfaces to be Ga droplets, confirmed by its removal using HCl treatment.

Using the optimized growth conditions obtained from growth studies on sapphire (T_{sub} = 400 C, Ga:Se = 1:100), we next explored the growth of GaSe on GaN templates. The films were grown for one hour and the growth rate was found to be 0.75 nm/min with a total film thickness of 45 nm. While the lattice mismatch between GaN and GaSe (18%) is high, GaN provides a direct route for device design using 2D/GaN heterostructure based devices. X-ray diffraction of the films (Fig. 3.3(b)) showed diffraction peaks corresponding to (002), (004), (006), and (008) planes of GaSe. Complete surface coverage with spiral hillocks and atomic steps (RMS roughness = 0.85 nm) was obtained. However, the sample showed in-plane disorder (Fig. 3.3(a)) showing both m-plane and a-plane spacing, and the RHEED pattern was insensitive to substrate rotation.

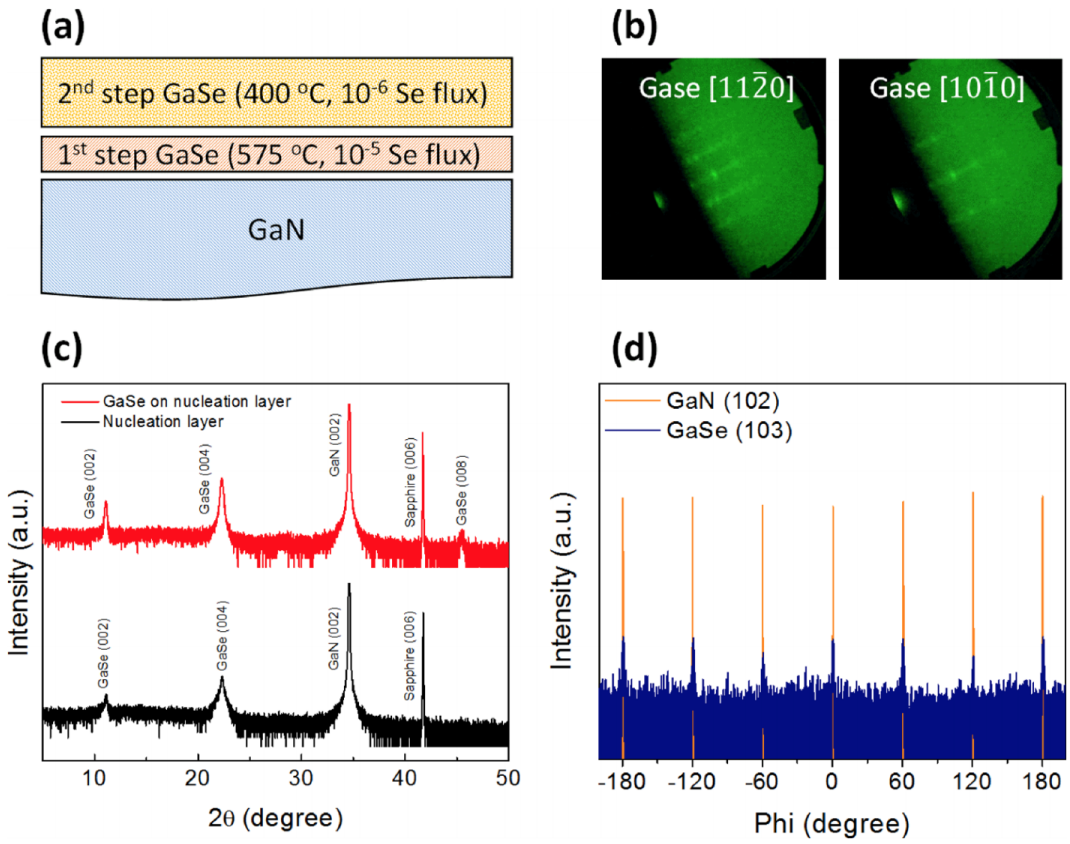


Figure 3.5: (a) Schematic of the two-step growth of GaSe on GaN substrates. (b) RHEED patterns of GaSe after the two-step growth. (c) XRD scan of GaSe after first nucleation step (black) and second (red) low temperature growth step. (d) XRD phi scan at GaSe(103) and GaN(102) planes confirming basal plane alignment.

Control of in-plane orientation of the crystal domains during nucleation is very critical to obtaining single crystalline GaSe films. GaSe growth temperature was hence increased from 400°C to 575°C to control the in-plane orientation. Higher growth temperature necessitates higher Se flux due to reduction in sticking coefficient of Se with increase in the substrate temperature. This is qualitatively similar to the effect of flux ratios observed at lower growth temperature of 400°C. The Se beam flux was increased to 1×10^{-5} Torr.

Figure 3.4(a) shows the XRD spectra of GaSe films grown at different growth

conditions on GaN substrates. The sample grown at 500°C showed the Ga_2Se_3 phase due to excess Se. With an increase in the Ga:Se ratio from 1:400 to 1:100 diffraction peaks corresponding to both GaSe(002) and Ga_2Se_3(111) planes were measured. With further increase in the Ga:Se ratio to 1:100, only GaSe(002) was detected at higher growth temperature of 575°C.

Figures 3.4(b)-3.4(e) show the RHEED patterns of GaN substrate and GaSe film grown at 575°C with Ga:Se = 1:100 along the [1 1 $\bar{2}$ 0] and [1 0 $\bar{1}$ 0] directions of the GaN substrate. The RHEED patterns corresponding to *m*- and *a*-planes of GaSe (Figs. 3.4(d) and 3.4(e), respectively) were observed along the same azimuth as GaN. The basal planes of GaSe was found to be perfectly aligned with the GaN substrate ($[1\ 1\ \bar{2}\ 0]_{GaSe}//[1\ 1\ \bar{2}\ 0]_{GaN}$ and $[1\ 0\ \bar{1}\ 0]_{GaSe}//[1\ 0\ \bar{1}\ 0]_{GaN}$) and six-fold symmetry of GaSe was clearly observed. Unlike the film grown at 400°C with in-plane disorder, GaSe streaks corresponding to *m*- and *a*-planes of GaSe appeared only at every 60° azimuthal rotation spacing. The inverse of the RHEED spacing ratio between GaN and GaSe was found to be 1.170, which is very close to the ratio (1.173) of bulk lattice constants of GaSe (3.74 nm) and GaN (3.189 nm). This clearly suggests that the epilayer is fully relaxed and the growth proceeds by van der Waals epitaxy.

While the higher temperature growths led to single phase films, surface coverage was found to be incomplete. A step height corresponding to 1 ML of GaSe (0.8 nm) was measured at the edge of a triangular domain that grew on top of another triangular domain. Large area (10 μm x 10 μm) AFM scan and STEM measurements confirmed the observation of incomplete surface coverage from AFM scans. More details regarding the microstructure

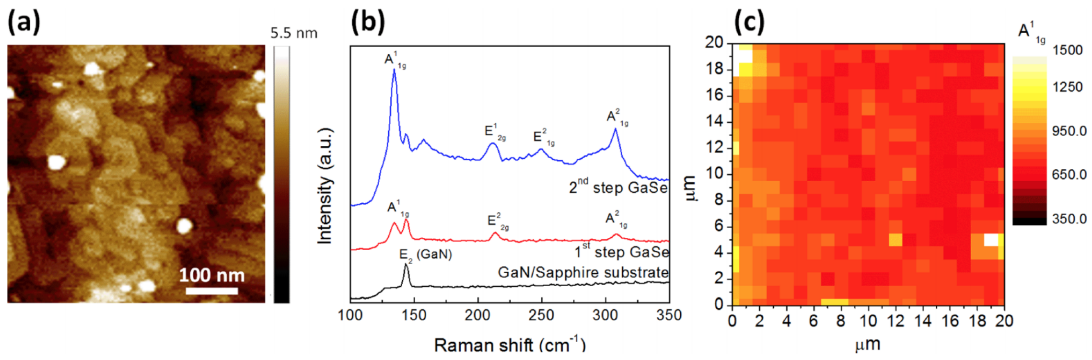


Figure 3.6: (a) AFM image of the GaSe after two-step growth. (b) Raman spectra of the GaSe film grown after first (red) and second (blue) steps. Substrate is also shown for comparison. (c) Raman intensity mapping of the A^1_{1g} peak over 20 μm by 20 μm.

of the film is discussed later in the manuscript.

While high temperature growth of GaSe at 575°C resulted in (002)-oriented single crystal domains, the layers did not coalesce to form a continuous layer. Growth at 400°C with a Ga:Se ratio of 1:100 resulted in coalesced (002)-oriented GaSe layers with in-plane disorder. To obtain single crystalline GaSe with complete surface coverage, we designed a two-step growth method illustrated in Fig. 3.5(a). After forming the nucleation layer at 575°C with 1 x 10^{-5} Torr of Se beam-equivalent pressure (BEP) flux, the growth temperature reduced to 400°C with a reduced Se flux of 1 $\times$ 10^{-6} Torr followed by 30 min. of GaSe growth with 1:100 of Ga:Se ratio. Figure 3.5(b) shows the RHEED patterns along the [1 1 $\bar{2}$ 0] and [1 0 $\bar{1}$ 0] azimuthal orientations. Six-fold symmetry was maintained after the second low temperature step, indicating that the basal planes are aligned with the GaN substrate and there is no in-plane disorder. Figure 3.5(c) displays XRD spectra of grown GaSe films after the first nucleation step (black) and the second low temperature growth step (red). The GaSe layers grew along the (002) orientation, and a higher order peak

(006) was observed after second step growth mainly due to the increased thickness of the film. No additional phase such as Ga_2Se_3 was observed after the second step growth. An off-axis scan of the GaSe(103) plane was performed, and six peaks with 60° spacing were observed. The scan was repeated along the (102) plane of GaN and six peaks were found at the identical azimuth angles as GaSe, confirming the observation of basal plane alignment from RHEED.

Figure 3.6(a) shows the surface morphology of GaSe after the two-step growth process with a rms roughness of 1.1 nm. Surface coverage was found to be complete. Figure 3.6(b) shows the Raman spectra for GaSe grown after the first nucleation step (red), and the second low temperature step (blue). The Raman mode corresponding to a shift of 143 cm^{-1} comes from the GaN/sapphire substrate. After the two-step growth, the Raman spectra matches the typical spectra expected from bulk GaSe with Raman modes at 134.3 cm^{-1} (A^1_{1g}), 211.7 cm^{-1} (E^1_{2g}), 250.2 $cm^{-}1$ (E^2_{1g}), and 307.6 cm^{-1} (A^2_{1g}) [186]. The A^1_{1g} and A^2_{1g} modes correspond to the out-of-plane vibration modes, while the E^2_{1g} and the E^2_{2g} modes are associated with the in-plane vibrational modes of GaSe. In contrast to the enhanced intensity of these Raman peaks with the film thickness, [187] no significant peak shift of A^2_{1g} mode due to the change in thickness was observed because of sufficiently thick GaSe film after the first step growth. The appearance of E^2_{1g} peak in GaSe has been reported in the literature [176, 188]. Nevertheless, at present the assignment of the new mode remains unclear. In addition, it is difficult to differentiate the polytypes from the Raman spectra as they show similar vibration modes [189]. Contour plot in Fig. 3.6(c) shows the intensity map of the dominant A^1_{1g} Raman mode over a 20 μm × 20 μm area indicating complete surface

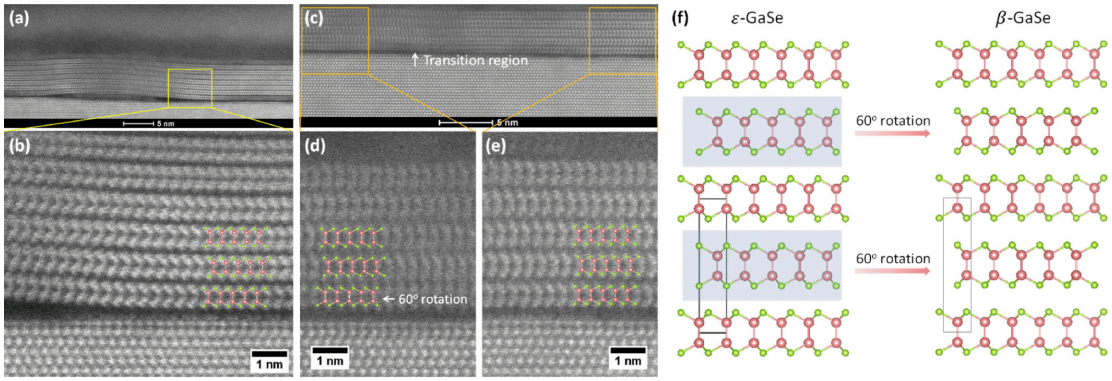


Figure 3.7: (a) Cross-sectional STEM image of GaSe film growth after first step at 575°C. (b) Magnified image from the boxed area in (a). (c) GaSe STEM image taken from the same sample but different area. (d) and (e) Magnified images from (c). (f) Ball-and-stick model of ϵ- and β-GaSe types. 60° rotation of every other layer in GaSe structure in ϵ-type turns out to be β-type.

coverage. Thus, this two-step growth method enables formation of coalesced multilayer GaSe films.

The microstructure of MBE-grown GaSe films were investigated in detail using STEM measurements. STEM images from two regions of the GaSe nucleation layer grown at 575°C is shown in Figs. 3.7(a) and 3.7(c). An abrupt GaSe/GaN interface and 5-8 GaSe monolayers separated by van der Waals gaps could be clearly resolved in the STEM images. Ball-and-stick model generated using VESTA is superimposed on the atomic resolution image to identify the stacking sequence. The stacking sequence indicates that the films grown are of the ϵ-GaSe polytype, in Fig. 3.7(b). However, a 60° rotation of the Se-Ga-Ga-Se tetralayer is observed in the region highlighted in Fig. 3.7(d), in which the Ga atoms sit on top of Se atom. Figure 3.7(f) shows the simulated crystal structure of ϵ-GaSe with a 60° rotation of every other layer resulting in β-GaSe polytype crystal structure. Such a rotation of the basal plane would not be captured in the RHEED or XRD measurements

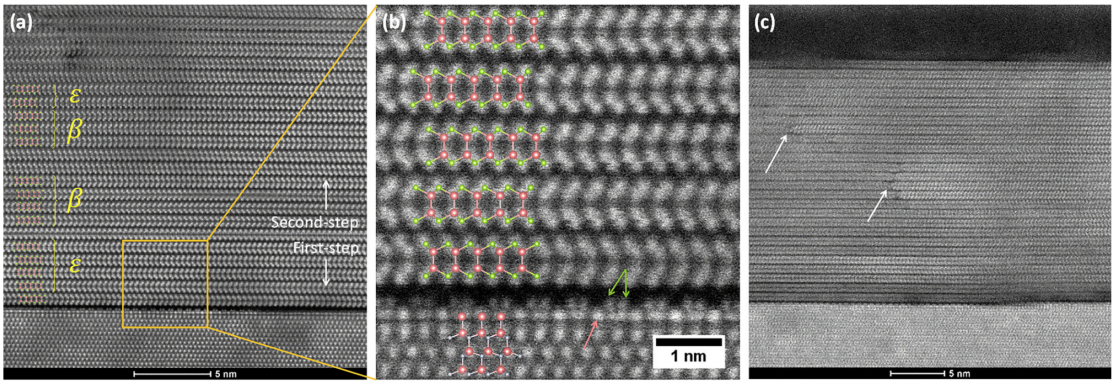


Figure 3.8: (a) and (b) Cross sectional STEM images of GaSe after two-step growth taken from different region. (c) Magnified image from boxed area in (b). Ball-and-stick models of GaSe and GaN are also presented. (c) Defects formed in the middle of GaSe film are marked with an arrow.

due to the six-fold symmetry of both the β and ϵ polytypes of GaSe. In spite of the rotation of the first tetralayer, subsequent GaSe stacking is pure ϵ-type. This may be attributed to the fact that the ϵ-polytype is energetically more stable than the β-type [190]. Similar lattice rotations and the resultant formation of grain boundaries have been reported in the case of MoS_2 [191, 192, 193]. Dumcenco *et al.* [193] has reported simulated data on the binding energies for MoS_2 and sapphire substrate as a function of orientation angle of MoS_2 grains. It was pointed out that only 0° or 60° orientations of the lattice were energetically favorable and stable.

The microstructure of the coalesced GaSe films grown using the two-step method was also investigated using crosssection STEM. Total number of layers after two-step growth was found to be 25-27 from STEM measurements, and 20-22 layers were grown in the second step. This implies a growth rate of 0.7 nm/min, which is similar to the low growth temperature (T_{sub} = 400°C) sample. The first five layers are identical to the nucleation

sample. A region with 60° rotation of first layer was also observed in the two-step sample and is shown in Fig. 3.8(a). However, inclusions of β-type is observed along with the dominant ϵ-type GaSe. Figure 3.8(b) shows a magnified image of a region cropped from the boxed region in Fig. 3.8(a). Surface reconstruction of the GaN surface can be clearly observed in the image. Ga atoms (red arrow) at the surface are bonded directly to a Ga atom below it, suggesting a 1×1 reconstruction of Ga atoms. On top of the surface Ga atoms, two atoms (green arrows) were observed above every second Ga atom. We hypothesize that these could be Se atoms passivating the GaN surface. This suggests that van der Waals epitaxy can be used to maintain surface reconstructions on the GaN surface, and which could have important implications for Fermi level pinning and dangling bond termination at heterostructure interfaces. The electronic properties of these artificial two-dimensional interfacial layers could be of great interest, but are outside the scope of the present work. We also observed that defects formed in one area of GaSe film did not propagate along c-axis towards surface due to the absence of bonding between individual 2D layers (Fig. 3.8(c)). However, certain amount of defect propagation is indeed observed and further careful study is required to understand extended defects in 2D crystals. The GaSe growth study has provided an overall understanding of 2D material growth. The growth rate is predominantly determined by the amount of Ga flux. However, unlike Ga, migration-enhanced epitaxy may be more effective in the case of TMD growth using refractory metal, such as Mo, W, or Nb.

3.3 Large-Area $SnSe_2$/GaN Heterojunction Diodes Grown by Molecular Beam Epitaxy

Heterogeneous integration of two-dimensional (2D) and three-dimensional (3D) materials could enable device architectures that are not possible for conventional semiconductor heterojunctions. The absence of out-of-plane chemical bonds in 2D layered materials enables flexibility for epitaxy of 3D materials, [124, 125] and can therefore enable combinations of materials for devices such as heterojunction bipolar transistors (HBTs), vertical tunneling devices, [182] and hot electron transistors [194].

The synthesis of 2D/3D heterojunctions has been investigated extensively using mechanically exfoliated 2D crystals transferred onto bulk crystals [158, 195, 196, 197] and wafer-scale chemical vapor transport [160, 198] or chemical vapor deposition [199, 200, 201] growth of 2D materials on epitaxial templates and molecular beam epitaxy (MBE). The method used in this work, MBE, offers some distinct advantages due to the ability to realize sharp interfaces, excellent control of background impurities, and powerful *in situ* characterization techniques [169, 202]. Previous work on MBE growth of metal dichalcogenides ($MoSe_2$, $HfSe_2$, WSe_2, and $SnSe_2$) on 3D substrates has shown epitaxial registry between the 2D material and 3D bulk substrates [172, 173, 203].

To date, band lineups for various heterojunctions between 2D and 3D materials have been proposed. For instance, type-I band alignment was demonstrated in *n*-MoS_2/*p*-Si, [204] *p*-MoS_2/*n*-SiC, [163] and *p*-MoS_2/*n*-GaN [181, 205]. Unlike transition metal dichalcogenides, Sn has two oxidation states (Sn^{2+} and Sn^{4+}) which give two stoichiometric phases, SnSe and $SnSe_2$. SnSe is an orthorhombic layered structure [206] with

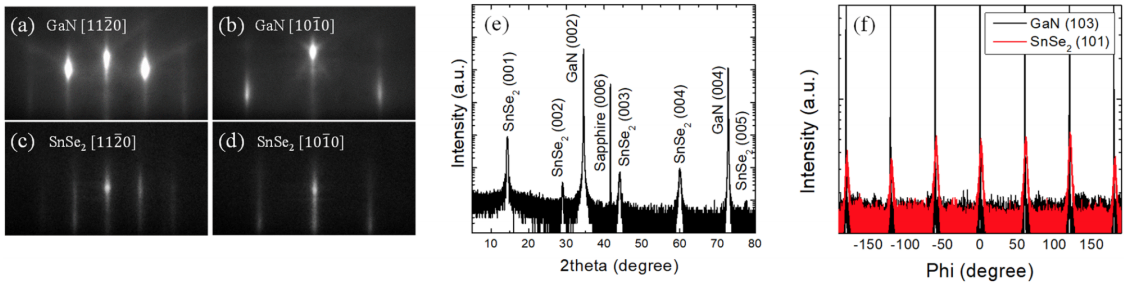


Figure 3.9: (a)(d) RHEED patterns of $SnSe_2$ and GaN along the [11$\bar{2}$0] and [10$\bar{1}$0] azimuthal directions. (e) XRD spectra of $SnSe_2$ on the GaN/sapphire substrate exhibiting the (001) family of diffraction peaks. (f) XRD ϕ scan of GaN(103) and $SnSe_2$(101) planes confirms the basal plane alignment.

p-type conductivity [207], while $SnSe_2$ is intrinsically an n-type semiconductor [208] and is known to have two crystal structures. One is the 2H phase with D^{6h} ($P6_3/mmc$) symmetry and the other is the 1T phase with D^{3d} (P3m1) symmetry. The bulk 1T phase of $SnSe_2$ has been reported to have a direct energy bandgap of 1 eV [171, 208] with an electron affinity of 5 eV [203]. This high electron affinity has been exploited to form type-III heterojunctions with black phosphorus [209] and WSe_2 [203].

In this section, we report on the growth and electronic properties of $SnSe_2$/GaN heterojunctions. The combination of such a high electron affinity low bandgap material such as $SnSe_2$ with a wide bandgap material such as GaN presents a unique heterojunction combination that is not possible with the III-Nitride system alone. While the bandgap of InGaN can be tuned to be as low as 1 eV, lattice mismatch between InN and GaN (11%) makes it very challenging to grow high composition InGaN on GaN.

The epitaxial growth of $SnSe_2$ on GaN was performed in a Veeco GEN930 MBE system with a standard thermal effusion cell for Ga and Sn. A valved cracker source (with

the cracker zone at 950°C) was used to evaporate Se. The sample surfaces were monitored *in situ* by reflection high-energy electron diffraction (RHEED) operated at 15 keV. The structural quality of the $SnSe_2$ films was evaluated through X-ray diffractometry (XRD) (Bruker, D8 Discover) and Raman spectroscopy (Renishaw) equipped with a 514 nm laser. The thickness of the $SnSe_2$ film was measured by X-ray reflectometry (XRR) (Bruker, D8 Discover). Atomic force microscopy (AFM) (Bruker Icon 3) was used to examine the surface morphology of the film. *VESTA* software [185] was used to generate graphical illustrations of the $SnSe_2$ crystal structure.

Semi-insulating and *n*-type (0001) oriented GaN/sapphire substrates were used for the study. Pre-growth surface preparation included solvent cleaning followed by a 1 hr. 400°C anneal under ultra-high vacuum conditions (1×10^{-9} Torr). Samples were then loaded into the growth chamber (base pressure 7×10^{-10} Torr) and exposed to the Ga polish procedure to remove gallium sub-oxides on the GaN surface prior to the growth. The procedure used is as follows. The GaN surface was exposed to a Ga flux of 1×10^{-8} Torr at 400°C until the RHEED intensity dropped. The substrates were then heated to 700°C for 30 min to recover the GaN RHEED pattern, followed by a ramp down to the growth temperature of 210°C. The substrate temperature was measured using a thermocouple attached to the continuous azimuthal rotation (CAR) substrate heater.

For growth of $SnSe_2$, the Se:Sn beam equivalent pressure (BEP) flux ratio (measured using a nude ion gauge with a tungsten filament) was maintained at $\sim$250. The surface was covered with Se by opening the Se shutter for two minutes. Growth was then initiated by opening the Sn shutter. This procedure is qualitatively similar to that de-

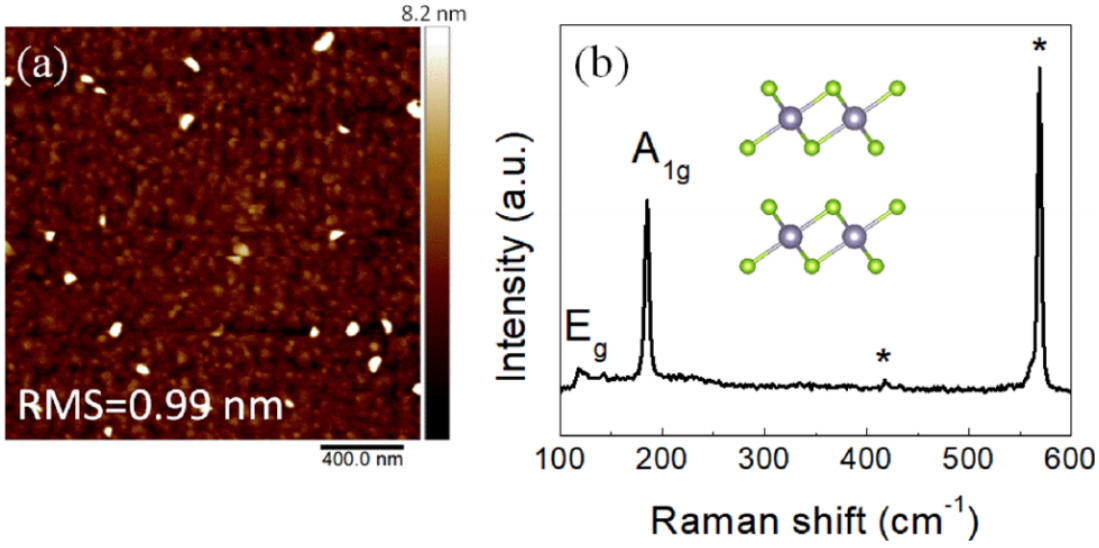


Figure 3.10: (a) 2 μm $\times$ 2 μm atomic force microscopy image of $SnSe_2$ after growth with the RMS roughness of 0.99 nm. (b) Raman spectra of $SnSe_2$ on the GaN/sapphire substrate with characteristic E_g and A_g^1 peaks.

scribed previously for the growth of GaSe on GaN [202]. Growth was carried out for 1 hour and terminated by closing all shutters and immediately cooling down the sample to room temperature.

Figures 3.9(a)-3.9(d) show the RHEED patterns of the GaN substrate before growth and the $SnSe_2$ film after growth was completed, along the $[11\bar{2}0]$ and $[10\bar{1}0]$ directions. The streaky RHEED patterns observed in both azimuthal orientations indicate two-dimensional growth with azimuthally aligned to the GaN substrate. The RHEED spacing for the GaN and $SnSe_2$ patterns was found to have a ratio of 0.85, which matches the experimentally expected ratio (0.848) from bulk in-plane lattice constants of $SnSe_2$ (a = 3.76 Å) and GaN (a = 3.189 Å). We conclude that the hexagonal basal plane lattice for $SnSe_2$ and GaN materials is aligned along the same crystallographic direction despite their

large lattice mismatch of 18%.

Figure 3.9(e) shows the on-axis (001)-oriented high resolution XRD spectrum of the $SnSe_2$/GaN structure, and the $SnSe_2$ peaks are found to be at the theoretically expected positions. No other phases were observed in the scan. The thickness of the crystalline $SnSe_2$ film was determined by X-ray reflection measurements to be 21 nm. Off-axis azimuthal scan [Fig. 3.9(f)] was done using a thick (>200 nm) $SnSe_2$ film. A full range of 360 scans (ϕ) for the $SnSe_2$(101) plane and GaN(102) plane were done, and six peaks were found at the identical azimuth angles for both $SnSe_2$ and GaN, confirming that the two hexagonal unit cells are epitaxially aligned. This is in agreement with our conclusion from RHEED measurements.

Figure 3.10(a) shows the surface morphology of $SnSe_2$. The RMS roughness was calculated to be 0.99 nm for a 4×4 μm^2 region. As shown in Fig. 3.10(b), two characteristic Raman active modes for $SnSe_2$ at 112 (in-plane mode, E_g) and 186.27 (out-of-plane mode, A_g^1) cm^{-1} are present in the spectrum, which corresponds to 1T phase $SnSe_2$ as reported for the MBE grown [203] and exfoliated bulk film [196, 210]. The corresponding 1T $SnSe_2$ crystal structure is shown in the inset of (b). The asterisk indicates the Raman modes at 419 and 570 cm^{-1} for sapphire (A_g^1) and GaN (E_2), respectively [182].

For electrical characterization of the $SnSe_2$/GaN heterojunction, Ti/Au/Ni contacts were evaporated using e-beam evaporation to form ohmic contacts to the $SnSe_2$. The contact to the n-GaN layer was formed by an indium dot. Inductively coupled plasma reactive ion etching (ICPRIE) with BCl_3/Ar chemistry was used for the device mesa isolation. Hall measurements on $SnSe_2$ films on semi-insulating GaN substrates were found to exhibit

n-type conductivity with a carrier concentration of 1.3×10^{19} cm^3 and an electron mobility of 4.7 cm^2 V^{-1} s^{-1}.

3.4 Conclusion

In summary, we have developed a two-step method to grow continuous, crystalline films of multilayer ϵ-GaSe on GaN(0001). To achieve this, we first optimized the growth of GaSe films on c-plane sapphire and GaN(0001) substrates in the low temperature regime (optimized T_{sub} = 400°C). On both substrates, this produced continuous films of (002)-oriented GaSe with random in-plane orientation of domains. In contrast, high temperature (575°C) growth on GaN(0001) resulted in discontinuous GaSe films, but with well-defined in-plane orientation aligned to the substrate lattice. For continuous, crystalline films, we combined these two growth modes into a two-step process where the first step is a high temperature growth to establish well-defined in-plane orientation, and the second step is a low temperature growth to coalesce the nucleated domains into a continuous film. This work illustrates the advantage of molecular beam epitaxy in realizing the growth of large area 2D crystals with high material quality. We also have demonstrated large area heterojunctions of layered-$SnSe_2$ on GaN using MBE. We characterized the heterojunction between n-$SnSe_2$ and n-GaN with RHEED, XRD, AFM, Raman and electrical transport. Despite the large lattice mismatch, we are able to integrate non-magnetic 2D semiconductors with 3D GaN substrates. This demonstration of the 2D/3D heterojunction demonstrates the potential for 2D/3D heterojunctions for high performance device applications.

Chapter 4

Room Temperature Intrinsic Ferromagnetism in Epitaxial Manganese Selenide Films in the Monolayer Limit

4.1 Abstract

Monolayer van der Waals (vdW) magnets provide an exciting opportunity for exploring two-dimensional (2D) magnetism for scientific and technological advances, but the intrinsic ferromagnetism has only been observed at low temperatures. Here, we report the observation of room temperature ferromagnetism in manganese selenide ($MnSe_x$) films grown by molecular beam epitaxy (MBE). Magnetic and structural characterization pro-

vides strong evidence that in the monolayer limit, the ferromagnetism originates from a vdW manganese diselenide ($MnSe_2$) monolayer, while for thicker films it could originate from a combination of vdW $MnSe_2$ and/or interfacial magnetism of α-MnSe(111). Magnetization measurements of monolayer $MnSe_x$ films on GaSe and $SnSe_2$ epilayers show ferromagnetic ordering with large saturation magnetization of $\sim$4 Bohr magnetons per Mn, which is consistent with density functional theory calculations predicting ferromagnetism in monolayer 1T-$MnSe_2$. Growing $MnSe_x$ films on GaSe up to high thickness ($\sim$40 nm) produces α-MnSe(111), and an enhanced magnetic moment ($\sim$2x) compared to the monolayer $MnSe_x$ samples. Detailed structural characterization by scanning transmission electron microscopy (STEM), scanning tunneling microscopy (STM), and reflection high energy electron diffraction (RHEED) reveal an abrupt and clean interface between GaSe(0001) and α-MnSe(111). In particular, the structure measured by STEM is consistent with the presence of a $MnSe_2$ monolayer at the interface. These results hold promise for potential applications in energy efficient information storage and processing.

4.2 Introduction

The study of magnetism in two dimensions (2D) has fascinated physicists for decades, inspiring theoretical studies of phase transitions [33, 34] and topological order [211] as well as their experimental realization in physical systems [20, 212, 213, 214]. Recently, intrinsic ferromagnetism has been demonstrated in van der Waals (vdW) crystals in the monolayer limit, [90, 93] which creates new opportunities for science and applications related to the potential for highly tunable magnetic properties via electrostatic gating, strain, and

proximity effects [17, 89, 215, 216, 217, 218, 219, 220]. This is particularly important for spintronics and valleytronics with 2D vdW heterostructures, where the monolayer magnets could provide a route toward low energy magnetization switching and proximity interactions for non-volatile logic [221, 222, 223, 224, 225, 226]. However, ferromagnetism in monolayer magnets has so far been limited to low temperatures, below ∼60 K [90, 93]. In this Letter, we report the observation of room temperature ferromagnetism in manganese selenide ($MnSe_x$) films grown by molecular beam epitaxy (MBE). Magnetic and structural characterization provides strong evidence that in the monolayer limit, the ferromagnetism originates from a vdW manganese diselenide ($MnSe_2$) monolayer, while for thicker films it could originate from a combination of vdW $MnSe_2$ and/or interfacial magnetism of alpha-MnSe(111). This behavior differs of bulk $MnSe_x$ compounds such as $MnSe_2$ (pyrite structure) and α-MnSe (rocksalt structure) which are not ferromagnetic [227, 228]. On the other hand, density functional theory (DFT) calculations have predicted the stability of vdW $MnSe_2$ monolayers with 1T structure (Figure 4.1a) as well as a ferromagnetic ground state with substantial exchange splitting for high Curie temperatures [229, 230]. Our results are consistent with these predictions.

Our investigation consists of material synthesis by MBE, magnetic characterization by superconducting quantum interference device (SQUID) magnetometry, and structural characterization by *in situ* reflection high energy electron diffraction (RHEED), scanning transmission electron microscopy (STEM), scanning tunneling microscopy (STM), atomic force microscopy (AFM), and x-ray diffraction (XRD). To outline our study, we start by growing ∼one monolayer (ML) of manganese selenide ($MnSe_x$) on vdW GaSe(0001) on

GaAs(111) and vdW $SnSe_2$(0001) on GaAs(111) substrates. Magnetic measurements by SQUID show ferromagnetism at room temperature, and the similarity of the loop shapes and saturation magnetic moment on two different substrates help eliminate potential artifacts related to substrate interaction. In growing thicker films on GaSe substrates, the RHEED patterns remain streaky up to several tens of nanometers, and XRD scans reveal that the growth converts to rocksalt α-MnSe(111). SQUID measurements exhibit room temperature ferromagnetism with larger saturation magnetic moment ($\sim$2x) than the $\sim$1 ML $MnSe_x$, and XRD scans reveal a new peak consistent with vdW transition metal dichalcogenides. Because α-MnSe is not ferromagnetic, this provides evidence for ferromagnetic vdW $MnSe_2$ layers forming at the interface of GaSe and α-MnSe(111). Detailed structural characterization by STEM, STM, and RHEED reveal an abrupt and clean interface between GaSe(0001) and α-MnSe(111). In particular, the structure measured by STEM is consistent with the presence of a $MnSe_2$ monolayer at the interface. This provides strong evidence for the room temperature ferromagnetism originating from vdW $MnSe_2$ monolayers.

4.3 Results and Discussion

The $MnSe_x$ samples are prepared via van der Waals epitaxy, [124, 126] in a Veeco GEN930 MBE chamber equipped with a liquid nitrogen cryoshroud and base pressure of 2×10^{-10} Torr. We investigate the growth of $MnSe_x$ on two different base layers, GaSe(0001) on GaAs(111)B and $SnSe_2$(0001) on GaAs(111)B. The growth of the GaSe, $SnSe_2$, and $MnSe_x$ layers are performed under a Se overpressure and the growth rate is determined by the Ga, Sn, or Mn flux. Details of the growth are provided in the Appendix, sec. B. For

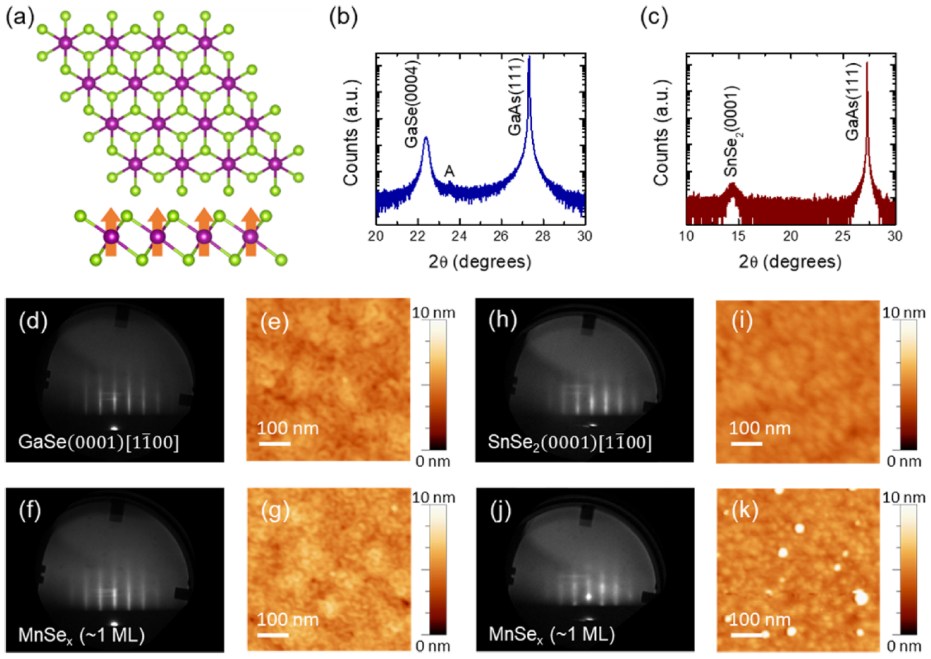


Figure 4.1: MBE growth and structural properties of monolayer $MnSe_x$. (a) Top and side views of 1T-$MnSe_2$ lattice with purple and green balls representing Mn and Se atoms, respectively. Arrows indicate location of magnetic moments. (b, c) θ-2θ XRD scans of $\sim$1 ML $MnSe_x$ on the 55 nm base layer of GaSe (blue) and on the 12 nm base layer of $SnSe_2$ (wine), respectively. (d) RHEED image along the [1$\bar{1}$00] crystallographic axis of the GaSe base layer on GaAs(111)B and (e) the corresponding AFM image. (f) RHEED image of $\sim$1 ML of $MnSe_x$ on the GaSe base layer with (g) the corresponding AFM image showing a smooth morphology. (h) RHEED image along the [1$\bar{1}$00] crystallographic axis of $SnSe_2$ on GaAs(111)B and (i) the corresponding AFM image. (j) RHEED image of $\sim$1 ML $MnSe_x$ on the $SnSe_2$ base layer with (k) the corresponding AFM image showing an island morphology.

the growth of $MnSe_x$ on the GaSe(0001) surface, we deposit a 55 nm GaSe base layer on GaAs(111)B at 400°C [178, 202]. Figures 4.1d and 4.1e show a streaky RHEED pattern and an AFM image of the GaSe base layer that displays atomically smooth terraces and monolayer steps with a spiral hillock morphology, respectively. After growth of ∼1 ML $MnSe_x$ at 400°C, the RHEED pattern remains streaky (Figure 4.1f) and the AFM image in Figure 4.1g shows similar atomically smooth morphology as the GaSe base layer. The RHEED pattern rotates with six-fold rotation symmetry which confirms in-plane epitaxial registry. For characterization by XRD and SQUID, the sample is capped with 5 nm GaSe and amorphous Se to protect the sample from oxidation before being removed from the chamber. The θ-2θ XRD scan for the ∼1 ML $MnSe_x$ on GaSe (Figure 4.1b) exhibits two prominent peaks coming from the GaAs(111) substrate and the GaSe base layer (2θ = 22.4°). An additional A peak is also observed at $2\theta = 23.5°$, for which the origin of the peak is not known.

We investigate the magnetic properties of the $MnSe_x$ layers by SQUID magnetometry. Room temperature, out-of-plane magnetization scans reveal a ferromagnetic hysteresis loop for a ∼1 ML $MnSe_x$ sample on the GaSe base layer (Figure 4.2a). The inset shows the unprocessed SQUID data which includes diamagnetic and paramagnetic contributions (see Chapter 5 for details of background subtraction). The ferromagnetic hysteresis loop exhibits a coercivity of ∼150 Oe and a saturation magnetic moment of $\sim 3.3 \times 10^{-5}$ emu/cm^2 (this represents the total moment, but normalized to the sample area), which corresponds to ∼4.4 μ_B per Mn.

To rule out the possibility that the ferromagnetism is generated by a substrate-

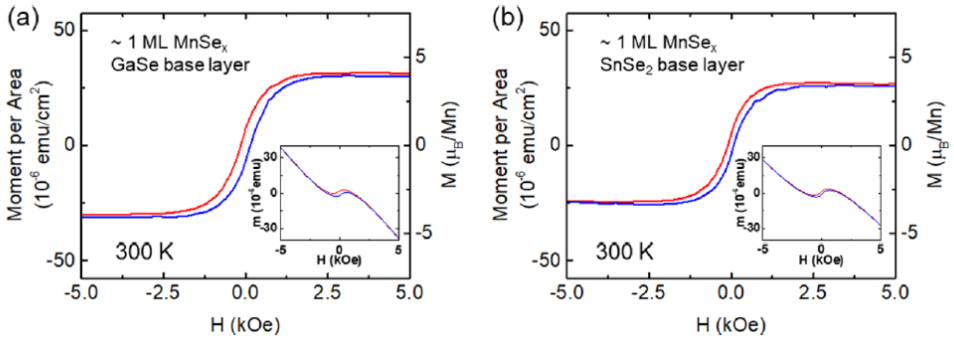


Figure 4.2: Out-of-plane room temperature SQUID magnetometry measurements on 1 ML $MnSe_x$. (a) Magnetic hysteresis loop of 1 ML $MnSe_x$ on the GaSe base layer showing ferromagnetic ordering. Inset: the unprocessed SQUID data prior to background subtraction. (b) Magnetization loop of 1 ML $MnSe_x$ on the $SnSe_2$ base layer. Inset: the unprocessed SQUID data prior to background subtraction.

specific artifact, we develop the growth of $MnSe_x$ on another substrate, $SnSe_2$(0001) grown on GaAs(111)B. For this study, we grow 12 nm of $SnSe_2$ on GaAs(111)B at 165°C [206]. The streaky RHEED pattern (Figure 4.1h) indicates an atomically smooth surface, which is verified by AFM scans (Figure 4.1i). After deposition of ∼1 ML $MnSe_x$ at 165°C, the RHEED pattern starts becoming spotty indicating 3D growth (Figure 4.1j) and the corresponding AFM image confirms the 3D growth with island formation as shown in Figure 4.1k. The RHEED pattern rotates with six-fold rotation symmetry which confirms in-plane epitaxial registry. For XRD and SQUID, an additional protection layer of $SnSe_2$ (12 nm) is deposited and the sample is capped with amorphous Se. The θ-2θ XRD scan (Figure 4.1c) shows two large peaks from the GaAs(111) substrate and the 12 nm $SnSe_2$ base layer (2θ = 14.5°), and the A peak is absent. Room temperature, out-of-plane magnetization scans reveal a ferromagnetic hysteresis loop for a ∼1 ML $MnSe_x$ sample on the $SnSe_2$ base layer (Figure 4.2b). The ferromagnetic hysteresis loop exhibits a coercivity of ∼100 Oe and a

saturation magnetic moment of $\sim 3.2 \times 10^{-5}$ emu/cm^2 which corresponds to $\sim 4.2\ \mu_B$/Mn. These values are very similar to that observed in GaSe base layer samples. The absence of the A peak while still observing ferromagnetism indicates that any associated structures are not relevant for the magnetic signal.

The observation of room temperature ferromagnetism with similar characteristics for both $SnSe_2$ and GaSe base layers implies that the ferromagnetism does not originate from the base layer vdW materials. For example, the formation of certain magnetic compounds such as GaMn [231] in the GaSe samples would provide no explanation for the ferromagnetism observed in the $SnSe_2$ samples. Furthermore, the large magnetic moment ($\sim 4\ \mu_B$/Mn) cannot be explained by the formation of a dilute magnetic semiconductor (e.g. $Ga_{1-x}Mn_xSe$ [232] or $Sn_{1-x}Mn_xSe_2$ [71]) due to interdiffusion of Mn into the base layer. Although room temperature ferromagnetism has been observed in $Sn_{1-x}Mn_xSe_2$ for Mn concentration up to $\sim 70\%$, only a small net saturation magnetic moment of $\sim 0.09\ \mu_B$/Mn has been reported [71]. Thus, if the observed ferromagnetism in our samples were due to interdiffusion into the base layer, we would expect characteristics that are different from we observe, and the GaSe and $SnSe_2$ samples should be different from each other. This provides strong evidence that the observed ferromagnetism originates from the deposited $MnSe_x$ monolayers.

To possibly identify the structural composition of $MnSe_x$, we attempt to grow thicker films on GaSe and $SnSe_2$ base layers. For the case of GaSe, the growth of $MnSe_x$ maintains a streaky RHEED pattern through several tens of nanometers. Figures 4.3a,b show the initial RHEED pattern for a 20 nm GaSe base layer and Figures 4.3c,d show

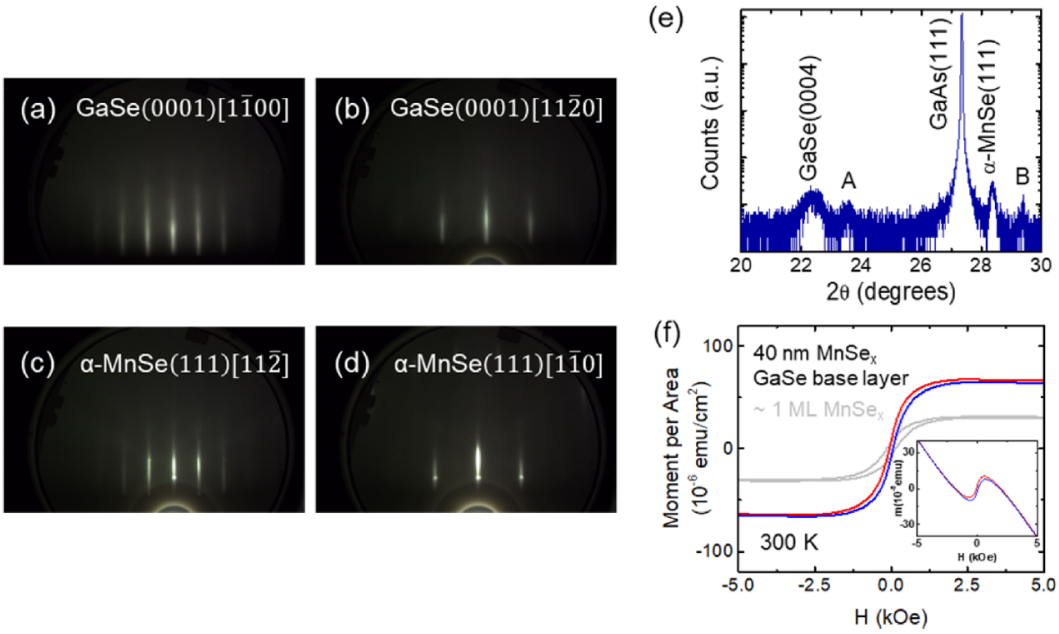


Figure 4.3: Structural and magnetic characterization of thick $MnSe_x$ films. (a, b) GaSe RHEED images along the [1$\bar{1}$00] and [11$\bar{2}$0] crystallographic axes, respectively, and (c, d) RHEED of 40 nm $MnSe_x$ film epitaxially aligned to the GaSe base layer. (e) θ-2θ XRD scan of a 40 nm $MnSe_x$ film on GaSe showing additional peaks at 28.3° and 29.4°. (f) Magnetic hysteresis loop of a 40 nm $MnSe_x$ film (red and blue) in comparison to ~1 ML $MnSe_x$ (gray) showing a larger magnitude of signal.

RHEED after ∼40 nm of $MnSe_x$ growth. The θ-2θ XRD scan (Figure 4.3e) provides an explanation for the persistent streaky pattern. Compared to the XRD scan of the ∼1 ML $MnSe_x$ on 55 nm GaSe shown in Figure 4.1b, the main new feature is the emergent of a large peak appearing at $2\theta = 28.3°$, which indicates the presence of (111)-oriented α-MnSe [233]. α-MnSe is a thermodynamically stable bulk structure [228], which explains the persistence of streaky, crystalline growth out to large thicknesses. We also observe an additional B peak at $2\theta = 29.4°$, which corresponds to a lattice spacing of 6.07 Å (for 2nd order diffraction). This does not correspond to any peak in bulk $MnSe_2$, α-MnSe, or other known Mn-Se compounds [233, 234], but is similar to the layer spacing for vdW layered transition metal dichalcogenides: 6.00 Å for $TiSe_2$, 6.10 Å for VSe_2, 6.15 Å for MoS_2, 6.16 Å for WS_2, 6.46 Å for $MoSe_2$, 6.48 Å for WSe_2 [235, 236, 237, 238, 239]. In addition to the emergence of new XRD peaks in the thicker $MnSe_x$ films, an enhancement in the magnetization is also observed. As shown in Figure 4.3f, the magnetic hysteresis loop has similar coercivity (∼75 Oe) but more than double the saturation magnetic moment per area ($\sim 7.3 \times 10^{-5}$ emu/cm^2) as compared to the ∼1 ML $MnSe_x$ sample on GaSe (Figure 4.2b). Because α-MnSe is not ferromagnetic, the enhanced saturation magnetic moment suggests that the ferromagnetic signal is likely coming from the interface between α-MnSe and GaSe.

To better understand the structure at the α-MnSe/GaSe interface, which is likely providing the ferromagnetic ordering, we investigate few-layer $MnSe_x$ films. Figure 4.4a shows the $MnSe_x$ growth evolution viewing the RHEED images as a function of time during the first ∼30 seconds (∼3 ML) of $MnSe_x$ deposition. Linecuts of the $[1\bar{1}00]_{GaSe}$ RHEED pattern are taken along the white dashed line in the inset of Figure 4.4a. The red curve

shows the linecut for the GaSe base layer, the blue curve shows the linecut after ∼3 ML of deposition, and the greyscale image shows the evolution of the RHEED linecut during the growth. Notably, the spacing of the RHEED streaks becomes smaller with $MnSe_x$ deposition, which indicates that the in-plane lattice constant increases with $MnSe_x$ deposition. The ratio of the RHEED spacing between GaSe and MnSe is 1.0244, which is very close to the expected ratio of 1.0285 for the bulk in-plane lattice constants of α-MnSe(111) (3.862 Å) and GaSe(0001) (3.755 Å). This confirms what we observed earlier in the XRD scans (Figure 4.3c) showing the α-MnSe(111) phase. The streakiness and six-fold rotational symmetry of the RHEED patterns also suggests that we have epitaxial alignment between each material ($[11\bar{2}]_{MnSe}//[1\bar{1}00]_{GaSe}$ and $[1\bar{1}0]_{MnSe}//[[11\bar{2}0]_{GaSe}$). Figure 4.4b shows the in-plane lattice constant of the $MnSe_x$ film normalized by the GaSe in-plane lattice constant (a_{film}/a_{GaSe}) as a function of time and thickness. The structural transition from the GaSe base layer is abrupt and transitions to the bulk α-MnSe lattice constant within one monolayer of $MnSe_x$ deposition. The formation of α-MnSe(111) at the $MnSe_x$/GaSe interface is further confirmed by STM. The surface structure, lattice constant (3.90 Å), and band gap (∼3.39 eV) measured with dI/dV spectroscopy on a ∼3 ML $MnSe_x$ sample (Figure 4.4) are in good agreement with that of bulk α-MnSe, which is distinct from the same measurement performed on GaSe base layer (Figure 4.4c).

The cross-sectional STEM high angle annular dark field (HAADF) images in Figure 4.4e demonstrate high quality growth of GaSe [202] on GaAs with the epitaxial relationship of $[111]_{GaAs}//[0002]_{GaSe}$. We observe the γ-GaSe polytype in two orientations that are related by a 30° in-plane rotation. Because the α-MnSe overlayer is registered

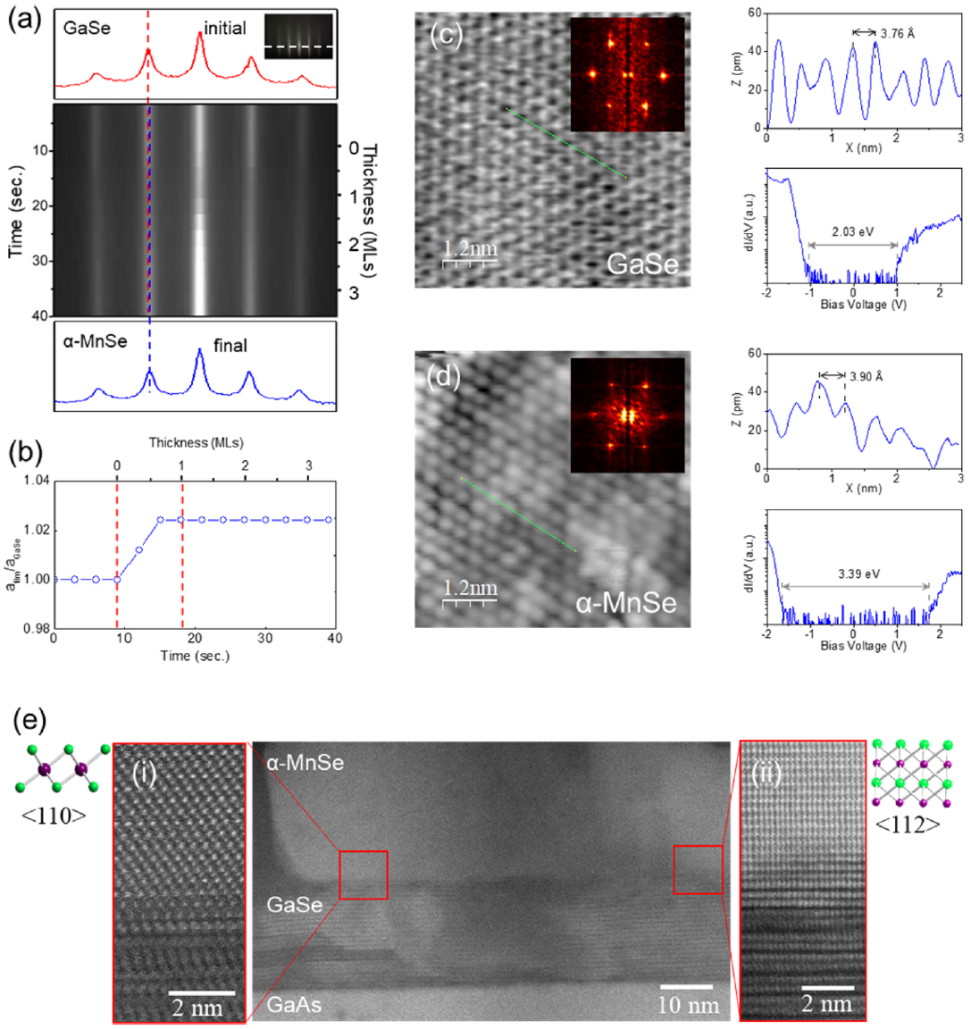


Figure 4.4: RHEED line profile and high resolution imaging of the α-MnSe/GaSe interface. (a) RHEED line profile of MBE growth evolution from the GaSe base layer to ~3 layers of $MnSe_x$ (inset showing region of GaSe RHEED image that the line profile is taken from). (b) Lattice constant ratio as a function of thickness showing abrupt change from GaSe to α-MnSe(111) lattice within ~1 ML of $MnSe_x$ deposition. (c) STM topography image, Fourier transform, line profile, and dI/dV spectrum on a GaSe base layer sample. The image is taken with an etched PtIr tip, with V = 2.0 V and I = 0.2 nA. (d) Same set of data taken on another sample with ~3 ML $MnSe_x$ sample grown on GaSe. (e) High resolution STEM HAADF imaging of α-MnSe(111) and GaSe with different orientations. (i) α-MnSe(111) viewed along <110> and (ii) shows α-MnSe viewed along <112>. Both images are collected from the areas indicated by the boxes in the middle image. There is no tilting of the specimen between imaging the two areas. These samples are grown at 300°C.

with the GaSe lattice, the $[1\bar{1}00]_{GaSe}$ and $[11\bar{2}0]_{GaSe}$ viewing directions can be imaged simultaneously without any tilting of the specimen. Figure 4.4e shows HAADF images that contains two different orientations of α-MnSe, including high magnification images (Figure 4.4e(i) and (ii)) that clearly show the rotated atomic lattices). Both have the relationship $[111]_{\alpha-MnSe}//[0002]_{GaSe}$, although Figure 4.4e(i) is oriented along <110> and Figure 4.4e(ii) is along <112>. The former also confirms the similarity between α-MnSe along <110> and 1T-$MnSe_2$ along $[11\bar{2}0]$ as discussed below. The structure in both orientations is consistent with the presence of a $MnSe_2$ monolayer at the interface and it should be noted that if 1T-$MnSe_2$ along $[11\bar{2}0]$ also undergoes a 30° in-plane rotation, the atoms align vertically similar to the GaSe $[1\bar{1}00]$ direction shown in the schematic in Figure 4.4e. However, we have no direct evidence from imaging or compositional mapping for the presence of this phase. In any case, the interface between the GaSe and MnSe layers is abrupt with no evidence for segregation or contaminants.

The clean, sharp and crystalline interface between GaSe and α-MnSe(111) observed in STEM indicates that the monolayer $MnSe_x$ should have similar structure as the α-MnSe(111). This brings a key insight on the origin of the observed ferromagnetism in monolayer $MnSe_x$ (Figure 4.2). It is important to notice that a single monolayer of α-MnSe(111) is virtually identical to a monolayer of vdW $MnSe_2$ with 1T structure. This is depicted in Figures 4.5a,b which show the top view, side view, and nearest-neighbor coordination diagrams (insets) for the α-MnSe(111) and vdW 1T-$MnSe_2$ lattices, respectively. The similarity of the structures is evident in the top view and nearest-neighbor coordination diagrams. Most importantly, the side view of the lattices shows clearly that a

single monolayer of α-MnSe(111), which is the Se-Mn-Se atomic trilayer highlighted by the dashed lines in Figure 4.5a, is equivalent to the 1T-$MnSe_2$ shown in the side view of Figure 4.5b. Furthermore, DFT calculations show that the 1T structure is thermodynamically stable for monolayer $MnSe_2$ and is ferromagnetic close to room temperature. Their predicted magnetic moment (3.0-3.7 μ_B/Mn) is consistent with our experimental observation in Figure 4.2. In addition, as discussed earlier in Figure 4.4, the smooth evolution of the RHEED pattern from GaSe to α-MnSe without intermediate patterns, the rapid transition to α-MnSe(111) as confirmed by STM, and the STEM images provide strong evidence that the first monolayer forms in the 1T-$MnSe_2$ structure. Based on these considerations, we conclude that the room temperature ferromagnetism in monolayer $MnSe_x$ originates from magnetic ordering of vdW 1T-$MnSe_2$.

It is also important to discuss the ferromagnetism in the thick $MnSe_x$ samples which exhibit slightly larger magnetic moment per area than in the monolayer. We consider two possible mechanisms that could contribute to the magnetic signal. One is the stabilization of one or more vdW $MnSe_2$ layer at the interface. This would be consistent with the experimental results from STEM and XRD (B peak). The other possibility is that the surface of α-MnSe(111) could exhibit interfacial ferromagnetism, such as that observed in Cr_2O_3 [240]. It would be very interesting to investigate these two possibilities in future studies. Nevertheless, due to the structural similarities between α-MnSe(111) and 1T-$MnSe_2$, there is no distinction between these two mechanisms in the monolayer limit.

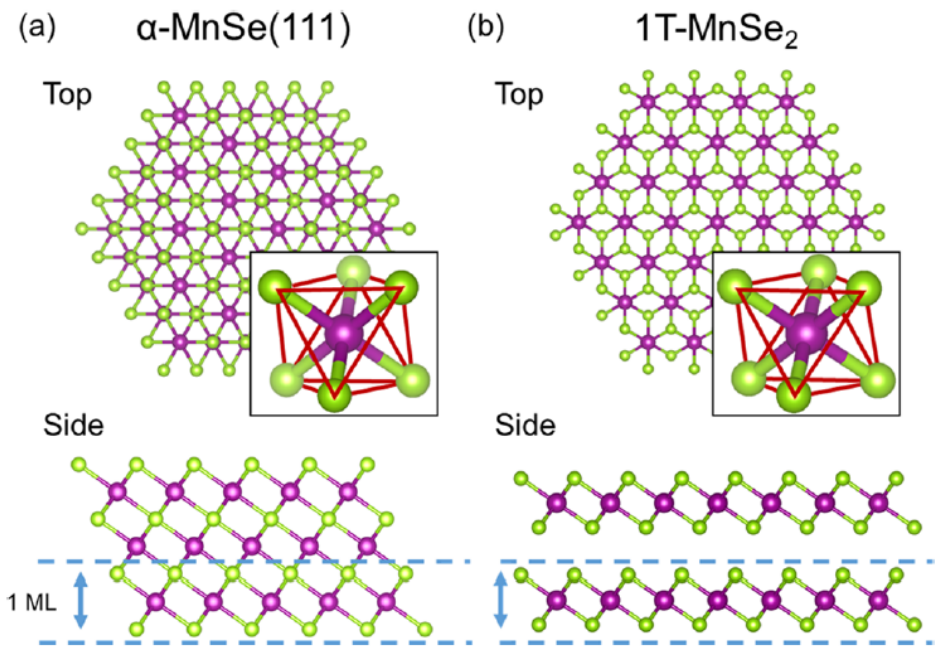


Figure 4.5: Crystal structure diagrams of α-MnSe(111) and monolayer 1T-$MnSe_2$. (a) Ball-and-stick model of α-MnSe(111) hexagonal lattice (top view) with inset showing octahedral coordination. The Mn atom is purple, and the Se atom is green. The side view shows that 1 ML of α-MnSe(111) is equivalent to 1 ML 1T-$MnSe_2$. (b) Ball-and-stick model of 1T-$MnSe_2$ hexagonal lattice (top view) with the inset showing octahedral coordination. The side view shows that 1T-$MnSe_2$ is equivalent to 1 ML α-MnSe(111).

4.4 Conclusions

In conclusion, we have observed room temperature ferromagnetism in epitaxial manganese selenide films grown by MBE. In the monolayer limit, we attribute the magnetic signal to intrinsic ferromagnetism of a vdW manganese diselenide ($MnSe_2$) monolayer, while for thicker films it could originate from a combination of vdW $MnSe_2$ and/or interfacial magnetism of α-MnSe(111). This enables the integration of room temperature ferromagnetism into 2D layered vdW heterostructures in a variety of ways. For monolayers, the vdW $MnSe_2$ could be grown on appropriate vdW surfaces (either exfoliated or epitaxial layers) and capped with other vdW materials to produce the isolated $MnSe_2$ vdW layers. This could be used for studies of vertical magnetic tunneling junctions, magnetic proximity effect, and gate tunable magnetism. For thick α-MnSe(111) structures, its insulating character could allow it be used as a gate dielectric for spin field-effect structures and gate tunable magnetic proximity effect. In addition, direct measurement of the magnetism and atomic scale magnetic ordering by spin-polarized STM could help realize the full potential of 2D magnets for spintronics and valleytronics.

Chapter 5

Importance of Paramagnetic Background Subtraction for Determining the Magnetic Moment in Epitaxially Grown Ultrathin van der Waals Magnets

5.1 Abstract

Due to the atomically thin nature of monolayer and few-layer van der Waals magnets, the undesired background signal from the substrate can have significant contribution when characterizing their magnetic properties. This brings challenges in accurately de-

termining the magnitude of the magnetic moment of the epitaxially grown van der Waals magnets on bulk substrates. In this paper, we discuss the impact of the background subtraction method for accurately determining the magnetic moments in such systems. Using the recently reported intrinsic two-dimensional (2D) van der Waals ferromagnet $MnSe_2$ as an example, we show that a normal diamagnetic background subtraction method in analyzing the bulk magnetometry measurement will result in an unexpectedly large magnetic moment (greater than $\sim$10 μ_B per formula unit). Through our systematic growth study, we identify an additional paramagnetic signal due to unintentional Mn doping of the substrate. To extract the correct magnetic moment, a paramagnetic background should also be considered. This yields a total magnetic moment of $\sim$4 μ_B per formula unit in monolayer $MnSe_2$, which is in close agreement to the theoretically predicted value.

5.2 Introduction

Realizing and understanding magnetism in two-dimensional (2D) van der Waals materials has been a fascinating topic for physicists for many decades. Although extensively studied theoretically [33, 34, 211, 219], the experimental demonstration of intrinsic ferromagnetic ordering in 2D materials was not achieved until 2017 [90, 93]. Using the mechanical exfoliation method on van der Waals CrI_3 and $Cr_2Ge_2Te_6$, researchers thinned the crystals down to monolayers (bilayers for $Cr_2Ge_2Te_6$) and obtained ferromagnetic signals from μm-sized flakes at cryogenic temperatures. Since these discoveries, extensive studies have been performed on both materials, and exciting properties, such as gate tunable magnetism [241, 242, 243, 244, 245], strong magnetic proximity when coupled to a non-magnetic

material [217], giant tunneling magnetoresistance and spin-filtering effects [97, 98, 99, 246] have been reported. Meanwhile, other 2D van der Waals magnets such as $FePS_3$ [86, 247] and Fe_3GeTe_2 [103, 104, 105], have also been discovered and studied extensively in their bulk form and after mechanical exfoliation down to the multilayer and monolayer limit. Another breakthrough in the development of 2D magnets is the epitaxial growth of monolayer van der Waals magnets in the transition metal dichalcogenide (TMDC) family. By using molecular beam epitaxy (MBE), Bonilla, *et al.* and O'Hara, *et al.* have separately reported ferromagnetism in large area van der Waals materials, VSe_2 [106] and $MnSe_2$ [107] down to the monolayer limit. Remarkably, the ferromagnetism in both VSe_2 and $MnSe_2$ persists up to and above room temperature, which is crucial for industrial applications in magnetic memory. These advances in 2D van der Waals magnets show great promise for future information storage and non-volatile logic technologies [248].

The ability to synthesize large area van der Waals magnets also opens the possibility to measure their magnetic properties via bulk magnetometry methods, such as superconducting quantum interference device (SQUID) and/or vibrating sample magnetometry (VSM). However, challenges have also arisen when characterizing the 2D magnets with the above techniques.

Due to the atomically thin nature of the monolayer and few-layer van der Waals magnets, the undesired magnetic background signal from the substrate can have significant contribution to the total magnetization measurement. This brings difficulty in accurately determining the magnetic moment in these materials. For example, an extremely large magnetic moment of $\sim$15 μ_B per formula unit was reported for a monolayer of VSe_2 grown on

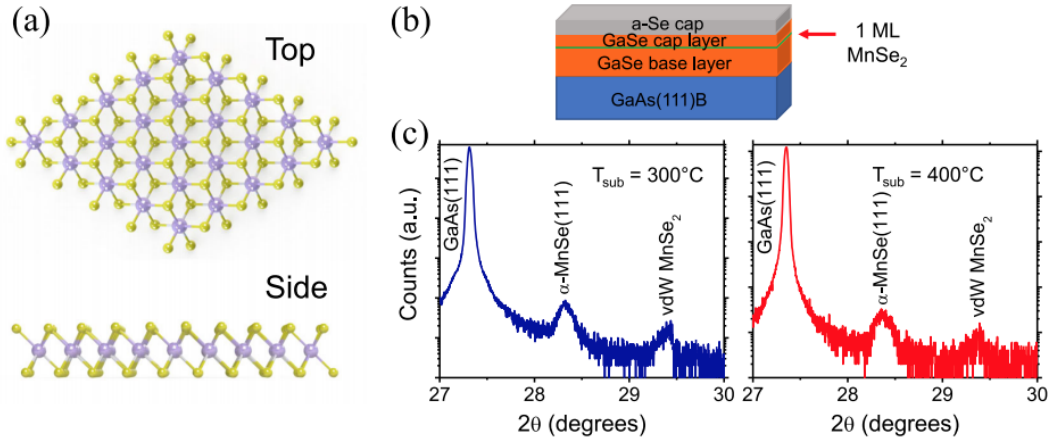


Figure 5.1: Lattice structure and properties of monolayer 1T-$MnSe_2$. (a) Ball-and-stick model showing top and side views of monolayer 1T-$MnSe_2$. Purple represents Mn and yellow represents Se. (b) Schematic showing the $MnSe_2$/GaSe(0001) heterostructure grown on a GaAs(111)B substrate. (c) XRD characterization of 40 nm MnSe films grown on GaSe(0001)/GaAs(111)B substrates showing additional peaks corresponding to α-MnSe(111) and 1T-$MnSe_2$.

highly oriented pyrolytic graphite (HOPG) and MoS_2 [106], which exceeds the theoretically predicted value of $\sim$0.7 μ_B per formula unit [218]. On the other hand, the magnetic moment of $\sim$4 μ_B per formula unit reported for a monolayer of $MnSe_2$ grown on GaSe(0001) [107] is in agreement with density functional theory (DFT) calculations [229, 230]. Such discrepancies in the experimentally obtained total magnetic moment can be due to different background subtraction methods when analyzing the magnetization results, where different contributions of the background signal are considered. The choice of the background subtraction method can strongly affect the total magnetic moment extracted from the experimental results.

In this Letter, we use epitaxially grown $MnSe_2$ monolayers on GaSe(0001) on GaAs(111)B substrates as an example to demonstrate how the background subtraction

method can affect the value of the magnetic moment extracted from the experimental measurement. Importantly, systematic control measurements identify the presence of a paramagnetic signal that originates from unintentional Mn impurities in the substrate, most likely incorporated in the GaSe layer during synthesis. When the background subtraction only accounts for the diamagnetism from the substrate and ignores the presence of the paramagnetic signal, we obtain unexpectedly large magnetic moment values greater than $\sim$10 μ_B per Mn. On the other hand, when the background subtraction includes both the diamagnetic and paramagnetic components, we obtain magnetic moment values of $\sim$4 μ_B per Mn, which is consistent with DFT calculations [229, 230]. Analysis of the background subtraction procedure including the paramagnetic component demonstrates its improved reliability and accuracy as compared to typical procedures only considering the diamagnetic component. Moreover, our results show that a careful background subtraction is crucial for further study of monolayer and few-layer van der Waals magnets grown by MBE on bulk substrates.

5.3 Experimental Methods

The $MnSe_2$ samples are prepared by van der Waals epitaxy in a Veeco GEN930 MBE chamber on GaSe(0001)/GaAs(111)B substrates following the recipe of O'Hara, *et al.* [107] in a recent report with a base pressure of 2×10^{-10} Torr. Epi-ready, un-doped GaAs(111)B substrates (AXT, single-side polished, 0.5 mm thick, $0° \pm 0.5°$ offcut, 1.4×10^8 Ω-cm resistivity) are indium-bonded to an unpolished Si backing wafer and annealed under a Se flux (beam equivalent pressure (BEP) of $\sim 2 \times 10^{-6}$ Torr) at 600°C for 20 min.

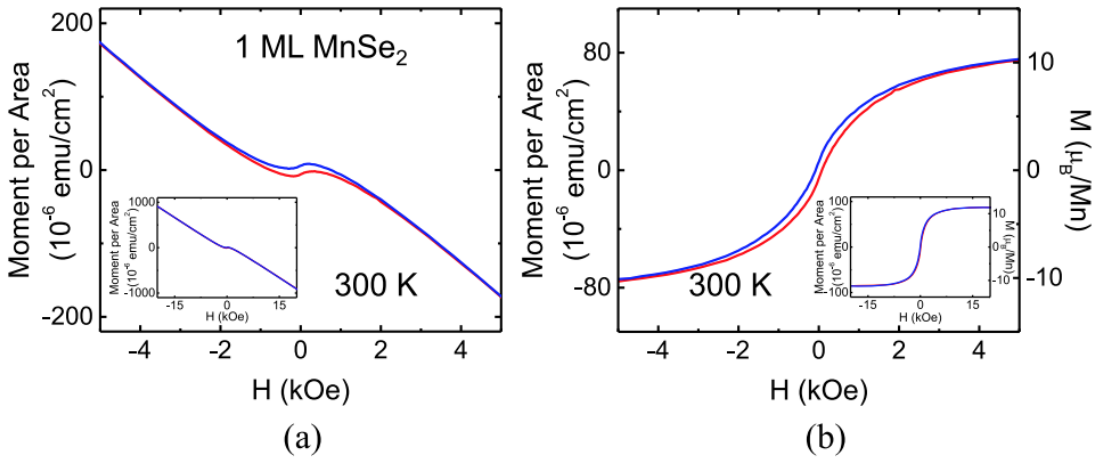


Figure 5.2: Room temperature, out-of-plane magnetic hysteresis loop of 1 ML $MnSe_2$. (a) Raw bulk magnetization loop showing diamagnetic background from substrate. Inset: Full range M(H) scan up to higher magnetic fields. (b) Bulk magnetization loop after linear diamagnetic background subtraction of raw data. Inset: Full range M(H) scan up to higher magnetic fields.

under ultra-high vacuum to remove the surface oxide and terminate the surface with Se. The sample is then cooled to a substrate temperature of 400°C for the base layer growth of GaSe. The growth is monitored in real-time via reflection high-energy electron diffraction (RHEED) at an operating voltage of 15 kV. The substrate temperature is measured using a thermocouple that is attached to the continuous azimuthal rotation (CAR) manipulator substrate heater. Standard Knudsen-style effusion cells are used for the deposition of Ga (United Mineral & Chemical Corporation, 99.99999%) and Mn (Alfa Aesar, 99.98%) with typical cell temperatures of 1000°C and 800°C, respectively, while a valved cracking source is operated at 950°C (bulk zone, 290°C) for the deposition of atomic Se (United Mineral & Chemical Corporation, 99.9999%). The growth is performed under a Se overpressure with a BEP flux ratio of ∼100 for Se:Ga and ∼60 for Se:Mn, where the Se re-evaporates. The beam

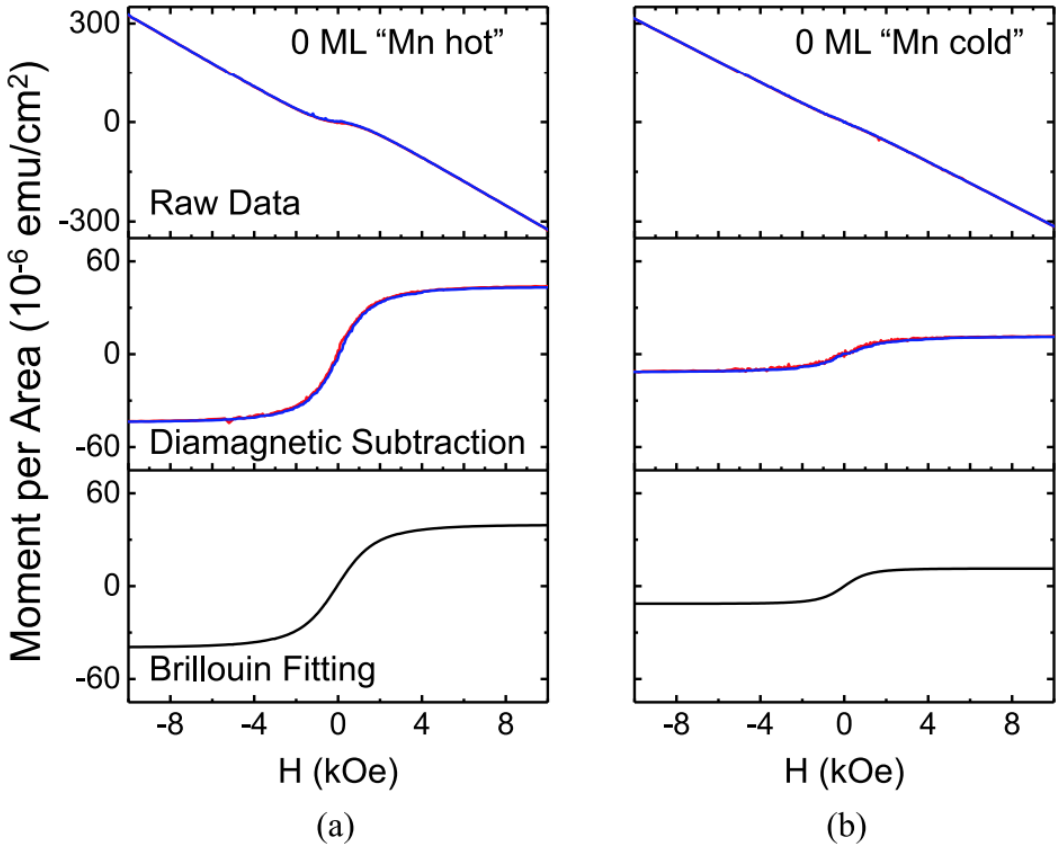


Figure 5.3: 0 ML $MnSe_2$ magnetization control measurements with standard linear background subtraction and Brillouin function fitting. (a) M(H) measurement of 0 ML Mn hot control sample using $T_{Mn} = 800°C$. (b) M(H) measurement of 0 ML Mn cold control sample using $T_{Mn} = 620°C$.

fluxes are measured using a nude ion gauge with a tungsten filament positioned for growth and the corresponding deposition rate is calibrated based on film thicknesses determined by x-ray reflectometry (Bruker, D8 Discover). The typical deposition rate is 1 nm/min for GaSe and 0.1 ML/sec for $MnSe_2$. Samples are capped with amorphous selenium (a-Se) at room temperature prior to removal from the chamber to protect the surface from oxidation and degradation. The lattice structure for monolayer $MnSe_2$ and the heterostructure for

the samples discussed in this study are shown in Figures 5.1a and 5.1b, respectively.

The GaSe base layer growths are followed by two different growth recipes for van der Waals $MnSe_2$. The first keeps the sample temperature at 400°C while the second lowers the sample temperature to 300°C for the deposition of $MnSe_2$. The former is employed by closing the Ga shutter (while the Se shutter remains open) and opening the Mn shutter immediately. This provides streakier RHEED patterns up to high thicknesses (> 40 nm) and transitions to antiferromagnetic α-MnSe(111) according to x-ray diffraction (XRD) measurements, shown in Figure 5.1c. The latter is employed by closing both the Ga and Se shutters and cooling the sample to 300°C. Once the sample temperature is stable, the Se and Mn shutters are opened to deposit $MnSe_2$ layers. This recipe leads to rougher films according the spotty RHEED patterns when the sample gets thicker (> 5 MLs) [107]. XRD scans show identical peaks to the 400°C growth, shown in Figure 5.1c. While the results of this paper apply for both types of samples, the representative analysis is presented for samples grown at 400°C.

Superconducting quantum interference device (SQUID) magnetometry (Quantum Design, MPMS XL) measurements are used to measure the magnetic properties of the samples. Samples are mounted in the out-of-plane orientation (with the magnetic field applied perpendicular to the film surface) and are measured at room temperature. The magnetic moment per formula unit is determined by dividing the Bohr magneton (μ_B) by the number of Mn atoms in a single monolayer of $MnSe_2$ grown on the substrate. Within a monolayer, the concentration of Mn is $\sim 7.00 \times 10^{14}$ cm^{-2}.

5.4 Results and Discussion

Monolayer $MnSe_2$ films are grown on 55 nm GaSe(0001)/GaAs(111)B and are capped with 5 nm GaSe and amorphous Se before removing the sample from the MBE chamber (schematic shown in Figure 5.1b). Room temperature, out-of-plane magnetization loops show magnetic hysteresis indicating ferromagnetic ordering for 1 ML $MnSe_2$ on the GaSe base layer. Figure 5.2a shows the SQUID magnetization loop without any background subtracted and is normalized to the area of the sample.

The 1 ML $MnSe_2$ hysteresis loop shows an obvious linear diamagnetic background at high magnetic field, which arises from the bulk GaAs(111) substrate. The standard data analysis procedure for extracting the ferromagnetic signal is using a linear background subtraction to remove the diamagnetic signal from the substrate. Figure 5.2b shows the magnetization loop after applying a linear fit to the diamagnetic background in Figure 5.2a and subtracting out the signal. Although the hysteresis loop clearly closes at low magnetic field ($\sim$2 kOe), the magnetic moment does not saturate until higher fields ($\sim$15 kOe), indicating a possible paramagnetic component. In addition, the saturation moment at room temperature is calculated to be $\sim$12 μ_B/Mn (Figure 5.2b, inset) after subtracting the linear background, which is approximately three times as large than what is predicted in DFT calculations [230]. The strong and non-saturating magnetic moment at high magnetic field draws attention for understanding the contributions to the bulk magnetization loop.

An interesting question is to understand what is contributing to the large background signal in the 1 ML $MnSe_2$ SQUID magnetization loop. One possibility is that the background signal comes from the GaSe(0001) base layer. It is worthwhile mentioning that

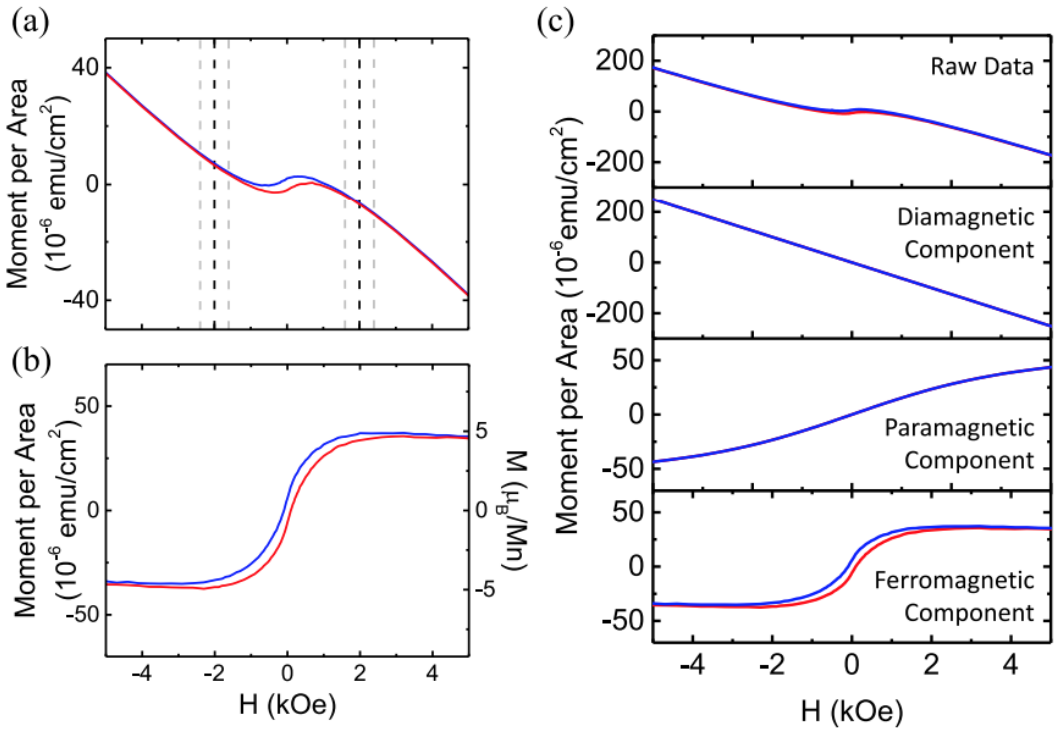


Figure 5.4: 1 ML $MnSe_2$ magnetic hysteresis loop using new background subtraction method considering diamagnetic and paramagnetic components using a Brillouin function background subtraction method. (a) Raw M(H) loop showing fitting parameters (dashed lines). (b) Final ferromagnetic hysteresis loop after background subtraction. (c) Background subtraction components (raw data, diamagnetic, paramagnetic, and ferromagnetic contributions) in 1 ML $MnSe_2$ grown on a 55 nm GaSe/GaAs(111) substrate.

during the annealing of the GaAs substrate and growth of the GaSe base layer, the Mn effusion cell is at its deposition temperature (T_{Mn} = 800°C). Although the Mn effusion cell is masked by a shutter during this process, trace amounts of Mn impurities might possibly bypass the shutter and incorporate into the base layer and/or substrate due to the relatively high vapor pressure of Mn. To examine this case, we systematically study the GaSe base layer growth under identical conditions and characterize its magnetic properties.

To investigate the contribution of the GaSe base layer to the magnetic signal,

we grow a 60 nm GaSe(0001)/GaAs(111)B sample under identical conditions to the 1 ML $MnSe_2$ sample with the Mn cell maintained at its deposition temperature of 800°C (we label this as: 0 ML Mn hot). The magnetic properties of this sample show a non-linear signal which has a large saturation magnetic moment of $\sim 4.3 \times 10^{-5}$ emu/cm^2 with no remanent magnetization after the diamagnetic background subtraction (Figure 5.3b). There is no $MnSe_2$ deposited in this case and the saturation magnetic moment has similar order of magnitude to what is shown in Figure 5.2, so the paramagnetic-like signal should only come from the substrate. We further employ a Brillouin fitting on the extracted curve, which is shown in the bottom panel in Figure 5.3a. The Brillouin fitting agrees very well with the observed non-linear signal, which confirms the paramagnetic signature in this sample.

The Mn impurities that are potentially incorporating inside the $Ga_{1-x}Mn_xSe$ matrix may contain randomly oriented magnetic moments that have no direct exchange interaction with each other [232]. This can give rise to a paramagnetic contribution in the magnetization signal which can be explained by the Brillouin function. To further confirm that the paramagnetic signal is coming from Mn doping in the GaSe(0001) base layer, we grow a nominally identical 0 ML control sample but with the Mn effusion cell temperature lowered to an idle state ($T_{Mn} = 620$°C, which we label as: 0 ML Mn cold). By lowering the temperature of the effusion cell, the Mn vapor pressure should decrease leading to less impurities in the base layer and/or substrate. Indeed, after measuring the magnetic properties via SQUID, the magnetization signal is nearly linear and the paramagnetic contribution is much smaller (Figure 5.3b). This further confirms that there is a large paramagnetic contribution from the GaSe base layer for our 1 ML $MnSe_2$ sample, shown in Figure 5.2.

H_{cut} (kOe)	M_{PM} (10^{-6} emu/cm^2)	M_{FM} (10^{-6} emu/cm^2)	M_{FM} (u_B/Mn)
1.8	56	31	4.1
2.0	52	36	4.7
2.2	49	39	5.1

Table 5.1: Detailed description of Brillouin fitting parameters to determine magnetic moment in 1 ML $MnSe_2$ and 0 ML $MnSe_2$ control samples.

The control experiment of the "0 ML $MnSe_2$" sample shows that to accurately determine the ferromagnetic signal in our $MnSe_2$/GaSe(0001) samples, one has to also consider the paramagnetic contribution from the substrate. We apply a new method for background subtraction to the 1 ML $MnSe_2$ sample discussed in Figure 5.2. We proceed with the following equation to fit the non-hysteretic part of the SQUID data ($|H| \geq H_{cut}$),

$$m(H) = A_{dia}H + A_{para}B_{\frac{5}{2}}((\frac{5}{2}g^*\mu_B)/(k_BT)H) + sign(H)m_{sat} \tag{5.1}$$

where A_{dia},A_{para},g^*,and m_{sat} are fitting parameters. The first term is a diamagnetic background that is linear in H. The second term is a paramagnetic background described by a Brillouin function with $J = 5/2$ for Mn, and g^* is an effective g-factor observed in dilute magnetic semiconductors [249]. The last term is the saturated ferromagnetic magnetization, which adds as a positive/negative offset (m_{sat}) depending on the direction of the applied magnetic field.

To determine the magnetic moment per formula unit in the 1 ML $MnSe_2$ sample, we proceed with this new fitting method. Figure 5.4a shows the raw SQUID measurement for this sample. The measurement was performed up to $\pm$30 kOe, and the full range of data were used for the fitting. For the new method of background subtraction, we select a cutoff field, H_{cut}, that bounds the range of the ferromagnetic hysteresis loop. To demonstrate, we proceed with H_{cut} = 2 kOe and fit the data with Equation 5.1. After the fit is completed,

the first two terms of Equation 5.1 (i.e. the diamagnetic and paramagnetic contributions) are subtracted from the raw data to yield the ferromagnetic hysteresis loop, shown in Figure 5.4b. Figure 5.4c shows the raw data, diamagnetic component, paramagnetic component, and ferromagnetic component over the field range of ±5 kOe. This yields a value for m_{sat} of 4.7 μ_B/Mn which is in agreement with theoretical calculations [230].

The result of the fitting process depends on the choice of H_{cut}, which is determined by the field value that the hysteresis loop in the SQUID signal closes. An uncertainty in choosing H_{cut} could in principle affect the extracted ferromagnetic signal. To show the robustness of the background subtraction method, we further performed the same fitting process with a few different H_{cut} values, as shown in Table 5.1. The change of the H_{cut} indeed changes the extracted magnetic moment in both the paramagnetic and ferromagnetic component. However, the total change of both components is within 20%, which indicate that the fitting method is reliable in determining the ferromagnetic response of the van der Waals magnet $MnSe_2$.

5.5 Conclusions

In summary, we have demonstrated that unintentional Mn doping of the GaSe(0001) base layer can introduce a strong paramagnetic signal in the MBE grown van der Waals magnet $MnSe_2$. This provides the physical basis for a new method of background subtraction that separates out diamagnetic and paramagnetic contributions from the ferromagnetic signal of monolayer $MnSe_2$. This is shown to be a reliable method for extracting the ferromagnetic hysteresis loop and value of the magnetic moment and should be considered for

future studies of van der Waals magnets grown by MBE. Our study further shows the importance of performing control experiments on the magnetic background signal for epitaxially grown van der Waals magnets on a case-by-case basis. Further studies including comparisons with complementary techniques that are less sensitive to background signals, such as magneto-optic Kerr effect or anomalous Hall effect, will also be beneficial for accurately determining the magnetic moments in such systems.

Chapter 6

Integration of $MnSe_2$ on Topological Insulator, Bi_2Se_3

6.1 Motivation

Van der Waals magnets are particularly interesting due to their high surface sensitivity owed to their large surface-to-volume ratio. This is useful for studying the effects of electrostatic gating, strain, and proximity-induced phenomena which may be advantageous in developing highly tunable spintronic devices and energy efficient magnetoelectronics. With recent reports of ferromagnetism in 2D materials such as CrI_3 and $Cr_2Ge_2Te_6$, achieving this is now possible but limited at low temperatures [90, 93]. With new studies showing room temperature ferromagnetism in $MnSe_2$ and VSe_2 grown by molecular beam epitaxy (MBE) [106, 107], real-world applications now are possible.

Combining a 2D magnet with a high z material, or a material with large spin-orbit

coupling is advantageous for looking at properties such as novel magnetic textures, quantum anomalous Hall effect, and spin-orbit torque [87, 250, 251, 252]. This requires a high quality, sharp interface in order to properly couple the magnetism of the overlayer and the spin-orbit coupling of the underlying substrate. Particularly, the proximity effects between the 2D magnet and a topological insulator (Bi_2Se_3) is of great interest. For the magnetic proximity effect (MPE), the effective magnetic field induced in the topological insulator through proximity with a 2D magnet can break the time-reversal symmetry of its surface state, which can cause a gap opening in the surface state and lead to a quantum anomalous Hall state in the topological insulator [64, 253, 254]. On the other hand, the strong spin-orbit coupling in the topological insulator can affect the magnetic properties, such as the magnetic anisotropy, in the 2D magnet [106]. Furthermore, the spin-orbit coupling in the topological insulator layer can generte an interface Dzyaloshinskii-Moriya interaction (DMI) in the 2D magnet, which is required for generating possible magnetic skyrmion phases in the system [255]. Such 2D magnet/TI heterostructures with clean interfaces are ideal for studying the MPE as well as potentially induced magnetic phases. In this work, we study the integration of monolayer $MnSe_2$ on Bi_2Se_3 by using a combination of molecular beam epitaxy (MBE) and spin-polarized scanning tunneling microscopy (SP-STM).

6.2 Results and Discussion

20 nm Bi_2Se_3 films were grown by MBE on sapphire(0001) substrates with details described elsewhere [64, 256]. Samples were then capped with amorphous Se, mounted onto a Ferrovac tantalum flagship paddle and transferred to another MBE chamber (base

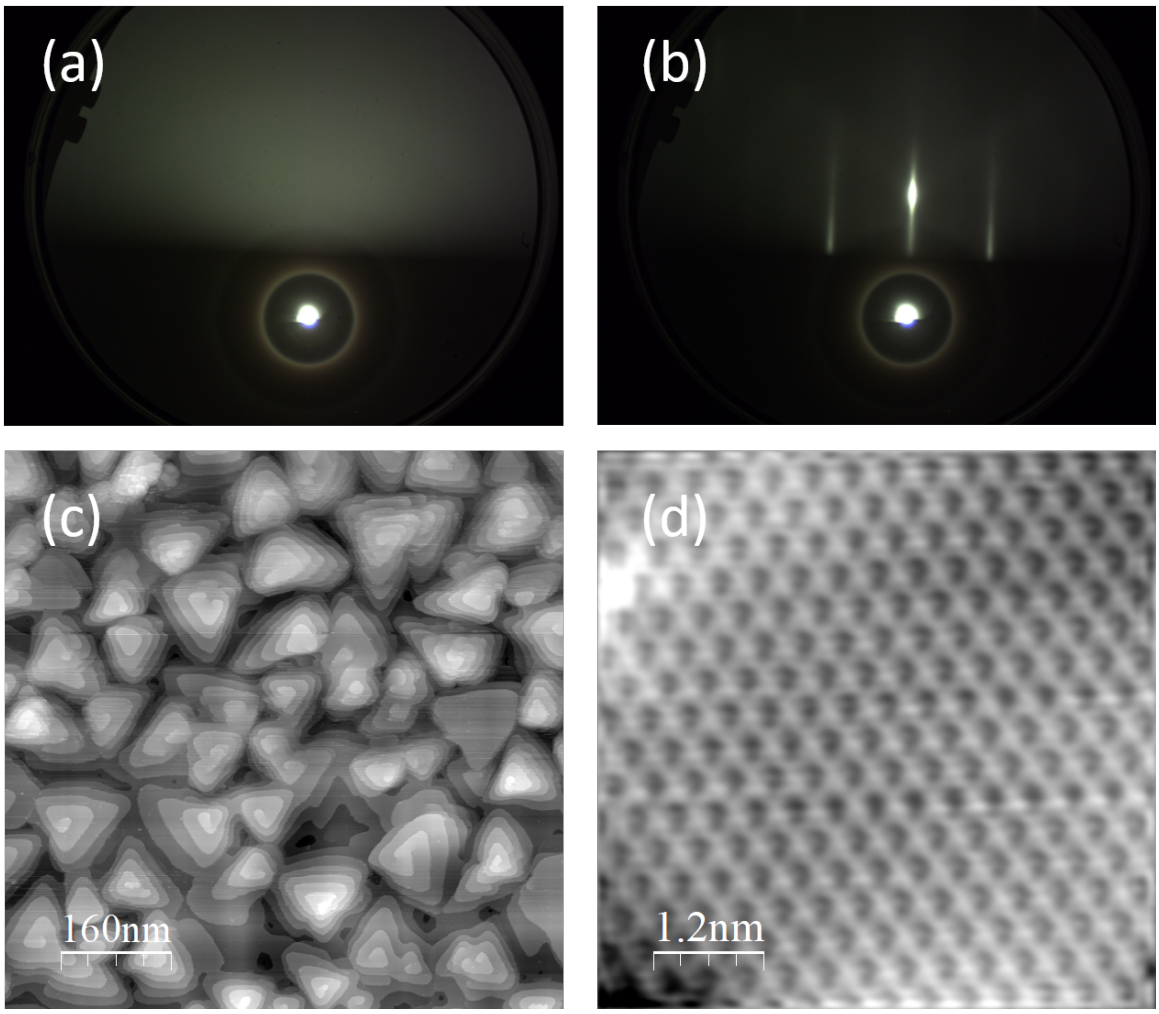


Figure 6.1: RHEED images and STM measurements on Bi_2Se_3 grown on sapphire(0001) substrates. (a) Se-capped Bi_2Se_3 after transferring to another MBE chamber for $MnSe_x$ growth, (b) de-capped Bi_2Se_3 after annealing at 200°C for 30 minutes, (c) topography image showing ultraclean, smooth surface of Bi_2Se_3 after de-capping, and (d) atomic resolution of Bi_2Se_3.

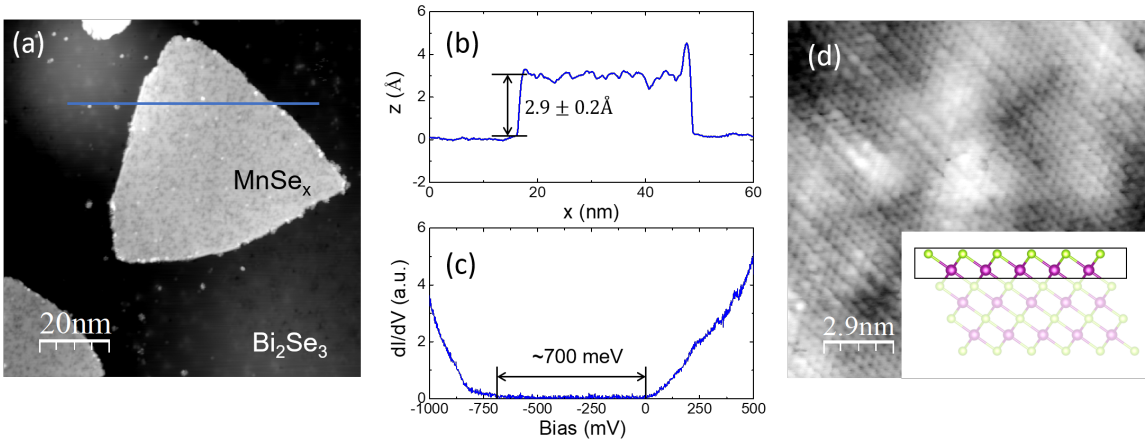


Figure 6.2: STM measurements showing $MnSe_x$ grown on Bi_2Se_3. (a) Topography image of an $MnSe_x$ triangle on the surface, (b) and (c) showing height scale and electronic structure corresponding to possible α-MnSe(111) phase. (d) Zoomed in atomic resolution image confirming that these properties are consistent with a bilayer of α-MnSe(111).

pressure 2×10^{-10}) for $MnSe_x$ growth. Bi_2Se_3 samples are then decapped at ~200°C for 30 minutes prior to growth. Cleanliness of the interface is shown in the STM images in Figure 6.1 from a sample that was de-capped via annealing. Atomic resolution images of the Bi_2Se_3 substrates show lattice parameters that match bulk values previously reported [64]. Samples are then heated to 400°C for $MnSe_x$ deposition. Elemental Mn (99.98%, Alfa Aesar) is evaporated from a standard Knudsen-style effusion cell (operated at T_{Mn} = 745°C), while atomic species of Se is deposited from a valved cracking source (Veeco) as previously noted in other studies. Samples are monitored via *in situ* reflection high energy electron diffraction (RHEED) with operation at 15 kV. Note that due to the larger mass of the tantalum paddles, the substrate heater reads a higher temperature of approximately 300°C difference from normal sample mounting described in previous work. ~1 monolayer (ML) and 40 nm $MnSe_x$ samples are grown on the Bi_2Se_3/sapphire(0001) surfaces for the work reported in

this Chapter.

$\sim$1 ML $MnSe_x$ samples were grown by MBE and transferred under ultra-high vacuum ($\sim 1 \times 10^{-9}$ Torr) via a Ferrovac vacuum suitcase to a separate STM chamber. As mentioned in Hinkle, *et al.*, deposition of certain metals on top of topological insulators leads to a low sticking coefficient and possible magnetic dead layers [253]. This work is taken into consideration when co-depositing Mn and Se on the surface of the topological insulator. In the deposition of $MnSe_x$, we observe interesting features in the RHEED and STM. The RHEED images show no change from the Bi_2Se_3 substrate. When measured by STM, the $MnSe_x$ layers deposited do not fully cover the Bi_2Se_3 surface, and only have about $\sim$10% of monolayer coverage. Figure 6.2 shows part of the deposited regions that stuck to the surface, which are possible α-MnSe(111) layers. These small triangles of $MnSe_x$ are found showing a height difference from the underlying substrate of 2.9 $\pm$ 0.2 Å and a electronic gap of $\sim$700 meV [257]. Zooming in on these regions show atomic resolution and confirms a bilayer of α-MnSe(111), shown in Figure 6.2 with the inset highlighting a ball-and-stick model of the structure described. As mentioned in previous work α-MnSe(111) is a antiferromagnetic material with a rock salt structure and has a closely related lattice structure to the underlying substrate [107, 254].

Interestingly, while scanning in other regions of the sample, we observed nucleation of a different structural phase at the edge of the α-MnSe(111) triangles. These extended domain regions show different contrast in the topography measurements due to the different lattice height of 5.8 $\pm$ 0.1 Å which is similar to the XRD *d*-spacing reported in [107, 258] for 1T-$MnSe_2$. Figure 6.3 shows the difference in dI/dV spectroscopy in the two regions, with

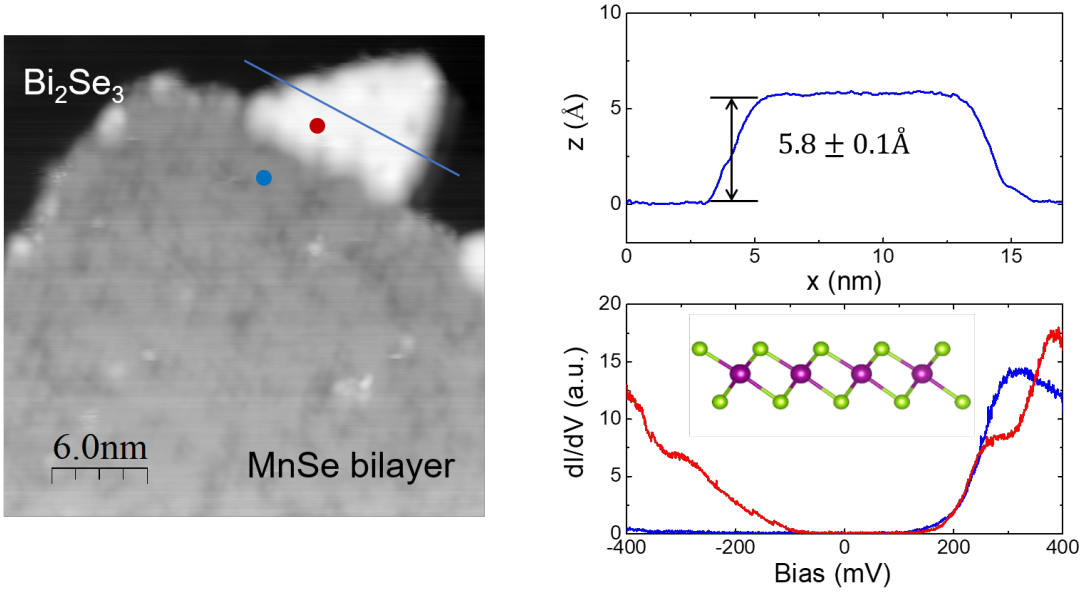


Figure 6.3: STM topography and spectroscopy measurements showing $MnSe_x$ grown on Bi_2Se_3. This region shows a α-MnSe(111) bilayer attached to a 1T-$MnSe_2$ triangle.

blue showing the electronic structure of the α-MnSe(111) and red showing the electronic structure of the possible 1T-$MnSe_2$ region. These observations confirm that these are two different structural phases that are growing on the Bi_2Se_3 surface. The reason why the 1T-$MnSe_2$ may be nucleating on the edge of the α-MnSe(111) bilayer is possibly due to creation of preferential nucleation sites and extended compact domains giving rise to a new material which has an extremely similar lattice structure [259].

To understand the magnetic properties of these layers, we used etched antiferromagnetic Cr tips to measure a magnetic contrast as a function of applied magnetic field at 5 K. Four different regions of the small compact triangle are measured to confirm what we observe. During the spectroscopy measurements, dI/dV, we sweep an applied field of 1 T and see interesting behavior and it is important to explain what may be happening here.

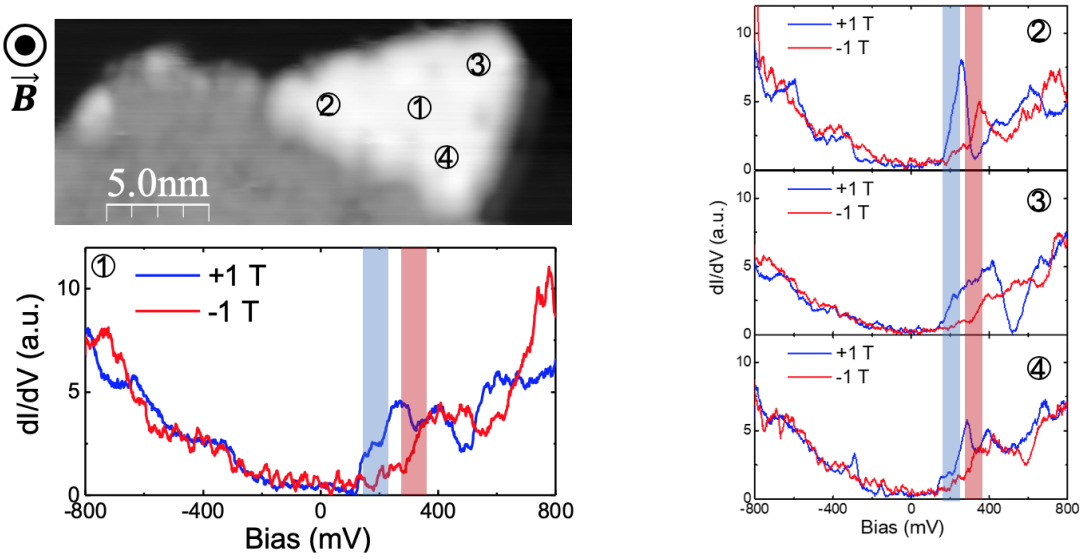


Figure 6.4: SP-STM spectroscopy on the 1T-$MnSe_2$ phase in four different regions showing ferromagnetic ordering.

In SP-STM, when both the surface and the tip are magnetic, the imbalance of the spin-up and spin-down electrons around the Fermi level lead to an additional contribution to the tunnel current [54, 76, 130, 131, 132]. Figure 6.4 shows the differential conductance measurements where we see a asymmetric effect when sweeping the field back and forth which is repeatable on different areas of the sample. The asymmetry reflects the energy-dependent spin-polarization of the tunnel junction between the tip and the sample, which in general may mean that this area is ferromagnetic.

To confirm that this area is indeed ferromagnetic, it is important to identify the magnetic ordering of the α-MnSe(111) bilayer and Bi_2Se_3 substrate mentioned earlier. Figure 6.5 shows the dI/dV scans as a function of external magnetic field on the adjacent layer and underlying substrate. In these measurements, we do not observe any asymmetry that

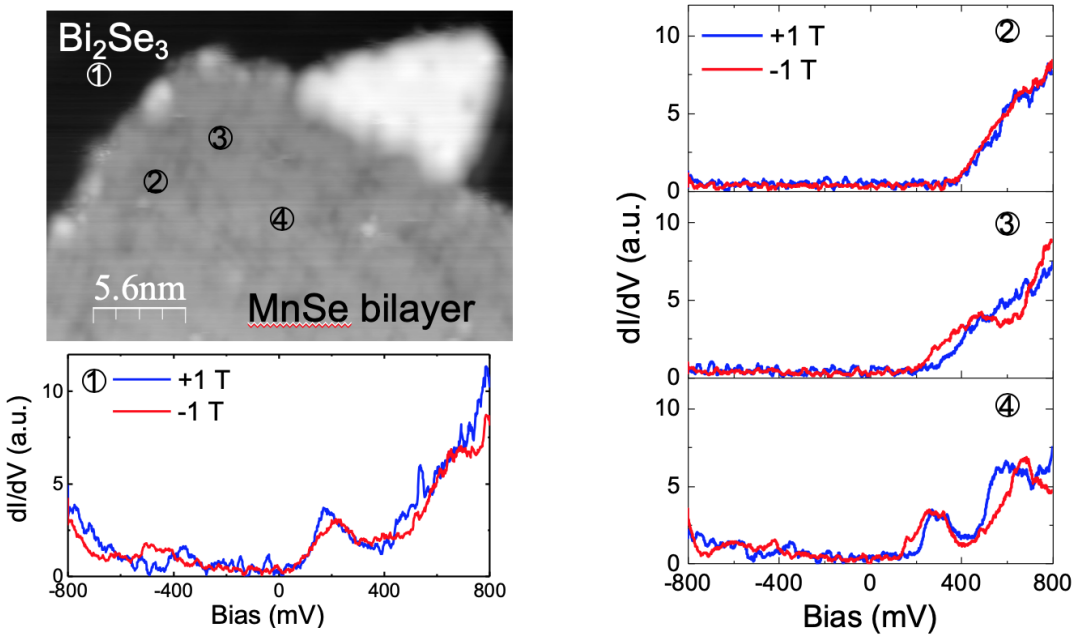


Figure 6.5: SP-STM spectroscopy on the bilayer α-MnSe(111) phase in four different regions showing zero magnetization.

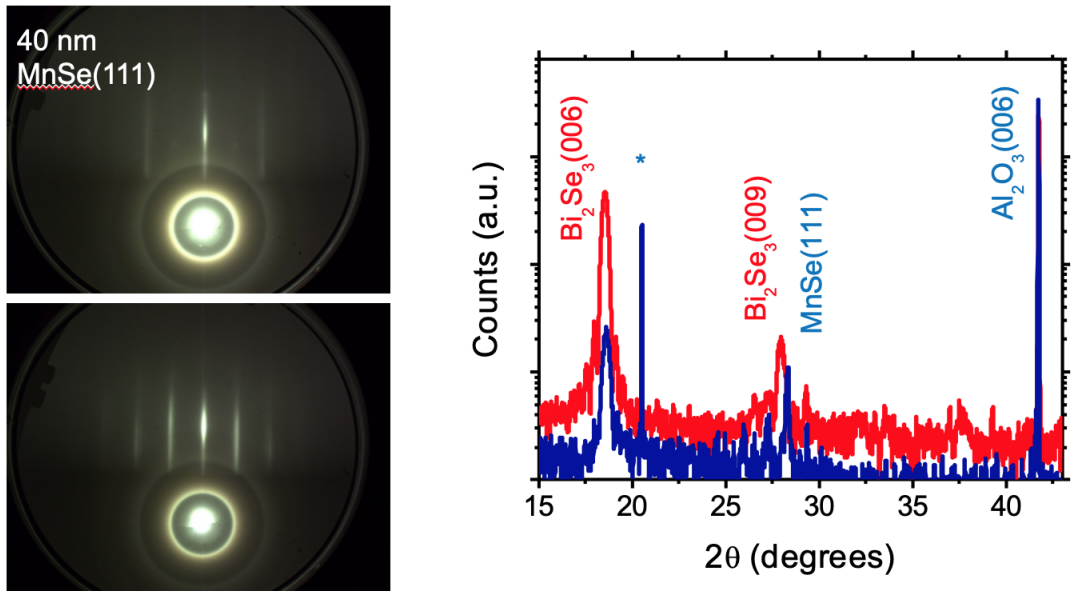


Figure 6.6: RHEED and XRD showing growth of α-MnSe(111) on Bi_2Se_3 up to high thicknesses.

may attribute to a net magnetization. Each region shows virtually no dependence on magnetic field which confirms that the Bi_2Se_3 is a non-magnetic material and the α-MnSe(111) is an antiferromagnet with a net zero magnetization. We also grow 40 nm films of $MnSe_x$ to study the structure of the material at higher thicknesses. Figure 6.6 shows RHEED patterns along two different azimuthal orientations of the as-grown α-MnSe(111) film. Samples are capped with amorphous Se and measured by *ex situ* XRD to confirm the bulk structure. XRD further confirms that α-MnSe(111) is indeed growing on the surface of the Bi_2Se_3 and is the preferred thermodynamic structure.

6.3 Conclusions

In summary, we report the first direct atomic and magnetic imaging of an MBE-grown 1T-$MnSe_2$ monolayer on a Bi_2Se_3 substrates. We learn that the magnetic $MnSe_2$ monolayer nucleates off of preferential growth sites on an α-MnSe(111) bilayer which will need to be considered for other studies of this material. Nevertheless, this is a gigantic breakthrough in the field of 2D magnets and will become a foundation for studying future phenomena such as layer dependence, novel spin textures, and engineering structures using the spin-polarized tip.

Chapter 7

Epitaxial growth of van der Waals VSe_2 layers on HOPG and GaAs Surfaces

7.1 Motivation

Recent experimental breakthroughs open up possibilities to study magnetism in 2D materials [90, 93, 106, 107]. With limitations to growth on van der Waals substrates and small grain size, understanding growth kinetics by molecular beam epitaxy (MBE) is important to understand growth conditions for thermodynamic equilibrium phases. Here, we report the MBE growth of vanadium diselenide thin films on GaAs(111)B and HOPG substrates. A comprehensive microstructural and chemical study has been carried out by the use of x-ray diffraction, transmission electron microscopy, scanning tunneling microscopy

and x-ray photoelectron spectroscopy for the growth on GaAs substrates and a systematic study of how the growth temperature effects the domain size of the VSe_2 overlayers. The fundamental understanding gained through these investigations has enabled integration of VSe_2 on a insulating 3D substrate with epitaxial registry and we are able to study its structure up to thick layers, also we have developed a way to study how the magnetism may depend on the grain size and structure of the VSe_2 epilayer.

7.2 Introduction

The exploration of two-dimensional (2D) materials has received appreciable attention since the first isolation of monolayer graphene [59, 62, 154, 221]. Being only a few atoms thick, the reduced dimensionality in 2D materials can strongly influence their electronic, optical and magnetic properties compared to their bulk analogues. For example, when reduced to monolayer thickness, the low energy dispersion of electrons in graphene becomes massless-Dirac fermion like [59, 221] while the electronic band structure in transition metal dichalcogenides (e.g. MoS_2, WSe_2) undergoes an indirect to direct gap transition with 100% valley selective with circular polarized light [62, 154, 192]. Other examples include tunable magnetism in hole-doped monolayer GaSe [260], strong Ising pairing in superconducting $NbSe_2$ atomic layers [61], and quantum spin Hall states in monolayer 1T'-WTe_2 [261]. Controlling the material thickness and further studying how their properties depend on the number of layers is essential for understanding 2D materials.

Among the family of 2D materials, VSe_2 is of particular interest, because both its electronic and magnetic properties are significantly different in the monolayer limit [106,

218, 262]. Bulk VSe_2 may exhibit two polymorphs in which it forms, which are the semiconducting 2H (trigonal prismatic) or metallic 1T (octahedral) phase. 1T-VSe_2 forms in a layered van der Waals hexagonal structure, with each V atom octahedrally-coordinated by six surrounding Se atoms. Bulk 1T-VSe_2 undergoes a ($4 \times 4 \times 3$) charge density wave (CDW) transition with $T_c = 110$ K [106, 235, 263]. However, the monolayer shows a ($\sqrt{7} \times \sqrt{3}$) CDW with altered-symmetry-type compared to the (4×4) CDW in the bulk [264]. On the other hand, although bulk 1T-VSe_2 is reported to be paramagnetic [235, 263], it has been shown to be ferromagnetic in its monolayer form with a Curie temperature above room temperature [106]. The drastic differences in bulk and monolayer 1T-VSe_2 make it an advantageous material system to further study how its properties change with increased thickness from the monolayer limit.

Here, we demonstrate growth of large-area, high-quality 1T-VSe_2 on GaAs(111)B substrates by molecular beam epitaxy (MBE) up to high thickness. X-ray diffractometry (XRD) and scanning transmission electron microscopy (STEM) confirms the formation of high quality 1T-VSe_2 layers. X-ray photoelectron spectroscopy (XPS) measurements were conducted to confirm the chemical composition and air stability of VSe_2 on GaAs. Using scanning tunneling microscopy (STM), we further confirm the formation of 1T-VSe_2 on GaAs(111)B and measure its local electronic properties with scanning tunneling spectroscopy (STS). These results establish a baseline for understanding and controlling the number of layers of VSe_2 thin films grown by MBE.

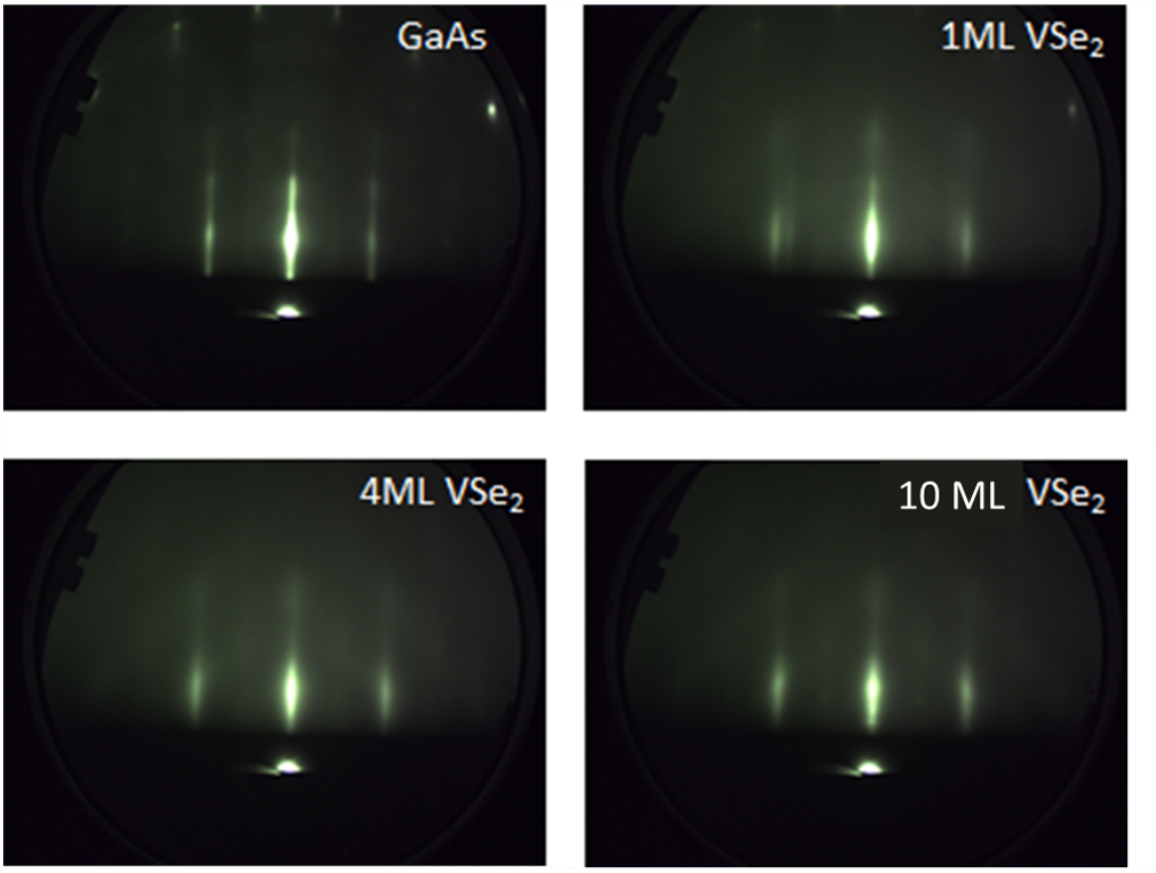


Figure 7.1: RHEED images of VSe_2 growth on GaAs(111) substrate.

7.3 Experimental Methods

VSe_2 growths are prepared by van der Waals epitaxy in a Veeco GEN930 chamber with a base pressure of 2×10^{-10} Torr. GaAs(111)B substrates (AXT, single-side polished, 0.5 mm thick, $\pm$ 0.5° miscut, 1.4×10^8 Ω-cm) are prepared by indium bonding to a 3 in. unpolished Si wafer then loading into the chamber and annealing at 400°C for 15 minutes under UHV conditions (1×10^{-9} Torr) to remove any surface impurities. The GaAs is then loaded into the growth chamber and exposed to a Ga flux (United Mineral & Chemical Corporation, 99.99999%, 1×10^{-8} Torr) at 450°C for 2-4 minutes to remove the native oxides on the surface via Ga polishing [265]. The substrate is then heated to and annealed 600°C under a Se flux (1×10^{-7} Torr) for 15 minutes to remove any excess sub-oxides and terminate the surface with Se atoms then cooled to the growth temperature. Elemental Se (United Mineral & Chemical Corporation, 99.9999% is evaporated from a standard Knudson-type effusion cell with a typical cell temperature of 170°C and Elemental V (ESPI Metals, 99.98%) is evaporated using a quad-rod *electron*-beam evaporator (MANTIS). The beam fluxes are measured using a nude ion gauge with a tungsten filament positioned at the sample growth position and the corresponding growth rate is calibrated based on nominal film thicknesses measured by *ex situ* x-ray reflectometry (XRR). *In situ* RHEED is used to monitor the growth and annealing procedures in real-time with an operation voltage of 15 kV. The VSe_2 growth is performed in an adsorption-limited growth regime at a beam-equivalent pressure (BEP) V:Se ratio of ∼1:1000, where the excess Se re-evaporates. Samples are capped with amorphous Se or Te after growth at room temperature to perform *ex situ* structural characterization.

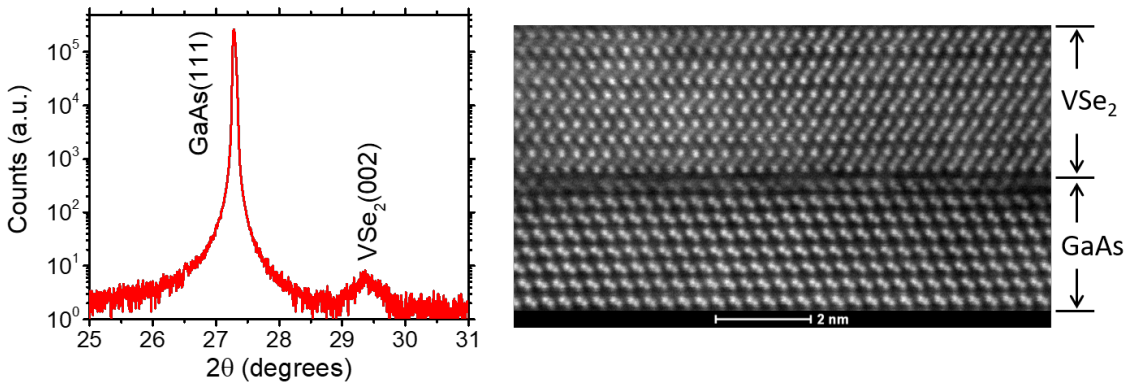


Figure 7.2: Structural characterization of thick VSe_2 films grown by MBE on GaAs. X-ray diffraction showing 30 ML VSe_2 film on GaAs(111) (left) and (right) STEM image of 5 ML VSe_2 on GaAs showing 1T structure and sharp interface transition.

7.4 MBE Growth of VSe_2 on GaAs(111) substrates

Our study began with determining the growth temperature window of VSe_2 on GaAs(111)B substrates for the highest quality thin films. At low temperature growths below 150°C, the RHEED pattern becomes dim after co-deposition of V and Se confirming an amorphous film from the large sticking coefficient of Se and low adatom mobility of V. At temperatures above 250°C, the RHEED pattern is streaky initially after deposition of V and Se, but then quickly becomes spotty after 1-2 monolayers (MLs) of growth. The sticking coefficient of the Se atoms decreases with higher substrate temperature leading to less coverage of chalcogen adatoms and the low adatom mobility leads to a smaller nucleation density and a 3D growth mode. For lower temperature growth, the sticking coefficient of the chalcogen adatoms increases leading to non-crystalline Se layers on the surface. At a GaAs substrate temperature of 200°C (± 10°C), the RHEED pattern of the VSe_2 remains streaky to approximately 30 MLs, which indicates atomically smooth films

up to high thickness which opens up an opportunity to study layer dependence. The co-deposition of VSe_2 films on GaAs are illustrated in the Figure 7.1 showing RHEED images as a function of thickness. Although growth temperature window is narrow, the RHEED pattern remains streaky and the intensity remains constant through larger thicknesses up to 30 MLs. After deposition of 1 ML (Figure 7.1, top right panel), the VSe_2 RHEED streaks coexist with the underlying GaAs(111) showing a clear structural transition. The inverse ratio of the RHEED spacing between the VSe_2 and GaAs(111) is measured to be 1.15, which is very close to the expected value of 1.17 for bulk in-plane lattice constants of 1T-VSe_2(0001) and GaAs(111). After 2 MLs of growth, the VSe_2 streaks no longer coexist with the underlying GaAs and remain streaky with six-fold rotational symmetry which suggests we have an epitaxial alignment between the two materials, $[1\bar{1}00]_{VSe_2}//[11\bar{2}]_{GaAs}$ and $[11\bar{2}0]_{VSe_2}//[1\bar{1}0]_{GaAs}$.

Using the optimized growth conditions to grow thicker films of high-quality, crystalline VSe_2 on GaAs, we performed structural measurements that can measure the bulk properties of our films. To determine the crystallographic orientation of the film, XRD measurements are performed on 30 ML VSe_2 films grown on GaAs. θ-2θ XRD scans show a weak (002) 1T-VSe_2 peak, shown in Figure 7.2 (left panel). While we expected a stronger peak due to the higher thickness, previous reports on 1T-VSe_2 bulk crystals show peak intensity of low counts [266], which may be related to the small scattering cross section of (002) planes in 1T-VSe_2. To further confirm the high crystalline quality of the film, atomic structure and interface quality, we perform high resolution scanning transmission electron microscopy (STEM). High resolution, cross-sectional STEM images shown in Figure 7.2

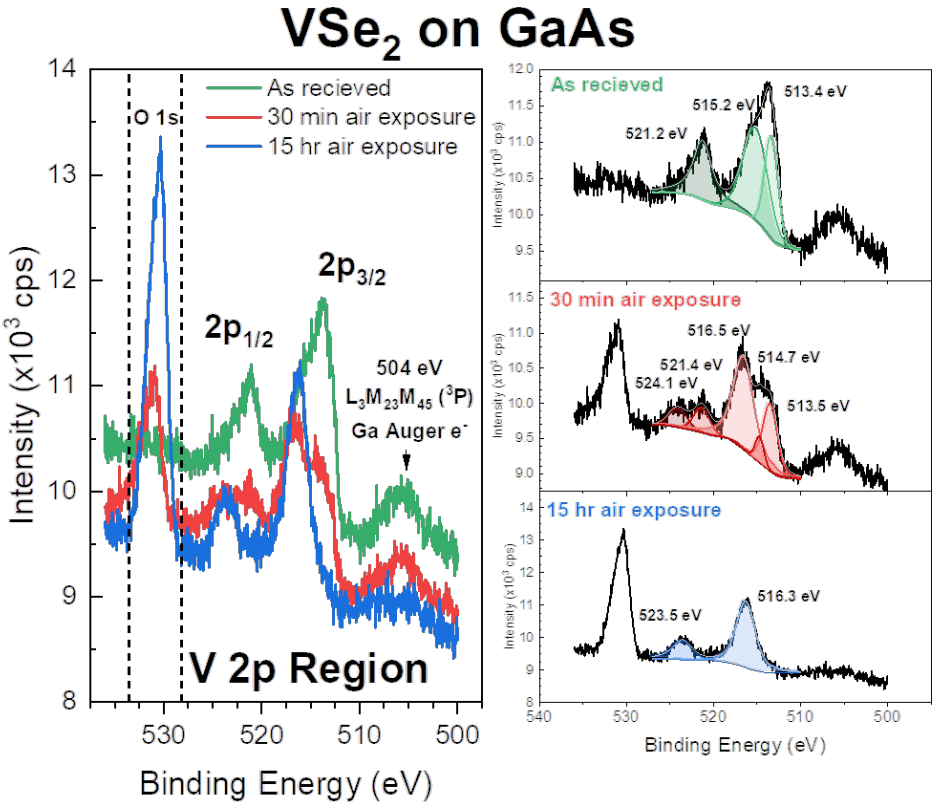


Figure 7.3: XPS spectra of 1 ML VSe_2 growth on GaAs surfaces.

(right panel) demonstrate a high quality growth of VSe_2 on GaAs. The interface shows no evidence of clusters, defects, or misfit dislocations, further confirming van der Waals epitaxy. The high atomic resolution also confirms the octahedral 1T structure of the VSe_2 films grown on GaAs.

In order to study the air stability and chemical composition of our samples, we performed x-ray photoelectron spectroscopy (XPS) measurements. First, in order to transfer samples under UHV without exposing the sample to potential surface oxidation, we used a

Ferrovac UHV suitcase to keep samples under vacuum while moving from the MBE growth chamber to the XPS system. Shown in Figure 7.3, characteristic peaks of both Se and vanadium are found in the XPS spectra of the as grown VSe_2 film. For the characteristic peaks ($2p_{1/2}$ and $2p_{3/2}$ of vanadium), we compare the difference of the as-grown film, 30 minutes after air exposure and 15 hours after air exposure. Unlike air stability reported for films grown on HOPG and MoS_2 substrates [106], our samples show characteristics of oxidation on the vanadium XPS spectra.

The formation of VSe_2 on GaAs is further confirmed by STM. $\sim$1 ML samples were grown and not capped then transferred via vacuum suitcase to UHV chamber for the STM measurement at 5 K. The surface atomic structure is imaged through a topography measurement showing a well-ordered hexagonal lattice and very smooth surface and determine an in-plane lattice constant of 3.3 - 3.5 Å, which agrees well with the Se-Se distance reported in literature [106, 267] and a metallic electronic structure via dI/dV spectroscopy (Figure 7.4).

Although there has been a report about observing room temperature intrinsic ferromagnetism in monolayer VSe_2, we did not observe any signature of magnetic ordering in our samples (measurements not shown). We grew multiple samples of varied thicknesses of 0.5 - 1.5 MLs and measured their magnetic properties via SQUID magnetometry and magneto-optic Kerr effect (MOKE). There was no observation of ferromagnetism in the samples we grew on GaAs. We recognize that many factors may contribute to not observing ferromagnetic ordering including, a small magnetic moment for which the theoretical value is 0.7 μ_B/formula unit, the magnetic domain nucleation which may potentially cancel off

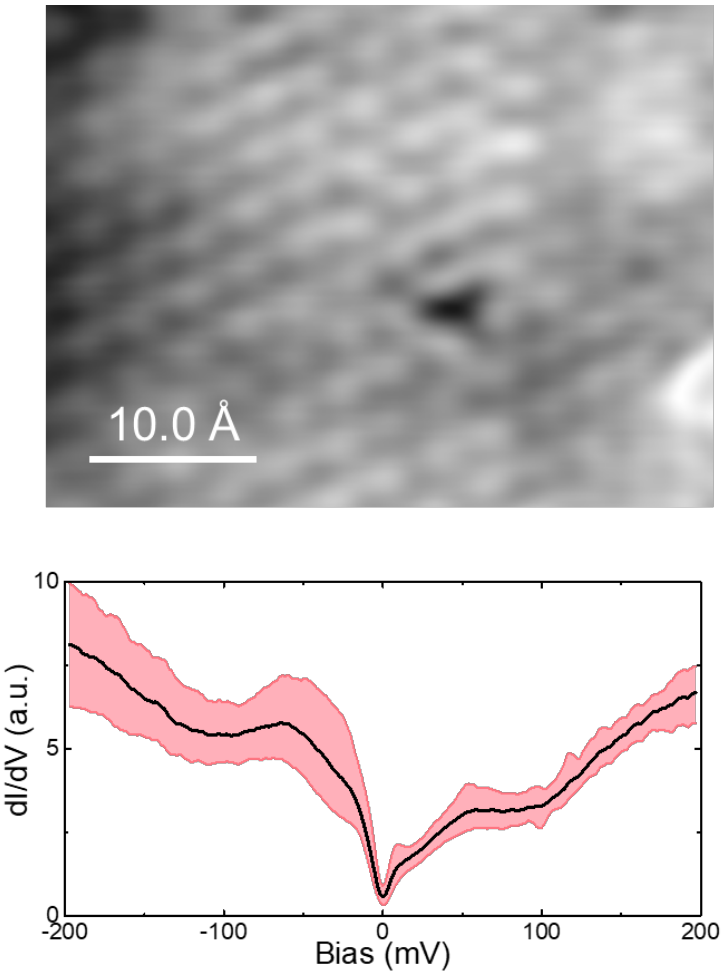


Figure 7.4: STM and dI/dV spectroscopy measurements of VSe_2 on GaAs showing metallic structure.

the ferromagnetism, and the film coverage which may be low and not measurable in bulk magnetization measurements.

7.5 Growth of VSe_2 on HOPG surfaces

To develop an understanding of why we see no ferromagnetism in our VSe_2 films grown on GaAs(111), we revert back to studying growth on highly-oriented pyrolytic graphite (HOPG) substrates per the Bonilla, *et al*. report [106]. A reason why we may not be observing magnetism is that the morphology of the VSe_2 monolayer may have many small grains that could possibly create a non-magnetic layer upon growth from scattering. This is very challenging to study on commercial GaAs(111) wafers due to the surface roughness of the substrate. HOPG surfaces are inert, clean upon cleavage and have very large terrace widths which makes it preferable to study nucleation of MBE-grown epilayers.

Following recent reports of MBE-grown transition metal dichalcogenides (TMDCs) run into many device challenges due to their small grain size (<200 nm) compared to CVD-grown TMDCs [169, 170, 171, 172, 173, 192]. Most of the reports show films with almost full coverage consisting of small grains, indicating high density of nucleation and grain boundary formation within the film. In [259], they were able to show a complex competition between kinetic factors including adsorption, desorption, on-substrate diffusion, and edge diffusion, which all have a significant influence on grain size. They specifically learned from growing WSe_2, that lowering the transition metal (TM) flux in conjunction with an elevated substrate temperature reduces the nucleation density while providing a Se-rich environment promotes a 2D growth mode [259]. With this knowledge for WSe_2 layers, we will use it to

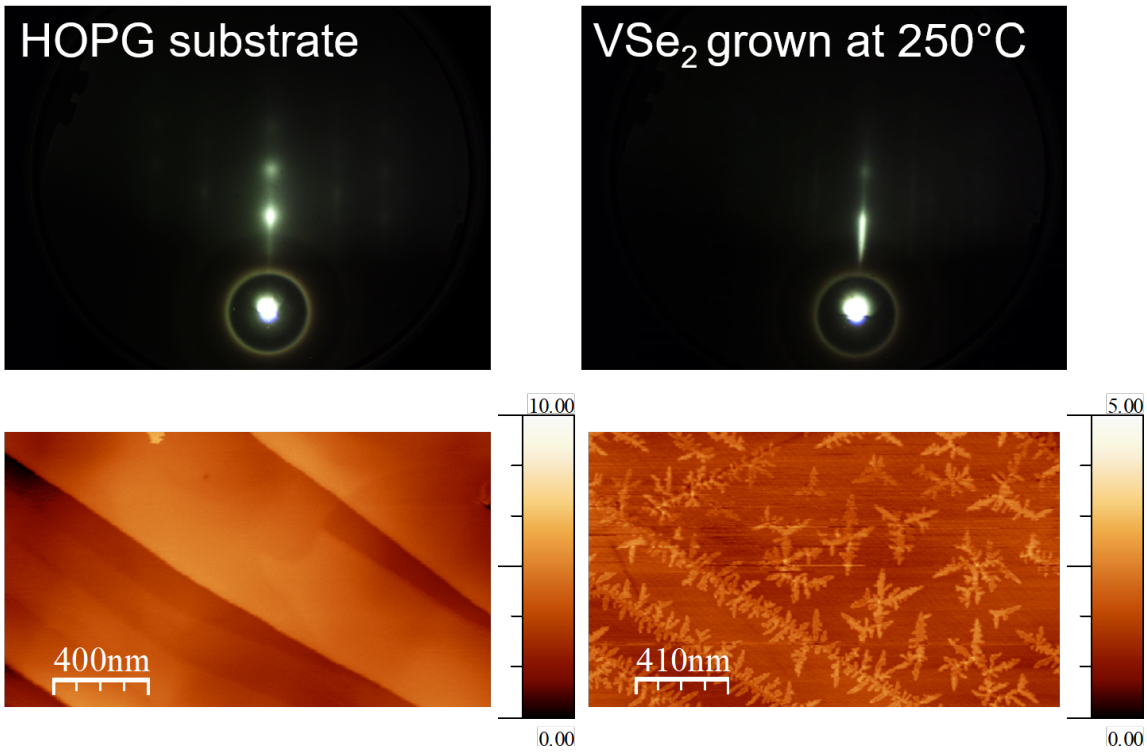


Figure 7.5: RHEED and AFM images of HOPG substrate and VSe_2 grown on HOPG at 250°C showing streaky patterns and flat dendrite sub-monolayer coverage. Height scale is in nm.

study the nucleation for another TMDC, VSe_2.

Few-layer VSe_2 films are prepared via van der Waals epitaxy in a Veeco GEN930 chamber with a base pressure of 2×10^{-10} Torr. HOPG substrates (ZYA Grade from SPI, 10 mm × 10 mm × 1 mm) are prepared by cleaving the top layers with scotch tape until a clean, smooth surface is exposed. The substrate is then loaded into the MBE chamber and annealed at 600°C for 12 hours to remove any surface adsorbates. Elemental vanadium (V) (99.98%, ESPI Metals USA) is evaporated from a four-pocket MANTIS quad *electron*-beam source and atomic Se (99.9999%, United Mineral & Chemical Corporation) is deposited from a valved cracking source operated at 950°C (bulk zone, 290°C). The growth is performed

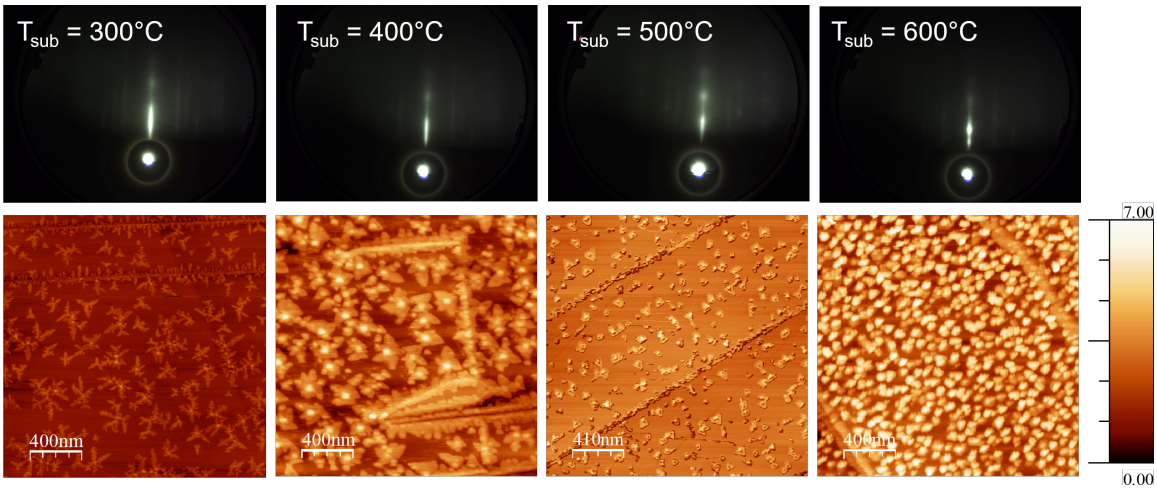


Figure 7.6: RHEED and AFM images showcasing change in grain growth of VSe_2 overlayers on HOPG. From left to right: 300°C, 400°C, 500°C, and 600°C growth. Height scale is in nm.

under an adsorption-limited regime (e.g. Se overpressure) to develop compositional VSe_2 films due to the re-evaporation of the Se species. The beam flux is typically performed at ∼1000 for a Se:V beam equivalent pressure (BEP) ratio. Beam fluxes are measured using a nude ion gauge positioned for growth and the corresponding deposition rate is calibrated based on nominal film thicknesses via *ex situ* x-ray reflectometry (XRR), and reflection high energy electron diffraction (RHEED) imaging during growth. Film morphology is studied using a combination of RHEED patterns and atomic force microscopy (AFM) (Bruker Icon 3).

Pursuit of a VSe_2 monolayer with large grains began with an investigation of nucleation and morphology as a function of growth temperature on HOPG. 1T-VSe_2 is the preferred thermodynamic phase when grown by co-deposition MBE techniques [106, 267]. Figure 7.5 shows both RHEED and AFM images of the HOPG substrate and a smooth VSe_2 monolayer grown at 250°C at a fixed BEP ratio. At substrate temperatures below ∼200°C,

the RHEED pattern during VSe_2 growth dims out indicating a disordered, amorphous growth mode likely due to the larger sticking coefficient of Se adatoms at lower temperatures. The VSe_2 RHEED pattern is streaky with irregularly spaced streaks denoting in-plane disorder which matches the underlying HOPG substrate. This invariance occurs because the HOPG substrate is not single crystalline, but rather has a textured, (0001) out-of-plane orientation and the grains have random in-plane orientations [268]. Thus, the RHEED images of the HOPG and the VSe_2 overlayer are a superposition of all azimuthal angles. Due to this circumstance, the epitaxial relationship between VSe_2 and the HOPG substrate cannot be determined. While the RHEED patterns are streaky in this thickness limit resulting in a smooth film, it does not give useful information on the domain width or structure. The corresponding AFM image shows that the terrace step edges of the HOPG substrate are preferred nucleation sites for VSe_2 growth and also indicates that the overlayer prefers to grow into random structures with branches. This preferential growth structure with high nucleation density at a low substrate temperature indicates a close relationship between the adatom density and stable nuclei formation [259, 269] which we will study further as a function of growth temperature.

The chalcogen sticking coefficient is much lower than that of the transition metal due to the short mean lifetime and mean free path of Se adatoms [259]. Since desorption is negligible at low growth temperatures, most the chalcogen adatoms are able to form stable domains that exceed a critical nucleus size [259]. However, the desorption rate increases exponentially at elevated substrate temperatures from being close to the evaporation temperature of Se, which is an Arrhenius-related process [64]. More adatoms desorb from the

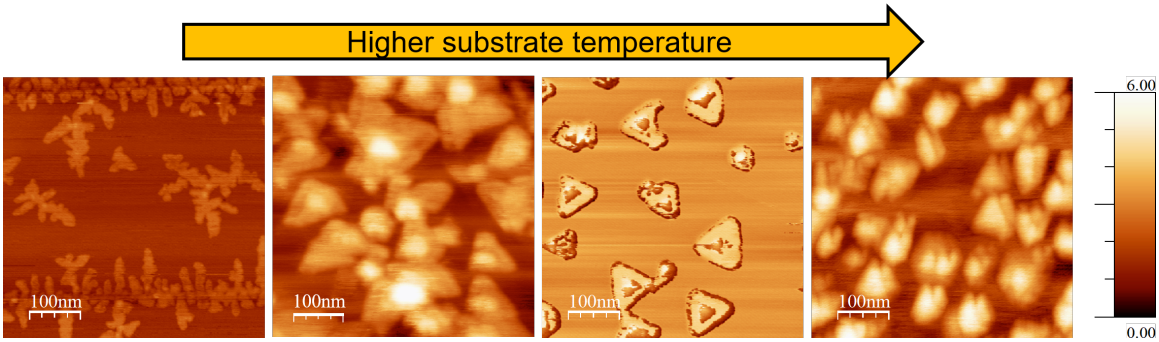


Figure 7.7: Zoomed in AFM images showcasing change in grain growth of VSe_2 overlayers on HOPG. From left to right: 300°C, 400°C, 500°C, and 600°C growth. Height scale is in nm.

surface at these elevated temperatures before forming stable nuclei, reducing the overall adatom density and sticking coefficient, as mentioned earlier. RHEED and corresponding AFM images in Figure 7.6 show the growth of VSe_2 on HOPG as a function of substrate temperature. Lower coverage and island growth are observed for elevated temperatures above 500°C while lower temperatures show larger coverage with smoother layers. The RHEED patterns show a trend that is directly related to the morphology displayed. Streaky patterns are observed at lower temperatures (< 500°C), indicating good short-range ordering and atomic-scale smoothness, while at elevated temperatures the RHEED shows spotty patterns, which is characteristic of island growth processes. The RHEED patterns at all growth temperatures do not change with azimuthal rotation due to the underlying HOPG substrate, as mentioned earlier.

The corresponding AFM images in 7.6 are consisitent with the RHEED patterns shown but also show more features of the domain size and width. Compact domains with triangular shape are observed under conditions of high desorption rate (achieved via low V flux with an elevated substrate temperature of $T_{sub} = 500$°C), while discontinuous domains

are observed when the desorption rate is decreased is decreased (Figure 7.6, $T_{sub} < 500°C$). At growth temperatures above 500°C, there is not enough Se supply leading to columnar structures and metal clusters which strongly influence the nucleation. The randomly dendrite-type branched, highly discontinuous domains are referred to as fractals [259, 269]. This fractal-to-compact transition is the result of the competition between adatom attachment and edge diffusion processes [259]. The latter being responsible for the relaxation of the domain from the initial shape (often random and branching) to the thermodynamically favorable configuration (compact triangle) [259, 269]. Compact, triangular domains are produced close to the adsorption-desorption equilibrium, in which the growth rate and sticking coefficient are relatively low. The fractal structure may be undesirable since defects could be created along the rough edges as domains grow [259, 269], which may give rise to a non-magnetic layer.

In the zoomed-in AFM images in Figure 7.7, the fractal-to-compact to island transition can be clearly seen as we increase substrate temperature. For the compact triangular domain samples grown at $T_{sub} = 500°C$, the surface coverage is relatively low in the monolayer limit due to the low adatom density of the chalcogen atoms. Thicker layers seem to prefer to grow on top of the compact triangles as one can see in the AFM image. At the edges of some of the compact triangles, some further nucleation is observed. This transition may be associated with the expanded domains which capture more chalcogen adatoms, breaking the equilibrium between attachment and edge diffusion leading to a possible fractal structure [259].

Due to the low lateral monolayer coverage of the compact triangular domain growth

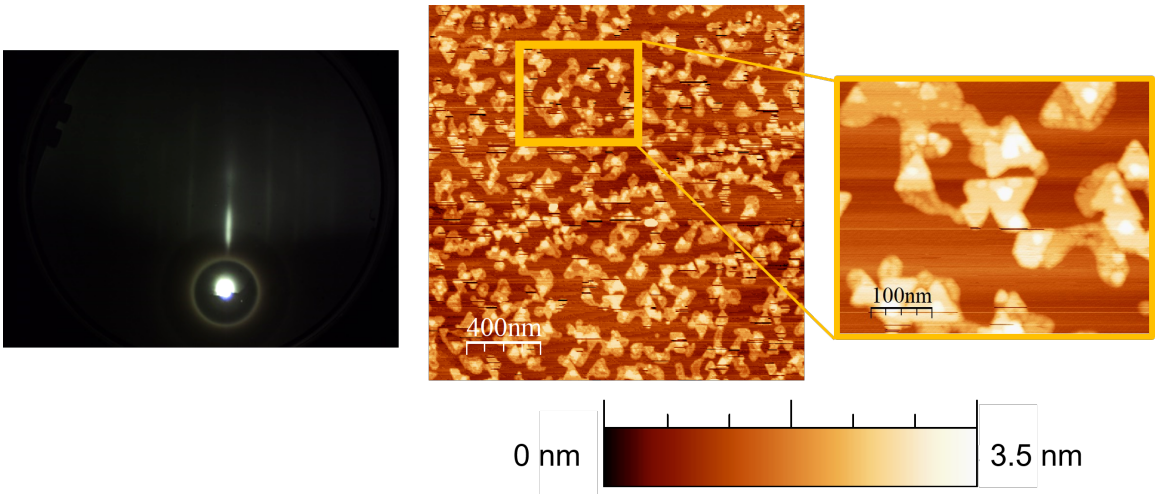


Figure 7.8: RHEED and corresponding AFM images of VSe_2 post annealing on HOPG.

using a T_{sub} of 500°C, practical applications in need of wafer-scale films will not be feasible. Combining both the lower temperature fractal larger area growth with higher temperature compact domain growth will be an ideal way to alleviate this issue. To do so, we grew few-layered VSe_2 films at 300°C and post annealed at 500°C under no flux for 30 minutes in order to attempt to promote lateral growth. What we observe are some interesting features, which include both compact triangular domains, expanded branches connecting the compact domains and regions exposing the underlying HOPG substrate (Figure 7.8). While larger larger coverage is observed, the lack of homogeneity and lateral coalescence throught the film still leaves a concern. This will need to be further investigated by studying the post annealing process under a Se flux to initiate more chalcogen adatom mobility giving potential rise for more lateral continuity in the film.

It is also important to see if ferromagnetism exists in these compact domain films, which were reported in previous work [106]. For this study, we mechanically exfoliate the

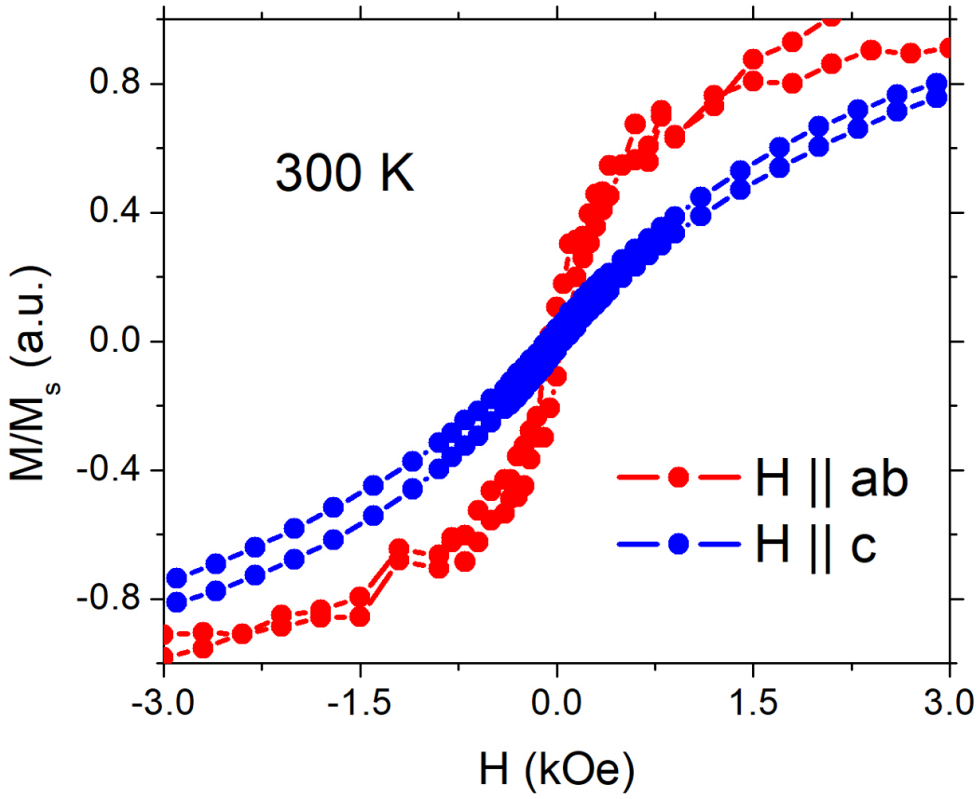


Figure 7.9: Room temperature SQUID measurement on ∼1 ML VSe_2 grown on HOPG at T_{sub} = 500°C showing easy plane magnetization.

top layer of the T_{sub} = 500°C sample with kapton tape and encapsulate it with more tape to protect it from damage prior to loading inside the magnetometer. The sample is measured in both in-plane and out-of-plane orientations at room temperature using SQUID magnetometry. Our observations, shown in Figure 7.9, show a preferred magnetization pointing into the sample plane as previously reported in [106]. This leads us to believe that the VSe_2 grain nucleation is extremely important into realizing ferromagnetism in these materials and may be very difficult to study on other substrates that have smaller terrace

widths.

The results of this nucleation and growth study indicate that to limit the nucleation density and promote 2D layered growth, it is necessary to have an elevated substrate temperature with an Se-rich environment. This is important, while having the transition metal flux low, to suppress the formation of V-rich nuclei, which in turn suppresses vertical growth and promotes 2D growth. It should be noted that this has only been studied in WSe_2 films grown by MBE and needs to be studied on other TMDC materials grown by MBE and other thin film deposition techniques. By using the strategies used in [259], we developed a way to grow large-domain VSe_2 films which is crucial for both device applications and realizing magnetism in these materials which will lay a foundation for future studies of other 2D TMDCs that may hold magnetic ordering. We have achieved monolayer compact domains with a width of ∼100-120 nm, which is a drastic improvement from the discontinuous, branch-like domains formed at lower temperatures.

7.6 Conclusions

In this Chapter, we have demonstrated that high quality VSe_2 can be grown on both van der Waals and 3D substrates via van der Waals epitaxy. Despite the large lattice mismatch with the substrate, the grown VSe_2 films have no misfit dislocations or epitaxial strain and are rotationally aligned to the GaAs(111) and HOPG substrates. Due to the lack of ferromagnetism observed in samples grown on GaAs substrates, we studied the growth nucleation and domain formation on HOPG substrates and learned that the substrate temperature is extremely critical in obtaining a 2D growth mode. Growing in an

Se-rich environment and at an elevated substrate temperature (while keeping the V flux fixed), enables compact domain growth of triangular structures and growing at low temperatures enables growth of discontinuous branch-like structures. The knowledge gained from this study provides a road map into realizing interesting phenomena in TMDC structures grown by MBE.

Chapter 8

Suppression of Magnetic Ordering in Fe-Deficient $Fe_3 - xGeTe_2$ from Application of Pressure

8.1 Abstract

Two-dimensional (2D) van der Waals magnets with multiple functionalities are becoming increasingly important for future technologies in spintronics and valleytronics. Application of external pressure is desired to explore interesting phenomena such as the underlying physical mechanisms of the intrinsic magnetism. In this work, the magnetic, electronic, and structural properties of van der Waals-layered, Fe-deficient $Fe_{3-x}GeTe_2$ is systematically investigated by application of high pressure. Magnetotransport measurements show a suppression of Curie temperature (T_c) with an increasing pressure up to 19.4

GPa. The electrical resistance of $Fe_{3-x}GeTe_2$ shows a change from a metallic ($dR/dT > 0$) to a less metallic ($dR/dT < 0$) phase, while the transverse magnetoresistance (MR) is negative with an increase in magnitude (below T_c) with pressure. High-pressure x-ray diffraction (HP-XRD) shows no structural phase change in the hexagonal crystal for pressures up to 29.4 GPa but a clear compression of the unit cell parameters. The decrease in the T_c is due to the lattice shrinkage from pressurization which leads to a weakening of the exchange interaction, while the increase in MR may be related to shrinkage of the van der Waals gap leading to a stronger interlayer coupling. These results indicate that the application of pressure can complement other external stimuli such as chemical doping and strain when manipulating the material properties of van der Waals magnets which are of high interest for next-generation spintronic technologies.

8.2 Introduction

Recent studies showing intrinsic ferromagnetism in the monolayer limit of van der Waals (vdW) materials has opened many opportunities to study two-dimensional (2D) magnetism and other scientific explorations [90, 93]. Fascinating properties such as layer dependence, gate-tunable magnetism and giant magnetoresistances in tunneling junctions consisting of mechanically exfoliated CrI_3 [97, 98, 100], and room temperature ferromagnetic ordering in large-area films of monolayer $MnSe_2$ [107, 258] and VSe_2 [106] grown by molecular beam epitaxy have been reported showing the potential integration for spin-based technological applications. Among the recently studied 2D magnets, $Fe_{3-x}GeTe_2$ is of interest due to its high Curie temperature, T_c, strong perpendicular magnetic anisotropy,

competing magnetic phases, and tunable magnetic properties depending on the concentration of Fe and its thickness [102, 104, 270, 271, 272, 273, 274, 275, 276, 277, 278].

Since many chalcogen-based materials (consisting of S, Se, and Te) can be exfoliated down to single atomic sheets, there is interest in developing a better understanding of the complexity of the bulk parent compound. This is of interest due to the possibilities of creating more structurally and magnetically stable 2D materials. To develop a better insight of their bulk counterparts, studies under varied environmental conditions will give a firmer foundation for going toward the 2D limit of these compounds.

Application of pressure offers a unique way of modifying the relative strengths of the exchange interactions by altering the respective interatomic separations of the crystal [279, 280, 281, 282]. A recent example showing a pressure-induced spin-reorientation transition in vdW $Cr_2Ge_2Te_6$, shows that due to their weak vdW coupling between layers, pressure may cause drastic magnetic and structural transitions [283, 284]. In this Letter, we demonstrate that the crystal structure, electronic properties and magnetic properties can be drastically manipulated by applying high pressure. In particular, we find that the intrinsic magnetoresistance can dramatically change by increasing the pressure within our measured range, which is due to both shrinking of the $Fe_{3-x}GeTe_2$ lattice and suppression of the magnetic moment leading to a decrease in T_c. This work indicates that pressure provides an effective approach to reliably control the magnetic properties in vdW ferromagnets and it offers a new route for exploring exotic properties of the 3D counterparts of 2D vdW materials.

8.3 Methods

Crystals of Fe-deficient $Fe_{2.75}GeTe_2$ were grown from a Te flux according to a modified literature procedure [285]. 80.4 mg Fe granules (2 eq., 99.98%, Alfa Aesar), 52.3 mg Ge powder (1 eq., 99.999%, Alfa Aesar), and 367.4 mg Te lumps (4 eq., 99.999%, Alfa Aesar) were heated in an alumina crucible in an evacuated quartz ampoule to 950°C, kept there for 12 hrs., cooled to 875°C at a rate of 60°C/hr. and to 675°C at a rate of 3°C/hr. The mixture was quenched to air and the hot flux removed by centrifugation, yielding metallic crystals of several mm edge length. Sample composition is confirmed via Rutherford back scattering (RBS) measurements.

Lattice parameters of the samples in ambient conditions were determined using standard x-ray diffraction (XRD) measurements (Bruker, D8 Discover) with a Cu K-α source ($\lambda = 1.54$ Å). Pressure-dependent XRD scans were performed at sector 16-BMD of the Advanced Photon Source (APS) at Argonne National Laboratory using a 30 keV x-ray source ($\lambda = 0.4133$ Å). Samples were powdered and loaded into a gas-driven-membrane diamond anvil cell (DAC) with a rhenium gasket and neon gas as the pressure-transmitting medium. The pressure is determined via gold powder mixed with the sample and confirmed with ruby spectroscopy at select pressures [142, 286]. The XRD patterns are collected by an area detector and converted into powder patterns using DIOPTAS [148]. A CeO_2 calibration crystal was used to determine the instrument parameters for refinements via GSAS-II [151, 152]. All measurements were performed at room temperature at a pressure range between 0.7 and 29.4 GPa.

Bulk magnetization measurements are employed by a 5 T SQUID magnetometer

(Quantum Design). For pressure measurements inside the magnetometer, the sample is mounted inside a high-pressure cell module (Almax easyLab Mcell 10) that is part of a Cu-Be attachment mounted to a DC SQUID rod. Prior to pressurization, the sample is immersed in a pressure-transmitting medium of Daphne mineral oil. Pressure is applied to the sample through the transmitting medium by exerting a force on a series of tungsten carbide pistons via a mechanical press (Mpress Mk2) and the pressure is determined from the superconducting transition temperature of a Sn manometer that is inside the pressure cell next to the sample. The magnetization measurements are performed from 5 to 350 K with the sample in an out-of-plane orientation with respect to the external magnetic field of the SQUID. The maximum pressure range for this experiment is from 0 to 1 GPa.

Electrical and magneto-transport measurements are performed in a 16 T physical property measurement system (PPMS) (Quantum Design) using the AC transport option. High-pressure transport is performed on a crystalline sample using an eight-probe *designer* DAC [138] with steatite as the pressure-transmitting medium and ruby as the pressure calibrant. Samples in this study are pressurized up to 19.4 GPa.

8.4 Results and Discussion

Fe-deficient $Fe_{2.75}GeTe_2$ is a weak itinerant ferromagnet that crystallizes into a hexagonal structure with a space group of $P6_3/mmc$ as projected in Figure 8.1a. The crystal consists of layered Fe_3Ge slabs sandwiched between two van der Waals-bonded Te layers. Ambient pressure XRD measurements (Figure 8.1b) are indexed and obtain lattice parameters of $a = 3.95553$ Å and $c = 16.38871$ Å, which are very close to previous reports (a

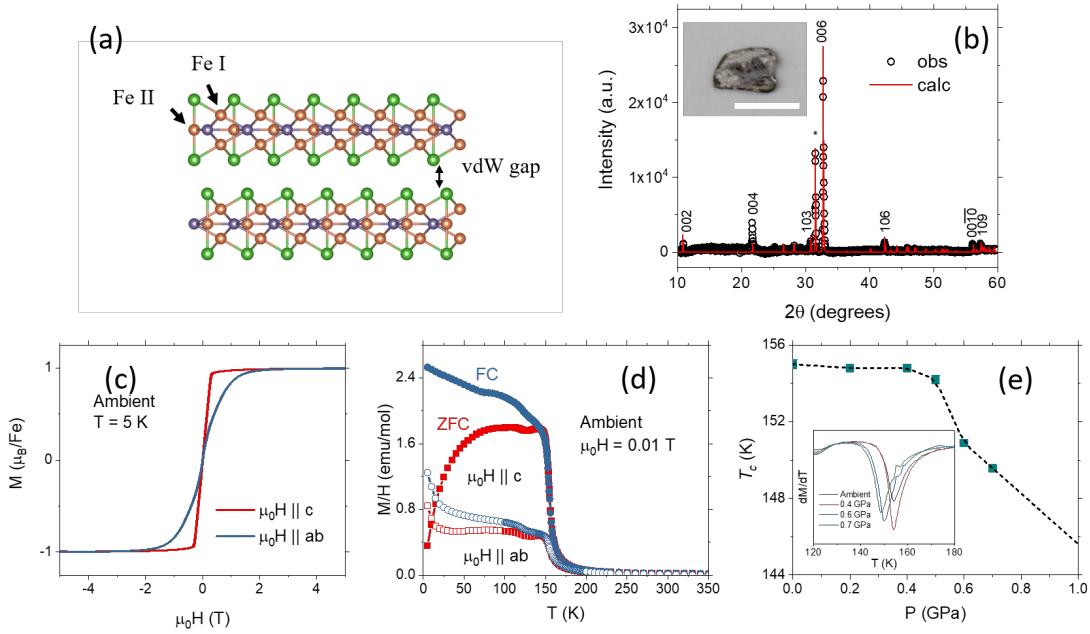


Figure 8.1: Structural and magnetic properties of $Fe_{2.75}GeTe_2$ at ambient and low hydrostatic pressures. (a) Ball-and-stick model of $Fe_{3-x}GeTe_2$, (b) ambient pressure XRD (inset shows laboratory photograph of crystal, scale bar is 5 mm) and star labeled peaks are the $FeTe_2$ impurities. (c) Ambient bulk M(H) loops showing easy axis anisotropy at 5 K, (d) M(T) showing a T_c at ∼150 K and (e) M(T) hydrostatic pressure measurements showing small decrease in T_c.

= 3.95001(7) Å and c = 16.4019(4) Å at 200 K [285]). Our samples contain an Fe-deficient phase of non-magnetic $FeTe_2$ (orthorhombic, $Pnnm$) impurities which is considered for the XRD refinement analysis but excluded from paper. Figures 8.1c-d shows the magnetic properties at ambient pressures, showing a preferred out-of-plane magnetization along the c axis of the crystal and a T_c of ∼150 K. Under hydrostatic pressure from 0 to 1 GPa, bulk magnetization measurements as a function of temperature show a slight decrease in its T_c. Figure 8.1e presents the results of the zero-field-cooled (ZFC) magnetization, M(T), measured with an external magnetic field of 0.01 T as a function of pressure. With increasing external pressure, the paramagnetic to ferromagnetic phase transition temperature decreases to ∼145 K. This transition temperature is determined via differentiation of the M(T) curves, dM/dT, shown in the inset of Figure 8.1e. The variation of the T_c is likely due to the sensitivity of the magnetic exchange interactions in relation to the deformation of the lattice structure of $Fe_{2.75}GeTe_2$. In order to develop a further understanding of how the compression of the crystal affects the magnetic properties we move to apply higher pressures using a DAC.

Based on previous chemical doping studies of $Fe_{3-x}GeTe_2$ crystals, the T_c is directly related to the amount of Fe vacancies which distort the lattice [285]. With less Fe vacancies, the lattice expands along the a axis but contracts along the c axis leading to an increase in the T_c to 220 K, close to room temperature. While this work is used as a guide, the application of hydrostatic pressure is expected to shrink both crystal axes, for which it will affect the ordering temperature differently. Figure 8.2a displays the refinement of the high-pressure XRD at 0.8 GPa denoting the $Fe_{2.75}GeTe_2$, $FeTe_2$, Au pressure

marker, and Re gasket phases. All $Fe_{2.75}GeTe_2$ diffraction peaks are well indexed with the hexagonal $P6_3/mmc$ structure and gradually shift to a higher angle with increasing pressure, indicating a smaller unit cell. There are a few low intensity, unidentifiable peaks at higher pressures in consistent positions which were excluded from the refinement. Lattice contraction at higher pressures up to 29.4 GPa is shown in the XRD patterns in Figure 8.2b. This shows no obvious sign of a structural phase transition and can be well described by the Rose-Vinet equation of state (EOS) [144] with $B = 52$ GPa and $B = 5.77$ [144] (Figure 8.2f) which is close to other van der Waals crystals under high pressure [287]. Figures 8.2c-e show the refined lattice constants a, and c, and the c/a ratio further confirming compression of the unit cell. It is found that the reduction of the c-axis is relatively more significant than that of the a-axis due to the weak interlayer vdW interaction. There are no signs of significant disruption in the lattice from these curves but there is a small anomaly in the pressure range from 9.3 to 18.4 GPa, which may be due to the solidification of neon gas at 9.3 GPa ($2\theta = 18.8°$) that persists until 18.4 GPa ($2\theta = 19.9°$) when it merges with another sample peak. Nevertheless, the XRD confirms that the hexagonal crystal structure of $Fe_{2.75}GeTe_2$ persists up to the highest measured pressures near 30 GPa.

To develop an understanding on how the structural compression effects the materials electronic and magnetic properties at high pressures, we performed longitudinal and transverse resistance (R_{xx} and R_{xy}) measurements at selected pressures with and without applied magnetic fields. Figure 8.3a displays a schematic of a *designer* DAC which permits these measurements and allows us to perform a novel, high-pressure electrical- and magneto-transport study. Temperature-dependent longitudinal resistance, $R_{xx}(T)$, as a function of

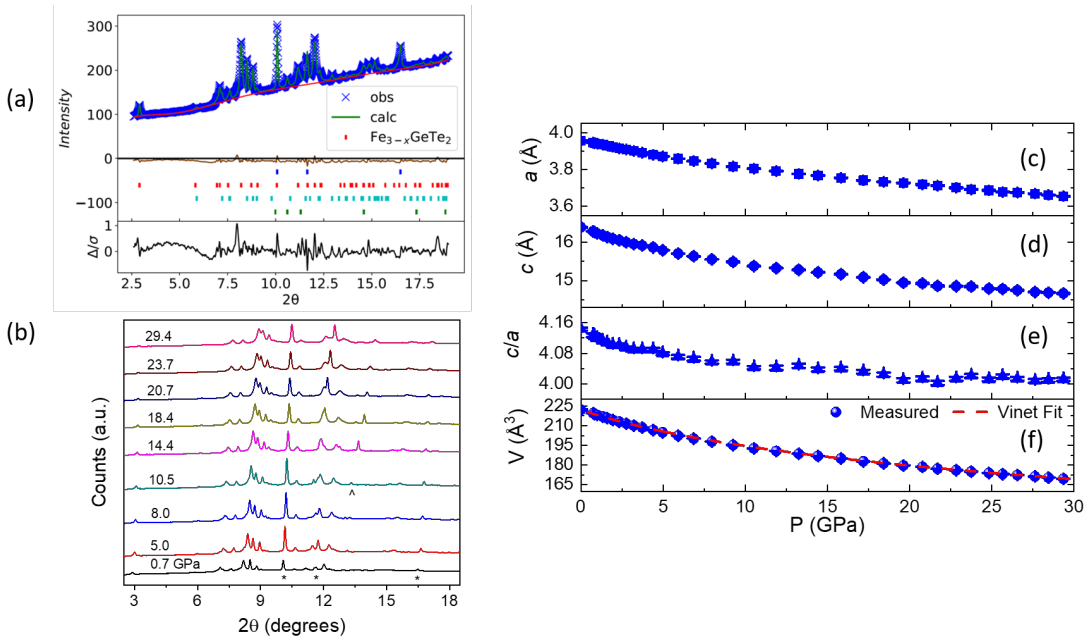


Figure 8.2: High pressure XRD measurements on $Fe_{2.75}GeTe_2$. (a) Rietveld refinement of powdered sample at 0.7 GPa, blue, red, teal, and green tick marks refer to Au, $Fe_{2.75}GeTe_2$, $FeTe_2$, and Rh gasket peaks, respectively. (b) XRD spectra at select pressures showing increase in angle which corresponds to shrinking of lattice. (c-f) Lattice parameters and cell volume as a function of pressure with Rose-Vinet EOS fitting well to the curve.

pressure with no applied field is shown in Figure 8.3b and is normalized to the room temperature resistance value for comparison. The electronic properties change as a function of applied pressure, from a metallic state at ambient pressure to a less metallic state with increasing pressure up to 16.2 GPa. In a concurrent report on Fe-rich Fe_3GeTe_2 (bulk T_c = 220 K), researchers denoted a kink in the ρ_{xx}(T) curve which represents the transition from a ferromagnetic phase to a non-magnetic phase after taking a derivative, dρ_{xx}/dT, where this becomes indistinguishable at pressures above 13.4 GPa (T_c = 120 K) [288]. In our work, we observe similar broadening of the derivative of the R_{xx}(T) curve in pressures above 4.1 GPa (shown in Figure 8.3c), which makes it challenging to determine the T_c from this method. The reason why we are seeing broadening at lower pressures is due to the lower starting T_c from Fe vacancies. Other methods include taking the intercept between the two different slopes on the R_{xx}(T) curve or marking a middle point of the d(ρ, R)$_{xx}$/dT broad peak (or kink) which corresponds to the transition temperature [289]. It is clear from our case that while we increase pressure, the transition temperature has a decreasing trend according to the mentioned methods but difficult to determine an actual numerical value for T_c.

To quantify T_c as a function of pressure, we continue our investigation by studying the transverse magnetoresistance (MR) as a function of applied magnetic field (Rxx(H) and R_{xy}(H)). Figure 8.4 presents both the symmetric (R_{xx}) and antisymmetric components (R_{xy}) of the MR curves at select temperatures as a function of pressure. The R_{xx}(H) data has been normalized by calculating the MR (%) given in the equation below

$$MR(\%) = \frac{\Delta R}{R} = \frac{R - R_0}{R_0} \tag{8.1}$$

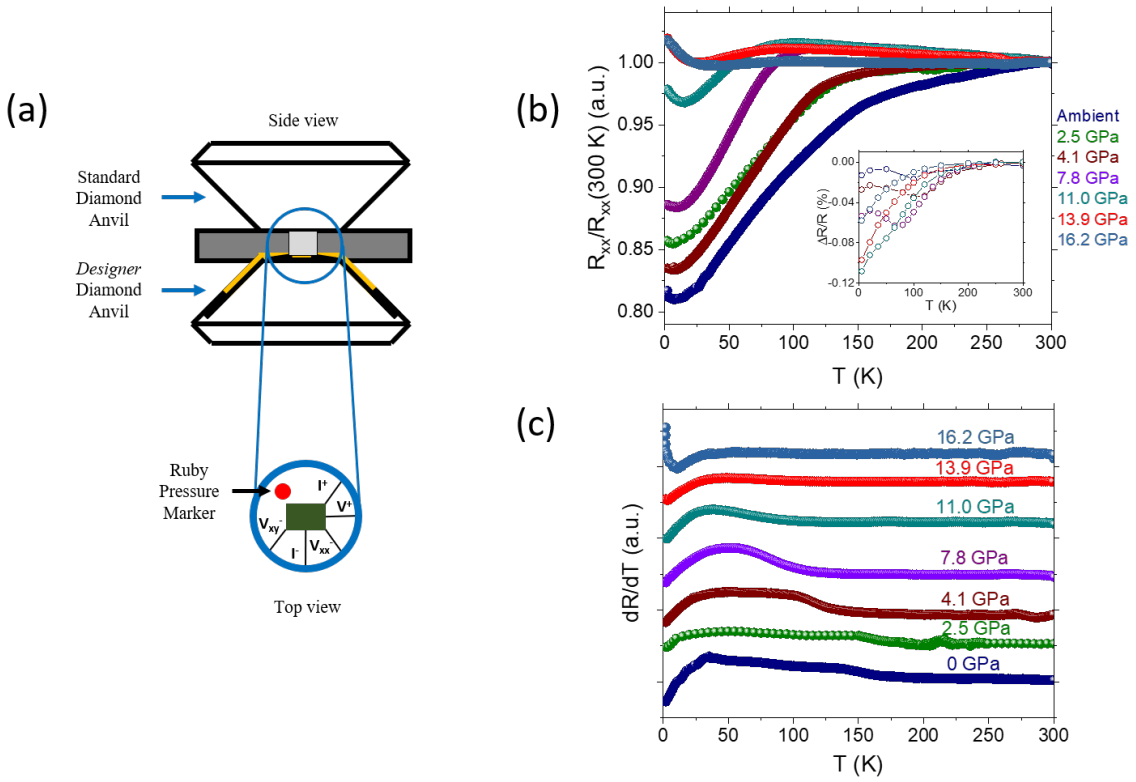


Figure 8.3: High pressure electrical transport measurements on $Fe_{2.75}GeTe_2$. (a) Schematic of *designer* DAC showing how sample is loaded and wired up for measurement. (b) Temperature-dependent resistance as a function of pressure showing transition from metallic to less metallic state at higher pressure and (c) differentiation of resistance measurements showing transition of ordering temperature with higher pressures.

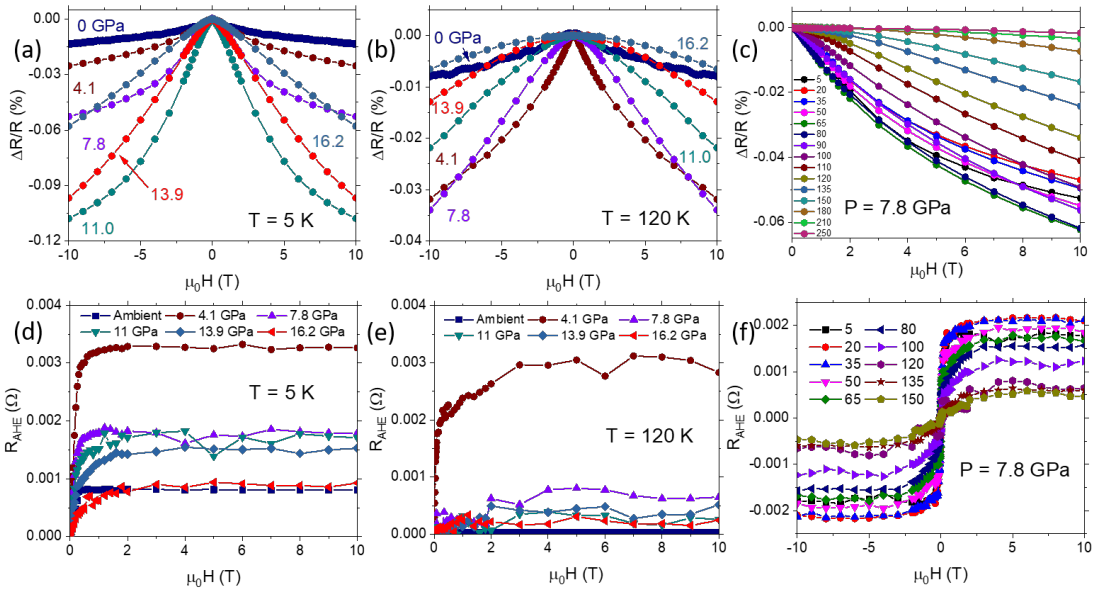


Figure 8.4: High pressure magnetotransport measurements on $Fe_{2.75}GeTe_2$. (a,b) Transverse MR measurements at select pressures showing T_c lowering with higher pressure and (c) transverse MR as a function of temperature at 7.8 GPa denoting quadratic-to-linear transition. (d,e) AHE measurements at select pressures showing decrease in saturation magnitude with pressure and (f) AHE as a function of temperature at 7.8 GPa.

where R is the resistance at a given magnetic field and R_0 is the resistance at zero field. The symmetric MR curves show interesting features such as negative MR, which is not common in normal metals [135] but has been observed in ferromagnetic materials [290, 291, 292], and an increase in magnitude of the MR up to 11 GPa and then a gradual decrease in magnitude at higher pressures. At higher fields, the MR also shows a quadratic-to-linear transition at higher pressures, where lower pressures have a quadratic dependence with applied field and higher pressures have a linear dependence (Figures 8.4a and 8.4b). This transition may be related to the transition temperature decreasing with increasing pressure and will need to be investigated further with temperature dependence.

Figure 8.4c displays a temperature-dependent MR curve at a pressure of 7.8 GPa

showing a quadratic-to-linear transition near what we expect the T_c to be from R_{xx}(T) measurements. Due to the broadening of the dR_{xx}/dT curve, we first roughly quantify the T_c by taking a linear fit of both the lower temperature regions and higher temperature regions of the R_{xx}(T) curve then identifying the intercept of those two linear fits as a T_c = 93 K. Second, we look at the temperature-dependent MR curve and further quantify the T_c as the temperature region where the curvature transitions from quadratic to linear which is ∼100 K. To quantify T_c value for pressure ranges 0 to 11 GPa, we will use a combination of both R(T) and MR curvature and will use the equation below

$$\Delta T_c = \frac{T_{c,R(T)} + T_{c,MR}}{2} \tag{8.2}$$

where ΔT_c is the averaged Curie temperature that is a combination of taking the intercept of the two slopes in R_{xx}(T) measurements ($T_{c,R(T)}$) and the quadratic-to-linear transition in the MR measurements ($T_{c,MR}$). In the case of 7.8 GPa, the magnetic ordering temperature of the $Fe_{2.75}GeTe_2$ is determined to be 96.5 K, a 54.5 K decrease from ambient pressure conditions. For pressures above 11 GPa, we will just use the quadratic-to-linear transition of the MR curve as the determining factor for the ordering temperature. A table below is given for each pressure step showing a drastic decrease in the T_c, using our equations.

It is clear that the pressurization has a drastic effect on the ferromagnetic transition temperature. A closer look at Figures 8.4a and 8.4b shows how the lowering of the T_c changes the shape and size of the MR curve. At 5 K, which is well below the transition temperature at ambient pressure, the magnitude of the MR increases from 1.3% to 10.8% as a function of increasing pressure until 11 GPa where the magnitude of the MR begins to decrease to 5.8% at 16.2 GPa. The initial increase in magnitude is likely due to a stronger

Pressure (GPa)	$T_{c,R(T)}$ (K)	$T_{c,MR}$ (K)	ΔT_c (K)	Quantified T_c (K)
0	145	150	147.5	147.5
2.5	132.3	n/a	n/a	132.3
4.1	121.6	135	128.3	128.3
7.8	93	100	96.5	96.5
11	78.7	72.5	75.6	75.6
13.9	n/a	50	n/a	50
16.2	n/a	35	n/a	35

Table 8.1: Determination of magnetic ordering temperature at select pressures.

interlayer exchange coupling while the van der Waals gap shrinks (as noted in the XRD data), converting the bulk $Fe_{2.75}GeTe_2$ from a quasi-2D to a quasi-3D structure. While the likelihood of Fe atoms from other unit layers possibly fill the vacancies in the crystal with pressurization, the decrease in T_c contradicts this since we would expect an increase in T_c with less Fe vacancies [285]. With increasing pressure up to 16.2 GPa, the magnitude of the MR decreases which is directly related to the T_c decreasing, meaning the sample is experiencing more thermal fluctuations at higher pressures. For higher temperatures near the T_c at ambient pressure (120 K), the curve shows a similar trend while also starting with a smaller MR (%) due to the metallic nature of the crystal. The magnitude of the MR increases up to 7.8 GPa but then decreases at higher pressures. This confirms the trend that when the unit cell shrinks initially the exchange coupling between layer units becomes stronger, giving rise to a larger MR, then when the T_c is closer to a given temperature, thermal fluctuations cause the MR to monotonically decrease. It is also important to note that once above T_c, the shape of the MR changes from a sharp, quadratic convex (below T_c) to a broad, linear concave (well above T_c) curvature which confirms our observations from before.

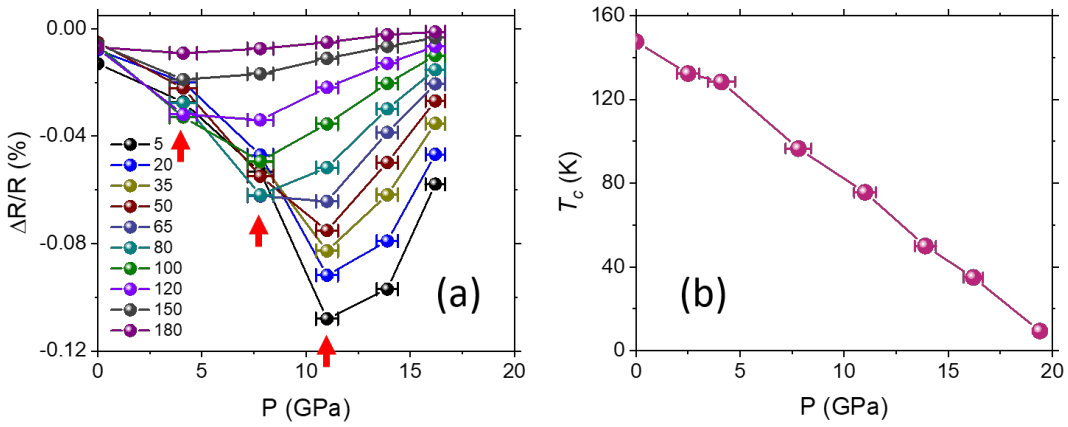


Figure 8.5: Transverse MR (%) as a function of pressure at select temperatures of $Fe_{2.75}GeTe_2$ showing transition temperature and T_c showing a monotonic decrease with increasing pressure

To confirm these observations further, we look at the antisymmetrized $R_{xy}(H)$ data. For ferromagnetic conductors, the ordinary Hall component (R_{xy}) has an additional non-linear ferromagnetic contribution to it typically noted as the anomalous Hall effect (AHE) [102, 293, 294]. To isolate the AHE contribution, we fit the slope over the field range where the R_{xy} appears to saturate which is from 0.5 T to 10 T. This linear component is then subtracted from the overall signal to yield the AHE component as shown in the equation here

$$R_{AHE} = R_{xy} - R_H H_z, \tag{8.3}$$

where R_{AHE} is the isolated AHE contribution to the signal, which is shown in Figures 8.4d-f as a function of applied magnetic field. Our observations show that with application of pressure, the overall saturation value of the R_{AHE} signal decreases with increase in pressure as observed in Wang, X., *et al.* [288], but the overall squareness does not remain due to the decrease in T_c and suppression of the Fe magnetic moment.

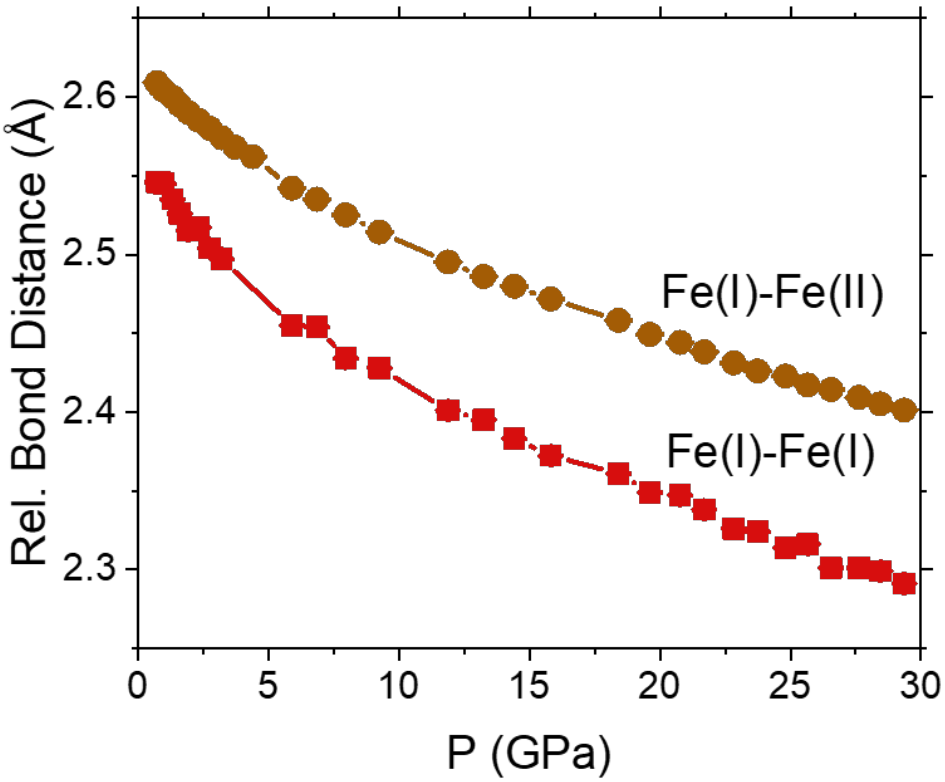


Figure 8.6: Relative bond distance of Fe(I) and Fe(II) atoms showing decrease with pressure.

Figure 8.5 displays our observations discussed earlier. The MR curves in Figure 8.5a show the change in MR (%) at 4.1 GPa from 150 K to higher temperatures where the T_c begins to decrease with increase in pressure and the Fe moment becomes more suppressed. There are also two other anomalies at 7.8 GPa for a temperature range of 80 to 120 K and 11 GPa for the temperatures less than 80 K which further indicates the T_c becomes more suppressed at higher pressure. This pressure-dependent reduction of the T_c is displayed in Figure 8.5b showing a linear monotonic decrease in the magnetic ordering temperature with increasing application of pressure. With pressures above 19.4 GPa, the magnetic moment of the Fe is completely suppressed, and we are not able to measure any magnetism in the sample. It is important to discuss why the ferromagnetic ordering is heavily suppressed by hydrostatic pressurization. One possibility is that due to the deficiency of Fe in the crystal, the pressurization can cause a disruption of the magnetic exchange by increasing the disorder in the system via manipulation of the interatomic distances. In [285], the reduced T_c correlates with the expansion of c, an increase in Fe(I)-Fe(I) bond distance, and a decrease in Fe(I)-Fe(II) bond distance. In our case, we see a reduction in c, and a decrease in both Fe(I)-Fe(I) and Fe(I)-Fe(II) (Figure 8.6) atomic distances with high pressure which gives rise to a reduced T_c. Since $Fe_{2.75}GeTe_2$ is an itinerant ferromagnet, we expect that the spins will become more delocalized with pressure. Unfortunately, we are not able to perform bulk magnetization measurements at high pressures in order to extract an effective magnetic moment to quantify the Rhodes-Wohlfarth ratio as a function of pressure [39, 295].

8.5 Conclusions

In summary, we have systematically studied the effect of hydrostatic pressure on Fe-deficient $Fe_{2.75}GeTe_2$. With the absence of applied pressure, it shows negative magnetoresistance, metallic behavior and strong easy axis anisotropy. Meanwhile, with application of high pressure, the T_c decreases from ∼150 K to nearly full suppression (∼10 K) at 19.4 GPa owing to the shrinking of the lattice and relative Fe-Fe bond distance. The electronic properties show a transition from a metallic to an insulating state with increasing pressure up to 19.4 GPa. Magnetoresistance measurements show an initial increase in magnitude with applied pressure owed to a stronger interlayer exchange interaction followed by a decrease in magnitude with the lowering of the ordering temperature. The demonstration of the suppression of T_c in $Fe_{2.75}GeTe_2$ shows that high pressure can probe regimes that cannot be achieved by other techniques such as chemical doping or strain and can also potentially be used to study underlying mechanisms of magnetic ordering in these systems.

Chapter 9

Conclusions

With these recent works demonstrating magnetism in 2D van der Waals materials and the subsequent tunability of these materials shows the possibility for future technological advances in spintronics and other fields. In this Dissertation, I have shown the (1) synthesis of 2D magnets by MBE, (2) detailed structural characterization of said materials (i.e. $MnSe_2$, VSe_2), (3) systematic magnetic characterization, and (4) pressure-dependent studies on the properties of their bulk counterparts. Bringing together wafer scale development, room temperature ferromagnetism, and large tunability can open up many realms of possibilities to make future magnetic tunnel junctions and spin filtering devices and for studying interesting phenomena in extreme conditions. There remains to be seen what may come of these materials, but their interest may surpass typical 3D magnets used in industry in the coming decades.

Bibliography

[1] J. M. D. Coey. *Magnetism and Magnetic Materials*. Cambridge University Press, Cambridge, 2010.

[2] Nicola A. Spaldin. *Magnetic Materials: Fundamentals and Applications*. Cambridge University Press, Cambridge, 2 edition, 2010.

[3] M. N. Baibich, J. M. Broto, A. Fert, F. Nguyen Van Dau, F. Petroff, P. Etienne, G. Creuzet, A. Friederich, and J. Chazelas. Giant magnetoresistance of (001)Fe/(001)Cr magnetic superlattices. *Physical Review Letters*, 61(21):2472–2475, 1988. PRL.

[4] G. Binasch, P. Grnberg, F. Saurenbach, and W. Zinn. Enhanced magnetoresistance in layered magnetic structures with antiferromagnetic interlayer exchange. *Physical Review B*, 39(7):4828–4830, 1989. PRB.

[5] M. Julliere. Tunneling between ferromagnetic films. *Physics Letters A*, 54(3):225–226, 1975.

[6] P. M. Tedrow and R. Meservey. Spin-dependent tunneling into ferromagnetic nickel. *Physical Review Letters*, 26(4):192–195, 1971. PRL.

[7] Stuart S. P. Parkin, Christian Kaiser, Alex Panchula, Philip M. Rice, Brian Hughes, Mahesh Samant, and See-Hun Yang. Giant tunnelling magnetoresistance at room temperature with MgO (100) tunnel barriers. *Nature Materials*, 3(12):862–867, 2004.

[8] Shinji Yuasa, Taro Nagahama, Akio Fukushima, Yoshishige Suzuki, and Koji Ando. Giant room-temperature magnetoresistance in single-crystal Fe/MgO/Fe magnetic tunnel junctions. *Nature Materials*, 3(12):868–871, 2004.

[9] Albert Fert. Nobel lecture: Origin, development, and future of spintronics. *Reviews of Modern Physics*, 80(4):1517–1530, 2008. RMP.

[10] S. S. P. Parkin, R. F. C. Farrow, T. A. Rabedeau, R. F. Marks, G. R. Harp, Q. Lam, C. Chappert, M. F. Toney, R. Savoy, and R. Geiss. Giant magnetoresistance in as-grown epitaxial films of phase-separated Co-Cu and Co-Ag. *Europhysics Letters (EPL)*, 22(6):455–462, 1993.

[11] Ricardo C. Sousa and I. Lucian Prejbeanu. Non-volatile magnetic random access memories (MRAM). *Comptes Rendus Physique*, 6(9):1013–1021, 2005.

[12] D. P. Arnold. Review of microscale magnetic power generation. *IEEE Transactions on Magnetics*, 43(11):3940–3951, 2007.

[13] Hans Christoph; Stohr, Jachim; Siegmann. *Magnetism, From Fundamentals to Nanoscale Dynamics*. Springer Series in Solid-State Sciences. Springer-Verlag Berlin Heidelberg, 2006.

[14] Y. Sui, L. Yue, R. Skomski, X. Z. Li, J. Zhou, and D. J. Sellmyer. CoPt hard magnetic nanoparticle films synthesized by high temperature chemical reduction. *Journal of Applied Physics*, 93(10):7571–7573, 2003.

[15] Donald O. Smith. Anisotropy in permalloy films. *Journal of Applied Physics*, 30(4):S264–S265, 1959.

[16] Zhiyong Wang, Chi Tang, Raymond Sachs, Yafis Barlas, and Jing Shi. Proximity-induced ferromagnetism in graphene revealed by the anomalous hall effect. *Physical Review Letters*, 114(1):016603, 2015. PRL.

[17] Simranjeet Singh, Jyoti Katoch, Tiancong Zhu, Keng-Yuan Meng, Tianyu Liu, Jack T. Brangham, Fengyuan Yang, Michael E. Flatt, and Roland K. Kawakami. Strong modulation of spin currents in bilayer graphene by static and fluctuating proximity exchange fields. *Physical Review Letters*, 118(18):187201, 2017. PRL.

[18] Z. Q. Qiu, J. Pearson, and S. D. Bader. Asymmetry of the spin reorientation transition in ultrathin Fe films and wedges grown on Ag(100). *Physical Review Letters*, 70(7):1006–1009, 1993. PRL.

[19] R. Sellmann, H. Fritzsche, H. Maletta, V. Leiner, and R. Siebrecht. Spin-reorientation transition and magnetic phase diagrams of thin epitaxial Au(111)/Co films with W and Au overlayers. *Physical Review B*, 64(5):054418, 2001. PRB.

[20] Z. Q. Qiu, J. Pearson, and S. D. Bader. Magnetic phase transition of ultrathin Fe films on Ag(111). *Physical Review Letters*, 67(12):1646–1649, 1991. PRL.

[21] Z. Q. Qiu, J. Pearson, and S. D. Bader. Two-dimensional ising transition of epitaxial Fe films grown on Ag(100). *Physical Review B*, 49(13):8797–8801, 1994. PRB.

[22] Hans-Joacim Elmers. Ferromagnetic monolayers. *International Journal of Modern Physics B*, 09(24):3115–3180, 1995.

[23] Ulrich Gradmann and Joachim Mller. Very thin (2200 å) ferromagnetic NiFe films. *Journal of Applied Physics*, 39(2):1379–1381, 1968.

[24] G. Lugert and G. Bayreuther. Evidence for perpendicular magnetic anisotropy in Fe(110) epitaxial films in the monolayer range on gold. *Thin Solid Films*, 175:311–316, 1989.

[25] D. P. Pappas, K. P. Kmper, and H. Hopster. Reversible transition between perpendicular and in-plane magnetization in ultrathin films. *Physical Review Letters*, 64(26):3179–3182, 1990. PRL.

[26] H. Fritzsche, J. Kohlhepp, H. J. Elmers, and U. Gradmann. Angular dependence of perpendicular magnetic surface anisotropy and the spin-reorientation transition. *Physical Review B*, 49(22):15665–15668, 1994. PRB.

[27] C. Chappert, K. Le Dang, P. Beauvillain, H. Hurdequint, and D. Renard. Ferromagnetic resonance studies of very thin cobalt films on a gold substrate. *Physical Review B*, 34(5):3192–3197, 1986. PRB.

[28] Myron Bander and D. L. Mills. Ferromagnetism of ultrathin films. *Physical Review B*, 38(16):12015–12018, 1988. PRB.

[29] P. Bdeker, A. Schreyer, Zabel, and H. Spin-density waves and reorientation effects in thin epitaxial Cr films covered with ferromagnetic and paramagnetic layers. *Physical Review B*, 59(14):9408–9431, 1999. PRB.

[30] M. E. Lines. Examples of two dimensional ordered magnetic systems. *Physics Letters A*, 24(11):591–592, 1967.

[31] M. E. Lines. Magnetism in two dimensions. *Journal of Applied Physics*, 40(3):1352–1358, 1969.

[32] Charles Kittel. *Introduction to solid state physics*, volume 8. Wiley New York, 1976.

[33] N. D. Mermin and H. Wagner. Absence of ferromagnetism or antiferromagnetism in one- or two-dimensional isotropic heisenberg models. *Physical Review Letters*, 17(22):1133–1136, 1966. PRL.

[34] Lars Onsager. Crystal statistics. i. a two-dimensional model with an order-disorder transition. *Phys. Rev.*, 65(3-4):117–149, 1944.

[35] W. P. Wolf. The ising model and real magnetic materials. *Brazilian Journal of Physics*, 30:794–810, 2000.

[36] Michael E. Fisher, Shang-keng Ma, and B. G. Nickel. Critical exponents for long-range interactions. *Physical Review Letters*, 29(14):917–920, 1972. PRL.

[37] J. Kohlhepp, H. J. Elmers, S. Cordes, and U. Gradmann. Power laws of magnetization in ferromagnetic monolayers and the two-dimensional ising model. *Physical Review B*, 45(21):12287–12291, 1992. PRB.

[38] Babar Shabbir, Muhammad Nadeem, Zhigao Dai, Michael S. Fuhrer, Qi-Kun Xue, Xiaolin Wang, and Qiaoliang Bao. Long range intrinsic ferromagnetism in two dimensional materials and dissipationless future technologies. *Applied Physics Reviews*, 5(4):041105, 2018.

[39] EP Wohlfarth. Magnetic properties of crystallineand amorphous alloys: A systematic discussion based on the rhodes-wohlfarth plot. *Journal of Magnetism and Magnetic Materials*, 7(1-4):113–120, 1978.

[40] M. Stampanoni, A. Vaterlaus, M. Aeschlimann, and F. Meier. Magnetism of epitaxial bcc iron on Ag(001) observed by spin-polarized photoemission. *Physical Review Letters*, 59(21):2483–2485, 1987. PRL.

[41] C. Rau. Ferromagnetic order and critical behavior at surfaces of ultrathin epitaxial films. *Applied Physics A*, 49(6):579–587, 1989.

[42] W. Drr, M. Taborelli, O. Paul, R. Germar, W. Gudat, D. Pescia, and M. Landolt. Magnetic phase transition in two-dimensional ultrathin Fe films on Au(100). *Physical Review Letters*, 62(2):206–209, 1989. PRL.

[43] M. Przybylski and U. Gradmann. Ferromagnetic order in a Fe(110) monolayer on W(110) by mossbauer spectroscopy. *Physical Review Letters*, 59(10):1152–1155, 1987. PRL.

[44] H. J. Elmers, J. Hauschild, H. Hche, U. Gradmann, H. Bethge, D. Heuer, and U. Khler. Submonolayer magnetism of Fe(110) on W(110): Finite width scaling of stripes and percolation between islands. *Physical Review Letters*, 73(6):898–901, 1994. PRL.

[45] H. J. Elmers, G. Liu, and U. Gradmann. Magnetometry of the ferromagnetic monolayer Fe(110) on W(110) coated with Ag. *Physical Review Letters*, 63(5):566–569, 1989. PRL.

[46] D. Kerkmann, D. Pescia, and R. Allenspach. Two-dimensional magnet at Curie temperature: Epitaxial layers of Co on Cu(100). *Physical Review Letters*, 68(5):686–689, 1992. PRL.

[47] P. Krams, F. Lauks, R. L. Stamps, B. Hillebrands, and G. Gntherodt. Magnetic anisotropies of ultrathin Co(001) films on Cu(001). *Physical Review Letters*, 69(25):3674–3677, 1992. PRL.

[48] J. A. C. Bland, R. D. Bateson, B. Heinrich, Z. Celinski, and H. J. Lauter. Spin polarised neutron reflection studies of ultrathin magnetic films. *Journal of Magnetism and Magnetic Materials*, 104-107:1909–1912, 1992.

[49] C. A. Ballentine, R. L. Fink, J. Araya-Pochet, and J. L. Erskine. Magnetic phase transition in a two-dimensional system: p(1x1)-Ni on Cu(111). *Physical Review B*, 41(4):2631–2634, 1990. PRB.

[50] C. A. Ballentine, R. L. Fink, J. Araya-Pochet, and J. L. Erskine. Exploring magnetic properties of ultrathin epitaxial magnetic structures using magneto-optical techniques. *Applied Physics A*, 49(5):459–466, 1989.

[51] R. Miranda, Felix Yndurin, D. Chandesris, J. Lecante, and Y. Petroff. Magnetic exchange splitting of one layer of cobalt deposited on top of the (111) surface of copper. *Physical Review B*, 25(1):527–530, 1982. PRB.

[52] Gabriel Auts, Cyrille Barreteau, Daniel Spanjaard, and Marie-Catherine Desjonqures. Magnetism of iron: from the bulk to the monatomic wire. *Journal of Physics: Condensed Matter*, 18(29):6785–6813, 2006.

[53] S. Bhagwat, R. Thamankar, and F. O. Schumann. Evidence for superparamagnetism in ultrathin Fe and Fe_xMn_{1x} films on Cu(100). *Journal of Magnetism and Magnetic Materials*, 290-291:216–218, 2005.

[54] Jessica E. Bickel, Focko Meier, Jens Brede, Andr Kubetzka, Kirsten von Bergmann, and Roland Wiesendanger. Magnetic properties of monolayer Co islands on Ir(111) probed by spin-resolved scanning tunneling microscopy. *Physical Review B*, 84(5):054454, 2011. PRB.

[55] Wolfgang Kreuzpaintner, Birgit Wiedemann, Jochen Stahn, Jean-Franois Moulin, Sina Mayr, Thomas Mairoser, Andreas Schmehl, Alexander Herrnberger, Panagiotis Korelis, Martin Haese, Jingfan Ye, Matthias Pomm, Peter Bni, and Jochen Mannhart. In situ polarized neutron reflectometry: Epitaxial thin-film growth of Fe on Cu(001) by dc magnetron sputtering. *Physical Review Applied*, 7(5):054004, 2017. PRAPPLIED.

[56] G.; Liu C.; Robert M.; Rau, C.; Xing. Two-dimensional ferromagnetism of ultrathin artificial vanadium films. *Physics Letters A*, 135(3):227–231, 1988.

[57] Olle Eriksson, RC Albers, and AM Boring. Prediction of ferromagnetism and metamagnetism in 4d transition-metal overlayers on the (001) surface of Ag (4d= Tc, Ru, Rh, and Pd). *Physical review letters*, 66(10):1350, 1991.

[58] S Blgel. Two-dimensional ferromagnetism of 3d, 4d, and 5d transition metal monolayers on noble metal (001) substrates. *Physical review letters*, 68(6):851, 1992.

[59] K. S. Novoselov, A. K. Geim, S. V. Morozov, D. Jiang, Y. Zhang, S. V. Dubonos, I. V. Grigorieva, and A. A. Firsov. Electric field effect in atomically thin carbon films. *Science*, 306(5696):666–669, 2004.

[60] Xiaoxiang Xi, Liang Zhao, Zefang Wang, Helmuth Berger, Lszl Forr, Jie Shan, and Kin Fai Mak. Strongly enhanced charge-density-wave order in monolayer $NbSe_2$. *Nature Nanotechnology*, 10:765, 2015.

[61] Valla Fatemi, Sanfeng Wu, Yuan Cao, Landry Bretheau, Quinn D Gibson, Kenji Watanabe, Takashi Taniguchi, Robert J Cava, and Pablo Jarillo-Herrero. Electrically tunable low-density superconductivity in a monolayer topological insulator. *Science*, 362(6417):926–929, 2018.

[62] Kin Fai Mak, Changgu Lee, James Hone, Jie Shan, and Tony F. Heinz. Atomically thin MoS_2: A new direct-gap semiconductor. *Physical Review Letters*, 105(13):136805, 2010. PRL.

[63] Ki Kang Kim, Allen Hsu, Xiaoting Jia, Soo Min Kim, Yumeng Shi, Mario Hofmann, Daniel Nezich, Joaquin F Rodriguez-Nieva, Mildred Dresselhaus, and Tomas Palacios. Synthesis of monolayer hexagonal boron nitride on Cu foil using chemical vapor deposition. *Nano letters*, 12(1):161–166, 2011.

[64] Lee A. Walsh and Christopher L. Hinkle. van der waals epitaxy: 2D materials and topological insulators. *Applied Materials Today*, 9:504–515, 2017.

[65] Andrew J. Mannix, Brian Kiraly, Mark C. Hersam, and Nathan P. Guisinger. Synthesis and chemistry of elemental 2D materials. *Nature Reviews Chemistry*, 1:0014, 2017.

[66] Dinh Loc Duong, Seok Joon Yun, and Young Hee Lee. van der waals layered materials: Opportunities and challenges. *ACS Nano*, 11(12):11803–11830, 2017.

[67] Hui Li, Shuangchen Ruan, and Yu-Jia Zeng. Intrinsic van der waals magnetic materials from bulk to the 2D limit: New frontiers of spintronics. *Advanced Materials*, 31(27):1900065, 2019.

[68] Nitin Samarth. Magnetism in flatland. *Nature*, 546:216, 2017.

[69] Kenneth S. Burch, David Mandrus, and Je-Geun Park. Magnetism in two-dimensional van der waals materials. *Nature*, 563(7729):47–52, 2018.

[70] M. Gibertini, M. Koperski, A. F. Morpurgo, and K. S. Novoselov. Magnetic 2D materials and heterostructures. *Nature Nanotechnology*, 14(5):408–419, 2019.

[71] Sining Dong, Xinyu Liu, Xiang Li, Vasily Kanzyuba, Taehee Yoo, Sergei Rouvimov, Suresh Vishwanath, Huili G. Xing, Debdeep Jena, Margaret Dobrowolska, and Jacek K. Furdyna. Room temperature weak ferromagnetism in $Sn_{1x}Mn_xSe_2$ 2d films grown by molecular beam epitaxy. *APL Materials*, 4(3):032601, 2016.

[72] Kathleen M. McCreary, Adrian G. Swartz, Wei Han, Jaroslav Fabian, and Roland K. Kawakami. Magnetic moment formation in graphene detected by scattering of pure spin currents. *Physical Review Letters*, 109(18):186604, 2012. PRL.

[73] J. Zhou, Q. Wang, Q. Sun, X. S. Chen, Y. Kawazoe, and P. Jena. Ferromagnetism in semihydrogenated graphene sheet. *Nano Letters*, 9(11):3867–3870, 2009.

[74] J. ervenka, M. I. Katsnelson, and C. F. J. Flipse. Room-temperature ferromagnetism in graphite driven by two-dimensional networks of pointdefects. *Nature Physics*, 5:840, 2009.

[75] A. V. Krasheninnikov, P. O. Lehtinen, A. S. Foster, P. Pyykk, and R. M. Nieminen. Embedding transition-metal atoms in graphene: Structure, bonding, and magnetism. *Physical Review Letters*, 102(12):126807, 2009. PRL.

[76] Rgis Decker, Jens Brede, Nicolae Atodiresei, Vasile Caciuc, Stefan Blgel, and Roland Wiesendanger. Atomic-scale magnetism of cobalt-intercalated graphene. *Physical Review B*, 87(4):041403, 2013. PRB.

[77] A. J. M. Giesbers, K. Uhlov, M. Konen, E. C. Peters, M. Burghard, J. Aarts, and C. F. J. Flipse. Interface-induced room-temperature ferromagnetism in hydrogenated epitaxial graphene. *Physical Review Letters*, 111(16):166101, 2013. PRL.

[78] David L. Cortie, Yury Khaydukov, Thomas Keller, David J. Sprouster, Jacob S. Hughes, James P. Sullivan, Xiaolin L. Wang, Anton P. Le Brun, Joel Bertinshaw, Sara J. Callori, Robert Aughterson, Michael James, Peter J. Evans, Gerry Triani, and Frank Klose. Enhanced magnetization of cobalt defect clusters embedded in $TiO_{2-\delta}$ films. *ACS Applied Materials & Interfaces*, 9(10):8783–8795, 2017.

[79] Qing Tang, Yafei Li, Zhen Zhou, Yongsheng Chen, and Zhongfang Chen. Tuning electronic and magnetic properties of wurtzite ZnO nanosheets by surface hydrogenation. *ACS Applied Materials & Interfaces*, 2(8):2442–2447, 2010.

[80] Yandong Ma, Ying Dai, Meng Guo, Chengwang Niu, Lin Yu, and Baibiao Huang. Strain-induced magnetic transitions in half-fluorinated single layers of BN, GaN and graphene. *Nanoscale*, 3(5):2301–2306, 2011.

[81] J. B S Mendes, O. Alves Santos, L. M Meireles, R. G Lacerda, L. H Vilela-Leo, F. L A Machado, R. L Rodrguez-Surez, A. Azevedo, and S. M Rezende. Spin-current to charge-current conversion and magnetoresistance in a hybrid structure of graphene and yttrium iron garnet. *Physical Review Letters*, 115(22):226601, 2015. PRL.

[82] M. T. Dau, C. Vergnaud, M. Gay, C. J. Alvarez, A. Marty, C. Beign, D. Jalabert, J.-F. Jacquot, O. Renault, H. Okuno, and M. Jamet. van der waals epitaxy of Mn-doped $MoSe_2$ on mica. *APL Materials*, 7(5):051111, 2019.

[83] Paula Mariel Coelho, Hannu-Pekka Komsa, Kinga Lasek, Vijaysankar Kalappattil, Jeyakumar Karthikeyan, Manh-Huong Phan, Arkady V. Krasheninnikov, and Matthias Batzill. Room-temperature ferromagnetism in $MoTe_2$ by post-growth incorporation of vanadium impurities. *Advanced Electronic Materials*, 5(5):1900044, 2019.

[84] Y. C. Cheng, Z. Y. Zhu, W. B. Mi, Z. B. Guo, and U. Schwingenschlgl. Prediction of two-dimensional diluted magnetic semiconductors: Doped monolayer MoS_2 systems. *Physical Review B*, 87(10):100401, 2013. PRB.

[85] Tomasz Dietl. A ten-year perspective on dilute magnetic semiconductors and oxides. *Nature Materials*, 9:965, 2010.

[86] Jae-Ung Lee, Sungmin Lee, Ji Hoon Ryoo, Soonmin Kang, Tae Yun Kim, Pilkwang Kim, Cheol-Hwan Park, Je-Geun Park, and Hyeonsik Cheong. Ising-type magnetic ordering in atomically thin $FePS_3$. *Nano Letters*, 16(12):7433–7438, 2016.

[87] Cheng Gong and Xiang Zhang. Two-dimensional magnetic crystals and emergent heterostructure devices. *Science*, 363(6428):eaav4450, 2019.

[88] Shi-Jing Gong, Cheng Gong, Yu-Yun Sun, Wen-Yi Tong, Chun-Gang Duan, Jun-Hao Chu, and Xiang Zhang. Electrically induced 2D half-metallic antiferromagnets and spin field effect transistors. *Proceedings of the National Academy of Sciences*, 115(34):8511–8516, 2018.

[89] Johannes Christian Leutenantsmeyer, Alexey A. Kaverzin, Magdalena Wojtaszek, and Bart J. van Wees. Proximity induced room temperature ferromagnetism in graphene probed with spin currents. *2D Materials*, 4(1):014001, 2016.

[90] B. Huang, G. Clark, E. Navarro-Moratalla, D. R. Klein, R. Cheng, K. L. Seyler, D. Zhong, E. Schmidgall, M. A. McGuire, D. H. Cobden, W. Yao, D. Xiao, P. Jarillo-Herrero, and X. Xu. Layer-dependent ferromagnetism in a van der waals crystal down to the monolayer limit. *Nature*, 546(7657):270–273, 2017.

[91] Xingzhi Wang, Kezhao Du, Yu Yang Fredrik Liu, Peng Hu, Jun Zhang, Qing Zhang, Man Hon Samuel Owen, Xin Lu, Chee Kwan Gan, Pinaki Sengupta, Christian Kloc, and Qihua Xiong. Raman spectroscopy of atomically thin two-dimensional magnetic iron phosphorus trisulfide (feps3) crystals. *2D Materials*, 3(3):031009, 2016.

[92] K. C. Rule, G. J. McIntyre, S. J. Kennedy, and T. J. Hicks. Single-crystal and powder neutron diffraction experiments on $FePS_3$: Search for the magnetic structure. *Physical Review B*, 76(13):134402, 2007. PRB.

[93] Cheng Gong, Lin Li, Zhenglu Li, Huiwen Ji, Alex Stern, Yang Xia, Ting Cao, Wei Bao, Chenzhe Wang, Yuan Wang, Z. Q. Qiu, R. J. Cava, Steven G. Louie, Jing Xia, and Xiang Zhang. Discovery of intrinsic ferromagnetism in two-dimensional van der waals crystals. *Nature*, 546:265, 2017.

[94] D. Soriano, C. Cardoso, and J. Fernndez-Rossier. Interplay between interlayer exchange and stacking in CrI_3 bilayers. *Solid State Communications*, 299:113662, 2019.

[95] Xiaoyang Lin, Wei Yang, Kang L. Wang, and Weisheng Zhao. Two-dimensional spintronics for low-power electronics. *Nature Electronics*, 2(7):274–283, 2019.

[96] Xiaolong Chen, Zishu Zhou, Bingchen Deng, Zefei Wu, Fengnian Xia, Yi Cao, Le Zhang, Wei Huang, Ning Wang, and Lin Wang. Electrically tunable physical properties of two-dimensional materials. *Nano Today*, 27:99–119, 2019.

[97] Zhe Wang, Ignacio Gutierrez-Lazama, Nicolas Ubrig, Martin Kroner, Takashi Taniguchi, Kenji Watanabe, Atac Imamoglu, Enrico Giannini, and Alberto F. Morpurgo. Very large tunneling magnetoresistance in layered semiconductor CrI_3. *arXiv:1801.08188*, 2018.

[98] Tiancheng Song, Xinghan Cai, Matisse Wei-Yuan Tu, Xiaoou Zhang, Bevin Huang, Nathan P. Wilson, Kyle L. Seyler, Lin Zhu, Takashi Taniguchi, Kenji Watanabe, Michael A. McGuire, David H. Cobden, Di Xiao, Wang Yao, and Xiaodong Xu. Giant tunneling magnetoresistance in spin-filter van der waals heterostructures. *Science*, 2018.

[99] D. R. Klein, D. MacNeill, J. L. Lado, D. Soriano, E. Navarro-Moratalla, K. Watanabe, T. Taniguchi, S. Manni, P. Canfield, J. Fernndez-Rossier, and P. Jarillo-Herrero. Probing magnetism in 2D van der waals crystalline insulators via electron tunneling. *Science*, 2018.

[100] Shengwei Jiang, Lizhong Li, Zefang Wang, Jie Shan, and Kin Fai Mak. Spin tunnel field-effect transistors based on two-dimensional van der waals heterostructures. *Nature Electronics*, 2(4):159–163, 2019.

[101] Sergio O. Valenzuela and Stephan Roche. A barrier to spin filters. *Nature Electronics*, 1(6):328–329, 2018.

[102] Cheng Tan, Jinhwan Lee, Soon-Gil Jung, Tuson Park, Sultan Albarakati, James Partridge, Matthew R. Field, Dougal G. McCulloch, Lan Wang, and Changgu Lee. Hard magnetic properties in nanoflake van der waals Fe_3GeTe_2. *Nature Communications*, 9(1):1554, 2018.

[103] Zhe Wang, Deepak Sapkota, Takashi Taniguchi, Kenji Watanabe, David Mandrus, and Alberto F. Morpurgo. Tunneling spin valves based on Fe_3GeTe_2/hBN/Fe_3GeTe_2 van der waals heterostructures. *Nano Letters*, 2018.

[104] Zaiyao Fei, Bevin Huang, Paul Malinowski, Wenbo Wang, Tiancheng Song, Joshua Sanchez, Wang Yao, Di Xiao, Xiaoyang Zhu, Andrew May, Weida Wu, David Cobden, Jiun-Haw Chu, and Xiaodong Xu. Two-dimensional itinerant ising ferromagnetism in atomically thin Fe_3GeTe_2. *arXiv:1803.02559*, 2018.

[105] Yujun Deng, Yijun Yu, Yichen Song, Jingzhao Zhang, Nai Zhou Wang, Yi Zheng Wu, Junyi Zhu, Jing Wang, Xian Hui Chen, and Yuanbo Zhang. Gate-tunable room-temperature ferromagnetism in two-dimensional Fe_3GeTe_2. *arXiv:1803.02038*, 2018.

[106] Manuel Bonilla, Sadhu Kolekar, Yujing Ma, Horacio Coy Diaz, Vijaysankar Kalappattil, Raja Das, Tatiana Eggers, Humberto R. Gutierrez, Manh-Huong Phan, and Matthias Batzill. Strong room-temperature ferromagnetism in VSe_2 monolayers on van der waals substrates. *Nature Nanotechnology*, 2018.

[107] Dante J. OHara, Tiancong Zhu, Amanda H. Trout, Adam S. Ahmed, Yunqiu Kelly Luo, Choong Hee Lee, Mark R. Brenner, Siddharth Rajan, Jay A. Gupta, David W. McComb, and Roland K. Kawakami. Room temperature intrinsic ferromagnetism in epitaxial manganese selenide films in the monolayer limit. *Nano Letters*, 18(5):3125–3131, 2018.

[108] John R. Arthur. Molecular beam epitaxy. *Surface Science*, 500(1):189–217, 2002.

[109] A. Y. Cho. Advances in molecular beam epitaxy (MBE). *Journal of Crystal Growth*, 111(1):1–13, 1991.

[110] A. Y. Cho. How molecular beam epitaxy (MBE) began and its projection into the future. *Journal of Crystal Growth*, 201-202:1–7, 1999.

[111] E. F. Schubert. Delta doping of iiiv compound semiconductors: Fundamentals and device applications. *Journal of Vacuum Science & Technology A*, 8(3):2980–2996, 1990.

[112] D. G. Schlom, J. H. Haeni, J. Lettieri, C. D. Theis, W. Tian, J. C. Jiang, and X. Q. Pan. Oxide nano-engineering using MBE. *Materials Science and Engineering: B*, 87(3):282–291, 2001.

[113] Andreas Schmehl, Venu Vaithyanathan, Alexander Herrnberger, Stefan Thiel, Christoph Richter, Marco Liberati, Tassilo Heeg, Martin Rckerath, Lena Fitting Kourkoutis, Sebastian Mhlbauer, Peter Bni, David A. Muller, Yuri Barash, Jrgen Schubert, Yves Idzerda, Jochen Mannhart, and Darrell G. Schlom. Epitaxial integration of the highly spin-polarized ferromagnetic semiconductor EuO with silicon and GaN. *Nature Materials*, 6:882, 2007.

[114] J. R. Arthur and J. J. LePore. GaAs, GaP, and $GaAs_xP_{1x}$ epitaxial films grown by molecular beam deposition. *Journal of Vacuum Science and Technology*, 6(4):545–548, 1969.

[115] Igor V. Pinchuk, Patrick M. Odenthal, Adam S. Ahmed, Walid Amamou, Joshua E. Goldberger, and Roland K. Kawakami. Epitaxial co-deposition growth of $CaGe]_2$ films by molecular beam epitaxy for large area germanane, journal = Journal of Materials Research, volume = 29, number = 3, pages = 410-416, issn = 0884-2914, doi = 10.1557/jmr.2014.2, year = 2014, type = Journal Article.

[116] A. Y. Cho and I. Hayashi. PN junction formation during molecularbeam epitaxy of Gedoped GaAs. *Journal of Applied Physics*, 42(11):4422–4425, 1971.

[117] Darrell G. Schlom and Charles H. Ahn. Clear leap for superconductors. *Nature*, 456:582, 2008.

[118] Darrell G Schlom and Charles H Ahn. Materials science: Clear leap for superconductors. *Nature*, 456(7222):582, 2008.

[119] Shuji; Hasegawa. *Reflection High-Energy Electron Diffraction*, pages 1–14. 2012.

[120] Jrgen Klein. *Epitaktische Heterostrukturen aus dotierten Manganaten*. Thesis, 2001.

[121] M. Dabrowska-Szata. Analysis of RHEED pattern from semiconductor surfaces. *Materials Chemistry and Physics*, 81(2):257–259, 2003.

[122] Udo W; Pohl. *Epitaxy of Semiconductors: Introduction to Physical Properties*. Graduate Texts in Physics. Springer-Verlag Berlin Heidelberg, 1 edition, 2013.

[123] Atsushi Koma. Van der waals epitaxya new epitaxial growth method for a highly lattice-mismatched system. *Thin Solid Films*, 216(1):72–76, 1992.

[124] Atsushi Koma. Van der waals epitaxy for highly lattice-mismatched systems. *Journal of Crystal Growth*, 201-202:236–241, 1999.

[125] Atsushi Koma, Kazumasa Sunouchi, and Takao Miyajima. Fabrication and characterization of heterostructures with subnanometer thickness. *Microelectronic Engineering*, 2(1):129–136, 1984.

[126] Atsushi Koma and Kazuki Yoshimura. Ultrasharp interfaces grown with van der waals epitaxy. *Surface Science*, 174(1):556–560, 1986.

[127] Miho Yasaka. X-ray thin-film measurement techniques. *X-ray reflectivity measurement. The Rigaku Journal*, 26(12):1–9, 2010.

[128] Galja Pletikapi and Nadica Ivoevi DeNardis. Application of surface analytical methods for hazardous situation in the adriatic sea: monitoring of organic matter dynamics and oil pollution. *Natural Hazards & Earth System Sciences*, 17(1), 2017.

[129] Kunio Takayanagi, Yasumasa Tanishiro, Shigeki Takahashi, and Masaetsu Takahashi. Structure analysis of Si(111)-7 x 7 reconstructed surface by transmission electron diffraction. *Surface Science*, 164(2):367–392, 1985.

[130] Roland Wiesendanger. Spin mapping at the nanoscale and atomic scale. *Reviews of Modern Physics*, 81(4):1495–1550, 2009. RMP.

[131] Aurore Finco, Marco Perini, Andr Kubetzka, Kirsten von Bergmann, and Roland Wiesendanger. Magnetic domain walls in strain-patterned ultrathin films. *Physical Review B*, 98(17):174435, 2018. PRB.

[132] F. Marczinowski, K. von Bergmann, M. Bode, and R. Wiesendanger. Growth of Cr on Ir(111) studied by scanning tunneling microscopy. *Surface Science*, 600(5):1034–1039, 2006.

[133] M. Sawicki, W. Stefanowicz, and A. Ney. Sensitive SQUID magnetometry for studying nanomagnetism. *Semiconductor Science and Technology*, 26(6):064006, 2011.

[134] O. V. Snigirev, K. E. Andreev, A. M. Tishin, S. A. Gudoshnikov, and J. Bohr. Magnetic properties of thin Ni films measured by a dc SQUID-based magnetic microscope. *Physical Review B*, 55(21):14429–14433, 1997. PRB.

[135] A. B. Pippard. *Magnetoresistance in metals*. Cambridge University Press, Cambridge [Cambridgeshire] ;, 1989.

[136] Naoto Nagaosa, Jairo Sinova, Shigeki Onoda, A. H. MacDonald, and N. P. Ong. Anomalous hall effect. *Reviews of Modern Physics*, 82(2):1539–1592, 2010. RMP.

[137] A. Eiling and J. S. Schilling. Pressure and temperature dependence of electrical resistivity of Pb and Sn from 1-300k and 0-10 GPa-use as continuous resistive pressure monitor accurate over wide temperature range; superconductivity under pressure in Pb, Sn and In. *Journal of Physics F: Metal Physics*, 11(3):623–639, 1981.

[138] Samuel T. Weir, Jagannadham Akella, Chantel Aracne-Ruddle, Yogesh K. Vohra, and Shane A. Catledge. Epitaxial diamond encapsulation of metal microprobes for high pressure experiments. *Applied Physics Letters*, 77(21):3400–3402, 2000.

[139] Jeremy R. Patterson, Shane A. Catledge, Yogesh K. Vohra, Jagannadham Akella, and Samuel T. Weir. Electrical and mechanical properties of C_{70} fullerene and graphite under high pressures studied using designer diamond anvils. *Physical Review Letters*, 85(25):5364–5367, 2000. PRL.

[140] J. R. Jeffries, N. P. Butch, K. Kirshenbaum, S. R. Saha, G. Samudrala, S. T. Weir, Y. K. Vohra, and J. Paglione. Suppression of magnetism and development of superconductivity within the collapsed tetragonal phase of $ca_{0.67}sr_{0.33}fe_2as_2$ under pressure. *Physical Review B*, 85(18):184501, 2012. PRB.

[141] A.; Heller. Diamonds put the squeeze on materials. *Science & Technology Review*, December 2004 2004.

[142] H. K. Mao, P. M. Bell, J. W. Shaner, and D. J. Steinberg. Specific volume measurements of Cu, Mo, Pd, and Ag and calibration of the ruby R1 fluorescence pressure gauge from 0.06 to 1 Mbar. *Journal of Applied Physics*, 49(6):3276–3283, 1978.

[143] W. B. Daniels and Charles S. Smith. Pressure derivatives of the elastic constants of copper, silver, and gold to 10,000 bars. *Physical Review*, 111(3):713–721, 1958. PR.

[144] Pascal Vinet, John R. Smith, John Ferrante, and James H. Rose. Temperature effects on the universal equation of state of solids. *Physical Review B*, 35(4):1945–1953, 1987. PRB.

[145] Francis Birch. Finite elastic strain of cubic crystals. *Physical Review*, 71(11):809–824, 1947. PR.

[146] G. van der Laan. Applications of soft x-ray magnetic dichroism. *Journal of Physics: Conference Series*, 430:012127, 2013.

[147] Gerrit van der Laan and Adriana I. Figueroa. X-ray magnetic circular dichroisma versatile tool to study magnetism. *Coordination Chemistry Reviews*, 277-278:95–129, 2014.

[148] Clemens Prescher and Vitali B. Prakapenka. DIOPTAS: a program for reduction of two-dimensional x-ray diffraction data and data exploration. *High Pressure Research*, 35(3):223–230, 2015.

[149] A. P. Hammersley, S. O. Svensson, M. Hanfland, A. N. Fitch, and D. Hausermann. Two-dimensional detector software: From real detector to idealised image or two-theta scan. *High Pressure Research*, 14(4-6):235–248, 1996.

[150] M. I. McMahon. Diamonds on diamond: structural studies at extreme conditions on the diamond light source. *Philosophical Transactions of the Royal Society A: Mathematical, Physical and Engineering Sciences*, 373(2036):20130158, 2015.

[151] B. H.; Toby. EXPGUI, a graphical user interface for GSAS. *Journal of Applied Crystallography*, 34:210–213, 2001.

[152] Brian H. Toby and Robert B. Von Dreele. GSAS-ii: the genesis of a modern open-source all purpose crystallography software package. *Journal of Applied Crystallography*, 46(2):544–549, 2013.

[153] Xiao Huang, Zhiyuan Zeng, and Hua Zhang. Metal dichalcogenide nanosheets: preparation, properties and applications. *Chemical Society Reviews*, 42(5):1934–1946, 2013.

[154] Hualing Zeng, Junfeng Dai, Wang Yao, Di Xiao, and Xiaodong Cui. Valley polarization in MoS_2 monolayers by optical pumping. *Nature Nanotechnology*, 7:490, 2012.

[155] Aaron M. Jones, Hongyi Yu, Nirmal J. Ghimire, Sanfeng Wu, Grant Aivazian, Jason S. Ross, Bo Zhao, Jiaqiang Yan, David G. Mandrus, Di Xiao, Wang Yao, and Xiaodong Xu. Optical generation of excitonic valley coherence in monolayer WSe_2. *Nature Nanotechnology*, 8:634, 2013.

[156] Di Xiao, Gui-Bin Liu, Wanxiang Feng, Xiaodong Xu, and Wang Yao. Coupled spin and valley physics in monolayers of MoS_2 and other group-vi dichalcogenides. *Physical Review Letters*, 108(19):196802, 2012. PRL.

[157] Chuan Xu, Libin Wang, Zhibo Liu, Long Chen, Jingkun Guo, Ning Kang, Xiu-Liang Ma, Hui-Ming Cheng, and Wencai Ren. Large-area high-quality 2D ultrathin Mo_2C superconducting crystals. *Nature Materials*, 14:1135, 2015.

[158] B. Radisavljevic, A. Radenovic, J. Brivio, V. Giacometti, and A. Kis. Single-layer MoS_2 transistors. *Nature Nanotechnology*, 6:147, 2011.

[159] Woo Jong Yu, Yuan Liu, Hailong Zhou, Anxiang Yin, Zheng Li, Yu Huang, and Xiangfeng Duan. Highly efficient gate-tunable photocurrent generation in vertical heterostructures of layered materials. *Nature Nanotechnology*, 8:952, 2013.

[160] Madhavi Dave, Rajiv Vaidya, S. G. Patel, and A. R. Jani. High pressure effect on MoS_2 and $MoSe_2$ single crystals grown by CVT method. *Bulletin of Materials Science*, 27(2):213–216, 2004.

[161] S. Fathipour, H. Li, M. Remkar, L. Yeh, W. Tsai, Y. Lin, S. Fullerton-Shirey, and A. Seabaugh. Record high current density and low contact resistance in MoS_2 FETs by ion doping. In *2016 International Symposium on VLSI Technology, Systems and Application (VLSI-TSA)*, pages 1–2.

[162] Xiaoping Hong, Jonghwan Kim, Su-Fei Shi, Yu Zhang, Chenhao Jin, Yinghui Sun, Sefaattin Tongay, Junqiao Wu, Yanfeng Zhang, and Feng Wang. Ultrafast charge transfer in atomically thin MoS_2/WS_2 heterostructures. *Nature Nanotechnology*, 9:682, 2014.

[163] Choong Hee Lee, William McCulloch, Edwin W. Lee II, Lu Ma, Sriram Krishnamoorthy, Jinwoo Hwang, Yiying Wu, and Siddharth Rajan. Transferred large area single crystal MoS_2 field effect transistors. *Applied Physics Letters*, 107(19):193503, 2015.

[164] Chia-Hsin Wu, Chu-Shou Yang, Yen-Chi Wang, Hsi-Jung Huang, Yen-Teng Ho, Lin-Lung Wei, and Edward Yi Chang. Epitaxial single-crystal of GaSe epilayers grown on a c-sapphire substrate by molecular beam epitaxy. *physica status solidi (a)*, 212(10):2201–2204, 2015.

[165] Xiang Yuan, Lei Tang, Shanshan Liu, Peng Wang, Zhigang Chen, Cheng Zhang, Yanwen Liu, Weiyi Wang, Yichao Zou, Cong Liu, Nan Guo, Jin Zou, Peng Zhou, Weida Hu, and Faxian Xiu. Arrayed van der waals vertical heterostructures based on 2D GaSe grown by molecular beam epitaxy. *Nano Letters*, 15(5):3571–3577, 2015.

[166] Zeineb Ben Aziza, Hugo Henck, Debora Pierucci, Mathieu G. Silly, Emmanuel Lhuillier, Gilles Patriarche, Fausto Sirotti, Mahmoud Eddrief, and Abdelkarim Ouerghi. van der waals epitaxy of GaSe/graphene heterostructure: Electronic and interfacial properties. *ACS Nano*, 10(10):9679–9686, 2016.

[167] E. Xenogiannopoulou, P. Tsipas, K. E. Aretouli, D. Tsoutsou, S. A. Giamini, C. Bazioti, G. P. Dimitrakopulos, Ph Komninou, S. Brems, C. Huyghebaert, I. P. Radu, and A. Dimoulas. High-quality, large-area $MoSe_2$ and $MoSe_2/Bi_2Se_3$ heterostructures on AlN(0001)/Si(111) substrates by molecular beam epitaxy. *Nanoscale*, 7(17):7896–7905, 2015.

[168] K. E. Aretouli, P. Tsipas, D. Tsoutsou, J. Marquez-Velasco, E. Xenogiannopoulou, S. A. Giamini, E. Vassalou, N. Kelaidis, and A. Dimoulas. Two-dimensional semiconductor $HfSe_2$ and $MoSe_2/HfSe_2$ van der waals heterostructures by molecular beam epitaxy. *Applied Physics Letters*, 106(14):143105, 2015.

[169] Suresh Vishwanath, Xinyu Liu, Sergei Rouvimov, Patrick C. Mende, Angelica Azcatl, Stephen McDonnell, Robert M. Wallace, Randall M. Feenstra, Jacek K. Furdyna, Debdeep Jena, and Huili Grace Xing. Comprehensive structural and optical characterization of mbe grown $MoSe_2$ on graphite, CaF_2 and graphene. *2D Materials*, 2(2):024007, 2015.

[170] L. Jiao, H. J. Liu, J. L. Chen, Y. Yi, W. G. Chen, Y. Cai, J. N. Wang, X. Q. Dai, N. Wang, W. K. Ho, and M. H. Xie. Molecular-beam epitaxy of monolayer $MoSe_2$: growth characteristics and domain boundary formation. *New Journal of Physics*, 17(5):053023, 2015.

[171] Anupam Roy, Hema C. P. Movva, Biswarup Satpati, Kyounghwan Kim, Rik Dey, Amritesh Rai, Tanmoy Pramanik, Samaresh Guchhait, Emanuel Tutuc, and Sanjay K. Banerjee. Structural and electrical properties of $MoTe_2$ and $MoSe_2$ grown by molecular beam epitaxy. *ACS Applied Materials & Interfaces*, 8(11):7396–7402, 2016.

[172] H. J. Liu, L. Jiao, L. Xie, F. Yang, J. L. Chen, W. K. Ho, C. L. Gao, J. F. Jia, X. D. Cui, and M. H. Xie. Molecular-beam epitaxy of monolayer and bilayer WSe_2: a scanning tunneling microscopy/spectroscopy study and deduction of exciton binding energy. *2D Materials*, 2(3):034004, 2015.

[173] Ruoyu Yue, Adam T. Barton, Hui Zhu, Angelica Azcatl, Luis F. Pena, Jian Wang, Xin Peng, Ning Lu, Lanxia Cheng, Rafik Addou, Stephen McDonnell, Luigi Colombo, Julia W. P. Hsu, Jiyoung Kim, Moon J. Kim, Robert M. Wallace, and Christopher L. Hinkle. $HfSe_2$ thin films: 2D transition metal dichalcogenides grown by molecular beam epitaxy. *ACS Nano*, 9(1):474–480, 2015.

[174] A. Kuhn, A. Chevy, and R. Chevalier. Crystal structure and interatomic distances in GaSe. *physica status solidi (a)*, 31(2):469–475, 1975.

[175] Wenjuan Huang, Lin Gan, Huiqiao Li, Ying Ma, and Tianyou Zhai. 2D layered group iiiA metal chalcogenides: synthesis, properties and applications in electronics and optoelectronics. *CrystEngComm*, 18(22):3968–3984, 2016.

[176] Yubing Zhou, Yufeng Nie, Yujing Liu, Kai Yan, Jinhua Hong, Chuanhong Jin, Yu Zhou, Jianbo Yin, Zhongfan Liu, and Hailin Peng. Epitaxy and photoresponse of two-dimensional GaSe crystals on flexible transparent mica sheets. *ACS Nano*, 8(2):1485–1490, 2014.

[177] L. Leontie, I. Evtodiev, V. Nedeff, M. Stamate, and M. Caraman. Photoelectric properties of Bi_2O_3GaSe heterojunctions. *Applied Physics Letters*, 94(7):071903, 2009.

[178] Keiji Ueno, Hideki Abe, Koichiro Saiki, and Atsushi Koma. Heteroepitaxy of layered semiconductor GaSe on a GaAs(111)b surface. *Japanese Journal of Applied Physics*, 30(Part 2, No. 8A):L1352–L1354, 1991.

[179] Hideki Abe, Keiji Ueno, Koichiro Saiki, and Atsushi Koma. Heteroepitaxial growth of layered GaSe films on GaAs(001) surfaces. *Japanese Journal of Applied Physics*, 32(Part 2, No. 10A):L1444–L1447, 1993.

[180] Le Thanh Vinh, M. Eddrief, C. Sbenne, A. Sacuto, and M. Balkanski. Heteroepitaxy of GaSe layered semiconductor compound on Si(111) 7 x 7 substrate: a van der waals epitaxy? *Journal of Crystal Growth*, 135(1):1–10, 1994.

[181] Edwin W. Lee II, Choong Hee Lee, Pran K. Paul, Lu Ma, William D. McCulloch, Sriram Krishnamoorthy, Yiying Wu, Aaron R. Arehart, and Siddharth Rajan. Layer-transferred MoS_2/GaN PN diodes. *Applied Physics Letters*, 107(10):103505, 2015.

[182] Sriram Krishnamoorthy, Edwin W. Lee II, Choong Hee Lee, Yuewei Zhang, William D. McCulloch, Jared M. Johnson, Jinwoo Hwang, Yiying Wu, and Siddharth Rajan. High current density 2D/3D MoS_2/GaN esaki tunnel diodes. *Applied Physics Letters*, 109(18):183505, 2016.

[183] H. Cheng, J. M. DePuydt, M. A. Haase, and J. E. Potts. Molecularbeam epitaxy growth of ZnSe using a cracked selenium source. *Journal of Vacuum Science & Technology B: Microelectronics Processing and Phenomena*, 8(2):181–186, 1990.

[184] Thomas E. Beechem, Brian M. Kowalski, Michael T. Brumbach, Anthony E. McDonald, Catalin D. Spataru, Stephen W. Howell, Taisuke Ohta, Jesse A. Pask, and Nikolai G. Kalugin. Oxidation of ultrathin GaSe. *Applied Physics Letters*, 107(17):173103, 2015.

[185] K; Izumi F; Momma. VESTA: a three-dimensional visualization system for electronic and structural analysis. *Journal of Applied Crystallography*, 44(1272), 2011.

[186] K. Allakhverdiev, T. Baykara, Ellialtiolu, F. Hashimzade, D. Huseinova, K. Kawamura, A. A. Kaya, A. M. Kulibekov, and S. Onari. Lattice vibrations of pure and doped GaSe. *Materials Research Bulletin*, 41(4):751–763, 2006. (Gulubayov).

[187] Sidong Lei, Liehui Ge, Zheng Liu, Sina Najmaei, Gang Shi, Ge You, Jun Lou, Robert Vajtai, and Pulickel M. Ajayan. Synthesis and photoresponse of large GaSe atomic layers. *Nano Letters*, 13(6):2777–2781, 2013.

[188] Xufan Li, Ming-Wei Lin, Alexander A. Puretzky, Juan C. Idrobo, Cheng Ma, Miaofang Chi, Mina Yoon, Christopher M. Rouleau, Ivan I. Kravchenko, David B. Geohegan, and Kai Xiao. Controlled vapor phase growth of single crystalline, two-dimensional GaSe crystals with high photoresponse. *Scientific Reports*, 4:5497, 2014.

[189] R. M. Hoff, J. C. Irwin, and R. M. A. Lieth. Raman scattering in GaSe. *Canadian Journal of Physics*, 53(17):1606–1614, 1975.

[190] R. Longuinhos and J. Ribeiro-Soares. Ultra-weak interlayer coupling in two-dimensional gallium selenide. *Physical Chemistry Chemical Physics*, 18(36):25401–25408, 2016.

[191] Xiaolong Liu, Itamar Balla, Hadallia Bergeron, and Mark C. Hersam. Point defects and grain boundaries in rotationally commensurate MoS_2 on epitaxial graphene. *The Journal of Physical Chemistry C*, 120(37):20798–20805, 2016.

[192] Zheng Liu, Matin Amani, Sina Najmaei, Quan Xu, Xiaolong Zou, Wu Zhou, Ting Yu, Caiyu Qiu, A. Glen Birdwell, Frank J. Crowne, Robert Vajtai, Boris I. Yakobson, Zhenhai Xia, Madan Dubey, Pulickel M. Ajayan, and Jun Lou. Strain and structure heterogeneity in MoS_2 atomic layers grown by chemical vapour deposition. *Nature Communications*, 5:5246, 2014.

[193] Dumitru Dumcenco, Dmitry Ovchinnikov, Kolyo Marinov, Predrag Lazi, Marco Gibertini, Nicola Marzari, Oriol Lopez Sanchez, Yen-Cheng Kung, Daria Krasnozhon, Ming-Wei Chen, Simone Bertolazzi, Philippe Gillet, Anna Fontcuberta i Morral, Aleksandra Radenovic, and Andras Kis. Large-area epitaxial monolayer MoS_2. *ACS Nano*, 9(4):4611–4620, 2015.

[194] Sam Vaziri, Grzegorz Lupina, Christoph Henkel, Anderson D. Smith, Mikael stling, Jarek Dabrowski, Gunther Lippert, Wolfgang Mehr, and Max C. Lemme. A graphene-based hot electron transistor. *Nano Letters*, 13(4):1435–1439, 2013.

[195] Branimir Radisavljevic, Michael B. Whitwick, and Andras Kis. Small-signal amplifier based on single-layer MoS_2. *Applied Physics Letters*, 101(4):043103, 2012.

[196] Tengfei Pei, Lihong Bao, Guocai Wang, Ruisong Ma, Haifang Yang, Junjie Li, Changzhi Gu, Sokrates Pantelides, Shixuan Du, and Hong-jun Gao. Few-layer $SnSe_2$ transistors with high on/off ratios. *Applied Physics Letters*, 108(5):053506, 2016.

[197] Dmitry Ovchinnikov, Adrien Allain, Ying-Sheng Huang, Dumitru Dumcenco, and Andras Kis. Electrical transport properties of single-layer WS_2. *ACS Nano*, 8(8):8174–8181, 2014.

[198] Rajiv Vaidya, Madhavi Dave, S. S. Patel, S. G. Patel, and A. R. Jani. Growth of molybdenum disulphide using iodine as transport material. *Pramana*, 63(3):611–616, 2004.

[199] Lu Ma, Digbijoy N. Nath, Edwin W. Lee II, Choong Hee Lee, Mingzhe Yu, Aaron Arehart, Siddharth Rajan, and Yiying Wu. Epitaxial growth of large area single-crystalline few-layer MoS_2 with high space charge mobility of $192cm^2$ v^1 s^1. *Applied Physics Letters*, 105(7):072105, 2014.

[200] Masihhur R. Laskar, Lu Ma, Santhakumar Kannappan, Pil Sung Park, Sriram Krishnamoorthy, Digbijoy N. Nath, Wu Lu, Yiying Wu, and Siddharth Rajan. Large area single crystal (0001) oriented MoS_2. *Applied Physics Letters*, 102(25):252108, 2013.

[201] Xiaotian Zhang, Zakaria Y. Al Balushi, Fu Zhang, Tanushree H. Choudhury, Sarah M. Eichfeld, Nasim Alem, Thomas N. Jackson, Joshua A. Robinson, and Joan M. Redwing. Influence of carbon in metalorganic chemical vapor deposition of few-layer WSe_2 thin films. *Journal of Electronic Materials*, 45(12):6273–6279, 2016.

[202] Choong Hee Lee, Sriram Krishnamoorthy, Dante J. O'Hara, Mark R. Brenner, Jared M. Johnson, John S. Jamison, Roberto C. Myers, Roland K. Kawakami, Jinwoo Hwang, and Siddharth Rajan. Molecular beam epitaxy of 2D-layered gallium selenide on GaN substrates. *Journal of Applied Physics*, 121(9):094302, 2017.

[203] Kleopatra Emmanouil Aretouli, Dimitra Tsoutsou, Polychronis Tsipas, Jose Marquez-Velasco, Sigiava Aminalragia Giamini, Nicolaos Kelaidis, Vassilis Psycharis, and Athanasios Dimoulas. Epitaxial 2D $SnSe_2$/2D WSe_2 van der waals heterostructures. *ACS Applied Materials & Interfaces*, 8(35):23222–23229, 2016.

[204] Liu Wang, Jiansheng Jie, Zhibin Shao, Qing Zhang, Xiaohong Zhang, Yuming Wang, Zheng Sun, and Shuit-Tong Lee. MoS_2/Si heterojunction with vertically standing layered structure for ultrafast, high-detectivity, self-driven visiblenear infrared photodetectors. *Advanced Functional Materials*, 25(19):2910–2919, 2015.

[205] Pawan Mishra, Malleswararao Tangi, Tien Khee Ng, Mohamed Nejib Hedhili, Dalaver H. Anjum, Mohd Sharizal Alias, Chien-Chih Tseng, Lain-Jong Li, and Boon S. Ooi. Impact of N-plasma and Ga-irradiation on MoS]$_2$ layer in molecular beam epitaxy, journal = Applied Physics Letters, volume = 110, number = 1, pages = 012101, year = 2017, type = Journal Article.

[206] Brian D. Tracy, Xiang Li, Xinyu Liu, Jacek Furdyna, Margaret Dobrowolska, and David J. Smith. Characterization of structural defects in $SnSe_2$ thin films grown by molecular beam epitaxy on GaAs(111)B substrates. *Journal of Crystal Growth*, 453:58–64, 2016.

[207] J. C. Li, D. Li, X. Y. Qin, and J. Zhang. Enhanced thermoelectric performance of p-type SnSe doped with Zn. *Scripta Materialia*, 126:6–10, 2017.

[208] Peng Yu, Xuechao Yu, Wanglin Lu, Hsin Lin, Linfeng Sun, Kezhao Du, Fucai Liu, Wei Fu, Qingsheng Zeng, Zexiang Shen, Chuanhong Jin, Qi Jie Wang, and Zheng Liu. Fast photoresponse from 1T tin diselenide atomic layers. *Advanced Functional Materials*, 26(1):137–145, 2016.

[209] Rusen Yan, Sara Fathipour, Yimo Han, Bo Song, Shudong Xiao, Mingda Li, Nan Ma, Vladimir Protasenko, David A. Muller, Debdeep Jena, and Huili Grace Xing. Esaki diodes in van der waals heterojunctions with broken-gap energy band alignment. *Nano Letters*, 15(9):5791–5798, 2015.

[210] Chenglei Guo, Zhen Tian, Yanjun Xiao, Qixi Mi, and Jiamin Xue. Field-effect transistors of high-mobility few-layer $SnSe_2$. *Applied Physics Letters*, 109(20):203104, 2016.

[211] J. M. Kosterlitz and D. J. Thouless. Ordering, metastability and phase transitions in two-dimensional systems. *Journal of Physics C: Solid State Physics*, 6(7):1181, 1973.

[212] F. Huang, M. T. Kief, G. J. Mankey, and R. F. Willis. Magnetism in the few-monolayers limit: A surface magneto-optic kerr-effect study of the magnetic behavior of ultrathin films of Co, Ni, and Co-Ni alloys on Cu(100) and Cu(111). *Physical Review B*, 49(6):3962–3971, 1994. PRB.

[213] Hans-Joachim Elmers, Jens Hauschild, and Ulrich Gradmann. Critical behavior of the uniaxial ferromagnetic monolayer Fe(110) on W(110). *Physical Review B*, 54(21):15224–15233, 1996. PRB.

[214] L. J. De Jongh and A. R. Miedema. Experiments on simple magnetic model systems. *Advances in Physics*, 50(8):947–1170, 2001.

[215] Wenyu Xing, Yangyang Chen, Patrick M. Odenthal, Xiao Zhang, Wei Yuan, Tang Su, Qi Song, Tianyu Wang, Jiangnan Zhong, Shuang Jia, X. C. Xie, Yan Li, and Wei Han. Electric field effect in multilayer $Cr_2Ge_2Te_6$: a ferromagnetic 2D material. *2D Materials*, 4(2):024009, 2017.

[216] Chuan Zhao, Tenzin Norden, Peiyao Zhang, Puqin Zhao, Yingchun Cheng, Fan Sun, James P. Parry, Payam Taheri, Jieqiong Wang, Yihang Yang, Thomas Scrace, Kaifei Kang, Sen Yang, Guo-xing Miao, Renat Sabirianov, George Kioseoglou, Wei Huang, Athos Petrou, and Hao Zeng. Enhanced valley splitting in monolayer WSe_2 due to magnetic exchange field. *Nature Nanotechnology*, 12:757, 2017.

[217] Ding Zhong, Kyle L. Seyler, Xiayu Linpeng, Ran Cheng, Nikhil Sivadas, Bevin Huang, Emma Schmidgall, Takashi Taniguchi, Kenji Watanabe, Michael A. McGuire, Wang Yao, Di Xiao, Kai-Mei C. Fu, and Xiaodong Xu. Van der waals engineering of ferromagnetic semiconductor heterostructures for spin and valleytronics. *Science Advances*, 3(5), 2017.

[218] Yandong Ma, Ying Dai, Meng Guo, Chengwang Niu, Yingtao Zhu, and Baibiao Huang. Evidence of the existence of magnetism in pristine VX_2 monolayers (X = S, Se) and their strain-induced tunable magnetic properties. *ACS Nano*, 6(2):1695–1701, 2012.

[219] Nikhil Sivadas, Matthew W. Daniels, Robert H. Swendsen, Satoshi Okamoto, and Di Xiao. Magnetic ground state of semiconducting transition-metal trichalcogenide monolayers. *Phys. Rev. B*, 91(23):235425, 2015.

[220] Xingxing Li and Jinlong Yang. $CrXTe_3$ (X = Si, Ge) nanosheets: two dimensional intrinsic ferromagnetic semiconductors. *Journal of Materials Chemistry C*, 2(34):7071–7076, 2014.

[221] A. K. Geim and I. V. Grigorieva. Van der waals heterostructures. *Nature*, 499:419, 2013.

[222] Wei Han, Roland K. Kawakami, Martin Gmitra, and Jaroslav Fabian. Graphene spintronics. *Nature Nanotechnology*, 9:794, 2014.

[223] Behtash Behin-Aein, Deepanjan Datta, Sayeef Salahuddin, and Supriyo Datta. Proposal for an all-spin logic device with built-in memory. *Nature Nanotechnology*, 5:266, 2010.

[224] Roland K. Kawakami. Spin amplification by controlled symmetry breaking for spin-based logic. *2D Materials*, 2(3):034001, 2015.

[225] H. Dery, H. Wu, B. Ciftcioglu, M. Huang, Y. Song, R. Kawakami, J. Shi, I. Krivorotov, I. Zutic, and L. J. Sham. Nanospintronics based on magnetologic gates. *IEEE Transactions on Electron Devices*, 59(1):259–262, 2012.

[226] Hua Wen, Hanan Dery, Walid Amamou, Tiancong Zhu, Zhisheng Lin, Jing Shi, Igor uti, Ilya Krivorotov, L. J Sham, and Roland K. Kawakami. Experimental demonstration of XOR operation in graphene magnetologic gates at room temperature. *Physical Review Applied*, 5(4):044003, 2016. PRAPPLIED.

[227] Seinosuke Onari and Toshihiro Arai. Infrared lattice vibrations and dielectric dispersion in antiferromagnetic semiconductor $MnSe_2$. *Journal of the Physical Society of Japan*, 46(1):184–188, 1979.

[228] R. J. Pollard, V. H. McCann, and J. B. Ward. Magnetic structures of α-MnS and MnSe from 57Fe mossbauer spectroscopy. *Journal of Physics C: Solid State Physics*, 16(2):345–353, 1983.

[229] C. Ataca, H. ahin, and S. Ciraci. Stable, single-layer MX_2 transition-metal oxides and dichalcogenides in a honeycomb-like structure. *The Journal of Physical Chemistry C*, 116(16):8983–8999, 2012.

[230] Min Kan, Subash Adhikari, and Qiang Sun. Ferromagnetism in MnX_2 (X = S, Se) monolayers. *Physical Chemistry Chemical Physics*, 16(10):4990–4994, 2014.

[231] A. W. Arins, H. F. Jurca, J. Zarpellon, J. Varalda, I. L. Graff, W. H. Schreiner, and D. H. Mosca. Structure and magnetism of MnGa ultra-thin films on GaAs(111)b. *IEEE Transactions on Magnetics*, 49(12):5595–5598, 2013.

[232] T. M. Pekarek, B. C. Crooker, I. Miotkowski, and A. K. Ramdas. Magnetic measurements on the iii-vi diluted magnetic semiconductor $Ga_{1x}Mn_xSe$. *Journal of Applied Physics*, 83(11):6557–6559, 1998.

[233] Xiaodi Liu, Jianmin Ma, Peng Peng, and Wenjun Zheng. Hydrothermal synthesis of cubic $MnSe_2$ and octahedral α-MnSe microcrystals. *Journal of Crystal Growth*, 311(5):1359–1363, 2009.

[234] M. E. Schlesinger. The Mn-Se (manganese-selenium) system. *Journal of Phase Equilibria*, 19(6):588, 1998.

[235] Michel Bayard and M. J. Sienko. Anomalous electrical and magnetic properties of vanadium diselenide. *Journal of Solid State Chemistry*, 19(4):325–329, 1976.

[236] M. V. Kuznetsov, I. I. Ogorodnikov, A. S. Vorokh, A. S. Rasinkin, and A. N. Titov. Characterization of 1T-$TiSe_2$ surface by means of STM and XPD experiments and model calculations. *Surface Science*, 606(23):1760–1770, 2012.

[237] Roscoe G. Dickinson and Linus Pauling. The crystal structure of molybdenite. *Journal of the American Chemical Society*, 45(6):1466–1471, 1923.

[238] K. D. Bronsema, J. L. De Boer, and F. Jellinek. On the structure of molybdenum diselenide and disulfide. *Zeitschrift fr anorganische und allgemeine Chemie*, 540(910):15–17, 1986.

[239] W. J. Schutte, J. L. De Boer, and F. Jellinek. Crystal structures of tungsten disulfide and diselenide. *Journal of Solid State Chemistry*, 70(2):207–209, 1987.

[240] Xi He, Yi Wang, Ning Wu, Anthony N. Caruso, Elio Vescovo, Kirill D. Belashchenko, Peter A. Dowben, and Christian Binek. Robust isothermal electric control of exchange bias at room temperature. *Nature Materials*, 9:579, 2010.

[241] Xing Wenyu, Chen Yangyang, M. Odenthal Patrick, Zhang Xiao, Yuan Wei, Su Tang, Song Qi, Wang Tianyu, Zhong Jiangnan, Jia Shuang, X. C. Xie, Li Yan, and Han Wei. Electric field effect in multilayer $Cr_2Ge_2Te_6$: a ferromagnetic 2D material. *2D Materials*, 4(2):024009, 2017.

[242] Bevin Huang, Genevieve Clark, Dahlia R. Klein, David MacNeill, Efrn Navarro-Moratalla, Kyle L. Seyler, Nathan Wilson, Michael A. McGuire, David H. Cobden, Di Xiao, Wang Yao, Pablo Jarillo-Herrero, and Xiaodong Xu. Electrical control of 2d magnetism in bilayer CrI_3. *Nature Nanotechnology*, 2018.

[243] Shengwei Jiang, Lizhong Li, Zefang Wang, Kin Fai Mak, and Jie Shan. Controlling magnetism in 2D CrI_3 by electrostatic doping. *Nature Nanotechnology*, 2018.

[244] Shengwei Jiang, Jie Shan, and Kin Fai Mak. Electric-field switching of two-dimensional van der waals magnets. *Nature Materials*, 17(5):406–410, 2018.

[245] Zhi Wang, Tong-Yao Zhang, Mei Ding, Baojuan Dong, Yan-Xu Li, Mao-Lin Chen, Xiao-Xi Li, Yong Li, Da Li, Chuan-Kun Jia, Li-Dong Sun, Huaihong Guo, Dong-Ming Sun, Yuan-Sen Chen, Teng Yang, Jing Zhang, Shimpei Ono, Zheng Vitto Han, and Zhi-Dong Zhang. Electric-field control of magnetism in a few-layered van der waals magnet. *arXiv:1802.06255*, 2018.

[246] Hyun Ho Kim, Bowen Yang, Tarun Patel, Francois Sfigakis, Chenghe Li, Shangjie Tian, Hechang Lei, and Adam W. Tsen. One million percent tunnel magnetoresistance in a magnetic van der waals heterostructure. *arXiv:1804.00028*, 2018.

[247] Wang Xingzhi, Du Kezhao, Liu Yu Yang Fredrik, Hu Peng, Zhang Jun, Zhang Qing, Owen Man Hon Samuel, Lu Xin, Gan Chee Kwan, Sengupta Pinaki, Kloc Christian, and Xiong Qihua. Raman spectroscopy of atomically thin two-dimensional magnetic iron phosphorus trisulfide (feps 3) crystals. *2D Materials*, 3(3):031009, 2016.

[248] Igor uti, Alex Matos-Abiague, Benedikt Scharf, Hanan Dery, and Kirill Belashchenko. Proximitized materials. *Materials Today*, 2018.

[249] J. A. Gaj, R. Planel, and G. Fishman. Relation of magneto-optical properties of free excitons to spin alignment of Mn^{2+} ions in $Cd_{1x}Mn_xTe$. *Solid State Communications*, 29(5):435–438, 1979.

[250] Albert Fert, Vincent Cros, and Joao Sampaio. Skyrmions on the track. *Nature nanotechnology*, 8(3):152, 2013.

[251] Cui-Zu Chang, Jinsong Zhang, Xiao Feng, Jie Shen, Zuocheng Zhang, Minghua Guo, Kang Li, Yunbo Ou, Pang Wei, and Li-Li Wang. Experimental observation of the quantum anomalous hall effect in a magnetic topological insulator. *Science*, 340(6129):167–170, 2013.

[252] AR Mellnik, JS Lee, A Richardella, JL Grab, PJ Mintun, Mark H Fischer, Abolhassan Vaezi, Aurelien Manchon, E-A Kim, and Nitin Samarth. Spin-transfer torque generated by a topological insulator. *Nature*, 511(7510):449, 2014.

[253] Lee A Walsh, Christopher M Smyth, Adam T Barton, Qingxiao Wang, Zifan Che, Ruoyu Yue, Jiyoung Kim, Moon J Kim, Robert M Wallace, and Christopher L Hinkle. Interface chemistry of contact metals and ferromagnets on the topological insulator Bi_2Se_3. *The Journal of Physical Chemistry C*, 121(42):23551–23563, 2017.

[254] AV Matetskiy, IA Kibirev, T Hirahara, S Hasegawa, AV Zotov, and AA Saranin. Direct observation of a gap opening in topological interface states of $MnSe/Bi_2Se_3$ heterostructure. *Applied Physics Letters*, 107(9):091604, 2015.

[255] M Raju, A Yagil, Anjan Soumyanarayanan, Anthony KC Tan, A Almoalem, Fusheng Ma, OM Auslaender, and C Panagopoulos. The evolution of skyrmions in Ir/Fe/Co/Pt

multilayers and their topological hall signature. *Nature communications*, 10(1):696, 2019.

[256] Theresa P. Ginley and Stephanie Law. Growth of Bi_2Se_3 topological insulator films using a selenium cracker source. *Journal of Vacuum Science & Technology B*, 34(2):02L105, 2016.

[257] M. Prasad, A. K. Pandit, T. H. Ansari, and R. A. Singh. Electrical transport properties of manganese selenide. *Materials Chemistry and Physics*, 30(1):13–17, 1991.

[258] D. J. O' Hara, T. Zhu, and R. K. Kawakami. Importance of paramagnetic background subtraction for determining the magnetic moment in epitaxially grown ultrathin van der waals magnets. *IEEE Magnetics Letters*, 9:1–5, 2018.

[259] Ruoyu Yue, Yifan Nie, Lee A Walsh, Rafik Addou, Chaoping Liang, Ning Lu, Adam T Barton, Hui Zhu, Zifan Che, and Diego Barrera. Nucleation and growth of WSe_2: enabling large grain transition metal dichalcogenides. *2D Materials*, 4(4):045019, 2017.

[260] Ting Cao, Zhenglu Li, and Steven G. Louie. Tunable magnetism and half-metallicity in hole-doped monolayer GaSe. *Physical Review Letters*, 114(23):236602, 2015. PRL.

[261] Shujie Tang, Chaofan Zhang, Dillon Wong, Zahra Pedramrazi, Hsin-Zon Tsai, Chunjing Jia, Brian Moritz, Martin Claassen, Hyejin Ryu, Salman Kahn, Juan Jiang, Hao Yan, Makoto Hashimoto, Donghui Lu, Robert G. Moore, Chan-Cuk Hwang, Choongyu Hwang, Zahid Hussain, Yulin Chen, Miguel M. Ugeda, Zhi Liu, Xiaoming Xie, Thomas P. Devereaux, Michael F. Crommie, Sung-Kwan Mo, and Zhi-Xun Shen. Quantum spin hall state in monolayer 1T-WTe_2. *Nature Physics*, 13:683, 2017.

[262] Ping Kwan Johnny Wong, Wen Zhang, Fabio Bussolotti, Xinmao Yin, Tun Seng Herng, Lei Zhang, Yu Li Huang, Giovanni Vinai, Sridevi Krishnamurthi, Danil W. Bukhvalov, Yu Jie Zheng, Rebekah Chua, Alpha T. N'Diaye, Simon A. Morton, Chao-Yao Yang, Kui-Hon Ou Yang, Piero Torelli, Wei Chen, Kuan Eng Johnson Goh, Jun Ding, Minn-Tsong Lin, Geert Brocks, Michel P. de Jong, Antonio H. Castro Neto, and Andrew Thye Shen Wee. Evidence of spin frustration in a vanadium diselenide monolayer magnet. *Advanced Materials*, 31(23):1901185, 2019.

[263] CF Van Bruggen and C Haas. Magnetic susceptibility and electrical properties of VSe_2 single crystals. *Solid State Communications*, 20(3):251–254, 1976.

[264] rpd Psztor, Alessandro Scarfato, Cline Barreteau, Enrico Giannini, and Christoph Renner. Dimensional crossover of the charge density wave transition in thin exfoliated VSe_2. *2D Materials*, 4(4):041005, 2017.

[265] J. H. Lee, Zh. M. Wang, and G. J. Salamo. Ga-triggered oxide desorption from GaAs(100) and non-(100) substrates. *Applied Physics Letters*, 88(25):252108, 2006.

[266] Jiyong Yang, Weike Wang, Yan Liu, Haifeng Du, Wei Ning, Guolin Zheng, Chiming Jin, Yuyan Han, Ning Wang, Zhaorong Yang, Mingliang Tian, and Yuheng Zhang. Thickness dependence of the charge-density-wave transition temperature in VSe_2. *Applied Physics Letters*, 105(6):063109, 2014.

[267] Zhong-Liu Liu, Xu Wu, Yan Shao, Jing Qi, Yun Cao, Li Huang, Chen Liu, Jia-Ou Wang, Qi Zheng, and Zhi-Li Zhu. Epitaxially grown monolayer VSe_2: an air-stable magnetic two-dimensional material with low work function at edges. *Science Bulletin*, 63(7):419–425, 2018.

[268] Adam S. Ahmed, Hua Wen, Taisuke Ohta, Igor V. Pinchuk, Tiancong Zhu, Thomas Beechem, and Roland K. Kawakami. Molecular beam epitaxy growth of SrO buffer layers on graphite and graphene for the integration of complex oxides. *Journal of Crystal Growth*, 447:5–12, 2016.

[269] Yifan Nie, Chaoping Liang, Kehao Zhang, Rui Zhao, Sarah M. Eichfeld, Pil-Ryung Cha, Luigi Colombo, Joshua A. Robinson, Robert M. Wallace, and Kyeongjae Cho. First principles kinetic monte carlo study on the growth patterns of WSe_2 monolayer. *2D Materials*, 3(2):025029, 2016.

[270] Hans-Jrg Deiseroth, Krasimir Aleksandrov, Christof Reiner, Lorenz Kienle, and Reinhard K. Kremer. Fe_3GeTe_2 and Ni_3GeTe_2 - Two new layered transition-metal compounds: Crystal structures, HRTEM investigations, and magnetic and electrical properties. *European Journal of Inorganic Chemistry*, 2006(8):1561–1567, 2006.

[271] Dongseuk Kim, Sijin Park, Jinhwan Lee, Jungbum Yoon, Sungjung Joo, Taeyueb Kim, Kil-joon Min, Seung-Young Park, Changsoo Kim, Kyoung-Woong Moon, Changgu Lee, Jisang Hong, and Chanyong Hwang. Antiferromagnetic coupling of van der waals ferromagnetic Fe_3GeTe_2. *Nanotechnology*, 30(24):245701, 2019.

[272] Shanshan Liu, Xiang Yuan, Yichao Zou, Yu Sheng, Ce Huang, Enze Zhang, Jiwei Ling, Yanwen Liu, Weiyi Wang, Cheng Zhang, Jin Zou, Kaiyou Wang, and Faxian Xiu. Wafer-scale two-dimensional ferromagnetic Fe_3GeTe_2 thin films grown by molecular beam epitaxy. *npj 2D Materials and Applications*, 1(1):30, 2017.

[273] Jieyu Yi, Houlong Zhuang, Qiang Zou, Zhiming Wu, Guixin Cao, Siwei Tang, S. A. Calder, P. R. C. Kent, David Mandrus, and Zheng Gai. Competing antiferromagnetism in a quasi-2D itinerant ferromagnet: Fe_3GeTe_2. *2D Materials*, 4(1):011005, 2016.

[274] Yun Zhang, Haiyan Lu, Xiegang Zhu, Shiyong Tan, Wei Feng, Qin Liu, Wen Zhang, Qiuyun Chen, Yi Liu, Xuebing Luo, Donghua Xie, Lizhu Luo, Zhengjun Zhang, and Xinchun Lai. Emergence of kondo lattice behavior in a van der waals itinerant ferromagnet, Fe_3GeTe_2. *Science Advances*, 4(1):eaao6791, 2018.

[275] Qian Li, Mengmeng Yang, Cheng Gong, Rajesh V. Chopdekar, Alpha T. NDiaye, John Turner, Gong Chen, Andreas Scholl, Padraic Shafer, Elke Arenholz, Andreas K. Schmid, Sheng Wang, Kai Liu, Nan Gao, Alemayehu S. Admasu, Sang-Wook Cheong,

Chanyong Hwang, Jia Li, Feng Wang, Xiang Zhang, and Ziqiang Qiu. Patterning-induced ferromagnetism of Fe_3GeTe_2 van der waals materials beyond room temperature. *Nano Letters*, 18(9):5974–5980, 2018.

[276] Houlong L. Zhuang, P. R. C. Kent, and Richard G. Hennig. Strong anisotropy and magnetostriction in the two-dimensional stoner ferromagnet Fe_3GeTe_2. *Physical Review B*, 93(13):134407, 2016. PRB.

[277] Jian-Xin Zhu, Marc Janoschek, D. S. Chaves, J. C. Cezar, Tomasz Durakiewicz, Filip Ronning, Yasmine Sassa, Martin Mansson, B. L. Scott, N. Wakeham, Eric D. Bauer, and J. D. Thompson. Electronic correlation and magnetism in the ferromagnetic metal Fe_3GeTe_2. *Physical Review B*, 93(14):144404, 2016. PRB.

[278] Bin Chen, JinHu Yang, HangDong Wang, Masaki Imai, Hiroto Ohta, Chishiro Michioka, Kazuyoshi Yoshimura, and MingHu Fang. Magnetic properties of layered itinerant electron ferromagnet Fe_3GeTe_2. *Journal of the Physical Society of Japan*, 82(12):124711, 2013.

[279] H. Yoshida, J. Chiba, T. Kaneko, Y. Fujimori, and S. Abe. Pressure effect on the curie temperature of $CrBr_3$. *Physica B: Condensed Matter*, 237-238:525–526, 1997.

[280] Suchanda Mondal, Murugesan Kannan, Moumita Das, Linganan Govindaraj, Ratnadwip Singha, Biswarup Satpati, Sonachalam Arumugam, and Prabhat Mandal. Effect of hydrostatic pressure on ferromagnetism in two-dimensional CrI_3. *Physical Review B*, 99(18):180407, 2019. PRB.

[281] Z. E. Brubaker, R. L. Stillwell, P. Chow, Y. Xiao, C. Kenney-Benson, R. Ferry, D. Popov, S. B. Donald, P. Sderlind, D. J. Campbell, J. Paglione, K. Huang, R. E. Baumbach, R. J. Zieve, and J. R. Jeffries. Pressure-dependent intermediate valence behavior in $YbNiGa_4$ and $YbNiIn_4$. *Physical Review B*, 98(21):214115, 2018. PRB.

[282] Zhenhua Chi, Xuliang Chen, Fei Yen, Feng Peng, Yonghui Zhou, Jinlong Zhu, Yijin Zhang, Xiaodi Liu, Chuanlong Lin, Shengqi Chu, Yanchun Li, Jinggeng Zhao, Tomoko Kagayama, Yanming Ma, and Zhaorong Yang. Superconductivity in pristine $2H_a$-MoS_2 at ultrahigh pressure. *Physical Review Letters*, 120(3):037002, 2018. PRL.

[283] Zhisheng Lin, Mark Lohmann, Zulfikhar A. Ali, Chi Tang, Junxue Li, Wenyu Xing, Jiangnan Zhong, Shuang Jia, Wei Han, Sinisa Coh, Ward Beyermann, and Jing Shi. Pressure-induced spin reorientation transition in layered ferromagnetic insulator $Cr_2Ge_2Te_6$. *Physical Review Materials*, 2(5):051004, 2018. PRMATERIALS.

[284] Y. Sun, R. C. Xiao, G. T. Lin, R. R. Zhang, L. S. Ling, Z. W. Ma, X. Luo, W. J. Lu, Y. P. Sun, and Z. G. Sheng. Effects of hydrostatic pressure on spin-lattice coupling in two-dimensional ferromagnetic $Cr_2Ge_2Te_6$. *Applied Physics Letters*, 112(7):072409, 2018.

[285] Andrew F. May, Stuart Calder, Claudia Cantoni, Huibo Cao, and Michael A. McGuire. Magnetic structure and phase stability of the van der waals bonded ferromagnet $Fe_{3-x}GeTe_2$. *Physical Review B*, 93(1):014411, 2016. PRB.

[286] H. K. Mao, J. Xu, and P. M. Bell. Calibration of the ruby pressure gauge to 800 kbar under quasi-hydrostatic conditions. *Journal of Geophysical Research: Solid Earth*, 91(B5):4673–4676, 1986.

[287] Xuefei Wang, Xuliang Chen, Yonghui Zhou, Changyong Park, Chao An, Ying Zhou, Ranran Zhang, Chuanchuan Gu, Wenge Yang, and Zhaorong Yang. Pressure-induced iso-structural phase transition and metallization in WSe_2. *Scientific reports*, 7:46694, 2017.

[288] Xiangqi Wang, Zeyu Li, Min Zhang, Tao Hou, Jinggeng Zhao, Lin Li, Azizur Rahman, Zilong Xu, Junbo Gong, Zhenhua Chi, Rucheng Dai, Zhongping Wang, Zhenhua Qiao, and Zengming Zhang. Pressure-induced modification of the anomalous hall effect in layered Fe_3GeTe_2. *Physical Review B*, 100(1):014407, 2019. PRB.

[289] Udhara S Kaluarachchi, Sergey L Budko, Paul C Canfield, and Valentin Taufour. Tricritical wings and modulated magnetic phases in $LaCrGe_3$ under pressure. *Nature communications*, 8(1):546, 2017.

[290] R. von Helmolt, J. Wecker, B. Holzapfel, L. Schultz, and K. Samwer. Giant negative magnetoresistance in perovskitelike $La_{2/3}Ba_{1/3}MnO_x$ ferromagnetic films. *Physical Review Letters*, 71(14):2331–2333, 1993. PRL.

[291] D. Hammer, J. Wu, and C. Leighton. Metal-insulator transition, giant negative magnetoresistance, and ferromagnetism in $laco_{1-y}ni_yo_3$. *Physical Review B*, 69(13):134407, 2004. PRB.

[292] J. G. Checkelsky, Minhyea Lee, E. Morosan, R. J. Cava, and N. P. Ong. Anomalous hall effect and magnetoresistance in the layered ferromagnet $Fe_{14}TaS_2$: The inelastic regime. *Physical Review B*, 77(1):014433, 2008. PRB.

[293] Yu Liu, Eli Stavitski, Klaus Attenkofer, and C. Petrovic. Anomalous hall effect in the van der waals bonded ferromagnet $Fe_{3-x}GeTe_2$. *Physical Review B*, 97(16):165415, 2018. PRB.

[294] Yihao Wang, Cong Xian, Jian Wang, Bingjie Liu, Langsheng Ling, Lei Zhang, Liang Cao, Zhe Qu, and Yimin Xiong. Anisotropic anomalous hall effect in triangular itinerant ferromagnet Fe_3GeTe_2. *Physical Review B*, 96(13):134428, 2017. PRB.

[295] Tru Moriya. Recent progress in the theory of itinerant electron magnetism. *Journal of Magnetism and Magnetic Materials*, 14(1):1–46, 1979.

[296] C. M. B. Bacaltchuk, G. A. Castello-Branco, M. Ebrahimi, H. Garmestani, and A. D. Rollett. Effect of magnetic field applied during secondary annealing on texture and grain size of silicon steel. *Scripta Materialia*, 48(9):1343–1347, 2003.

[297] M. G. Benz and D. L. Martin. Mechanism of sintering in cobalt rareearth permanent-magnet alloys. *Journal of Applied Physics*, 43(7):3165–3170, 1972.

[298] David Brown, Bao-Min Ma, and Zhongmin Chen. Developments in the processing and properties of NdFeB-type permanent magnets. *Journal of Magnetism and Magnetic Materials*, 248(3):432–440, 2002.

[299] K. M. Chowdary, A. K. Giri, K. Pellerin, S. A. Majetich, and J. H. J. Scott. Annealing effects on the coercivity of $SmCo_5$ nanoparticles. *Journal of Applied Physics*, 85(8):4331–4333, 1999.

[300] B. Z. Cui, A. M. Gabay, W. F. Li, M. Marinescu, J. F. Liu, and G. C. Hadjipanayis. Anisotropic $SmCo_5$ nanoflakes by surfactant-assisted high energy ball milling. *Journal of Applied Physics*, 107(9):09A721, 2010.

[301] Wei-Bin Cui, Yukiko K. Takahashi, and Kazuhiro Hono. $Nd_2Fe_{14}B$/FeCo anisotropic nanocomposite films with a large maximum energy product. *Advanced Materials*, 24(48):6530–6535, 2012.

[302] O. Gutfleisch. Controlling the properties of high energy density permanent magnetic materials by different processing routes. *Journal of Physics D: Applied Physics*, 33(17):R157–R172, 2000.

[303] Yanglong Hou, Shouheng Sun, Chuanbing Rong, and J. Ping Liu. $SmCo_5$Fe nanocomposites synthesized from reductive annealing of oxide nanoparticles. *Applied Physics Letters*, 91(15):153117, 2007.

[304] Y. Hou, Z. Xu, S. Peng, C. Rong, J.P. Liu, and S. Sun. A facile synthesis of $SmCo_5$ magnets from core/shell Co/Sm_2O_3 nanoparticles. *Advanced Materials*, 19(20):3349–3352, 2007.

[305] G. S. Cargill III and T. Mizoguchi. Dipolar mechanisms for magnetic anisotropy in amorphous ferrimagnetic alloys. *Journal of Applied Physics*, 49(3):1753–1755, 1978.

[306] Paul J. Jorgensen and Robert W. Bartlett. Solid-phase sintering of $SmCo_5$. *Journal of the Less Common Metals*, 37(2):205–212, 1974.

[307] Hiroaki Kato, Terunobu Miyazaki, Masato Sagawa, and Keiichi Koyama. Coercivity enhancements by high-magnetic-field annealing in sintered Nd-Fe-B magnets. *Applied Physics Letters*, 84(21):4230–4232, 2004.

[308] E. F. Kneller and R. Hawig. The exchange-spring magnet: a new material principle for permanent magnets. *IEEE Transactions on Magnetics*, 27(4):3588–3560, 1991.

[309] Kaplesh Kumar. $RETM_5$ and RE_2TM_{17} permanent magnets development. *Journal of Applied Physics*, 63(6):R13–R57, 1988.

[310] B. A. Legrand, D. Chateigner, R. Perrier de la Bathie, and R. Tournier. Orientation by solidification in a magnetic field a new process to texture SmCo compounds used as permanent magnets. *Journal of Magnetism and Magnetic Materials*, 173(1):20–28, 1997.

[311] D. S. Li, H. Garmestani, Shi-shen Yan, M. Elkawni, M. B. Bacaltchuk, H. J. Schneider-Muntau, J. P. Liu, S. Saha, and J. A. Barnard. Effects of high magnetic field annealing on texture and magnetic properties of FePd. *Journal of Magnetism and Magnetic Materials*, 281(2):272–275, 2004.

[312] Hailing Li, Xiaohong Li, Defeng Guo, Li Lou, Wei Li, and Xiangyi Zhang. Three-dimensional self-assembly of core/shell-like nanostructures for high-performance nanocomposite permanent magnets. *Nano Letters*, 16(9):5631–5638, 2016.

[313] Fei Liu, Yanglong Hou, and Song Gao. Exchange-coupled nanocomposites: chemical synthesis, characterization and applications. *Chemical Society Reviews*, 43(23):8098–8113, 2014.

[314] Zhenhui Ma, Tianli Zhang, and Chengbao Jiang. Exchange-coupled $SmCo_5$/Co nanocomposites synthesized by a novel strategy. *RSC Advances*, 5(108):89128–89132, 2015.

[315] N. Masahashi, M. Matsuo, and K. Watanabe. Development of preferred orientation in annealing of Fe3.25%Si in a high magnetic field. *Journal of Materials Research*, 13(2):457–461, 1998.

[316] Raja K. Mishra, J. K. Chen, and G. Thomas. Effect of annealing on the microstructure of sintered NdFeB magnets. *Journal of Applied Physics*, 59(6):2244–2246, 1986.

[317] Ketan Patel, Jingming Zhang, and Shenqiang Ren. Rare-earth-free high energy product manganese-based magnetic materials. *Nanoscale*, 10(25):11701–11718, 2018.

[318] Chuanbing Rong, Ying Zhang, Narayan Poudyal, Izabela Szlufarska, Rainer J. Hebert, M. J. Kramer, and J. Ping Liu. Self-nanoscaling of the soft magnetic phase in bulk SmCo/Fe nanocomposite magnets. *Journal of Materials Science*, 46(18):6065–6074, 2011.

[319] M. Sagawa, S. Fujimura, N. Togawa, H. Yamamoto, and Y. Matsuura. New material for permanent magnets on a base of Nd and Fe (invited). *Journal of Applied Physics*, 55(6):2083–2087, 1984.

[320] S. Sawatzki, R. Heller, Ch. Mickel, M. Seifert, L. Schultz, and V. Neu. Largely enhanced energy density in epitaxial $SmCo_5$/Fe/$SmCo_5$ exchange spring trilayers. *Journal of Applied Physics*, 109(12):123922, 2011.

[321] A. D. Sheikh-Ali, D. A. Molodov, and H. Garmestani. Magnetically induced texture development in zinc alloy sheet. *Scripta Materialia*, 46(12):857–862, 2002.

[322] Bo Shen, Adriana Mendoza-Garcia, Sarah E. Baker, Scott K. McCall, Chao Yu, Li-heng Wu, and Shouheng Sun. Stabilizing fe nanoparticles in the $SmCo_5$ matrix. *Nano Letters*, 17(9):5695–5698, 2017.

[323] Ralph Skomski and J. M. D. Coey. Giant energy product in nanostructured two-phase magnets. *Physical Review B*, 48(21):15812–15816, 1993. PRB.

[324] K. Tanaka, T. Ichitsubo, and M. Koiwa. Effect of external fields on ordering of FePd. *Materials Science and Engineering: A*, 312(1):118–127, 2001.

[325] M. T. Thompson. Practical issues in the use of NdFeB permanent magnets in maglev, motors, bearings, and eddy current brakes. *Proceedings of the IEEE*, 97(11):1758–1767, 2009.

[326] Y. Tsubokawa, R. Shimizu, S. Hirosawa, and M. Sagawa. Effect of heat treatment on grainboundary microstructure in NdFeB sintered magnet. *Journal of Applied Physics*, 63(8):3319–3320, 1988.

[327] H. Y. Wang, X. K. Ma, Y. J. He, S. Mitani, and M. Motokawa. Enhancement in ordering of FePt films by magnetic field annealing. *Applied Physics Letters*, 85(12):2304–2306, 2004.

[328] J. Wecker, M. Katter, and L. Schultz. Mechanically alloyed SmCo materials. *Journal of Applied Physics*, 69(8):6058–6060, 1991.

[329] Hao Zeng, Jing Li, J. P. Liu, Zhong L. Wang, and Shouheng Sun. Exchange-coupled nanocomposite magnets by nanoparticle self-assembly. *Nature*, 420(6914):395–398, 2002.

[330] Hao Zeng, Jing Li, Z. L. Wang, J. P. Liu, and Shouheng Sun. Bimagnetic core/shell $FePt/Fe_3O_4$ nanoparticles. *Nano Letters*, 4(1):187–190, 2004.

[331] G. F. Zhou, S. Y. Fu, X. K. Sun, and Y. C. Chuang. Influence of annealing on the magnetic properties and microstructure of Nd-Fe-B based magnets. *physica status solidi (a)*, 121(1):257–264, 1990.

[332] J. Zhou, R. Skomski, Y. Liu, Y. C. Sui, W. Liu, and D. J. Sellmyer. Rapidly annealed exchange-coupled Sm-CoCo multilayers. *Journal of Applied Physics*, 97(10):10K304, 2005.

Appendix A

Thermal processing of Co/Sm multilayered films via isochronal magnetic field annealing

A.1 Abstract

Achieving and retaining a high energy density at high operating temperatures is an engineering challenge for hard-phase permanent magnets. Here, the control of coercivity and remanence is reported in $[Sm/Co]_n$ multilayered films via thermal processing. Magnetic and structural characterization shows that after isochronal annealing the $[Sm/Co]_n$ structure at moderate temperatures (750 K), the Sm reacts with Co and forms a $[Co/SmCo_5]_n$ structure. Magnetic field annealing in fields up to 50 kOe induces a uniaxial magnetic anisotropy in the elemental Co prior to the thermal reaction of Sm and Co. Low magnetic field anneals

below 10 kOe increase the squareness and coercivity of the Co/$SmCo_5$ structure while high fields up to 50 kOe begin to diminish the magnetic properties. Further isochronal annealing at higher temperatures above 800 K degrades the ferromagnetic properties, which is likely due to the structural decomposition of the $SmCo_5$ layers. This work demonstrates a method to investigate the both the effect of magnetic field annealing on the $SmCo_5$ compound and the operational limits of a potential nanocomposite magnet.

A.2 Introduction

Permanent magnets are key components in clean energy production such as compact motors in wind-powered turbine generators and in environmental protection such as regenerative braking in electric and hybrid vehicles. For compact high-performance applications, permanent magnets are generally composed of rare-earth-based intermetallic alloys (e.g. Sm-Co, Nd-Fe-B) which have high coercivity (H_C) and correspondingly large energy products ($|BH|_{Max}$) although these benefits are offset by high material cost and supply risks. Exchange spring magnets, which consist of a nanocomposite mixture of highly coercive magnetic hard phases that are exchange coupled to a magnetic soft phase with high remanence, offer the potential to increase the energy product while simultaneously reducing the critical rare-earth element material intensity [304, 308, 313, 314, 322, 323, 329, 330]. In compact motor technologies, permanent magnets need to retain both a high remanent magnetization and coercive field at high operating temperatures . Commercial standard $Nd_2Fe_{14}B$ magnets are limited by their low operating temperatures (e.g. 150°C) [298, 325], in which additional amounts of Tb and Dy preserve Nd's magnetic properties at high tem-

peratures, comes at a high cost. The Sm-Co system is appealing for such applications, due to high Curie temperatures of the materials ($SmCo_5$ (T_c = 750°C), Sm_2Co_{17} (T_c = 850°C), Co (T_c = 1115°C)) [300, 301, 304, 312, 318, 320], and excellent magnetocrystalline anisotropy.

The structural and magnetic properties of hard-phase permanent magnets (e.g. Sm-Co, $L1_0$ CoPt, Nd-Fe-B, MnBi) are sensitive to thermal processing conditions [298, 302, 310, 311, 327, 332], which leads to many challenges in achieving and retaining a high energy density. For instance, a high temperature anneal around 600°C is known to obtain a high coercivity in sintered Nd-Fe-B magnets [326, 331], while a magnetic field anneal can induce a preferred orientation of the crystal [307]. It is also known that upon rapid thermal annealing of Sm-Co/Co multilayered films at 525°C, an exchange-coupled, single-phase magnet can be obtained with a large energy product [332].

This work presents a study of isochronal annealing of superlattices of Sm and Co, wherein the coercive $SmCo_5$ phase is formed and exchange coupled to unreacted Co through successive heat treatments. Magnetic field annealing is employed to study the effects of imposing a preferential orientation during reaction, and the phase stability of the nanocomposite magnet is reported.

A.3 Materials and Methods

Samples are prepared by direct current (DC) magnetron sputtering in a high-vacuum chamber with a base pressure of $\sim 5 \times 10^{-7}$ Torr. Base layers of Co/Cu/Ti are grown on AlN wafers to create adhesion for the $[Sm/Co]_n$ growth. All samples are grown at

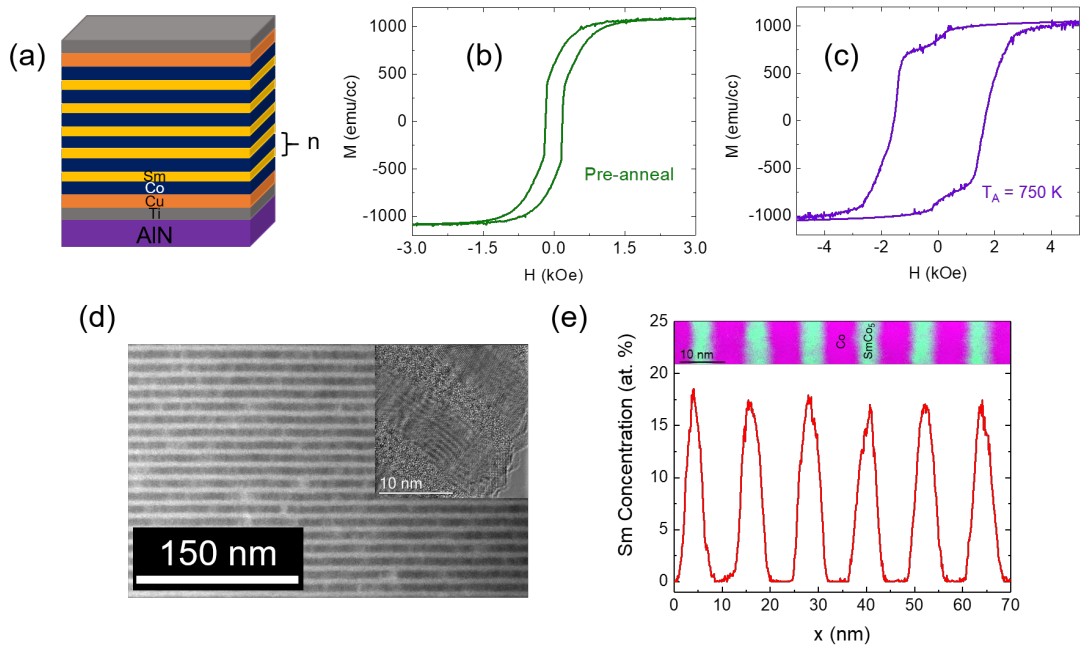


Figure A.1: Thermal processing of $[Sm/Co]_n$ multilayered films. (a) Schematic of a $[Sm/Co]_n$ multilayered stack prior to thermal reaction. (b-c) Room temperature in-plane ferromagnetic hysteresis loop of $[Sm(21.9\ Å)/Co(100\ Å)]_{167}$ before and after Sm-Co reaction at 750 K, respectively. (d) STEM image showing sharp, distinct alternate planes of Co and $SmCo_5$. Inset: Plan view TEM showing crystalline Co layers with adjacent amorphous $SmCo_5$ layers. (e) EELS linescan showing sharp transitions from Co to $SmCo_5$ layers. Inset: EELS map of the Co/$SmCo_5$ structure with purple representing the Co layers and teal representing the $SmCo_5$ layers, respectively.

room temperature. Elemental Sm and Co are evaporated from commercial standard sputtering targets. Capping layers consisting of Ti/Cu/Co are grown on top of the $[Sm/Co]_n$ multilayers to further protect the sample from surface oxidation and impurities. Film thicknesses are calibrated using flux measurements and cross-checked with x-ray reflectometry scans of elemental films. In this study, $[Sm/Co]_n$ multilayers consisting of the following structure: $[Sm(21.9\ Å)/Co(100\ Å)]_{167}$, are used with a total thickness of 2 μm. The samples are thermally processed by isochronal annealing in a 160 kOe physical properties measurement system (PPMS, Quantum Design) equipped with a vibrating sample magnetometer (VSM) oven option, allowing for sample temperatures of up to 1000 K. All anneals are performed for 1 hour in 100 K steps from room temperature, up to the 700 K, and 25 K steps thereafter (50 K/min ramp rate). In-plane magnetization loops, M(H), are measured at room temperature after each subsequent anneal. The crystal structure and composition of the samples are measured by electron energy loss spectroscopy (EELS) and scanning transmission electron microscopy (STEM). The element-specific magnetic properties of the samples are measured by soft x-ray absorption spectroscopy (XAS) and x-ray magnetic circular dichroism (XMCD) on beamline 6.3.1 of the Advanced Light Source.

A.4 Experimental Results and Discussion

The magnetic properties of the as-deposited $[Sm(21.9\ Å)/Co(100\ Å)]_{167}$ (total thickness = 2 μm) samples (schematic shown in Figure A.1a) are dominated by the elemental Co, as shown in the magnetization loop in Figure A.1b. Upon annealing at 750 K, the Sm-Co hard phase forms giving a coercive, two-phase ferromagnetic hysteresis loop shown in Figure

A.1c. Subsequent STEM micrographs are shown in Figure xxd showing sharp and distinct alternating planes of a Co (7 nm) and $SmCo_5$ (4 nm) structure after thermal processing. Figure A.1e shows an EELS linescan showing a 1:5 Sm:Co stoichiometric ratio by comparing the Sm concentration in the $SmCo_5$ to the adjacent elemental Co layers. The inset shows an EELS map encompassing the alternating layers of the Co/$SmCo_5$ structure. This confirms that the Sm is entirely consumed in the reaction with Co to give amorphous $SmCo_5$ layers and leaves an excess of adjacent crystalline Co layers, where the atomic structure of the crystalline layers is clearly shown in the Figure A.1d inset via plan view TEM. Continued anneals above 800 K begin to degrade the ferromagnetic properties of the sample, with a sharp decrease in the coercive field and remanent magnetization. This degradation at high temperatures (up to 1000 K) is likely due to the slow structural decomposition of $SmCo_5$ into Sm_2Co_{17}, Sm_2Co_7 ($T_C = 432°C$), and/or Sm_5Co_{19} ($T_C = 513°C$) [297, 306, 309, 328], as well as face-centered-cubic (fcc) Co and Sm_2O_3 [299].

Applying a magnetic field during the isochronal annealing process leads to a drastic increase in the magnetic remanence after an anneal at 500 K. This suggests the application of a magnetic field influences the magnetic anisotropy in the elemental Co. Figure A.2a shows a magnetization loop comparison of a 500 K anneal with and without an application of a 10 kOe applied field. Previous reports have shown that a well-defined uniaxial anisotropy can be obtained in amorphous soft magnets due to pairwise texture induced by magnetic field annealing [305]. Rotating the sample by 90° in-plane (transverse) and out-of-plane (perpendicular) confirms that a uniaxial magnetic anisotropy is induced.

Upon annealing at 750 K under several applied fields (Figure A.2c), similar mag-

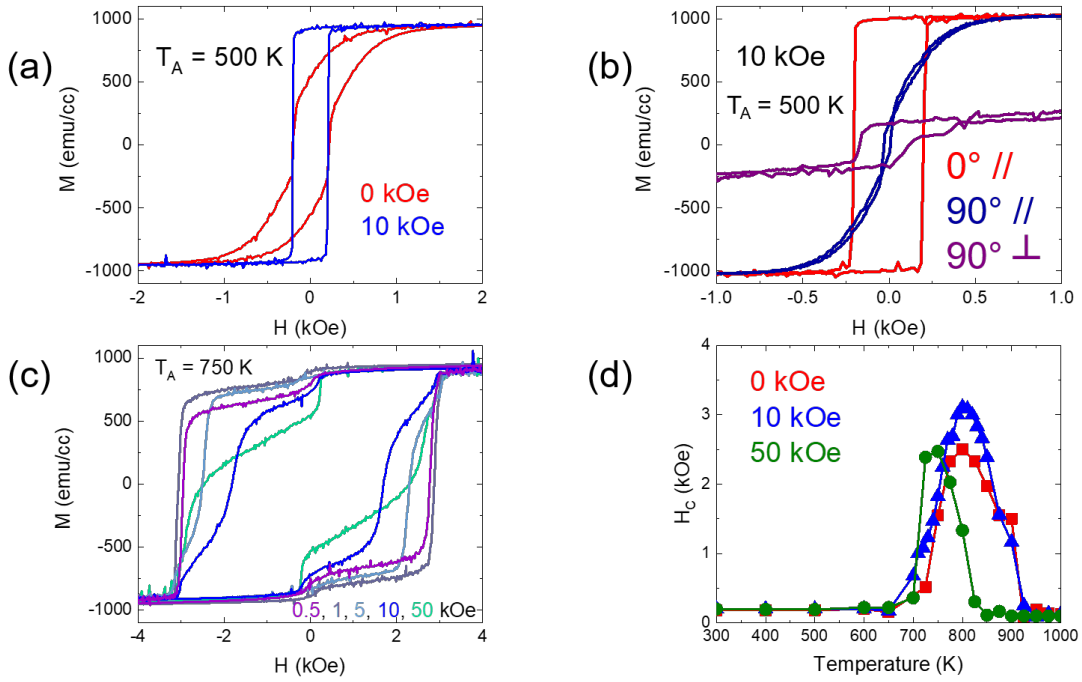


Figure A.2: Magnetic field annealing on $[Sm(21.9\ Å)/Co(100\ Å)]_{167}$ multilayered films. (a) In-plane magnetic hysteresis loops of $[Sm/Co]_n$ annealed at 500 K with (blue) and without (red) an applied external field showing change in magnetic remanence. (b) Angular dependence of 500 K field-annealed sample confirming an induced in-plane uniaxial magnetic anisotropy. (c) M(H) loops of $[Sm/Co]_n$ annealed at 750 K with an application of different external magnetic fields showing changes in the squareness and coercivity. (d) Coercive field as a function of annealing temperature at different applied external magnetic fields.

netic hysteresis loops are obtained compared to the samples with no applied field (Figure A.1c), suggesting that the formation of the $SmCo_5$ hard phase is not affected by the application of a magnetic field. In fact, at low and moderate fields, the loop squareness and coercivity increases as shown in Figures A.2c and d. This behavior may also be related to reports of preferential domain nucleation while annealing under a magnetic field [296, 310, 315, 321, 324], but the underlying mechanism remains unclear. Modifying the strength of the field applied during annealing suggests that higher values are detrimental, with a 10 kOe field yielding higher coercivities than a 50 kOe field.

If applied magnetic fields lead to orientation of elemental Co, then it is possible that higher fields can cause sufficient orientation to limit the exchange coupling or else drive a phase segregation that hinders $SmCo_5$ formation. Examining the ratio of hard to soft phases in the hysteresis loops in Figure A.2c reveals an increased fraction of soft, elemental Co for higher applied fields. High field-anneals from 10 to 50 kOe show a $\sim$60-70% hard/soft ratio with a two-phase hysteretic behavior, while low applied fields from 500 Oe to 5 kOe gives nearly a 100% single phase square loop. It is apparent that low and moderate applied fields act to orient the Co and improve the coercivity of the resulting $SmCo_5$, but higher fields lead to a diminished magnetic performance.

The magnetic field dependence and two-phase magnetic behavior can be further examined through element-specific XMCD hysteresis loops measured in surface sensitive total electron yield mode. Figure A.3a shows a hysteresis loop for Co at the L_3 edge after annealing at 800 K under a 10 kOe field. A low coercivity of $<$1 kOe is observed, in contrast to the hard phase previously observed in the bulk-sensitive VSM loops, and

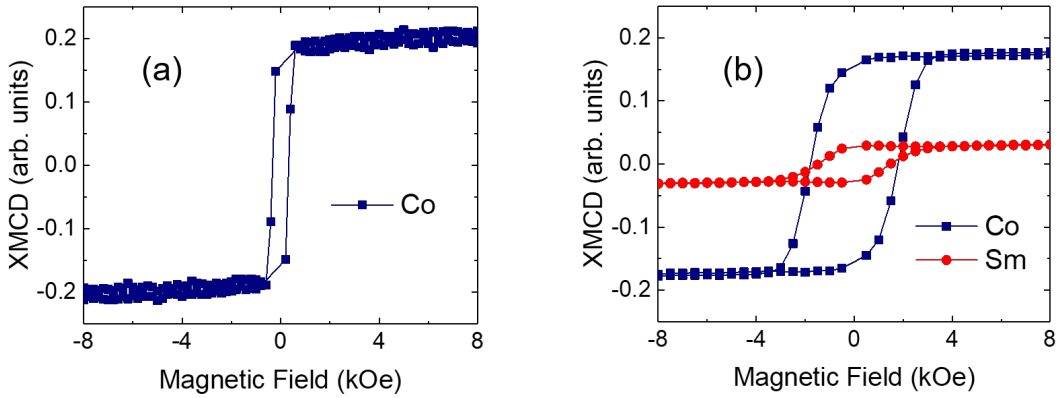


Figure A.3: Element-specific XMCD on a $[Sm(21.9\ Å)/Co(100\ Å)]_{167}$ multilayered film after an 800 K anneal under a 10 kOe field. (a) Elemental Co (blue) XMCD prior to mechanically polishing the surface of the film showing a soft magnetic hysteresis loop. (b) Elemental Co (blue) and Sm (red) XMCD after mechanically polishing off the top layers of the film showing hard magnetization loops of the two elements present, thus confirming $SmCo_5$ reaction.

no magnetic signal is observed for elemental Sm. To further investigate, the sample is mechanically polished to expose the $SmCo_5$ layer and re-measured. Figure A.3b shows a significantly larger coercivity for the Co XMCD magnetic hysteresis loop and the emergence of a coincident Sm XMCD loop. This indicates the presence of an unreacted, uncoupled layer of Co at the surface. Such spatial segregation could arise from interdiffusion of the Cu and Ti capping layers, which act to inhibit the Sm-Co reaction, and give rise to the two-phase behavior observed in the VSM hysteresis loops. XAS/XMCD spectra measurements (not shown) did not reveal any evidence of oxidation of the Sm or Co meaning the ferromagnetic signal is not a result of any related oxide compounds.

A.5 Summary and Conclusions

In summary, thermal processing is employed to study the ferromagnetic properties of a Sm/Co superlattice. Isochronal annealing of $[Sm/Co]_n$ multilayered films at moderate temperatures (750 K) forms a hard ferromagnetic hysteresis loop from a Sm and Co reaction. Annealing at higher temperatures (above 800 K) leads to decomposition of the $SmCo_5$ compound into different Sm-Co species such as Sm_2Co_{17}, Sm_2Co_7, Sm_5Co_{19} and/or the yielding of different byproducts such as fcc Co or Sm_2O_3. Further investigation using the application of low and high magnetic fields during the annealing process leads to an observation of a uniaxial magnetic anisotropy in the elemental Co and an influence on the loop squareness and coercivity in $SmCo_5$. Element-specific XMCD confirms the magnetic hard phase in the Sm and Co XMCD hysteresis loops after mechanically polishing the top layers of the structure. With this, a way to investigate the thermally-driven diffusion mechanisms for multilayered Sm/Co films and operational limits for reacted $SmCo_5$ layers is provided and can be a test bed for a potential nanocomposite magnet.

Appendix B

MBE Growth Recipes

B.1 γ-GaSe on GaAs(111)B

(1) Mount cleaved 10 $\times$ 10 mm^2 GaAs(111)B substrate to un-polished Si(100) backing wafer via indium bonding.

(2) Mount backing wafer onto uni-block and trolley.

(3) Load into load lock chamber and pump down to rough vacuum. Anneal at 200°C for 1 hour, then cool down.

(4) Open to buffer chamber and load sample onto buffer heater.

(5) Anneal sample at 400°C for 15 minutes then cool down to room temperature.

(6) In the meantime, measure beam fluxes of Ga and Se cracker to be 1:100 flux ratio.

(7) Load sample into main chamber after measuring fluxes and heat sample to 600°C.

(8) Anneal for 20 min. with Se open until native oxide is removed and GaAs

RHEED pattern appears.

(9) Cool down to 400°C with Se remaining open.

(10) Open Ga and Se shutters at 400°C and grow for desired time. Growth rate is typically 1 nm/min.

(11) Close both shutters, and cool to room temperature.

(12) If necessary, cap with amorphous chalcogen material (Se or Te).

B.2 $SnSe_2$ on GaAs(111)B

(1) Mount cleaved 10 × 10 mm^2 GaAs(111)B substrate to un-polished Si(100) backing wafer via indium bonding.

(2) Mount backing wafer onto uni-block and trolley.

(3) Load into load lock chamber and pump down to rough vacuum. Anneal at 200°C for 1 hour, then cool down.

(4) Open to buffer chamber and load sample onto buffer heater.

(5) Anneal sample at 400°C for 15 minutes then cool down to room temperature.

(6) In the meantime, measure beam fluxes of Sn and Se cracker to be 1:60 flux ratio.

(7) Load sample into main chamber after measuring fluxes and heat sample to 600°C.

(8) Anneal for 20 min. with Se open until native oxide is removed and GaAs RHEED pattern appears.

(9) Cool down to 165°C with Se remaining open.

(10) Open Sn and Se shutters at 165°C and grow for desired time. Growth rate is typically 3 nm/min.

(11) Close both shutters, and cool to room temperature.

(12) If necessary, cap with amorphous chalcogen material (Se or Te).

B.3 Monolayer $MnSe_2$ and α-MnSe(111)

For growth on GaSe/GaAs(111)B surfaces:

(1) After growth of GaSe base layer, deposit Mn and Se (close Ga shutter), Mn can grow at any flux ratio to Se, typically ran at 9-20 secs/ML depending on cell temperature.

(2) Close Mn and Se shutters and cool to room temperature (unless capping with more GaSe, then close Mn shutter and re-open Ga until capping thickness reached).

(3) Cap with amorphous chalcogen material.

For growth on $SnSe_2$/GaAs(111)B surfaces:

(1) After growth of $SnSe_2$ base layer, deposit Mn and Se (close Ga shutter), Mn can grow at any flux ratio to Se, typically ran at 9-20 secs/ML depending on cell temperature.

(2) Close Mn and Se shutters and cool to room temperature (unless capping with more $SnSe_2$, then close Mn shutter and re-open Ga until capping thickness reached).

(3) Cap with amorphous chalcogen material.

For growth on Bi_2Se_3/sapphire(0001):

(1) De-cap Bi_2Se_3 surface for 30 min. (annealing temperature around 200°C.

(2) Deposit Mn and Se below the decomposition temperature of Bi_2Se_3 for appropriate time.

(3) Close Mn and Se shutters, then cool down to room temperature

(4) Cap or transfer to another vacuum chamber via vacuum suitcase.

B.4 VSe_2 growth on GaAs(111)B

(1) Mount cleaved 10 × 10 mm^2 GaAs(111)B substrate to un-polished Si(100) backing wafer via indium bonding.

(2) Mount backing wafer onto uni-block and trolley.

(3) Load into load lock chamber and pump down to rough vacuum. Anneal at 200°C for 1 hour, then cool down.

(4) Open to buffer chamber and load sample onto buffer heater.

(5) Anneal sample at 400°C for 15 minutes then cool down to room temperature.

(6) In the meantime, measure beam fluxes of V and Se cracker to be 1:1000 flux ratio. The V is operated via the quad *e*-beam evaporator and needs to be operated at a moderate power which varies with the length of the rod. Lifetime of the rods are low, it is advised to have more than 1-2 rods during a growth run on the chamber (between maintenance periods).

(7) Load sample into main chamber after measuring fluxes and heat sample to 600°C.

(8) Anneal for 20 min. with Se open until native oxide is removed and GaAs RHEED pattern appears.

(9) Cool down to 200°C with Se remaining open.

(10) Open V and Se shutters at 200°C and grow for desired time.

(11) Close both shutters, and cool to room temperature.

(12) If necessary, cap with amorphous chalcogen material (Se or Te).